

博士論文

Development of Molecular Materials with Multifunctional Properties Based on  
Magnetism in Transition Metal Complexes

(磁性遷移金属錯体を基盤とした多重機能性を有する分子性固体の開発)

亀 潤 萌

**Development of Molecular Materials with Multifunctional Properties Based on  
Magnetism in Transition Metal Complexes**

A thesis submitted in partial fulfillment of the requirements for the degree of  
Doctor of Philosophy at The University of Tokyo.

by

Hajime Kamebuchi

© Hajime Kamebuchi, 2014

The University of Tokyo

All rights reserved. This thesis may not be reproduced in whole or in part, by photocopy  
or other means, without the permission of the author.

# **Supervisory Committee**

## **Development of Molecular Materials with Multifunctional Properties Based on Magnetism in Transition Metal Complexes**

by

Hajime Kamebuchi

The University of Tokyo, 2014

### **Supervisory Committee**

Dr. Norimichi Kojima, (Department of Basic Science, Graduate School of Arts and Sciences)  
**Supervisor**

Dr. Shuichi Hiraoka, (Department of Basic Science, Graduate School of Arts and Sciences)  
**Departmental Member**

Dr. Shin-ichi Nishikiori, (Department of Basic Science, Graduate School of Arts and Sciences)  
**Departmental Member**

Dr. Sayaka Uchida, (Department of Basic Science, Graduate School of Arts and Sciences)  
**Departmental Member**

Dr. Hiroshi Nishihara, (Department of Chemistry, School of Science)  
**Outside Member**

## Acknowledgments

This study was carried out at Graduate School of Arts and Sciences, The University of Tokyo, in the years 2010–2014. I am truly grateful for everyone who made this study possible.

My deepest gratitude goes to my supervisor Professor Norimichi Kojima. I appreciate the working environment and opportunities that he provided. He has been the pillar of strength and the driving force behind my Ph.D. studies. His laboratory is a truly unique place in so many ways. I have enjoyed interacting with my labmates both scientifically and socially.

I extend genuine thanks to Dr. Atsushi Okazawa for providing rich insights, questions, and advices as an assistant professor of Kojima's lab. In addition, he shared the challenges and joys of this study with me at any time and found time to review this thesis.

Many thanks to people who contributed at different stages during my graduate career: Dr. Yuki Wakisaka (Institute for Molecular Science) and Associate Professor Takashi Mizokawa (The University of Tokyo) for XAFS experiments, Associate Professor Jun Harada (Hokkaido University) and Professor Keiichiro Ogawa (The University of Tokyo) for X-ray crystallographic analysis, Dr. Goro Maruta (Hokkaido University) and Professor Sadamu Takeda (Hokkaido University) for solid-state  $^2\text{H}$ -MAS-NMR measurements, and Professor Cyrille Train (Laboratoire National des Champs Magnétiques Intenses, Université Joseph Fourier) and Professor Michel Verdaguer (Université Pierre et Marie Curie-Paris 6) for establishing the verdazyl-radical coordinated iron(II) system regarding Chapter 7. They are all my collaborators and true specialists in their fields.

Numerous people have influenced my graduate career both directly and indirectly including all the present and past members of Kojima's lab at the Graduate School of Arts and Sciences. This outstanding group has also grown and changed during the years, but retained the warm and welcoming atmosphere. They are all terrific people and I grateful for the chance to work with them and get to know them. Special thanks to Dr. Masaya Enomoto for his considerable help and valuable advice on conducting this research, and to Dr. Hideharu Shimizu, Taketomo Jo, Satoshi Tamaki, and Yu Fujimura for making every effort to develop the multifunctional films regarding Chapter 3 and 4 in collaboration with me.

Financial support was provided by Grant-in-Aid for JSPS Fellows from Japan Society for the

Promotion of Science (JSPS).

Last but not least, I would like to thank my family for their unconditional and vital support.

December 2014

Hajime Kamebuchi

# Contents

<b>Chapter 1. General Introduction</b> .....	1
1.1 Background of Materials Chemistry: A Historical Review .....	1
1.2 Materials Chemistry Based on Transition Metal Complexes .....	2
1.3 Molecular Magnetism .....	3
1.4 Metal–Radical Complexes .....	10
1.5 Spin-Crossover Complexes .....	14
1.5.1 Spin-crossover phenomenon .....	14
1.5.2 Light induced excited spin state trapping (LIESST) and its limitation .....	18
1.6 Organic–Inorganic Hybrid System .....	23
1.7 Aims of This Thesis .....	28
References .....	31
<b>Chapter 2. Experimental Theory</b> .....	36
2.1 Molecular Magnetism .....	36
2.1.1 Definitions and Fundamental Equations .....	36
2.1.2 Van Vleck Formula .....	38
2.1.3 Curie’s Law .....	39
2.1.4 Magnetism in Multinuclear Complexes .....	41
2.2 XAFS Spectroscopy .....	46
2.2.1 XANES .....	48
2.2.2 EXAFS .....	49
2.3 <sup>57</sup> Fe Mössbauer Spectroscopy .....	52
2.3.1 Isomer Shift .....	55
2.3.2 Quadrupole Splitting .....	58
2.4 Alternative Current Impedance Method .....	61
2.5 Solid State NMR Spectroscopy .....	66
2.5.1 Nuclear Dipole Interactions .....	66
2.5.2 Magic Angle Spinning (MAS) .....	68
2.5.3 Nuclear Quadrupolar Interactions and Detection of Molecular Motion .....	69
References .....	73

<b>Chapter 3. Development of a Proton Responsive Spin-Crossover Complex Film and Its Control of the Spin State Accompanied by Proton Flow</b>	75
3.1 Introduction	76
3.2 Materials and Methods	80
3.3 Results and Discussion	83
3.4 Conclusion	97
References	98
<b>Chapter 4. Development of the Transparent Films with pH-Sensitive Emission Properties</b>	101
4.1 Introduction	102
4.2 pH-Sensitive Emission in Metal Complexes	103
4.3 Materials and Methods	106
4.3.1 Synthesis of [(bpy) <sub>2</sub> Ru <sup>II</sup> (H <sub>2</sub> bpib)Ru <sup>II</sup> (bpy) <sub>2</sub> ](ClO <sub>4</sub> ) <sub>4</sub> •3H <sub>2</sub> O ( <b>1</b> )	106
4.3.2 Preparation of <b>1</b> @Nafion	107
4.3.3 Synthesis of [Ir <sup>III</sup> (Hbip)(Mebib)](PF <sub>6</sub> ) <sub>2</sub> ( <b>2</b> )	108
4.3.4 Preparation of <b>2</b> @Nafion	108
4.3.5 Optical spectroscopy	109
4.3.6 Quantum yield and lifetime measurements	109
4.3.7 Applying voltage to the emissive films	110
4.3.8 Proton conductivity	112
4.4 Results and Discussion	113
4.4.1 [(bpy) <sub>2</sub> Ru <sup>II</sup> (H <sub>2</sub> bpib)Ru <sup>II</sup> (bpy) <sub>2</sub> ] <b>@Nafion</b> ( <b>1</b> @Nafion)	113
4.4.2 [Ir <sup>III</sup> (Hbip)(Mebib)] <b>@Nafion</b> ( <b>2</b> @Nafion)	120
4.5 Conclusion	131
References	132
<b>Chapter 5. Fastener Effect on Uniaxial Chemical Pressure for One-Dimensional Spin-Crossover System, [Fe<sup>II</sup>(NH<sub>2</sub>-trz)<sub>3</sub>](C<sub>n</sub>H<sub>2n+1</sub>SO<sub>3</sub>)<sub>2</sub>•xH<sub>2</sub>O: Magnetostructural Correlation and Ligand Field Analysis</b>	134
5.1 Introduction	135
5.2 Review of the Material	139
5.3 Materials and Methods	154
5.4 Results and Discussion	156

5.5 Conclusion .....	170
References .....	172
<b>Chapter 6. Magnetic Switching by Photo-Irradiation in the Spin-Crossover</b>	
<b>Iron(III) Complex with Photoisomerizable Counteranion .....</b>	<b>178</b>
6.1 Introduction .....	179
6.2 Counteranion Dependence of Magnetism in $[\text{Fe}^{\text{III}}(\text{qsal})_2]\text{X}$ .....	182
6.3 Materials and Methods .....	188
6.4 Results and Discussion .....	190
6.5 Conclusion .....	203
References .....	204
<b>Chapter 7. A Tricky Water Molecule Coordinated to</b>	
<b>a Verdazyl Radical–Iron(II) Complex:</b>	
<b>A Multitechnique Approach .....</b>	<b>206</b>
7.1 Introduction .....	207
7.2 Materials and Methods .....	209
7.3 Results .....	212
7.4 Discussion .....	236
7.5 Conclusion .....	243
References .....	244
<b>Chapter 8. General Conclusions and Perspectives .....</b>	<b>247</b>

# 1. General Introduction

## 1.1 Background of Materials Chemistry: A Historical Review

In materials chemistry, the physical and chemical properties of elements are studied, and various molecular aggregates are then developed by freely manipulating these elements. Materials chemistry is a field focused on producing new functionality and novel physical properties, and is the essence of materials science. As atoms and molecules collectively form aggregates, various physical properties that cannot exist in isolated atoms and molecules can now be achieved, and these include optical properties, magnetic properties, and electrical properties, *etc.* In recent years, attractive physical properties, such as high-temperature superconductivity and ferromagnetism, have been realized not only in inorganic materials but also in molecular crystals. Research conducted in this field is not limited to solid-state physicists; rather, the molecular science can be developed by researchers in a wide range of fields, such as organic chemistry, coordination chemistry, biology, *etc.*

Historically, the subjects of research on solid state property have been inorganic compounds, which were developed from the viewpoint of both a basic understanding and future applications. However, at the mid-20th century, new organic materials became the subject of research on solid state property. Organic materials have the advantages of being lightweight, possessing diverse dimensionality, and being easy to process, *etc.* This field is expected to continue to develop in the future. On the other hand, the use of metal complexes as subjects of research on solid state property is relatively recent, beginning only in the latter half of the 20th century.

## **1.2 Materials Chemistry Based on Transition Metal Complexes**

Transition metal complexes are positioned at the crossroads of inorganic and organic materials, and combine the excellent properties of both organic and inorganic substances. These properties include the various electronic states possessed by transition metal ions, as well as the control of dimensionality and the electron donor-acceptor ability possessed by ligands. By combining them well, the resultant physical properties of the metal complex can be expected to exceed those of the inorganic and organic substances. For example, single-molecule magnets are molecule-based nanomagnets with high-spin ground states and uniaxial magnetic anisotropy due to double-minimum potentials for the spin sublevels. These molecules behave like magnets, showing slow magnetic relaxation at low temperatures. This is a behavior specific to the metal complex, and is not observed in organic or inorganic material alone. In addition, if the low-spin and high-spin states have ligand fields in a competing region, the “spin crossover phenomenon”, that is, a change in the spin states with regards to the original ground state in the same molecule, is observed by changing external conditions such as the temperature and pressure; this phenomenon is also specific to the metal complex. Furthermore, in a hybrid system of metal complexes and organic molecules, novel physical properties, such as magnetic-field-induced superconductivity or the coexistence of ferromagnetism and conductivity, have been widely reported. Metal complexes thus have the potential to exhibit attractive physical properties by utilizing the synergistic effects of organic and inorganic materials; this field is strongly expected to be further developed in the future.

## 1.3 Molecular Magnetism

Among the substances known as magnets, various materials are included, such as metals, metal oxides, alloys, transition metal complexes, and organic magnets. Of these materials, transition metal complex and organic magnets as molecular building blocks are generally referred to as molecular magnetic materials. Due to their high designability, great deal of studies have been carried out, and the major field known as molecular magnetism has been established.

Molecular magnetic materials have many distinctive characteristics compared to those of existing inorganic magnets. Research on these materials is thus distinct from that on inorganic magnetic materials which aim for a strong magnetic force, large coercivity, *etc.* By elucidating the mechanisms of ferromagnetic and antiferromagnetic interactions on a molecular level, the manipulation of magnetic characteristics by controlling external perturbations, which most recently include light and pressure, can be achieved in molecular magnets. This is in addition to switching from ferromagnetic/antiferromagnetic behavior. Studies on material design for the control of the magnetic properties have also been conducted extensively.

Studies on organic magnets have developed greatly, beginning from the discovery of multiplet carbene by Ito and the confirmation of its  $S = 2$  state via ESR measurement in 1967 (Figure 1.1).<sup>[1]</sup> The origin of paramagnetism is magnetic moments derived from the spins of unpaired electrons; many electron spins aligned in the same direction display ferromagnetism. Most of organic molecules are diamagnetic because they often have even numbers of electrons which are all paired up. Though radicals have unpaired electrons, aligning the spin direction within molecules in an intra- or intermolecular manner was considered to be difficult. However, Ito's report suggested that if the orientation of the minority spin is aligned, it should then be possible to create a ferromagnetic

material even in organic materials. Thereafter, the first organic ferromagnet, *p*-nitrophenyl nitronyl nitroxide (*p*-NPNN), was discovered by Tamura *et al.* in 1991, revealing that the radical spins are aligned between molecules within the crystal (Figure 1.2).<sup>[2]</sup> Furthermore, in 2000, a modified molecule with nitronyl nitroxide radicals on both ends of diarylethene, a photoisomerization molecule, was synthesized by Matsuda *et al.* Along with the isomerization from the open-form of diarylethene to a closed-form, the optical switching of magnetic interaction between radicals was reported (Figure 1.3).<sup>[3]</sup> In this way, a magnetic property was added to an organic compound not considered to be related to magnetic raw materials, and profound academic contributions to areas such as synthesis techniques and the quantitative understanding of magnetic interactions have been made up to this day.

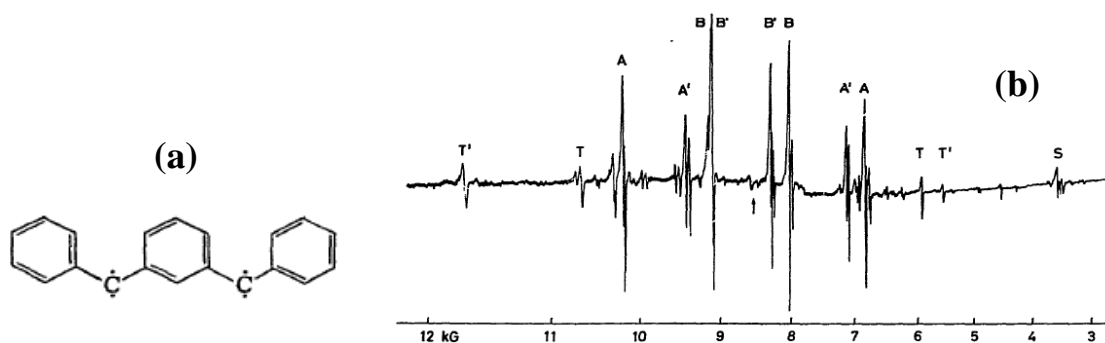


**Figure 1.1.** (a) Molecular structure of a multiplet carbene and (b) the ESR spectra.<sup>[1]</sup>

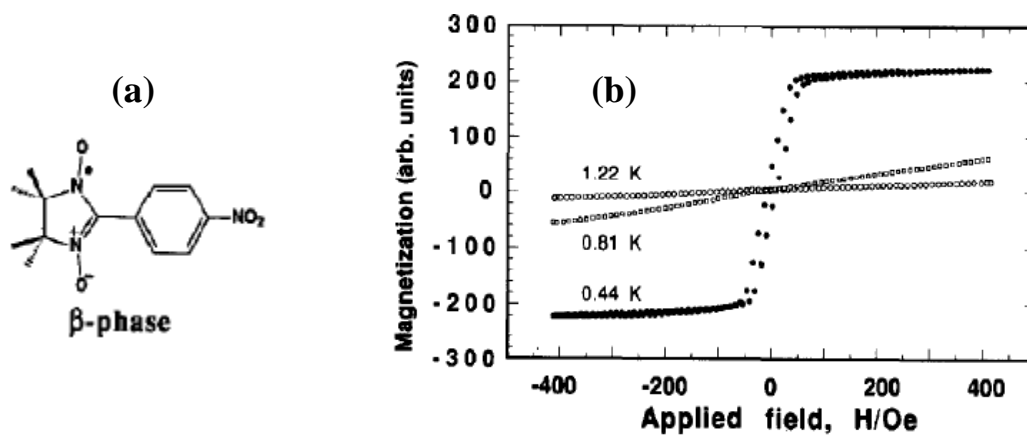


**Figure 1.2.** (a) Molecular structure of *p*-nitrophenyl nitronyl nitroxide (*p*-NPNN) in the  $\beta$ -phase and (b) the magnetization curve of *p*-NPNN ( $T_c = 0.60$  K).<sup>[2]</sup>

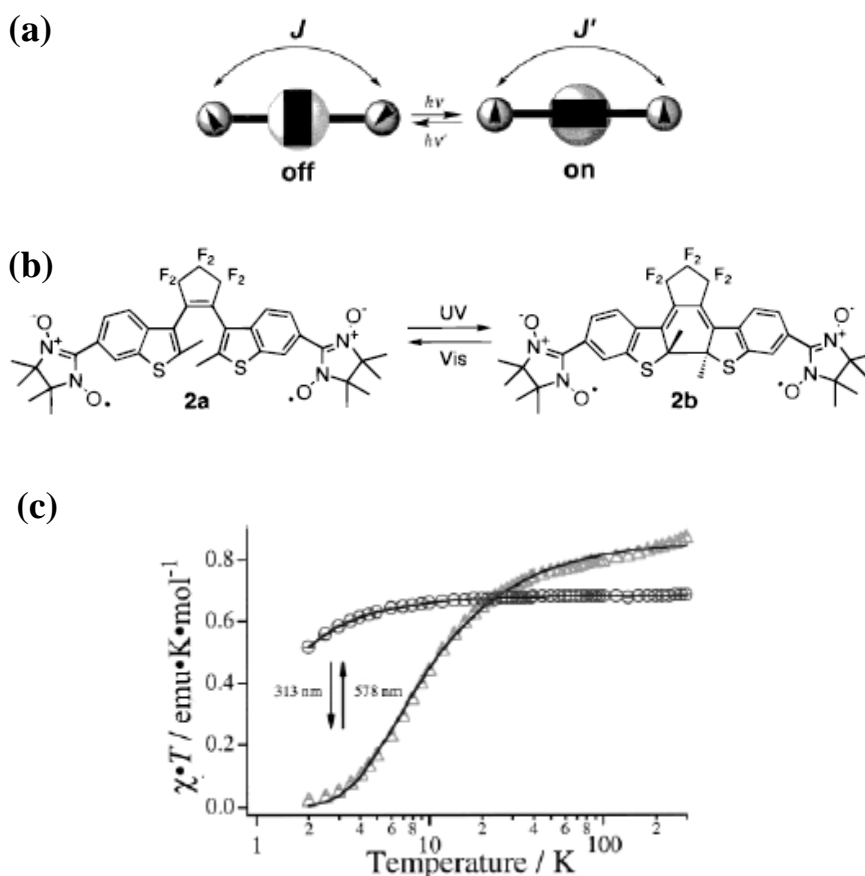


**Figure 1.3.** (a) Concept of photo-switching of magnetic interactions, (b) the photoisomerization of diarylethene with nitronyl nitroxide radicals, and (c) the changes in magnetic interactions due to the photoisomerization of the diarylethene derivative.<sup>[3]</sup>

For metal complexes, research on the development of materials utilizing the various spin states of transition metal ions and the control of dimensionality achieved with ligands has been conducted extensively. In recent years, the synthetic methods of various low-dimensional magnetic materials and assembled metal complexes have been established. Moreover, the discovery of novel functionality has much attracted attention due to the magnetic interaction between the metal ions and a controlled spin space.

One of the critical issues in molecular magnetism is the development of ferromagnetic materials with a high magnetic-transition temperature (high-temperature ferromagnets). A molecular magnetic material generally has weak intermolecular magnetic interactions, acting as a magnet at very low temperatures in many cases. However, in 1995, Ferlay *et al.* reported on a room temperature ferrimagnetic material  $V^{II}_{0.42}V^{III}_{0.58}[Cr^{III}(CN)_6]_{0.86} \cdot 2.8H_2O$  ( $T_c = 315$  K) based on Prussian blue analogues (Figure 1.4).<sup>[4]</sup> Concerning the magnetic interaction between  $M^{II}$  and  $Cr^{III}$  ( $t_{2g}^3$ ;  $S = 3/2$ ) in  $M^{II}[Cr^{III}(CN)_6]_{2/3} \cdot zH_2O$  ( $M = V, Cr, Mn, etc.$ ), the antiferromagnetic interaction between the  $t_{2g}$  orbitals competes with the ferromagnetic interaction between the  $t_{2g}$ - $e_g$  orbitals; when  $M = Ni, Cu, etc.$ , it becomes a ferromagnetic material; when  $M = Cr, Mn, etc.$ , it becomes a ferrimagnetic material. In the compound  $V^{II}_{0.42}V^{III}_{0.58}[Cr^{III}(CN)_6]_{0.86} \cdot 2.8H_2O$ , which contains vanadium ions without spins in the  $e_g$  orbitals, the strong antiferromagnetic interaction between the  $t_{2g}$  orbitals was maximized by canceling the ferromagnetic interaction between the  $t_{2g}$  orbitals and the  $e_g$  orbitals. Following that, in 1999, in addition to the  $K^IV^{II}[Cr^{III}(CN)_6]$  ( $T_c = 376$  K) compound reported by Holmes *et al.*,<sup>[5]</sup> Hatlevik *et al.* reported on a  $K^I_{0.058}V^{II/III}[Cr^{III}(CN)_6]_{0.79}(SO_4)_{0.058} \cdot 0.93H_2O$  ( $T_c = 372$  K) compound.<sup>[6]</sup>

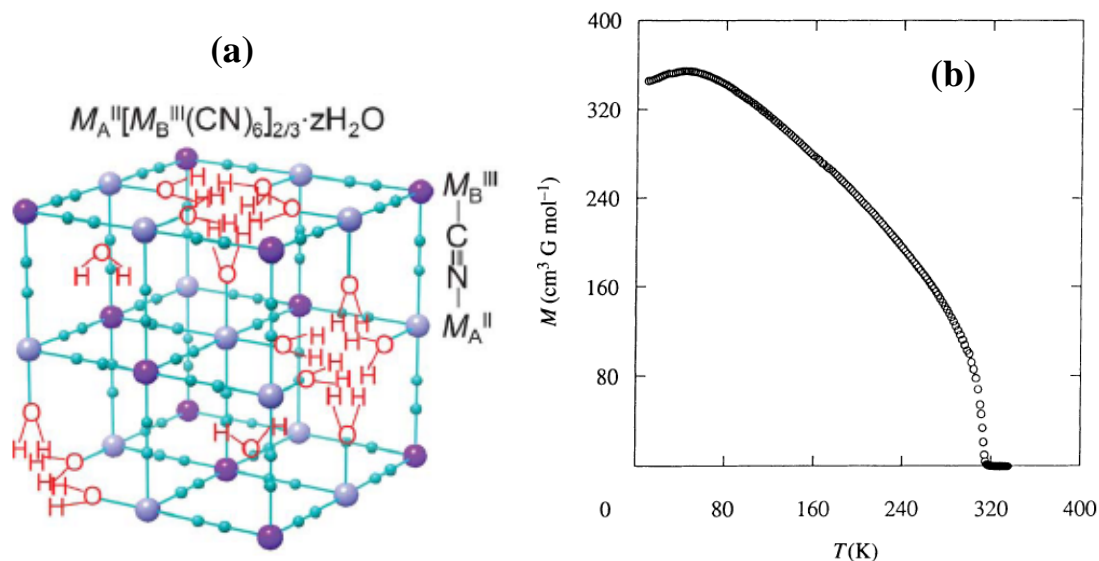


**Figure 1.4.** (a) Schematic illustration of the crystal structure of  $M_A^{II}[M_B^{III}(CN)_6]_{2/3} \cdot zH_2O$ ,<sup>[7]</sup> and (b) the temperature dependence of the magnetization of  $V^{II}_{0.42}V^{III}_{0.58}[Cr^{III}(CN)_6]_{0.86} \cdot 2.8H_2O$  under the weak magnetic field ( $H = 10$  G).<sup>[4]</sup>

Single-molecule magnets have recently become one of the most popular topics in molecular magnetism. The first single-molecule magnet was the Mn12 cluster,  $[Mn_{12}O_{12}(O_2CR)_{16}(H_2O)_4]$  ( $R = CH_3, C_2H_5, Ph, etc.$ ), developed by Sessoli and Gatteschi *et al.* in 1993. (Figure 1.5).<sup>[8,9]</sup> Spins in  $Mn^{IV}$  ( $S = 3/2$ ) and  $Mn^{III}$  ( $S = 2$ ) are antiferromagnetically coupled, resulting in the  $S = 10$  ground state. Furthermore, the magnetic anisotropy originates from the eight  $Mn^{III}$  ions with Jahn-Teller distortion; as the Jahn-Teller axes are substantially aligned in parallel, a large uniaxial anisotropy ( $D = -0.50$  cm<sup>-1</sup>) exists in the molecule. When considering a double-well potential model, a large energy barrier ( $DS_z^2$ ) must be overcome in order to cause a spin reversal. Therefore, at cryogenic temperatures, a slow magnetic relaxation is observed for this energy barrier, and a single molecule momentarily exhibits behavior as if it was a magnet (Figure 1.6).

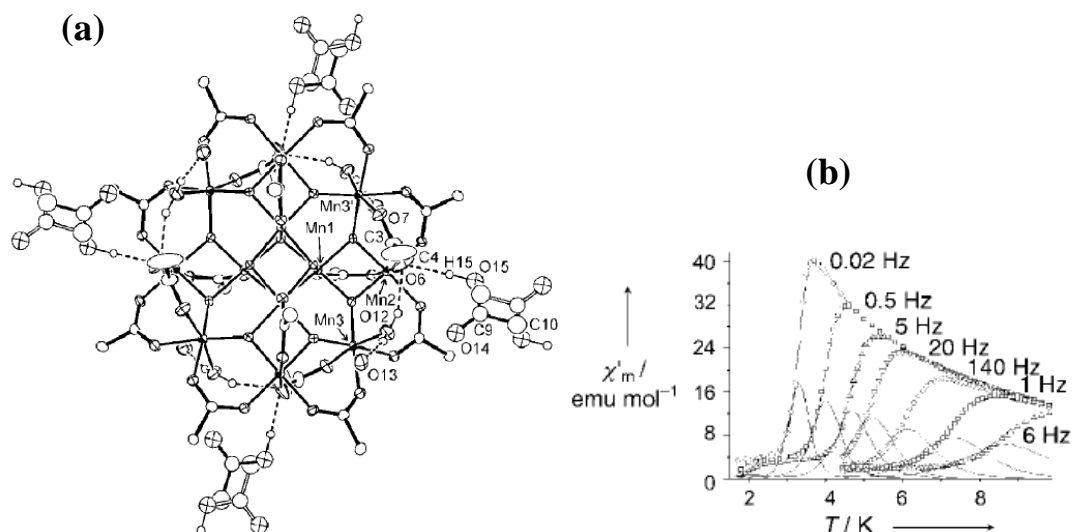


**Figure 1.5.** (a) ORTEP view of  $[\text{Mn}_{12}\text{O}_{12}(\text{CH}_3\text{COO})_{16}(\text{H}_2\text{O})_4]\cdot 2\text{CH}_3\text{COOH}\cdot 4\text{H}_2\text{O}$ , and (b) temperature and frequency dependences of the AC susceptibility (real part).<sup>[10]</sup>

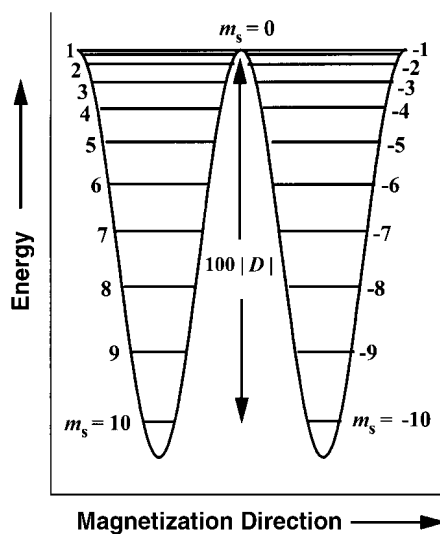


**Figure 1.6.** Energy potential of the Mn12 cluster ( $S = 10$ ) in zero field.<sup>[11]</sup>

Currently, in addition to the examples cited earlier, many other single-molecule magnets have also been reported. Famous ones include the Fe14 cluster by Evangelisti *et al.*,<sup>[12]</sup> the Cr7Ni heterometallic wheel by Ardavan *et al.*,<sup>[13]</sup> the Mn6 complex by Milios *et al.*,<sup>[14]</sup> *etc.* Furthermore, on top of the single-chain magnets reported by Caneschi *et al.* in 2001,<sup>[15]</sup> Ishikawa *et al.* reported in 2003 on a double-decker phthalocyanine complex using rare earth ions, which showed

single-molecule magnet behavior as a mononuclear species.<sup>[16]</sup> Great interest has therefore been generated in the concept of a single-molecule magnet that can become nanoscale magnetic memory. This is in contrast to the minimum unit of magnetic memory for a conventional magnet with a magnetic domain (sub-micron size). In order to improve the performance of single-molecule magnets, it is necessary to increase the height of the potential barrier ( $U = DS_z^2$ ). This can be achieved by increasing the spin quantum number ( $S$ ) and the magnetic anisotropy ( $D$ ), leading to the drastic improvement of the operating temperature (blocking temperature;  $T_B$ ) where a compound behaves as a single-molecule magnet.

## 1.4 Metal–Radical Complexes

As mentioned in the previous section, molecular magnetic materials have excellent advantages such as controllable physical properties utilizing the designability and multifunctionalization by the introduction of substituents. Meanwhile, the weak interaction between the molecules is a key drawback. The development of high-temperature ferromagnetic materials has therefore become an important issue in molecular magnetism. A promising technique that has attracted attention is the coordination of organic radicals into the transition metal ion directly. The realization of strong magnetic interaction is expected to be achieved by directly coordinating organic radicals with unpaired electrons to paramagnetic metal ions. This has the advantage of allowing for the control of the orthogonality between the 2p orbitals of the radicals and the d-orbitals or f-orbitals of the metal ions, through the selection of appropriate ligands. If the orbitals of the radicals and the metal ions strongly overlap, the spin directions become antiparallel to each other (antiferromagnetic interaction); if the orbitals are orthogonal, it is anticipated that the spin directions will be parallel to each other (ferromagnetic interaction). In this, let us consider nitroxide radicals as examples. For instance, for nitroxides coordinated to the axial site of metal ions with magnetic orbitals in  $d_{x^2-y^2}$  (Figure 1.7a), the magnetic orbitals between the radicals with a spin in  $\pi^*$  orbital and the metal ions are orthogonal to each other; these spins are considered to be coupled ferromagnetically. This case is uncommonly seen in copper(II) complexes.<sup>[17-20]</sup> Conversely, Figure 1.7b shows the case commonly found in copper(II) complexes, where the radicals are coordinated to the equatorial site. When the M-O-N angle is not at  $180^\circ$ , the overlap of the magnetic orbitals becomes great; the radical-metal spins are anticipated to be coupled antiferromagnetically, and extremely strong antiferromagnetic interaction has been observed experimentally.<sup>[21-24]</sup> The manner of overlapping of the magnetic

orbitals, as shown in Figure 1.7c and Figure 1.7d, can be seen in nickel(II) complexes,<sup>[25,26]</sup> cobalt(II) complexes,<sup>[26]</sup> and manganese(II) complexes.<sup>[27,28]</sup> In combination with hexafluoroacetylacetonate (hfac) in  $M(\text{hfac})_2(\text{RNO})_2$  type complexes, strong antiferromagnetic interactions have also been observed experimentally.

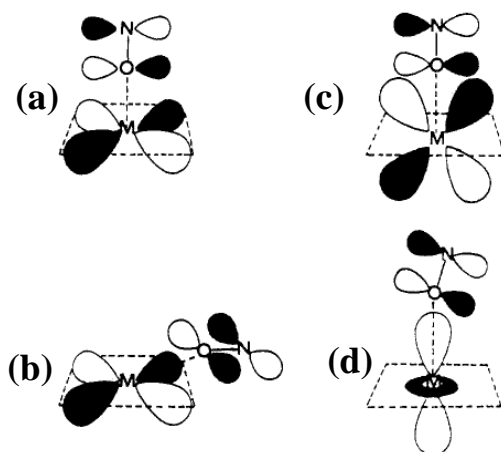


**Figure 1.7.** Several types of orbital overlap between d orbital of metal ion and  $\pi^*$  orbital of nitroxide radical.<sup>[29]</sup>

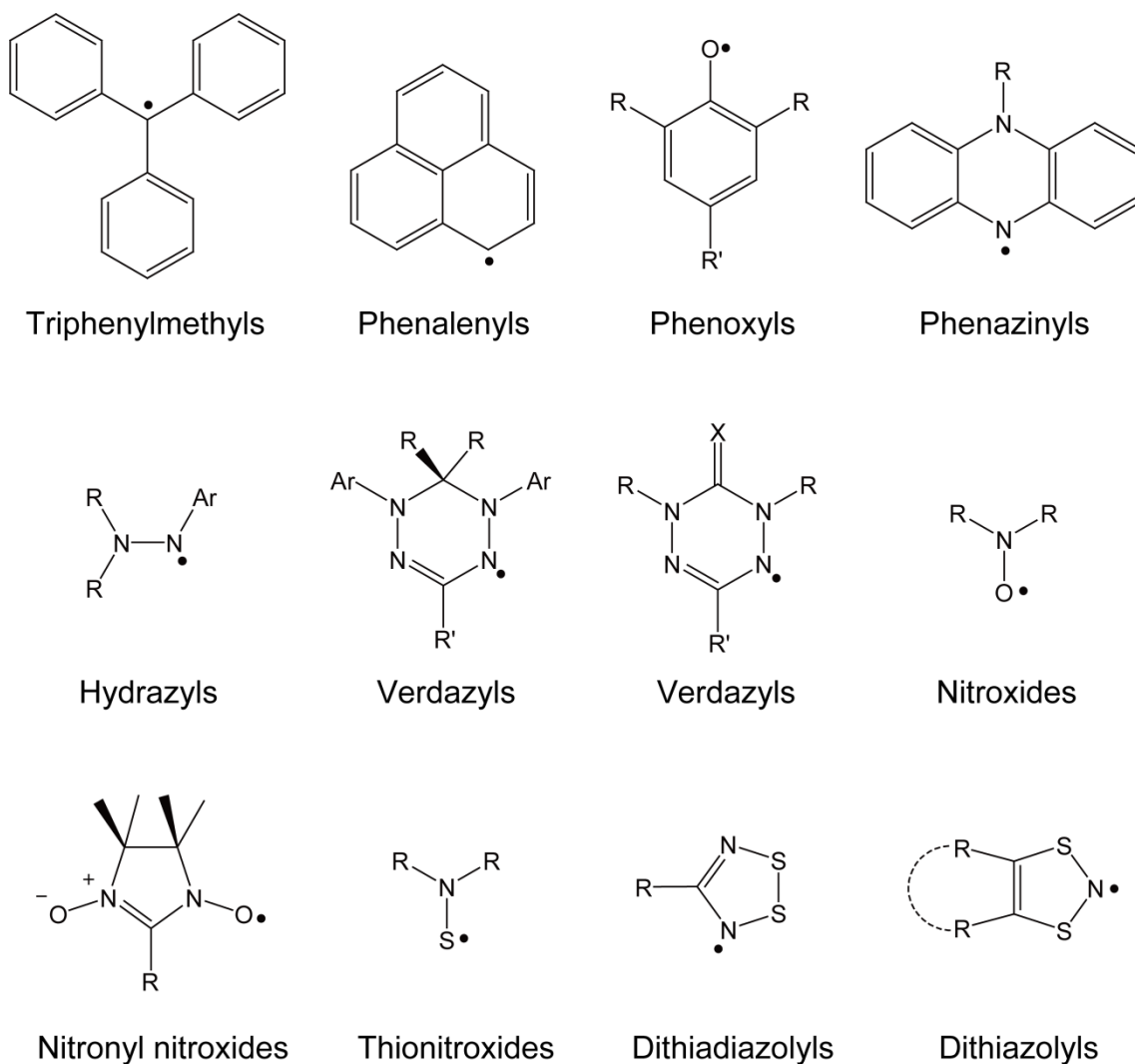


**Figure 1.8.** A variety of stable radicals.

By designing a complex with a coordination environment in which the  $\pi$  and  $d\sigma$  orbitals (orbitals with  $\sigma$  symmetry around the coordination bonds, such as  $d_{x^2-y^2}$  and  $d_{z^2}$ ) are orthogonal, it is possible to obtain ferromagnetic coupled molecules with a high-spin ground state between the spins in radical-transition metal ion. Using such a molecular design to attempt to construct molecular magnetic materials composed of radicals and metal ions is known as the "metal-radical approach".<sup>[29]</sup> As shown in Figure 1.8, various stable radicals<sup>[30]</sup> are used, and their ferromagnetic coupling has been very well-studied by manipulating the orthogonality between their magnetic orbitals.<sup>[31-34]</sup>

However, while it is necessary to be magnetically ordered in three dimensions when attempting to create a magnet, it is still difficult to control the structure of molecular magnetic materials in three dimensions, and only a few cases of substances becoming ferromagnetic at room temperature have been reported.<sup>[35,36]</sup> In the future, it is desired to develop a molecular ferromagnet whose magnetic ordering temperature is close to room temperature by molecular design and synthesis.

## 1.5 Spin-Crossover Complexes

### 1.5.1 Spin-crossover phenomenon

In six-coordinated transition metal ions with an octahedral symmetry, the five degenerate d-orbitals are split into three  $t_{2g}$  orbitals ( $d_{xy}$ ,  $d_{yz}$ ,  $d_{zx}$ ) and two  $e_g$  orbitals ( $d_{x^2-y^2}$ ,  $d_{z^2}$ ). This is known as ligand field splitting, and the magnitude of the d-d splitting is often expressed as  $10Dq$ . For example, in iron(II) ions ( $d^6$ ), when  $10Dq$  is small compared with the spin pairing energy, the electrons are accommodated in accordance with Hund's rule, avoiding electron-electron repulsion, and the paramagnetic high-spin state ( $S = 2$ ) becomes the ground state. When  $10Dq$  is large, all of the electrons are accommodated in the  $t_{2g}$  orbitals, breaking Hund's rule, and the non-magnetic low-spin state ( $S = 0$ ) becomes the ground state (Figure 1.9). It comes to the same thing as follows. When  $10Dq$  is small, as many spins as possible are placed in different orbitals in parallel because there is a affective gain in exchange energy due to the reduced electron-electron repulsion. This is similar to free ions. Conversely, when  $10Dq$  is large, the gain in orbital energy caused by placing all of the electrons in the  $t_{2g}$  orbital exceeds the gain in exchange energy.

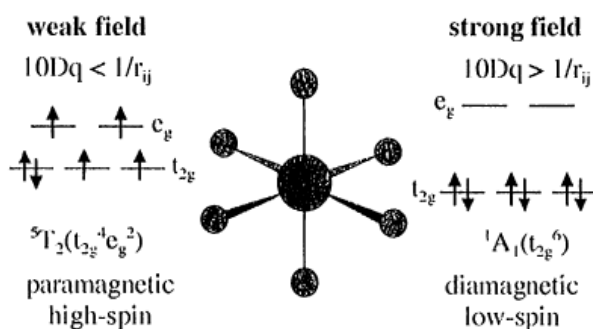


**Figure 1.9.** Two types of the electronic configuration as ground states in six-coordinated iron(II) complex with octahedral symmetry.<sup>[37]</sup>

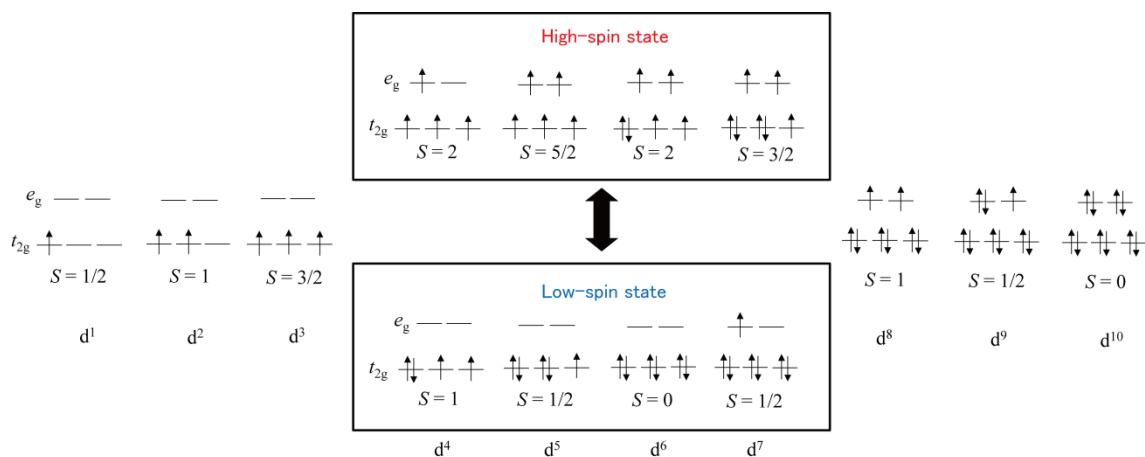


**Figure 1.10.** Possible spin ground states in six-coordinated transition metal complexes with octahedral symmetry.

In general, transition metal complexes with electron configurations of  $d^4$ – $d^7$  in the octahedral ligand field can take up two kinds of electron configurations as the ground state (Figure 1.10). This can be easily understood by looking at the Tanabe-Sugano diagram (Figure 1.11). The energy level diagram shows energy on the vertical axis and  $Dq/B$  on the horizontal axis ( $B$  is a Racah parameter). In the transition metal complex with a  $d^6$  electron configuration, there is a switch in the ground state at the boundary  $Dq/B = 2$ . Therefore, it is possible that the high-spin state and the low-spin state can be changed reversibly by external perturbations, such as the temperature, pressure, light, and the magnetic field around  $Dq/B = 2$  in the  $d^6$  complex. Such a phenomenon is known as the spin-crossover phenomenon. A metal complex exhibiting the spin-crossover phenomenon is referred to as a spin-crossover complex.

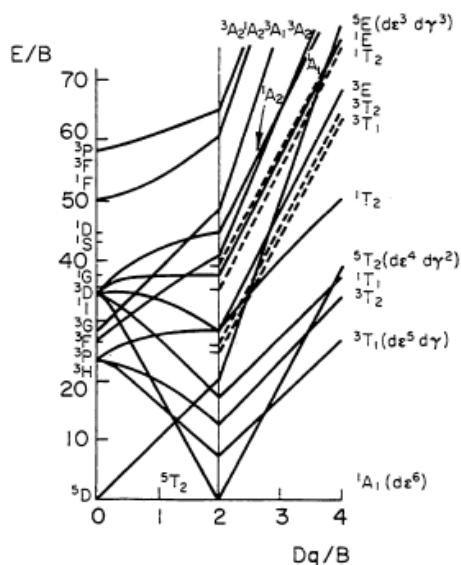


**Figure 1.11.** Tanabe-Sugano diagram for complexes with  $d^6$  electronic configuration.<sup>[38]</sup>

As background on the study of spin-crossover phenomenon, the iron(III) tris-dithiocarbamate complex,  $[\text{Fe}^{\text{III}}(\text{S}_2\text{CNRR}')_3]$ , reported by Cambi *et al.* in 1931 showed the abnormal temperature dependence of magnetic susceptibility.<sup>[39]</sup> This behavior was later explained using the spin-crossover behavior as a clue. Even now, many spin-crossover complexes are still being studied. The possibility of the spin-crossover phenomenon was pointed out theoretically by Tanabe and Sugano in 1954.<sup>[40]</sup> Baker and Boronich reported on the magnetic anomaly of the first spin-crossover iron(II) complex,  $[\text{Fe}^{\text{II}}(\text{phen})_2(\text{NCS})_2]$  (phen = 1,10-phenanthroline), in 1964.<sup>[41]</sup> In 1967, this magnetic anomaly was experimentally proven to be a spin-crossover phenomenon by König and Madeja (Figure 1.12).<sup>[42]</sup> Since then, spin-crossover iron (III) complexes<sup>[43]</sup> and cobalt(II) complexes<sup>[44]</sup> have also been reported. Among them, on top of being the most reported case, iron(II) complexes have attracted great deal of attention as molecular devices as they exhibit a spin change from paramagnetic ( $S = 2$ ) to non-magnetic ( $S = 0$ ). Extensive research is therefore being conducted on these complexes.<sup>[34,45]</sup>

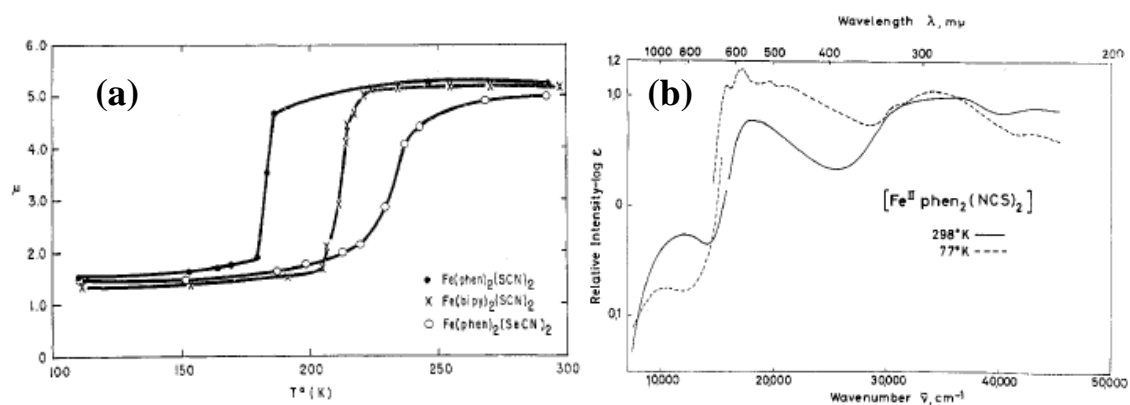


**Figure 1.12.** (a) Temperature dependence of the magnetic moment for  $[\text{Fe}^{\text{II}}(\text{phen})_2(\text{NCX})_2]$  ( $X = \text{S}, \text{Se}$ ),<sup>[41]</sup> and (b) temperature dependence of the optical absorption spectra for  $[\text{Fe}^{\text{II}}(\text{phen})_2(\text{NCS})_2]$ . The absorption intensity corresponding to the high-spin state ( $S = 2$ ;  ${}^5\text{T}_{2g} \rightarrow {}^5\text{E}_g$ ) is decreased by cooling, whereas that corresponding to the low-spin state ( $S = 0$ ;  ${}^1\text{A}_{1g} \rightarrow {}^1\text{T}_{1g}$ ) is increased.<sup>[42]</sup>

## 1.5.2 Light induced excited spin state trapping (LIESST) and its limitation

So far, many iron and cobalt spin-crossover complexes have been reported. Among them,  $[\text{Fe}(\text{ptz})_6](\text{BF}_4)_2$  (ptz = 1-propyltetrazole) uniquely exhibits a low-spin-to-high-spin change when irradiated at a low temperature with light corresponding to the optical transition between the d orbitals, yet the spin state after the transition is trapped (Figure 1.13).<sup>[46,47]</sup>

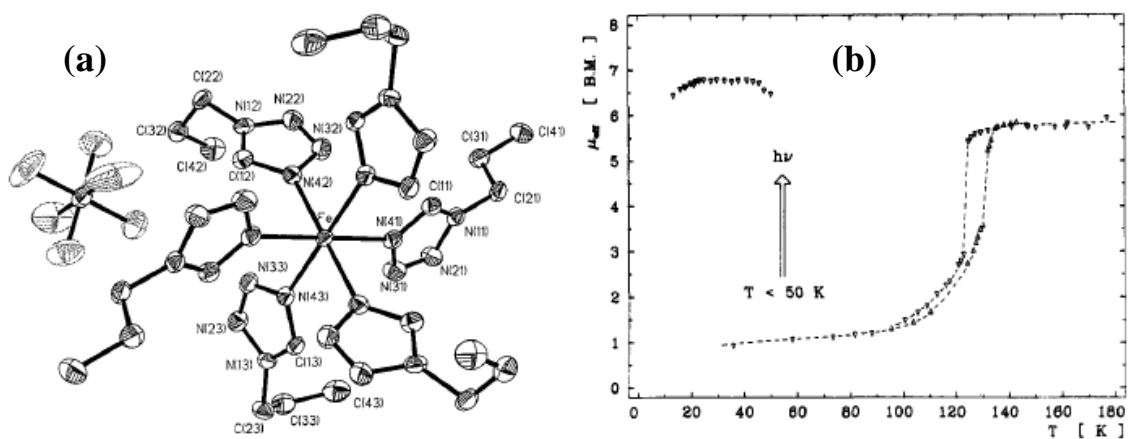


**Figure 1.13.** (a) Crystal structure of  $[\text{Fe}(\text{ptz})_6](\text{PF}_6)_2$ ,<sup>[48]</sup> and (b) temperature dependence of effective magnetic moment for  $[\text{Fe}(\text{ptz})_6](\text{BF}_4)_2$ .<sup>[49]</sup>

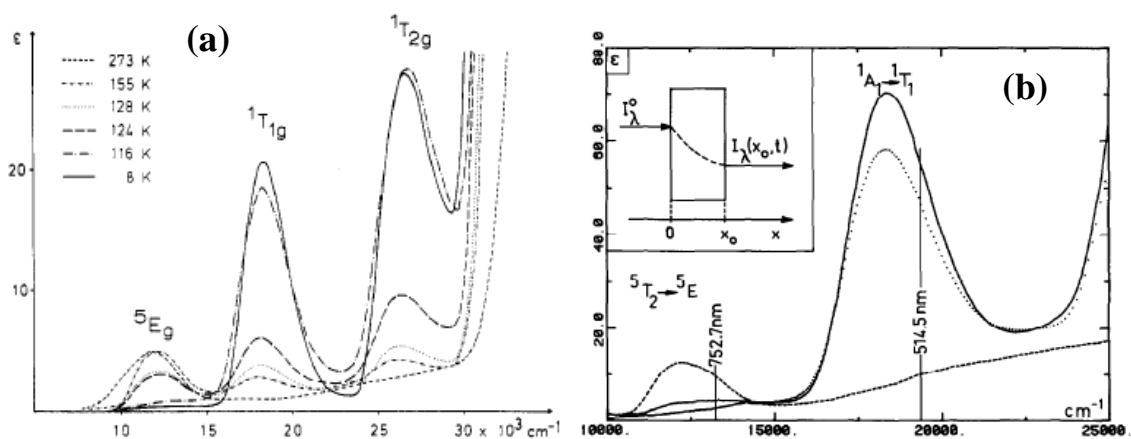


**Figure 1.14.** (a) Temperature dependence of the absorption spectra for  $[\text{Fe}(\text{ptz})_6](\text{BF}_4)_2$ , and (b) the absorption spectra of  $[\text{Fe}(\text{ptz})_6](\text{BF}_4)_2$  at 10 K. Solid line: before irradiation, broken line: after the light irradiation with  $\lambda = 514.5$  nm (Ar ion laser), dotted line = after the light irradiation with  $\lambda = 752.7$  nm (Kr ion laser).<sup>[50]</sup>

Figure 1.13(b) shows the temperature dependence of the magnetic susceptibility of  $[\text{Fe}(\text{ptz})_6](\text{BF}_4)_2$ .  $[\text{Fe}(\text{ptz})_6](\text{BF}_4)_2$  also shows the thermally-induced spin-crossover phenomenon with a transition from a high-spin state ( ${}^5\text{T}_{2g}$ ) to a low-spin state ( ${}^1\text{A}_{1g}$ ) at around 130 K ( $T_{c\uparrow} = 131.0$  (5) K,  $T_{c\downarrow} = 123.5$  (5) K). Furthermore, by irradiating with light corresponding to the transition of  ${}^1\text{A}_{1g} \rightarrow {}^1\text{T}_{1g}$  in a temperature range of 10 K to 50 K, the effective magnetic moment is increased from  $1.0 \mu_B$  to  $6.5\text{-}7.0 \mu_B$ . The spin change due to the light and heat has been proven with a visible absorption spectrum, as shown in Figure 1.14 (a). Along with the decrease in temperature, a decrease in the absorption intensity of the high-spin state ( ${}^5\text{T}_{2g} \rightarrow {}^5\text{E}_g$ ) and an increase in the absorption intensity of the low-spin state ( ${}^1\text{A}_{1g} \rightarrow {}^1\text{T}_{1g}$ ,  ${}^1\text{T}_{2g}$ ) are observed. It can be better understood from this figure that the crystal is colorless and transparent at the high-spin state, and is a reddish-purple color at the low-spin state. In addition, regarding the phenomena in Figure 1.14 (b), it is observed that the metastable high-spin state appears by irradiating with light with a wavelength of 514.5 nm (Ar ion laser), which corresponds to the low-spin state sample in the transition  ${}^1\text{A}_{1g} \rightarrow {}^1\text{T}_{1g}$ . Furthermore, the

low-spin state is restored by irradiating with light with a wavelength of 752.7 nm (Kr ion laser), which corresponds to the transition of  ${}^5T_{2g} \rightarrow {}^5E_g$ .

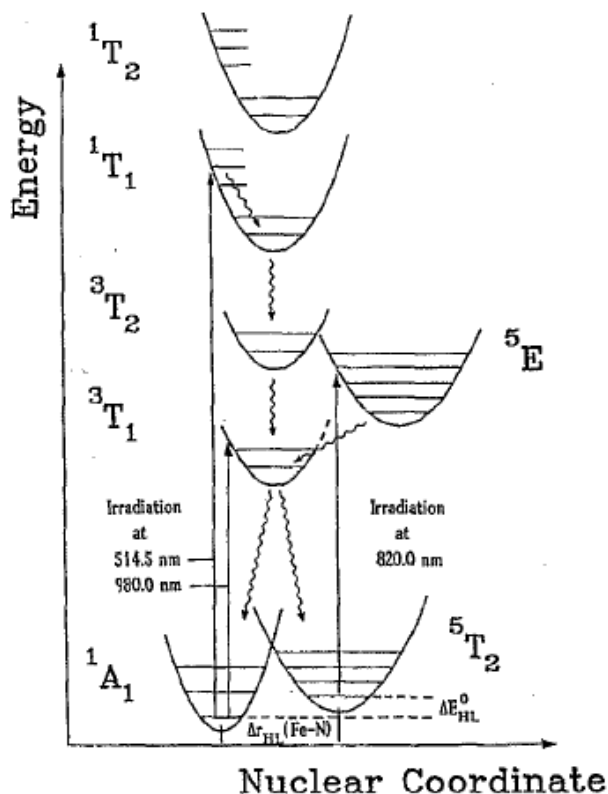
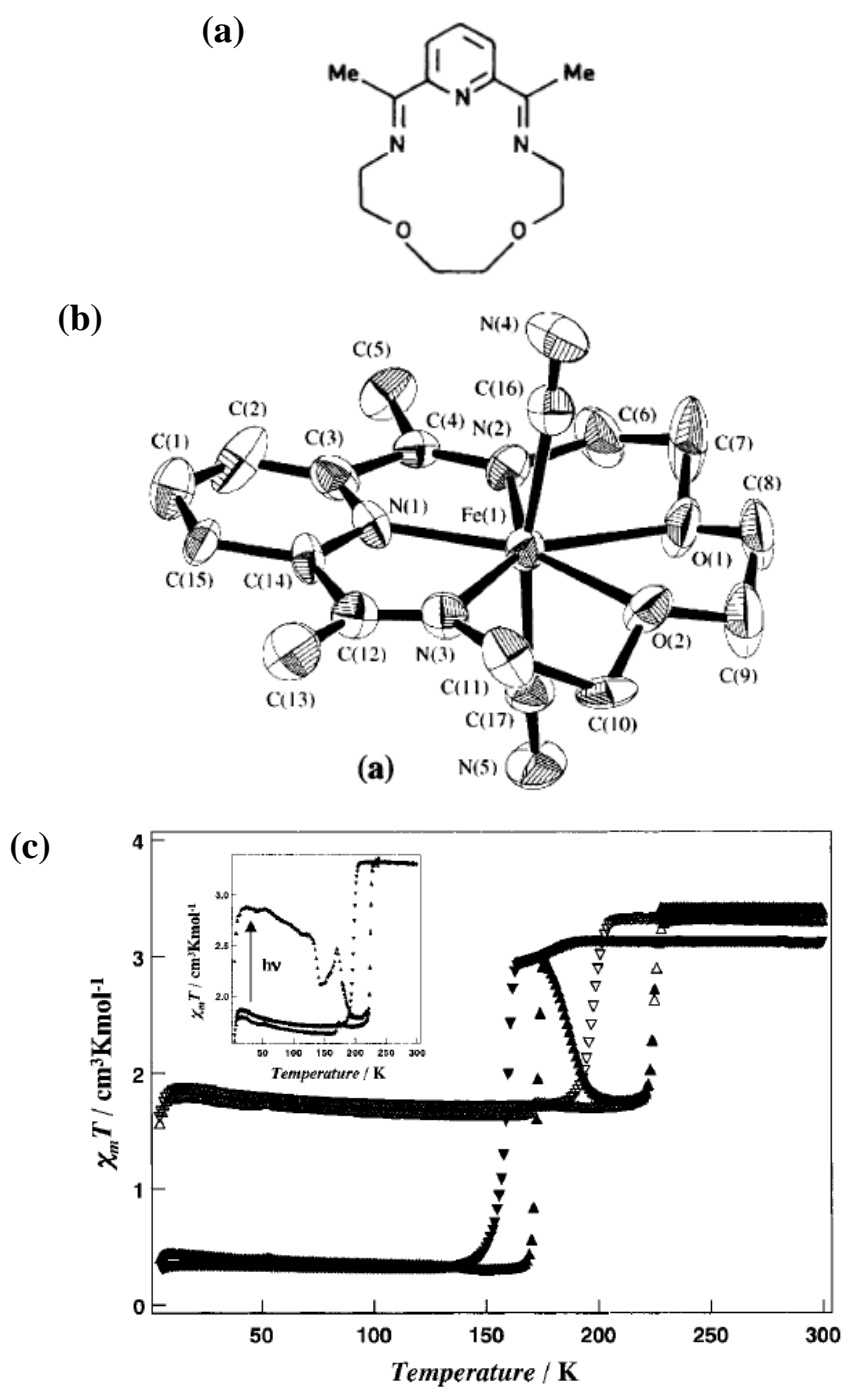


Figure 1.15. The mechanism of LIESST in  $d^6$  spin-crossover system.<sup>[51]</sup>

This low-spin-to-high-spin change induced by light is known as light induced excited spin state trapping (LIESST). Figure 1.15 is a diagram showing the mechanism of LIESST. An electron that is excited from the ground low-spin state ( ${}^1A_1$ ) to  ${}^1T_1$  by an Ar ion laser ( $\lambda = 514.5$  nm) relaxes via the unstable spin triplet state ( ${}^3T_2$ ,  ${}^3T_1$ ) to the initial state ( ${}^1A_1$ ) and to the metastable state ( ${}^5T_2$ ). Because of differences in the spin multiplicity and the potential barrier, the relaxation time from  ${}^5T_2$  to  ${}^1A_1$  is significantly longer at a low temperature. Therefore, most of the electrons are trapped in the high-spin state as excitation of electrons in the low-spin state is continued with laser light. Using the same mechanism, when the sample that is trapped in the high-spin state (metastable state) is

irradiated with a Kr ion laser ( $\lambda = 752.7$  nm), the excited electron of  $^5E$  state relaxes through  $^3T_1$  to the ground state ( $^1A_1$ ), and the sample reverts to a low-spin complex. Based on the above principle, application to an optical storage device can be considered as an example. Namely, it should be possible to write information with an Ar ion laser and erase the information with a Kr ion laser. The currently used method of magneto-optical recording involves local heating of the magnetic media with a laser; the magnetization is then allowed to disappear quickly, and subsequent magnetization is induced by an applied magnetic field to record information. Meanwhile, LIESST is intended to convert the electronic states directly and purely by light energy; as substances exhibiting this phenomenon can be novel optical recording materials, LIESST has been widely studied both at a fundamental level and in application.

Unfortunately, the LIESST relaxation temperature for  $[\text{Fe}(\text{ptz})_6](\text{BF}_4)_2$  is 60 K.<sup>[52]</sup> Hayami *et al.* reported on  $[\text{Fe}(\text{L})(\text{CN})_2]\cdot\text{H}_2\text{O}$  in 2001 (L: macrocyclic Schiff-base ligands derived from the condensation of 2,6-diacetylpyridine with 3,6-dioxaoctane-1,8-diamine), where the  $T_{\text{LIESST}}$  is 130 K as shown in Figure 1.16 (c) and is the world's highest temperature.<sup>[53]</sup> When considering its application in a device, the operating temperature is a major problem, and a dramatic increase in  $T_{\text{LIESST}}$  is desired.<sup>[54]</sup> In order to solve this problem, ligand driven light induced spin change (LD-LISC)<sup>[55-57]</sup> and counter ion driven light induced spin change (CID-LISC) have been attempted. As these are spin changes between the ground states, there are fewer problems related to thermal relaxation than for the LIESST phenomenon, and it also becomes possible to operate at or near room temperature. In addition, research related to spin change by external stimuli other than temperature and light, especially by electric fields, has been actively carried out. As described above, on the subject of control of magnetism using external stimuli, an excellent review has been written by Sato *et al.*<sup>[58]</sup>



**Figure 1.16.** (a) Molecular structure of ligand L,<sup>[59]</sup> (b) ORTEP view of  $[\text{Fe}(\text{L})(\text{CN})_2]$ , and (c) temperature dependence of magnetic susceptibility for  $[\text{Fe}(\text{L})(\text{CN})_2] \cdot \text{H}_2\text{O}$ . Inset: LIESST effect.

## 1.6 Organic–Inorganic Hybrid System

While organic materials generally have excellent processability, their low thermal conductivity and poor electrical conductivity are significant disadvantages. To compensate for these characteristics, the research and development of organic-inorganic hybrid systems with more sophisticated material design combining organic and inorganic materials have been carried out actively. Below is an overview of the specific physical properties found in organic-inorganic hybrid systems.

For  $\lambda$ -(BETS)<sub>2</sub>Fe<sub>x</sub>Ga<sub>1-x</sub>Cl<sub>4</sub> (BETS = bis(ethylenedithio)tetraselenafulvalene,  $0.35 \leq x \leq 0.5$ ), after having changed from the metallic phase to the superconducting phase at 4.6 K by lowering the temperature, the resulting substance appears to be in the insulating phase with antiferromagnetic ordering of the iron(III) ( $S = 5/2$ ) spins.<sup>[60]</sup> Not only does  $\lambda$ -(BETS)<sub>2</sub>FeCl<sub>4</sub> change from the metallic phase to the insulating phase at 8 K by the antiferromagnetic ordering of iron(III) ( $S = 5/2$ ) spins, but it is also well-known as a system exhibiting magnetic field-induced superconductivity.<sup>[61]</sup> The metal-insulator transition restores the metallic phase that disappears around an external magnetic field of 10.5 T; when an external magnetic field of more than 17 T is applied in parallel to the *a-c* plane (conductive layer), a superconductive phase induced by the magnetic field appears (Figure 1.16 (b)). This is explained by the strong antiferromagnetic interaction between the conduction electron spin in BETS and the iron(III) ( $S = 5/2$ ) spin. The internal magnetic field ( $H_J$ ) generated by the magnetic moments of the iron(III) ions in the organic conductive layer is opposite in direction to the external magnetic field ( $H$ ). When the external magnetic field  $H \approx H_J$ , the internal field coming from the conduction electron spins becomes almost canceled.<sup>[62]</sup> In other words, for a series of the systems, the interaction between the  $\pi$  electrons of BETS and the d-electrons of iron (III) plays an important role in the expression of novel physical properties.

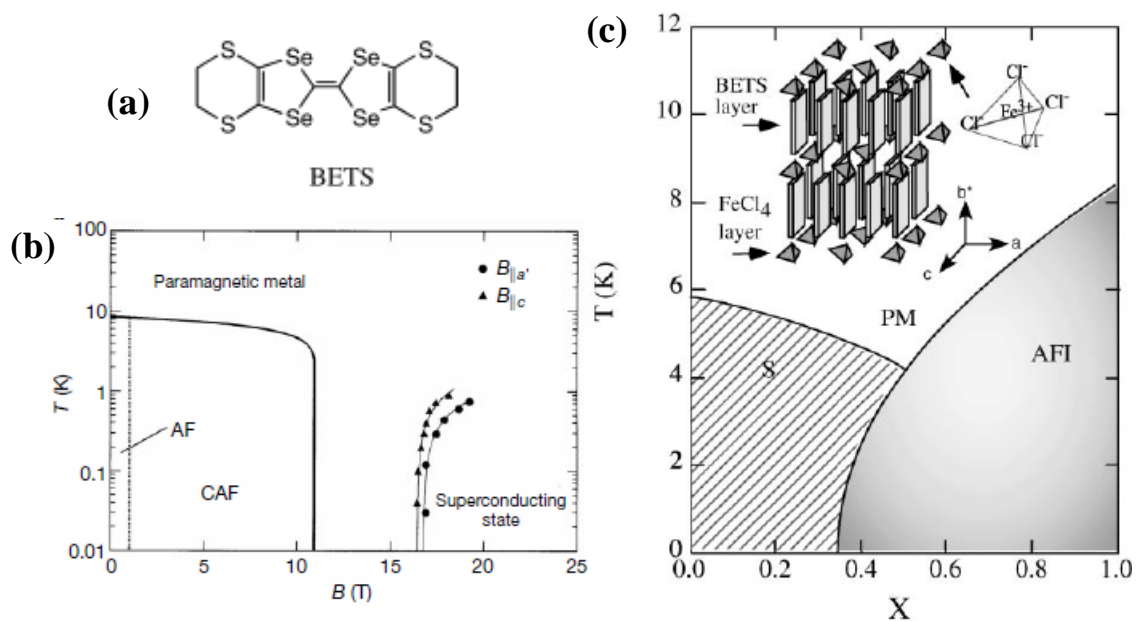


**Figure 1.16.** (a) Molecular structure of BETS,<sup>[63]</sup> (b) temperature versus magnetic field phase diagram for  $\lambda$ -(BETS)<sub>2</sub>FeCl<sub>4</sub> when the magnetic field is applied parallel to the  $a'$  or  $c$  axes, and (c) phase diagram of  $\lambda$ -(BETS)<sub>2</sub>Fe<sub>x</sub>Ga<sub>1-x</sub>Cl<sub>4</sub>. Inset: schematic illustration of the crystal structure of  $\lambda$ -(BETS)<sub>2</sub>FeCl<sub>4</sub>.

As a system in which ferromagnetism and the metallic phase coexist, (BEDT-TTF)<sub>3</sub>[Mn<sup>II</sup>Cr<sup>III</sup>(ox)<sub>3</sub>] (BEDT-TTF = bis(ethylenedithio)tetrathiafulvalene, ox = C<sub>2</sub>O<sub>4</sub><sup>2-</sup>) is mentioned here.<sup>[64]</sup> Although this system shows a ferromagnetic transition at 5.5 K, the temperature dependence of the resistivity is metallic until 2K. Moreover, a negative-magnetoresistance effect is observed below approximately 10 K. This is a novel physical property that is achieved without affecting the magnetism in [Mn<sup>II</sup>Cr<sup>III</sup>(ox)<sub>3</sub>] layer exhibiting two-dimensional ferromagnetism by interlayer BEDT-TTF molecules.

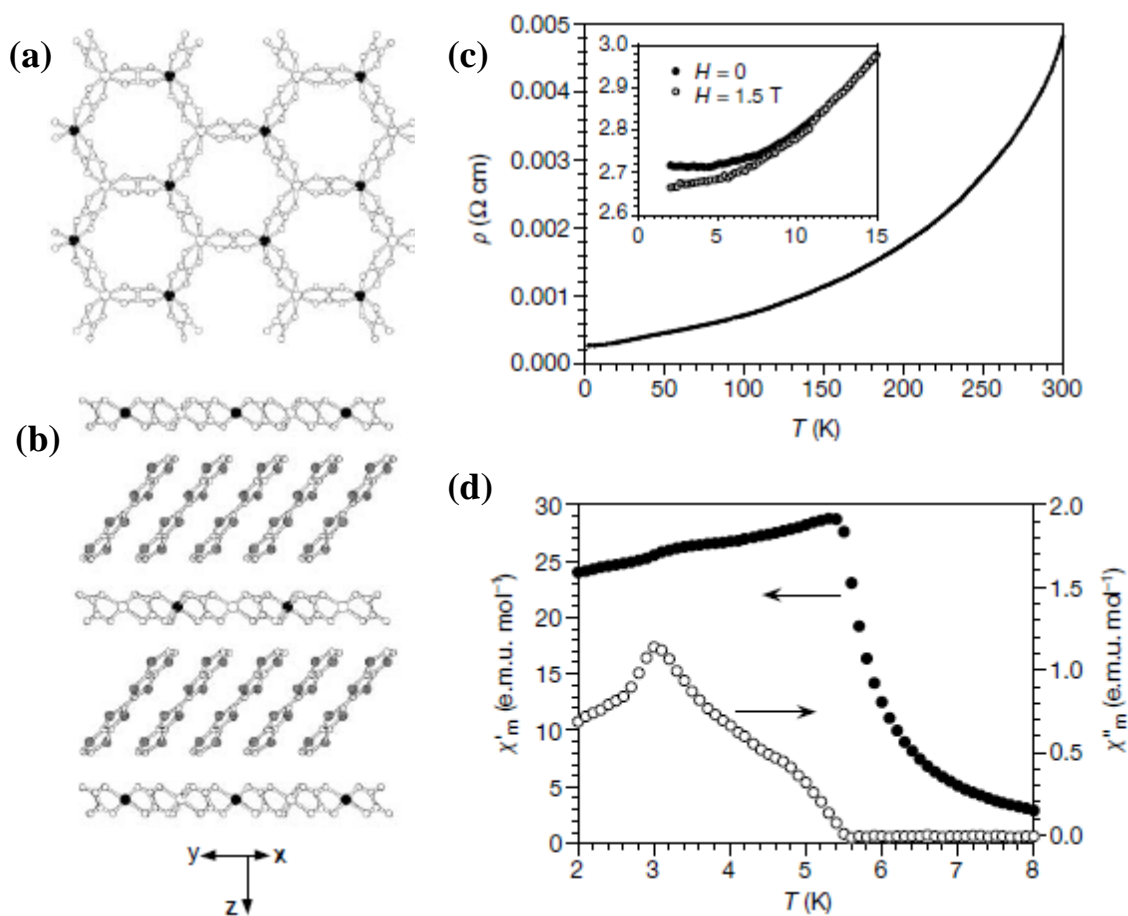


**Figure 1.17.** (a) Honeycomb network of  $[\text{Mn}^{\text{II}}\text{Cr}^{\text{III}}(\text{ox})_3]$ , (b) structure of  $(\text{BEDT-TTF})_3[\text{Mn}^{\text{II}}\text{Cr}^{\text{III}}(\text{ox})_3]$ , where BEDT-TTF is intercalated between  $[\text{Mn}^{\text{II}}\text{Cr}^{\text{III}}(\text{ox})_3]$  layers. (c) Temperature dependence of resistivity of  $(\text{BEDT-TTF})_3[\text{Mn}^{\text{II}}\text{Cr}^{\text{III}}(\text{ox})_3]$ , and (d) Temperature dependence of AC susceptibility of  $(\text{BEDT-TTF})_3[\text{Mn}^{\text{II}}\text{Cr}^{\text{III}}(\text{ox})_3]$  (AC frequency: 110 Hz).<sup>[64]</sup>

The coexistence of ferromagnetism and superconductivity has been studied both theoretically and experimentally since the 1950s. In contrast with ferromagnetism, which is said to involve spontaneous magnetization in which the electron spins are oriented in the same direction, in a typical superconducting state, the spins of two electrons show perfect diamagnetism, creating an antiparallel-oriented spin singlet pairing state. Therefore, ferromagnetism and superconductivity have long been considered as opposites. However, in recent years,  $(\text{Ce}_{1-x}\text{Gd}_x)\text{Ru}_2$ <sup>[65]</sup> and

$\text{RuSr}_2\text{GdCu}_2\text{O}_8$ ,<sup>[66]</sup> as well as uranium-based compounds such as  $\text{UGe}_2$ ,<sup>[67]</sup>  $\text{UIr}$ ,<sup>[68]</sup>  $\text{URhGe}$ ,<sup>[69]</sup> and  $\text{UCoGe}$ <sup>[70]</sup> have been reported as ferromagnetic superconductors, much to the surprise of superconductivity researchers. The  $[\text{M}^{\text{II}}_{0.66}\text{M}^{\text{III}}_{0.33}(\text{OH})_2][\text{TaS}_2]$  ( $\text{M}^{\text{II}} = \text{Ni}^{\text{II}}, \text{Zn}^{\text{II}}; \text{M}^{\text{III}} = \text{Al}^{\text{III}}, \text{Fe}^{\text{III}}$ ) compound was reported by Coronado *et al.* as an organic-inorganic hybrid system, and it has since attracted attention.<sup>[71]</sup>  $[\text{M}^{\text{II}}_{1-x}\text{M}^{\text{III}}_x(\text{OH})_2]$  is a cationic layered compound exhibiting ferromagnetism, with different metal ions bridged by hydroxides (Layered Double Hydroxide; LDH), while  $[\text{TaS}_2]$  is an anionic layered compound exhibiting superconductivity around 4 K. Synthesis can be carried out via self-assembly by electrostatic interaction in solution, and the magnetism can be controlled by changing  $\text{M}^{\text{II}}$  and  $\text{M}^{\text{III}}$ .

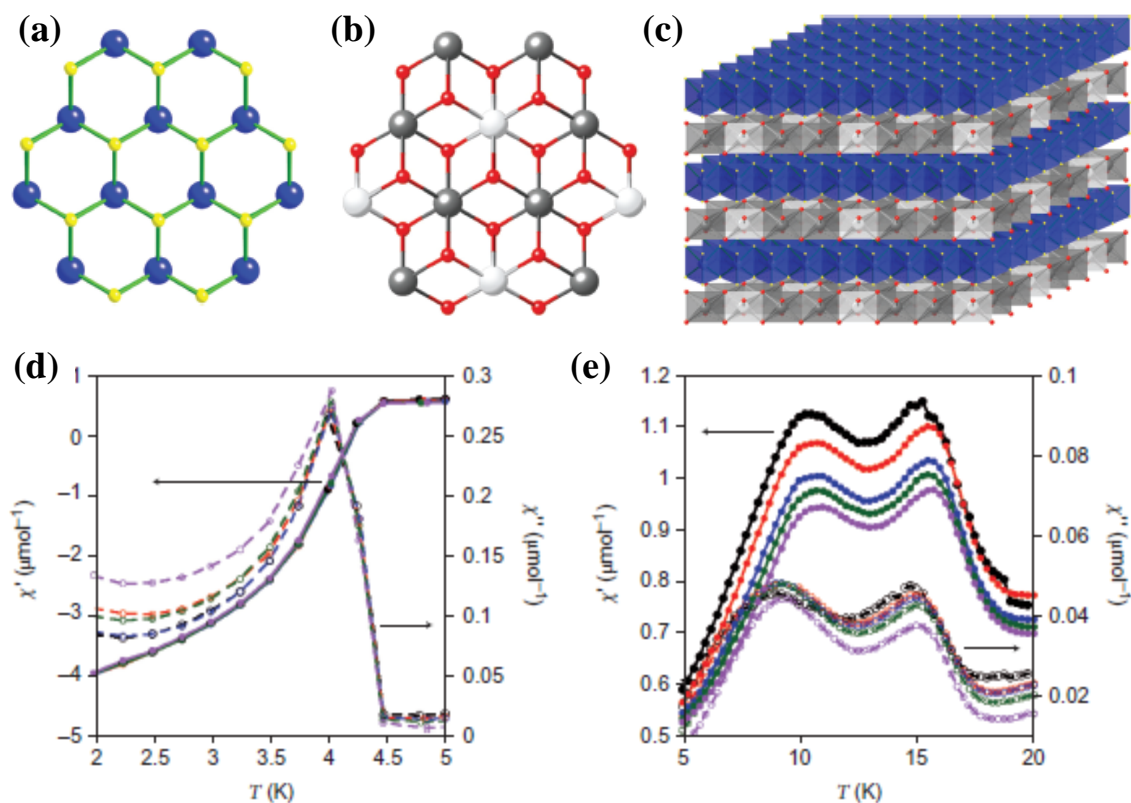


**Figure 1.18.** (a) Schematic picture of  $[\text{TaS}_2]^{0.33-}$  (blue = Ta , yellow = S), (b) schematic picture of  $[\text{Ni}_{0.66}\text{Al}_{0.33}(\text{OH})_2]^{0.33+}$  (gray = Ni, white = Al, red = O), (c) schematic picture of the alternately laminated ferromagnetic and superconducting layers from the view along the  $c$  axis, and (d),(e) temperature dependence of AC susceptibility of  $[\text{Ni}_{0.66}\text{Fe}_{0.33}(\text{OH})_2][\text{TaS}_2]$  ( $H = 3.95$  G; black = 1 Hz, red = 10 Hz, blue = 100 Hz, green = 1000 Hz).<sup>[71]</sup>

## 1.7 Aims of This Thesis

Based on the above backgrounds, this thesis aims to find interesting phenomena in terms of the “multifunctionality” in the solid state and under the ordinary environment (at normal temperature and ordinary pressure), for molecular aggregates formed from metal complexes. This first chapter gives an overview of the materials and concepts that can be developed in the field. Chapter 2 then describes an experimental theory related to this thesis.

Chapter 3 describes a development of pH-dependent spin-crossover complex films. There remains an ever-increasing interest and challenge to control the magnetic and optical properties of transition metal complexes by external stimuli in the field of materials chemistry since the discovery of the LIESST phenomenon. However, LIESST faces a severe dilemma that  $T_{\text{LIESST}}$  decreases with increasing the thermal spin-crossover transition temperature<sup>[54]</sup> and hence the highest  $T_{\text{LIESST}}$  remains at the level of 130 K as described in 1.5.2. Accordingly, it is desired to establish a renewed methodology for the spin-state switching at normal temperature and ordinary pressure. Moreover, electric field is preferable as an external stimulus because it is capable of easily and suitably performing control as well as light. To attain the objective, a highly proton-conductive membrane (Nafion) with a proton-responsive spin-crossover complex ( $[\text{Fe}^{\text{II}}(\text{diAMsar})]$  (diAMsar = 1,8-diaminosarcophagine)) was developed. The spin state of the film  $[\text{Fe}^{\text{II}}(\text{diAMsar})]@\text{Nafion}$  is potentially controllable by proton conduction under the applied voltage.

To expand this study, chapter 4 describes a development of pH-dependent emissive complex films. Transparent emissive materials have been drawing intense research interest due to their potential applications in LED (light emitting diode) illuminators, displays, ornaments, and so forth. Nafion gives homogeneous and any size of emissive films with flexibility and transparency very easily thanks to its cation exchange property. If the control of emission property by proton

conduction in the transparent film comes true, a new type of light emitting device whose emission can be controlled by applied voltage will be provided.

Chapter 5 describes a ligand field analysis in the pre-edge region of XANES (X-ray absorption near edge structure) spectra for one-dimensional  $\text{Fe}^{\text{II}}$  spin-crossover polymers  $[\text{Fe}^{\text{II}}(\text{NH}_2\text{-trz})_3](\text{C}_n\text{H}_{2n+1}\text{SO}_3)_2 \cdot x\text{H}_2\text{O}$  ( $\text{NH}_2\text{-trz}$  = 4-amino-1,2,4-triazole). In this system, uniaxial chemical pressure along  $[\text{Fe}^{\text{II}}(\text{NH}_2\text{-trz})_3]_{\infty}$  induced by the alkyl tail on alkanesulfonate as a counter-anion plays a crucial role on spin-crossover behavior. The spin-crossover temperature increases with increasing the length of alkyl tails in spite of the spacing between  $[\text{Fe}^{\text{II}}(\text{NH}_2\text{-trz})_3]_{\infty}$  chains by the extension of alkanesulfonate. This is clearly different from the control by (isotropic) external pressure. In addition, the pre-edge peaks in XANES spectra provide an important clue to elucidate the mechanism of the  $T_c$  increment. In this system, the magnetostructural correlation ties in closely with the ligand field parameters.

Chapter 6 describes an attempt to control the spin-crossover behavior of an  $\text{Fe}^{\text{III}}$  complex by the photoisomerization of counter-anion in the solid state. It could induce a change in intermolecular interaction of a spin-crossover unit. In this study, an anionic “spiropyran” was adopted as the photoisomerizable counter-anion whose photoisomerization undergoes at room temperature and in the solid state. As originally planned, the spin-crossover behavior of  $[\text{Fe}^{\text{III}}(\text{qsal})_2]^+$  ( $\text{Hqsal}$  = *N*-(8-quinolyl)salicylaldimine) was significantly varied after the light irradiation. This study demonstrated the CID-LISC effect on magnetism for the first time.

Chapter 7 describes an abnormal behavior of  $^{57}\text{Fe}$  Mössbauer spectra of verdazyl radical-coordinated  $\text{Fe}^{\text{II}}$  complex  $[\text{Fe}^{\text{II}}(\text{vdCOO})_2(\text{H}_2\text{O})_2] \cdot 2\text{H}_2\text{O}$  ( $\text{vdCOO}^-$  = 1,5-dimethyl-6-oxo-verdazyl-3-carboxylate) responsible for a “tricky” water molecule occupied in an axial position. The mononuclear complex shows an unexpected behavior in  $^{57}\text{Fe}$  Mössbauer spectra, where two doublets appear at 300 K, and the relative intensity strongly depends on

temperature. In this system, the coordinated water molecule tends to form hydrogen bonds with adjacent  $[\text{Fe}^{\text{II}}(\text{vdCOO})_2(\text{H}_2\text{O})_2]$  units at lower temperature. As the temperature increases, however, the population of the coordinated water which does not form hydrogen bonds increases. To sum up, the temperature dependence of the orientation of the coordinated water molecule affected the electronic state of central iron(II) ion. This interpretation was established by multitechnique; X-ray crystallography, solid state  $^2\text{H}$  NMR, and  $^{57}\text{Fe}$  Mössbauer spectroscopy. Besides, the molecular magnetism in the series of  $[\text{M}^{\text{II}}(\text{vdCOO})_2(\text{H}_2\text{O})_2]$  ( $\text{M} = \text{Fe}, \text{Co}, \text{Ni}$ ) was also studied in Chapter 7.

Chapter 8 eventually summarizes these studies, where some remarks on a future prospect and potential of materials chemistry were made in the end of the chapter.

## References

- [1] K. Ito, *Chem. Phys. Lett.*, **1**, 235 (1967).
- [2] M. Tamura, Y. Nakazawa, D. Shiomi, K. Nozawa, Y. Hosokoshi, M. Ishikawa, M. Takahashi, and M. Kinoshita, *Chem. Phys. Lett.*, **186**, 401 (1991).
- [3] K. Matsuda and M. Irie, *J. Am. Chem. Soc.*, **122**, 7195 (2000).
- [4] S. Ferlay, T. Mallah, R. Ouahès, P. Veillet, and M. Verdaguer, *Nature*, **378**, 701 (1995).
- [5] S. M. Holmes and G. S. Girolami, *J. Am. Chem. Soc.*, **121**, 5593 (1999).
- [6] O. Hatlevik, W. E. Buschmann, J. Zhang, J. L. Manson, and J. S. Miller, *Adv. Mater.*, **11**, 914 (1999).
- [7] H. Tokoro and S. Ohkoshi, *Dalton Trans.*, **40**, 6825 (2011).
- [8] R. Sessoli, H. L. Tsai, A. R. Schake, S. Wang, J. B. Vincent, K. Folting, D. Gatteschi, G. Christou, and D. N. Hendrickson, *J. Am. Chem. Soc.*, **115**, 1804 (1993).
- [9] R. Sessoli, D. Gatteschi, A. Caneschi, and M. A. Novak, *Nature*, **365**, 141 (1993).
- [10] D. Gatteschi and R. Sessoli, *Angew. Chem. Int. Ed.*, **42**, 268 (2003).
- [11] G. Christou, D. Gatteschi, D. N. Hendrickson, and R. Sessoli, *MRS Bull.*, **25**, 66 (2000).
- [12] M. Evangelisti, A. Candini, A. Ghirri, M. Affronte, E. K. Brechin, and E. J. L. McInnes, *Appl. Phys. Lett.*, **87**, 072504 (2005).
- [13] A. Ardavan, O. Rival, J. J. L. Morton, S. J. Blundell, A. M. Tyryshkin, G. A. Timco, and R. E. P. Winpenny, *Phys. Rev. Lett.*, **98**, 057201 (2007).
- [14] C. J. Milios, C. P. Raptopoulou, A. Terzis, F. Lloret, R. Vicente, S. P. Perlepes, and A. Escuer, *Angew. Chem. Int. Ed.*, **43**, 210 (2004).
- [15] A. Caneschi, D. Gatteschi, N. Laloti, C. Sangregorio, R. Sessoli, G. Venturi, A. Vindigni, A. Rettori, M. G. Pini, and M. A. Novak, *Angew. Chem. Int. Ed.*, **40**, 1760 (2001).

- [16] N. Ishikawa, M. Sugita, T. Ishikawa, S. Koshihara, and Y. Kaizu, *J. Am. Chem. Soc.*, **125**, 8694 (2003).
- [17] A. Caneschi, D. Gatteschi, A. Grand, J. Laugier, P. Rey, and L. Pardi, *Inorg. Chem.*, **27**, 1031 (1988).
- [18] D. Gatteschi, J. Laugier, P. Rey, and C. Zanchini, *Inorg. Chem.*, **26**, 938 (1987).
- [19] A. Bencini, C. Benelli, D. Gatteschi, and C. Zanchini, *J. Am. Chem. Soc.*, **106**, 5813 (1984).
- [20] C. Benelli, D. Gatteschi, D. W. Carnegie Jr., and R. L. Carlin, *J. Am. Chem. Soc.*, **107**, 2560 (1985).
- [21] M. H. Dickman and R. J. Doedens, *Inorg. Chem.*, **20**, 2677 (1981).
- [22] L. C. Porter, M. H. Dickman, and R. J. Doedens, *Inorg. Chem.*, **22**, 1962 (1983).
- [23] L. C. Porter and R. J. Doedens, *Inorg. Chem.*, **24**, 1006 (1985).
- [24] Y. Y. Lim and R. S. Drago, *Inorg. Chem.*, **11**, 1334 (1972).
- [25] A. Caneschi, D. Gatteschi, J. P. Renard, P. Rey, and R. Sessoli, *Inorg. Chem.*, **28**, 2940 (1989).
- [26] L. C. Porter, M. H. Dickman, and R. J. Doedens, *Inorg. Chem.*, **27**, 1548 (1988).
- [27] M. H. Dickman, L. C. Porter, and R. J. Doedens, *Inorg. Chem.*, **25**, 2595 (1986).
- [28] C. Benelli, D. Gatteschi, C. Zanchini, R. J. Doedens, M. H. Dickman, and L. C. Porter, *Inorg. Chem.*, **25**, 3453 (1986).
- [29] A. Caneschi, D. Gatteschi, R. Sessoli, and P. Rey, *Acc. Chem. Res.*, **22**, 393 (1989).
- [30] R. G. Hicks, *Org. Biomol. Chem.*, **5**, 1321 (2007).
- [31] O. Kahn, J. Galy, Y. Journaux, J. Jaud, and I. Morgenstern-Badarau, *J. Am. Chem. Soc.*, **104**, 2165 (1982).
- [32] Y. Journaux, O. Kahn, J. Zarembowitch, J. Galy, and J. Jaud, *J. Am. Chem. Soc.*, **105**, 7585 (1983).
- [33] O. Kahn, R. Prins, J. Reedijk, and J. S. Thompson, *Inorg. Chem.*, **26**, 3557 (1987).

- [34] T. Mallah, S. Thiébaud, M. Verdaguer, and P. Veillet, *Science*, **262**, 1554 (1993).
- [35] J. M. Manriquez, G. T. Yee, R. S. McLean, A. J. Epstein, and J. S. Miller, *Science*, **252**, 1415 (1991).
- [36] R. Jain, K. Kabir, J. B. Gilroy, K. A. R. Mitchell, K. C. Wong, and R. G. Hicks, *Nature*, **445**, 291 (2007).
- [37] P. Gülich and H. A. Goodwin, *Spin Crossover in Transition Metal Compounds I – III*, Springer, New York, (2004).
- [38] S. Sugano, Y. Tanabe, and H. Kamimura, *Multiplets of Transition Metal Ions, Pure and Applied Physics, Vol. 33*, Academic, New York (1970).
- [39] (a) L. Cambi and A. Cagnasso, *Atti. Accad. Naz. Lincei, Cl. Sci. Fis. Mat. Natl., Rend.*, **13**, 809 (1931). (b) L. Cambi and L. Szego., *Ber. Deutsch. Chem. Ges.*, **64**, 259 (1931). (c) L. Cambi, L. Szego, and A. Cagnasso, *Accad. Naz. Lincei, Cl. Sci. Fis. Mat. Natl., Rend.*, **15**, 23 (1932). (d) L. Cambi, L. Szego, and A. Cagnasso, *Accad. Naz. Lincei, Cl. Sci. Fis. Mat. Natl., Rend.*, **15**, 266 (1932). (e) L. Cambi and L. Szego., *Ber. Deutsch. Chem. Ges.*, **66**, 656 (1933).
- [40] Y. Tanabe and S. Sugano, *J. Phys. Soc. Jpn.*, **9**, 753, 766 (1954).
- [41] W. A. Baker, and H. M. Boronich, Jr., *Inorg. Chem.*, **3**, 1184 (1964).
- [42] E. König and K. Madeja, *Inorg. Chem.*, **6**, 48 (1967).
- [43] M. Nihei, T. Shiga, Y. Maeda, and H. Oshio, *Coord. Chem. Rev.*, **251**, 2606 (2007).
- [44] S. Hayami, Y. Komatsu, T. Shimizu, H. Kamihata, and Y. H. Lee, *Coord. Chem. Rev.*, **255**, 1981 (2011).
- [45] E. König, G. Ritter, and S. K. Kulshreshtha, *Chem. Rev.*, **85**, 219 (1985).
- [46] S. Decurtins, P. Gülich, C. P. Köhler, and H. Spiering, *Chem. Phys. Lett.*, **105**, 1 (1984).
- [47] (a) P. Gülich and A. Hauser, *Coord. Chem. Rev.*, **97**, 1 (1990). (b) A. Hauser, *Coord. Chem. Rev.*, **111**, 275 (1991). (c) P. Gülich, A. Hauser, and H. Spiering, *Angew. Chem. Int. Ed.*, **33**, 2024 (1994).

- (d) P. Gütllich, *Mol. Cryst. Liq. Cryst.*, **305**, 17 (1997).
- [48] J. Jeftić, R. Hinek, S. C. Capelli, and A. Hauser, *Inorg. Chem.*, **36**, 3080 (1997).
- [49] S. Decurtins, P. Gütllich, K. M. Hasselbach, A. Hauser, and H. Spiering, *Inorg. Chem.*, **24**, 2174 (1985).
- [50] A. Hauser, *Chem. Phys. Lett.*, **124**, 543 (1986).
- [51] A. Hauser, *J. Chem. Phys.*, **94**, 2741 (1991).
- [52] J. F. Létard, L. Capes, G. Chastanet, N. Moliner, S. Létard, J. A. Real, and O. Kahn, *Chem. Phys. Lett.*, **313**, 115 (1999).
- [53] S. Hayami, Z. Z. Gu, Y. Einaga, Y. Kobayashi, Y. Ishikawa, Y. Yamada, A. Fujishima, and O. Sato, *Inorg. Chem.*, **40**, 3240 (2001).
- [54] J. F. Létard, P. Guionneau, O. Nguyen, J. S. Costa, S. Marcén, G. Chastanet, M. Marchivie, and L. Goux-Capes, *Chem. Eur. J.*, **11**, 4582 (2005).
- [55] C. Roux, J. Zarembowitch, B. Gallois, T. Granier, and R. Claude, *Inorg. Chem.*, **33**, 2273 (1994).
- [56] M. L. Boillot, C. Roux, J. P. Audiére, A. Dausse, and J. Zarembowitch, *Inorg. Chem.*, **35**, 3975 (1996).
- [57] Y. Hasegawa, S. Kume, and H. Nishihara, *Dalton Trans.*, 280 (2009).
- [58] O. Sato, J. Tao, and Y. Z. Zhang, *Angew. Chem. Int. Ed.*, **46**, 2152 (2007).
- [59] S. M. Nelson, P. D. A. McIlroy, and C. S. Stevenson, *J. Chem. Soc. Dalton Trans.*, 991 (1986).
- [60] H. Kobayashi, A. Sato, E. Arai, H. Akutsu, A. Kobayashi, and P. Cassoux, *J. Am. Chem. Soc.*, **119**, 12392 (1997).
- [61] (a) S. Uji, H. Shinagawa, T. Terashima, T. Yakabe, Y. Terai, M. Tokumoto, A. Kobayashi, H. Tanaka, and H. Kobayashi, *Nature*, **410**, 908 (2001). (b) S. Uji, H. Shinagawa, T. Terashima, C. Terakura, T. Yakabe, Y. Terai, S. Yasuzuka, Y. Imanaka, M. Tokumoto, A. Kobayashi, F. Sakai, H.

- Tanaka, H. Kobayashi, L. Balicas, and J. S. Brooks, *J. Phys. Soc. Jpn.*, **2**, 370 (2003).
- [62] V. Jaccarino and M. Peter, *Phys. Rev. Lett.*, **9**, 290 (1962).
- [63] H. Kobayashi, H. B. Cui, and A. Kobayashi, *Chem. Rev.*, **104**, 5265 (2004).
- [64] E. Coronado, J. R. Galán-Mascarós, C. J. Gómez-García, and V. Laukhin, *Nature*, **408**, 447 (2000).
- [65] Y. Kitaoka, N. S. Chang, T. Ebisu, M. Matsumura, K. Asayama, and K. Kumagai, *J. Phys. Soc. Jpn.*, **54**, 1543 (1985).
- [66] J. E. McCrone, J. L. Tallon, J. R. Cooper, A.C. MacLaughlin, J. P. Attfield, and C. Bernhard, *Phys. Rev.*, **B68**, 064514 (2003).
- [67] S. S. Saxena, P. Agarwal, K. Ahilan, F. M. Grosche, R. K. W. Haselwimmer, M. J. Steiner, E. Pugh, I. R. Walker, S. R. Julian, P. Monthoux, G. G. Lonzarich, A. Huxley, I. Sheikin, D. Braithwaite, and J. Flouquet, *Nature*, **406**, 588 (2000).
- [68] T. C. Kobayashi, S. Fukushima, H. Hidaka, H. Kotegawa, T. Akazawa, E. Yamamoto, Y. Haga, R. Settai, and Y. Onuki, *Physica*, **B378**, 355 (2006).
- [69] D. Aoki, A. Huxley, E. Ressouche, D. Braithwaite, J. Flouquet, J. P. Brison, E. Lhotel, and C. Paulsen, *Nature*, **413**, 613 (2001).
- [70] D. Aoki, T. D. Matsuda, V. Taufour, E. Hassinger, G. Knebel, and J. Flouquet, *J. Phys. Soc. Jpn.*, **78**, 113709 (2009).
- [71] E. Coronado, C. Martí-Gastaldo, E. Navarro-Moratalla, A. Ribera, S. J. Blundell, and P. J. Baker, *Nat. Chem.*, **2**, 1031 (2010).
- [72] T. M. Barclay, R. G. Hicks, M. T. Lemaire, L. K. Thompson, and Z. Xu, *Chem. Commun.*, 1688 (2002).

## 2. Experimental Theory

### 2.1 Molecular Magnetism<sup>[1]</sup>

#### 2.1.1 Definitions and Fundamental Equations

Molecule-based magnetic materials contain a finite number of interacting spin centers (*e.g.* paramagnetic ions) and thus provide ideal opportunities to study basic concepts of magnetism. The principle of molecular magnetism in the present research is explained here. To begin with, let us consider a substance with a magnetic moment  $m$ . If the sample under a magnetic field newly creates a magnetic field, the phenomenon is referred to as “magnetization”, and a curved line representing the relationship between a homogeneous and stationary magnetic field and the magnetization is referred to as magnetization curve. Generally, with increasing the magnetic field  $H$ , the magnetization  $M$ , which is a magnetic moment per unit volume, is proportional to the magnetic field intensity when  $H$  is weak enough; one can write the relationship between  $M$  and  $H$  as follows:

$$M = \chi H \quad (2.1.1)$$

The gradient evaluated in a range unless the linear relationship is maintained is referred to as magnetic susceptibility  $\chi$ , which is evaluated by  $M$  divided by  $H$  in a DC measurement. Because the magnetization  $M$  includes a contribution of a demagnetizing field, a correction to eliminate the contribution of demagnetizing field in the case of evaluating the magnetic active elements only.

The magnetic property of metal complexes is generally evaluated by a temperature dependence of a molar magnetic susceptibility  $\chi_{\text{mol}}$  (emu/mol) and molar magnetization  $M_{\text{mol}}$  (emu Oe/mol). In principle  $\chi$  is the sum of the paramagnetic ( $\chi^{\text{para}}$ ) and diamagnetic ( $\chi^{\text{dia}}$ ) contributions.

$$\chi = \chi^{\text{para}} + \chi^{\text{dia}} \quad (2.1.2)$$

The molar diamagnetic susceptibility  $\chi^{\text{dia}}$  of a polyatomic molecule can be calculated by the equation;

$$\chi^{\text{dia}} = \sum_i n_i \chi_i + \sum \lambda \quad (2.1.3)$$

where  $\chi_i$  is an atomic susceptibility (Pascal constant:  $\chi_i \times 10^6$  emu/mol),  $n_i$  is a number of atom  $i$ , and  $\lambda$  is a correction factor.<sup>[2]</sup>

The parameters frequently used in molecular magnetism are the effective magnetic moment  $\mu_{\text{eff}}$  and  $\chi_{\text{mol}}T$ , which are written as:

$$\chi_{\text{mol}} = \frac{N \mu_{\text{eff}}^2 \mu_{\text{B}}^2}{3k_{\text{B}}T} \quad (2.1.4)$$

$$\mu_{\text{eff}} = \sqrt{\frac{3k_{\text{B}}\chi_{\text{mol}}T}{N\beta^2}} \cong \sqrt{8\chi_{\text{mol}}T} = 2.828(\chi_{\text{mol}}T)^{1/2} \quad (2.1.5)$$

where  $k_{\text{B}}$  is Boltzmann's constant ( $1.381 \times 10^{-23}$  J K<sup>-1</sup>),  $N$  is Avogadro constant ( $6.022 \times 10^{23}$  mol<sup>-1</sup>), and  $\mu_{\text{B}}$  is Bohr magneton ( $9.274 \times 10^{-24}$  J T<sup>-1</sup>). For the first transition metal ions with comparatively weak spin-orbit interactions, the effective magnetic moment is expressed by

$$\mu_{\text{eff}} = \sqrt{L(L+1) + 4S(S+1)} \quad (2.1.6)$$

where  $L$  is the total orbital angular momentum and  $S$  is the total spin angular momentum. In many cases, an orbital contribution in the first transition metal complexes can be neglected; the experimentally estimated  $\mu_{\text{eff}}$  can be expressed by

$$\mu_{\text{eff}} = \sqrt{4S(S+1)} = \sqrt{n(n+2)} \quad (2.1.7)$$

where  $n$  is a number of unpaired electrons. Equation (2.1.7) is referred to as the spin-only formula.

Accordingly, the effective magnetic moment per a molecule is

$$\mu_{\text{eff}} = \sqrt{4 \sum S_i(S_i + 1)} = \sqrt{\sum n_i(n_i + 2)} \quad (2.1.8)$$

where  $S_i$  is spin angular momentum of each metal ions and  $n_i$  is a number of unpaired electrons in  $i$ th atom.

## 2.1.2 Van Vleck Formula

Paramagnetism originates in a change in energy of atom under the magnetic field.

$$M = -\partial E / \partial H \quad (2.1.9)$$

To reach a formula of paramagnetism, energy levels of the atoms under the magnetic field and their Boltzmann distribution should be considered. When an atom exists in the magnetic field,  $i$ th energy level is generally expressed by a series of magnetic field:

$$W_i = W_i^{(0)} + W_i^{(1)}H + W_i^{(2)}H^2 + \dots \quad (2.1.10)$$

$W_i^{(0)}$  is the energy without magnetic field and  $W_i^{(1)}H$  and  $W_i^{(2)}H^2$  are first- and second-order Zeeman energy, respectively. In addition,  $W_i^{(1)}$  and  $W_i^{(2)}$  are referred to as first- and second-order Zeeman coefficient, respectively;

$$W_i^{(1)} = g\beta SH, \quad (2.1.11)$$

where  $g$  is Landé  $g$ -factor. Furthermore, it is not necessary to take the higher-order terms than the third order in to consideration. According to Equations (2.1.9) and (2.1.10), the magnetization of one atom is

$$M = -\partial W_i / \partial H = -W_i^{(1)} - 2W_i^{(2)}H \quad (2.1.12)$$

Considering the Boltzmann distribution of  $N$  (1 mol) atoms, the molar magnetic susceptibility is expressed by

$$\chi_{\text{mol}} = \frac{(N/H) \sum_i [-W_i^{(1)} - 2W_i^{(2)}H] \exp(-W_i/k_B T)}{\sum_i \exp(-W_i/k_B T)} \quad (2.1.13)$$

When the magnetic field is not extremely strong, the Zeeman splitting in first-order perturbation

reaches merely a few wavenumbers;  $1k_B T$  corresponds to *ca.*  $0.7 \text{ cm}^{-1}$ , and thermal energy at room temperature (300 K) then corresponds to *ca.*  $210 \text{ cm}^{-1}$ . Hence, the Zeeman splitting in first-order perturbation is sufficiently smaller than thermal energy  $k_B T$ , *i.e.*  $W_i^{(1)} \ll k_B T$ . Under such conditions, the following equation is true:

$$\exp(-W_i / k_B T) = 1 - W_i^{(1)} / k_B T \quad (2.1.14)$$

According to Equations (2.1.10) and (2.1.14),

$$\begin{aligned} \exp\left(-\frac{W_i}{k_B T}\right) &= \exp\left[\frac{-W_i^{(0)} - W_i^{(1)}H - W_i^{(2)}H^2 - \dots}{k_B T}\right] \\ &= \exp\left(-\frac{W_i^{(0)}}{k_B T}\right) \left[\left(1 - \frac{HW_i^{(1)}}{k_B T}\right) \left(1 - \frac{H^2W_i^{(2)}}{k_B T}\right) (\dots)\right] \end{aligned} \quad (2.1.15)$$

Hence, Equation (2.1.13) is

$$\chi_{\text{mol}} = \frac{(N/H) \sum_i [-W_i^{(1)} - 2W_i^{(2)}H] [\exp(-W_i^{(0)}/k_B T)] [\exp(1-W_i^{(1)}H/k_B T)] [\exp(1-W_i^{(2)}H^2/k_B T)]}{\sum_i [\exp(-W_i^{(0)}/k_B T)] [\exp(1-W_i^{(1)}H/k_B T)] [\exp(1-W_i^{(2)}H^2/k_B T)]}. \quad (2.1.16)$$

Developing Equation (2.1.16) and neglecting the terms which includes  $H$  (paramagnetic susceptibility is independent of the magnetic field),

$$\chi_{\text{mol}} = \frac{N \sum_i (-W_i^{(1)2} / k_B T - 2W_i^{(2)}) \exp(-W_i^{(0)}/k_B T)}{\sum_i \exp(-W_i^{(0)}/k_B T)} \quad (2.1.17)$$

This equation is called van Vleck formula, which is the general expression of paramagnetic susceptibility.

### 2.1.3 Curie's Law

The van Vleck formula can be simplified under a certain condition. When one single degenerate energy level exists,  $W_i^{(2)} = 0$  because there is no excited level. If  $W_i^{(0)}$  is set to a reference of energy,

$$\exp(-W_i^{(0)} / k_B T) = 1 \quad (2.1.18)$$

and thus

$$\chi_{\text{mol}} = \frac{N \sum_i W_i^{(1)2} / k_B T}{n} \quad (2.1.19)$$

where  $n$  is degeneracy of orbitals. Because  $\sum_i W_i^{(1)2}$  is a constant, Equations (2.1.17) or (2.1.19) are simply written as

$$\chi_{\text{mol}} = \frac{C}{T} \quad (2.1.20)$$

This relationship is called Curie's law, where  $C$  is the Curie constant. According to Equation (2.1.5), the effective magnetic moment is  $\mu_{\text{eff}} = 2.828(C)^{1/2}$ , namely, the effective magnetic moment does not depend on temperature. Besides, plots for the  $1/\chi_{\text{mol}}$  against temperature become a straight line with the gradient of  $1/C$ .

In the case that non-degenerate ground level and degenerate excited level above  $k_B T$  coexist,  $W_i^{(1)} = 0$  and  $\exp(-W_i^{(0)} / k_B T) = 1$  (Equation (2.1.18)) if  $W_i^{(0)}$  is set to a reference of energy. In addition,  $\exp(-W_j^{(0)} / k_B T) \approx 0$  because the distribution to  $j$  levels does not occur. Hence, Equation (2.1.17) is simplified as

$$\chi_{\text{mol}} = N \sum_i (-2W_i^{(2)}) \quad (2.1.21)$$

The second-order Zeeman effect raises  $j$  levels' energy and stabilize  $i$  levels, and thus  $W_i^{(2)} < 0$ . Accordingly,  $W_i^{(2)}$  contributes to paramagnetism and does not depend on temperature. This is referred to as "temperature-independent paramagnetism (T.I.P.), which is conventionally expressed by  $N\alpha$ . If the ground levels are also degenerated,

$$\chi_{\text{mol}} = \frac{C}{T} + N\alpha \quad (2.1.22)$$

Since  $N\alpha$  is a small value,  $\chi_{\text{mol}}$  satisfies the Curie's law at low temperature, but a deviation from the linear correlation in the  $1/\chi_{\text{mol}}$  versus  $T$  plot will appear at higher temperature due to the contribution by  $N\alpha$ . Besides, the value of  $N\alpha$  can be estimated from the  $1/(\chi_{\text{mol}} - N\alpha)$  versus  $T$  plot.

In the case that the ground and excited levels are both degenerated and the distribution to the excited levels occurs, the van Vleck formula cannot be simplified and the magnetic susceptibility shows a complicated behavior. In this case, however,  $\chi_{\text{mol}}$  accepts the following equation:

$$\chi_{\text{mol}} = \frac{C}{T - \theta} \quad (2.1.23)$$

This equation is called the Curie-Weiss law, where  $\theta$  is the Weiss constant. In the  $1/\chi_{\text{mol}}$  versus  $T$  plot, it becomes a straight line and intersects the temperature axis at  $T = \theta$ .

### 2.1.4 Magnetism in Multinuclear Complexes

When two paramagnetic ions are close to each other, the magnetic moments interact. Considering an exchange interaction between neighboring one electron atoms proposed by W. K. Heisenberg, the energies when the two spins are aligned parallel (F; ferro) or anti-parallel (AF; anti-ferro) are expressed by

$$E_{\text{F}} = \frac{Q - J}{1 - s} \quad E_{\text{AF}} = \frac{Q + J}{1 + s} \quad (2.1.24)$$

where  $Q$  is a Coulomb integral,  $J$  is an exchange integral, and  $s$  is an overlap integral. Since  $C \ll 1$  in this case, the energy difference between the two states is

$$E_{\text{F}} - E_{\text{AF}} = -2J \quad (2.1.25)$$

to interelectron repulsion. This exchange energy is expressed by the spin Hamiltonian:

$$\mathbf{H} = -2JS_1 \cdot S_2 \quad (2.1.26)$$

Here,  $S_1$  and  $S_2$  are spin angular momentum operators. Besides, the spins show greater tendency to be aligned anti-parallel with increasing overlap integral  $s$ , *i.e.* anti-ferromagnetic interactions depend on interatomic distances. Meanwhile, the spins are ferromagnetically coupled when  $s = 0$ , *i.e.* strict orthogonalization of the orbitals. In addition, Equation (2.1.26) can be rewrite for multinuclear complex as

$$\mathbf{H} = -2\sum J_{ij}S_i \cdot S_j, \quad (2.1.26)$$

and the exchange interaction in a multielectron system is expressed by

$$J = \frac{1}{n_i n_j} \sum_{i,j} J_{i,j} \quad (2.1.27)$$

where  $n_i$  and  $n_j$  are a number of unpaired electrons.

The magnitude of exchange interaction  $J$ , *i.e.* the energy difference between the ground and excited states, can be estimated from the analysis of temperature dependence of magnetic susceptibility. Hereafter, Equation (2.1.17) is transformed into a new equation suitable for multinuclear complexes. As an example, in the case of homo-dinuclear complex, spin-spin interaction creates the levels of  $S_T = 2S, 2S-1, \dots, 0$ , where  $S_1 = S_2 = S$ . Using the relationship,

$$S_T^2 = (S_1 + S_2)^2 = S_1^2 + S_2^2 + 2S_1 \cdot S_2, \quad (2.1.28)$$

the spin Hamiltonian is transformed into

$$\mathbf{H} = -J(S_T^2 - S_1^2 - S_2^2) \quad (2.1.29)$$

Neglecting  $S_1^2$  and  $S_2^2$  because they are constants, the Hamiltonian is simplified as

$$\mathbf{H} = -JS_T^2 \quad (2.1.30)$$

The energy of  $S_T$  level is given by

$$E(S_T) = -JS_T(S_T + 1) \quad (2.1.31)$$

Each  $S_T$  levels are split into  $(2S_T + 1)$  levels such as  $-g\beta S_T H, -g\beta(S_T - 1)H, \dots, +g\beta S_T H$  by the first-order Zeeman effect. Hence, the term of  $W_i^{(1)}$  in Equation (2.1.17) is written as

$$\frac{W_i^{(1)2}}{k_B T} = \frac{g^2 \mu_B^2}{k_B T} [S_T^2 + (S_T - 1)^2 + \dots + (-S_T)^2] = \frac{g^2 \mu_B^2 S_T (S_T + 1) (2S_T + 1)}{3} \quad (2.1.32)$$

Because each  $(2S_T + 1)$  levels generate the term of  $\exp(W_i^{(0)} / k_B T)$ , the denominator should be multiplied  $(2S_T + 1)$ . Therefore, we get the following equation with the T.I.P. term including the second-order Zeeman coefficient:

$$\chi_{\text{mol}} = \frac{N g^2 \mu_B^2 \sum S_T (S_T + 1) (2S_T + 1) \exp(-W_i^{(0)} / k_B T)}{3 k_B T \sum (2S_T + 1) \exp(-W_i^{(0)} / k_B T)} + N \alpha \quad (2.1.33)$$

Now, we can get the theoretical equation of the magnetic susceptibility of dinuclear complexes.

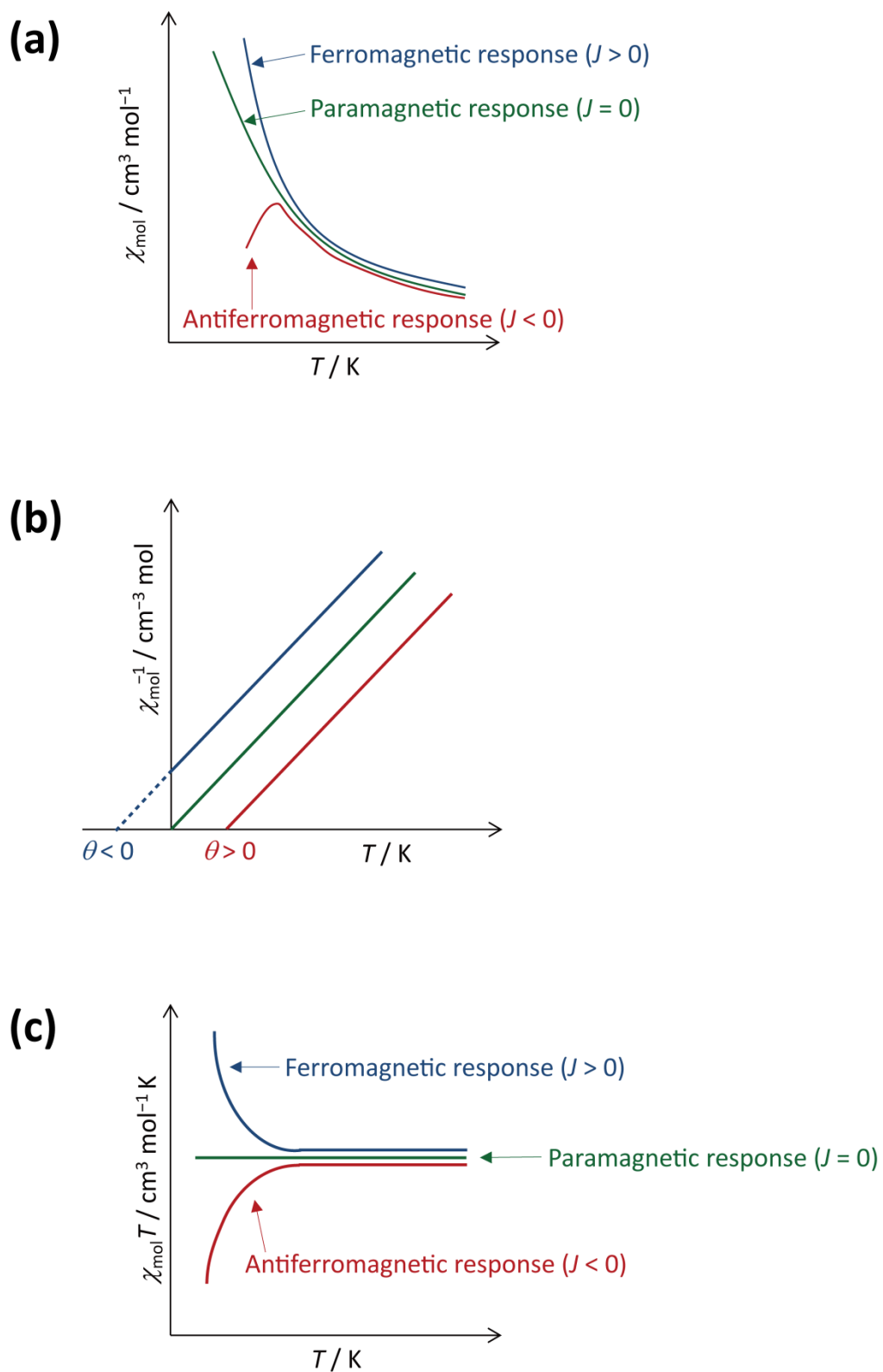


**Figure 2.1.1.** Temperature dependence of (a)  $\chi_{\text{mol}}$ , (b)  $1/\chi_{\text{mol}}$ , and (c)  $\chi_{\text{mol}}T$ .

As summarized in Figure 2.1.1, the data for temperature dependence of magnetic susceptibility provide important informations, *e.g.* the magnitude of exchange interactions ( $J$ ), intermolecular interactions ( $\theta$ ), T.I.P., *etc.* In many cases, temperature dependence of  $\chi_{\text{mol}}T$  clearly reflects the difference of  $J$ .

## 2.2 XAFS Spectroscopy<sup>[3]</sup>

Every atom has its respective characteristic ionization energy in the X-ray region and when it absorbs X-ray of with higher energy than that, core electrons are ejected as photoelectrons. Because of this, when X-ray absorbance is plotted against photon energy along the horizontal axis, it results in an X-ray absorption spectrum (XAS) similar to the one shown in Figure 2.2.2 (XAS spectrum). The X-ray absorption intensity shows a steep increase at certain energy corresponding to the ionization energy. This is called the (characteristic) absorption edge, and when one approaches a region of energy greater than the absorption edge, the intensity continues to reduce gradually, as the energy increases. The energy corresponding to the absorption edge continues to increase with the atomic number. However, since each atom has its respective characteristic absorption edge, XAS can be considered to be an analytical method with high elemental selectivity. Here, it is mentioned as XAS to assert that it is a spectroscopic technique, but it is similar to the method known as X-ray absorption fine structure (XAFS). Moreover, XAFS is an abbreviation that combines both X-ray absorption near-edge structure (XANES) and extended x-ray absorption fine structure (EXAFS).

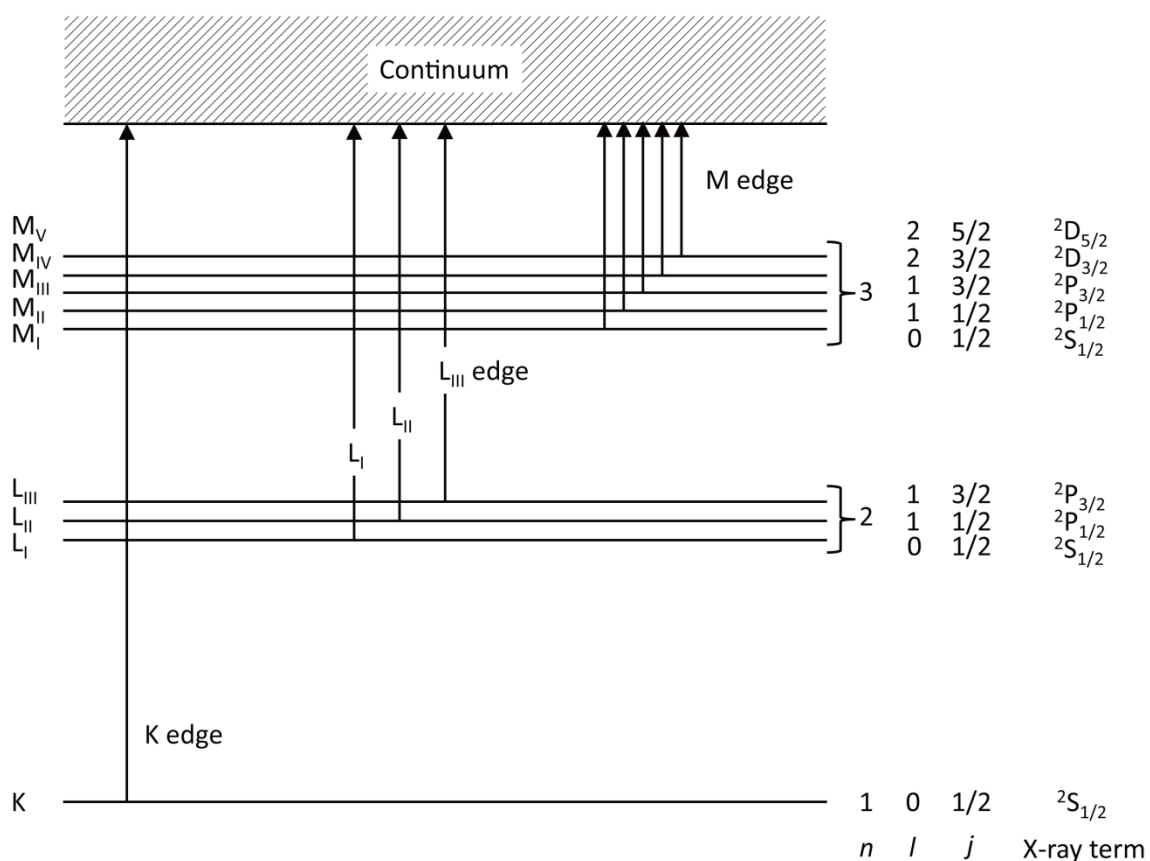


Figure 2.2.1. Classification of X-ray absorptions and energy levels.

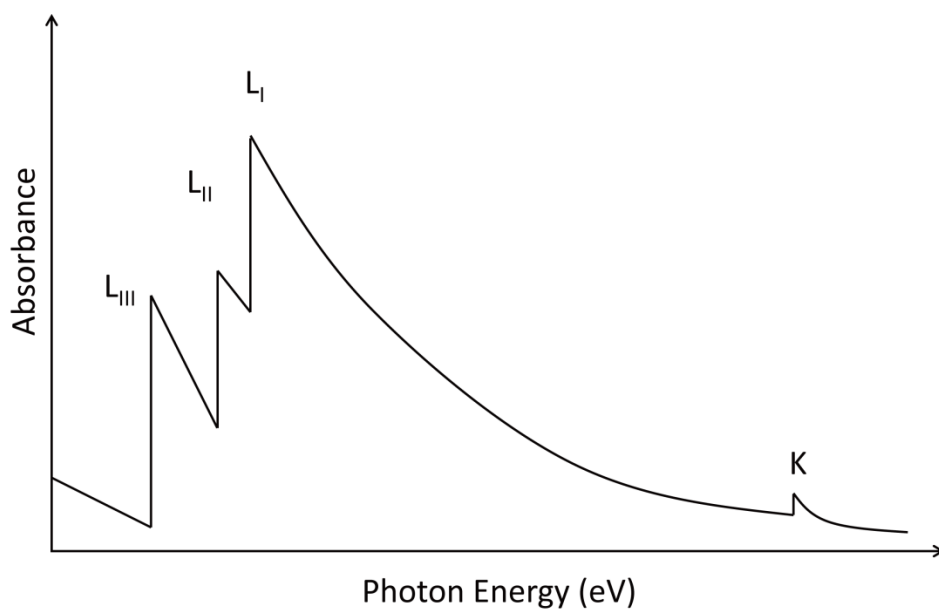
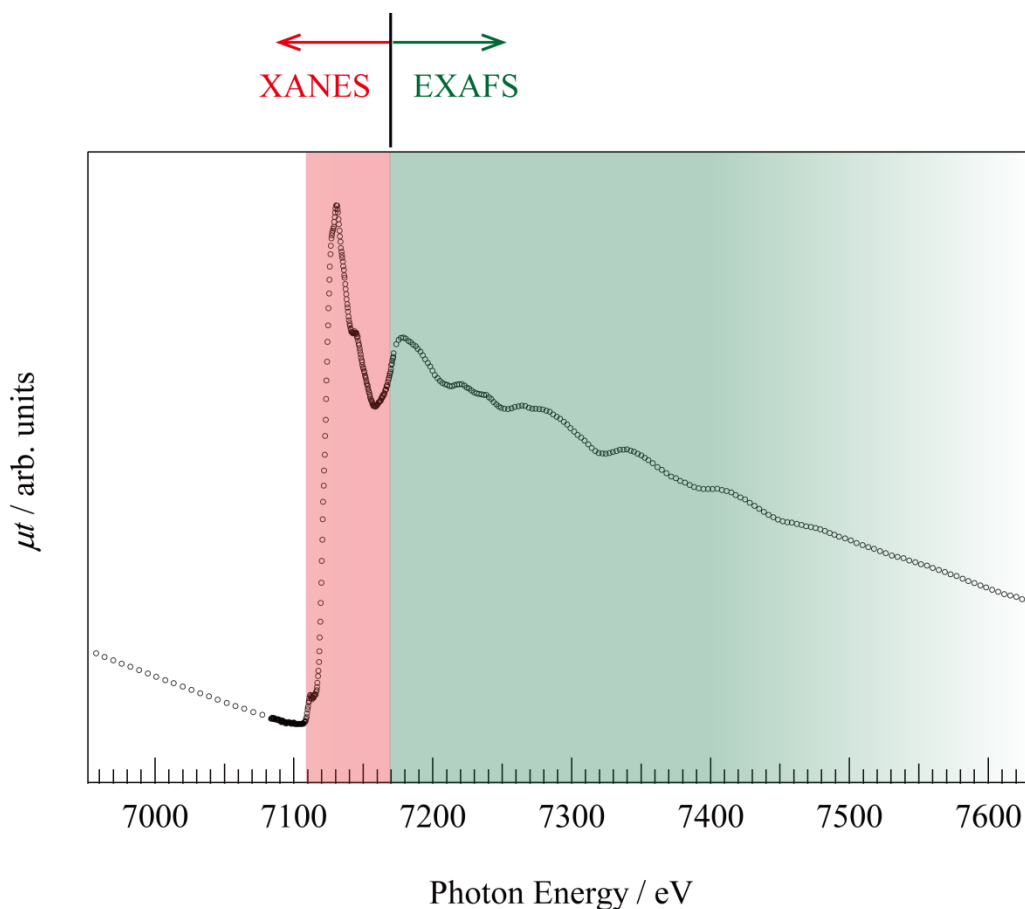


Figure 2.2.2. Schematic illustration of XAS spectrum.

### 2.2.1 XANES

A spectral structure with a considerable change is observed near the absorption edge of the XAS spectrum. This region is called XANES (Figure 2.2.3). XANES corresponds to transition from a core level to a vacant orbital or band, and it is extremely sensitive to changes in the arrangement or potential of the atom. In other words, XANES spectrum reflects the electronic state or the structure of the coordination environment of the X-ray absorbing atom (central metal ion). Thus, it is theoretically possible to obtain information such as the electronic state or coordinate structure of a metal complex if the XANES spectrum is analyzed.



**Figure 2.2.3.** XAS spectrum of  $\alpha\text{-Fe}_2\text{O}_3$  (Hematite). (The data were cited from Catalysis Research Center, Hokkaido University)<sup>[4]</sup>

### 2.2.2 EXAFS

In the region of energy higher than XANES, a fine spectral structure called as extended X-ray absorption fine structure (EXAFS) is observed (Figure 2.2.3). Since this is a phenomenon occurring due to the interference between the photoelectrons ejected from X-ray absorbing atom and the electrons scattered by the surrounding atoms (Figure 2.2.4), it differs from X-ray diffraction, and EXAFS can be observed also in the case of non-crystalline or liquid samples that do not have a periodic structure. It is possible to obtain structural information such as the type, number, or distance of the surrounding atoms, by analyzing EXAFS spectrum. The process of interference of atoms causing EXAFS can be explained accurately in terms of the EXAFS function  $\chi(k)$  (a function expressing the kinetic energy of a photoelectron ejected from an atom in wave number  $k$  (unit  $\text{\AA}^{-1}$ )) with the help of quantum mechanics, that is

$$\chi(k) = S_0^2 \sum_i \frac{N_i F_i(k_i)}{k_i r_i^2} e^{-2k_i^2 \sigma_i^2} \sin(2k_i r_i + \phi_i(k_i)) \quad (2.2.1)$$

where  $S_0^2$  is the reduction factor,  $N$  is the coordination number,  $F$  is the scattering amplitude,  $r$  is the interatomic distance,  $\sigma^2$  is the Debye-Waller factor, and  $\phi$  is the phase shift. In the case of a metal complex, it is possible to observe EXAFS spectrum because atoms of ligands or other metal ions are essentially present around the central ion, and by analyzing the spectrum, it may be possible to determine the type of ligand, coordination number, or distance from the central ion.

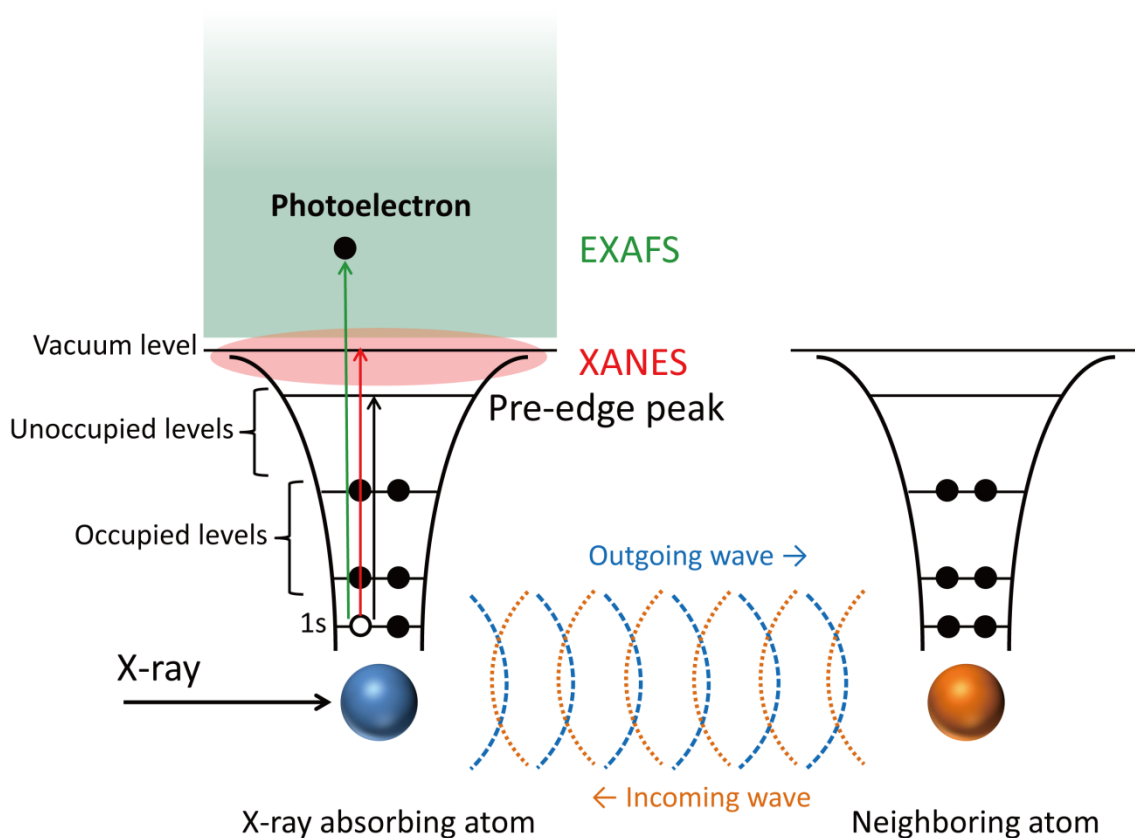


**Figure 2.2.4.** Mechanism of K-edge XAFS spectroscopy.

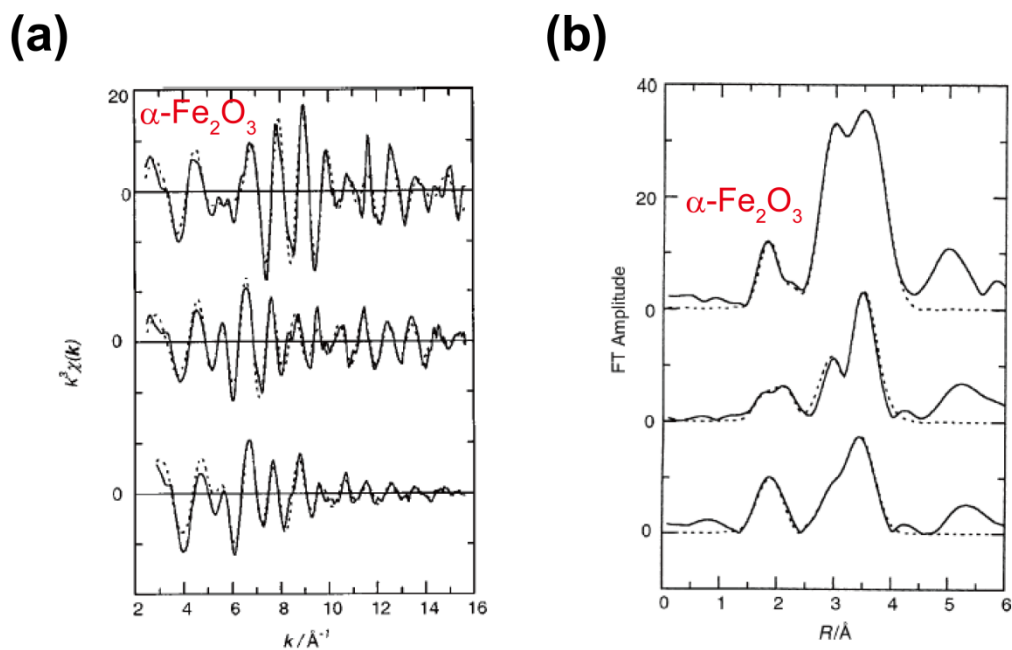


**Figure 2.2.5.** (a)  $k^3 \chi(k)$  for  $\alpha\text{-Fe}_2\text{O}_3$  (hematite; top) and (b) Modulus of Fourier transforms of  $k^3 \chi(k)$  for  $\alpha\text{-Fe}_2\text{O}_3$  (top). The solid and dashed lines are experimental and fit results, respectively.<sup>[5]</sup>

EXAFS function  $\chi(k)$  obtained from actual XAS measurement such as from the XAS spectrum in Figure 2.2.3 is shown in Figure 2.2.5. As  $k$  goes towards the high-wave-number side, for the EXAFS function undergoes attenuation and therefore, the function is usually weighted with  $k^2$  or  $k^3$  (here, weighted with  $k^3$ ). Since the horizontal axis indicates the kinetic energy of a photoelectron in terms of the EXAFS function (unit  $\text{\AA}^{-1}$ ), it is difficult to understand the correspondence with actual structural information. However, since the EXAFS function is sinusoidal, it is possible to obtain peaks at places corresponding to atomic positions after Fourier transformation. This is called the radial structure function (Figure 2.2.5). In the radial structure function, since the horizontal axis denotes distance ( $\text{\AA}$ ), the structure is determined more intuitively than in an EXAFS function. However, due to the effect known as phase shift, the distance expressed in the radial structure function is about 0.2–0.5  $\text{\AA}$  shorter than the actual distance (after carrying out Fourier transformation considering phase shift, it agrees with the actual distance).

## 2.3 $^{57}\text{Fe}$ Mössbauer Spectroscopy<sup>[6-8]</sup>

Mössbauer spectroscopy is a method involving the use of gamma radiation, and it is widely applied in the field of materials science, including magnetism. The principle of Mössbauer effect in  $^{57}\text{Fe}$  used in the present research is explained here.

The radioactive artificial element  $^{57}\text{Co}$  decays by electron capture (EC) into  $^{57}\text{Fe}$ . During the process of deexcitation to the ground state from the first excited state after passing through the second excited state of  $^{57}\text{Fe}$ , it emits gamma ray of 14.4 keV energy (Figure 2.3.1). As native iron contains  $^{57}\text{Fe}$  as a stable isotope with an abundance of about 2%, irradiating a sample containing iron with gamma radiation originated from  $^{57}\text{Co}$  may cause resonance absorption of the atomic nuclei (Figure 2.3.2).

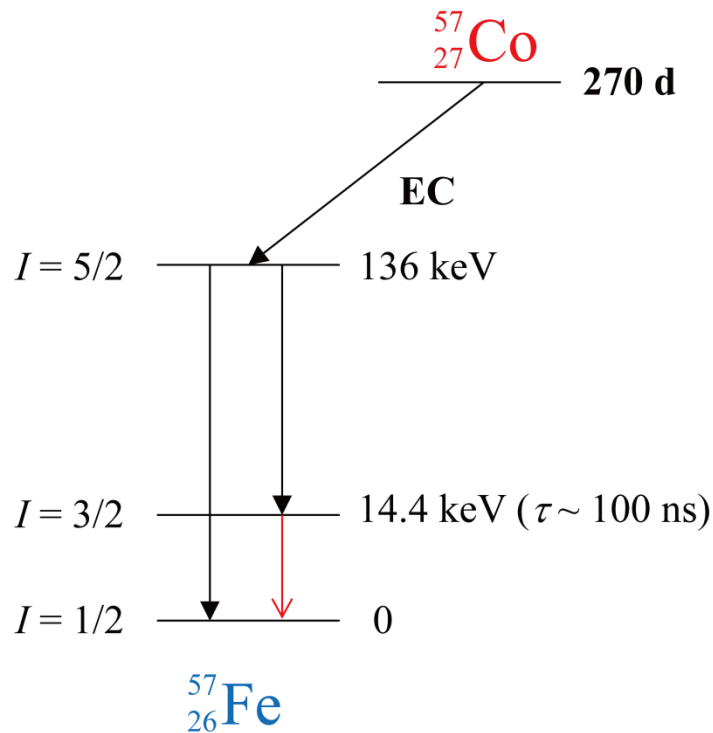


**Figure 2.3.1.** Decay scheme of  $^{57}\text{Co}$ .

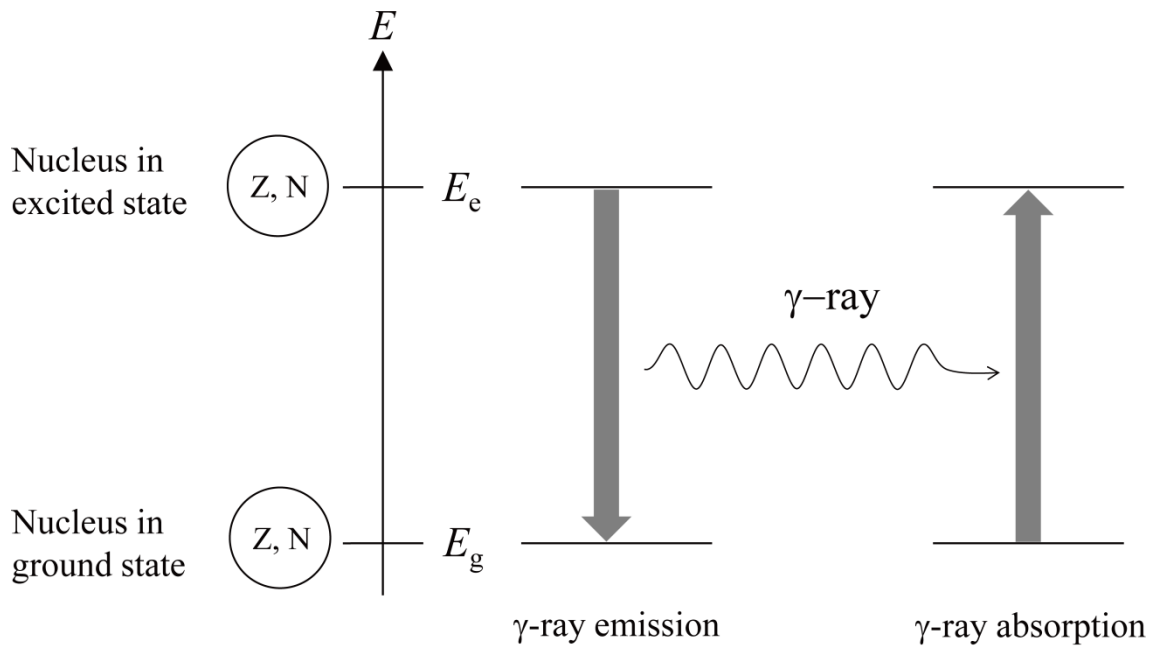


**Figure 2.3.2.** Gamma-ray emission from the light source and resonant absorption by a nucleus.

However, while emitting gamma radiation, the atomic nucleus recoils as required by the law of conservation of momentum, and the energy of the gamma radiation is partly consumed (Figure 2.3.3). Because of this, it was thought that this type of resonance absorption may not be taking place. However, in 1958, R. L. Mössbauer discovered that the emission and absorption of gamma radiation without losing recoil energy takes place with a certain amount of probability if the atomic nucleus is embedded in a crystal.<sup>[7]</sup> If the recoil velocity is  $v$  and mass is  $M$ , the recoil energy is  $(1/2)Mv^2$ , and therefore, the energy of gamma radiation ( $E$ ) becomes rather less than the level difference  $E_0$ . Furthermore, considering that the nucleus already has a velocity  $V$  in the direction of the gamma radiation, whereas  $v$  is in the opposite direction, the velocity of the nucleus due to gamma radiation becomes  $V-v$  and if the law of conservation of energy is applied,

$$MV^2 / 2 + E_0 = M (V - v)^2 / 2 + E \quad (2.3.1)$$

Furthermore, as the momentum  $p$  of gamma radiation is  $p = E/c$  ( $c$  is velocity of light), before and after the radiation,

$$MV = M (V - v) + E/c \quad (2.3.2)$$

The energy difference of gamma radiation  $\delta E = E_0 - E$  is obtained from the two equations,

$$\delta E = E_0 - E = (E^2/2Mc^2) - (EV/c) = \delta E_R - \delta E_D \quad (2.3.3)$$

The first term on the right hand side is always independent of  $V$  and hence it is the recoil energy. The second term is the ratio of  $V$  and the speed of light  $c$  and it is nothing but the Doppler Effect. In other words, if velocity is imparted to the source of the radiation in the direction of the radiation, the wavelength of the gamma radiation reduces and the energy increases, and therefore, the energy equivalent to the recoil energy is compensated. Moreover, the spreading of gamma radiation can be derived from the uncertainty principle, and the line width  $\Gamma$  in terms of uncertainty in energy and time can be expressed as

$$\Gamma \sim \Delta E \geq \hbar / \Delta t = h / 2\pi\Delta t \quad (2.3.4)$$

By using the Plank's constant  $h = 6.626 \times 10^{-34}$  J·s and lifetime of excited state of  $^{57}\text{Fe}$ ,  $\Delta t = 97.7 \times 10^{-9}$  s, the value of  $\Gamma$  becomes  $\Gamma = 6.8 \times 10^{-12}$  keV. The corresponding Doppler velocity  $v_D$  is approximately  $1 \text{ mm s}^{-1}$ . Thus, the Mössbauer spectrum can be obtained by counting transmitted

gamma rays (Figure 2.3.4) at various Doppler velocities. Factors involving Mössbauer effect and what we understand from them are explained below.

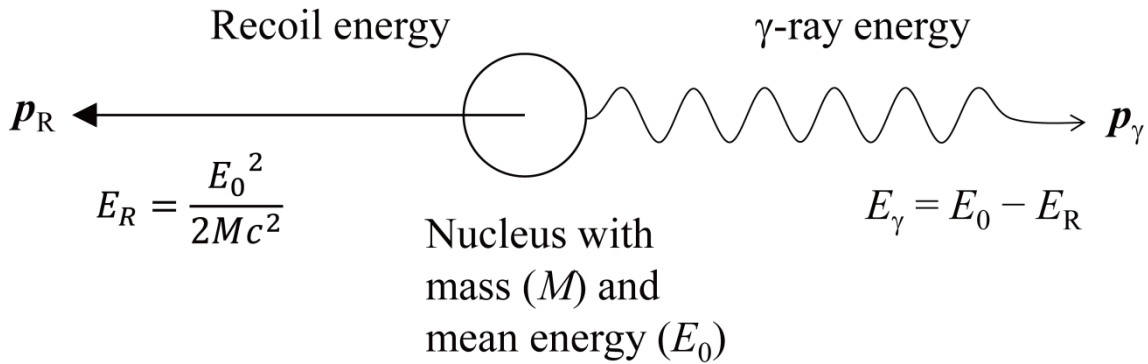


Figure 2.3.3. Recoil energy  $E_R$  and gamma-ray energy  $E_\gamma$ .

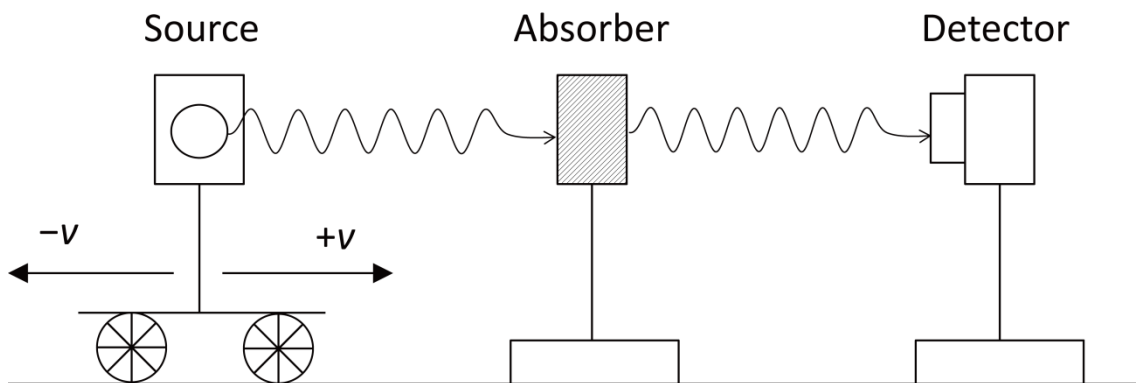


Figure 2.3.4. Schematic illustration of an experiment in Mössbauer spectroscopy.

### 2.3.1 Isomer Shift

A positively charged atomic nucleus is surrounded by negatively charged electrons. Higher the density of the negatively charged electron cloud, higher the stability of the atomic nucleus and lower the energy level. In other words, if the aggregated state such as the chemical bonding of the source of radiation and absorber is different, the state of the outer s electron will also be different, and

therefore, the shift of levels due to hyperfine interaction differs. Furthermore, in the ground state and excited state, the magnitude of nuclear-level shift differs. This is because the extent of the charge distribution of a nucleus differs between the ground state and excited state, and usually the size of the nucleus also increases in the high-energy state. (However,  $^{57}\text{Fe}$  is an exception where the nuclear radius decreases with an increase in the energy, and thus, the nucleus in the excited state is 0.052% smaller than that in the ground state.) Thus, the Mössbauer spectrum is observed for the first time by applying relatively the Doppler velocity, and a shift occurs in the central position of the spectrum due to Coulomb interaction (Figure 2.3.5). This is called the isomer shift ( $\delta$ ). If this is expressed in the form of the equation, we get

$$\delta = C \Delta R / R (|\phi_A(0)|^2 - |\phi_S(0)|^2) \quad (2.3.5)$$

Here,  $\delta$  represents the isomer shift;  $C$  is a constant that includes the nuclear charge and nuclear radius, hence  $C$  depends on the type of the nucleus;  $\Delta R$  is the difference in the radii ( $R_e - R_g$ ) of the nucleus between the excited state (suffix: e) and ground state (suffix: g);  $R$  is average value of the two;  $\phi(0)$  is the wave function of the electron in the nuclear site; and the suffixes A and S respectively represent the absorber and source of radiation.

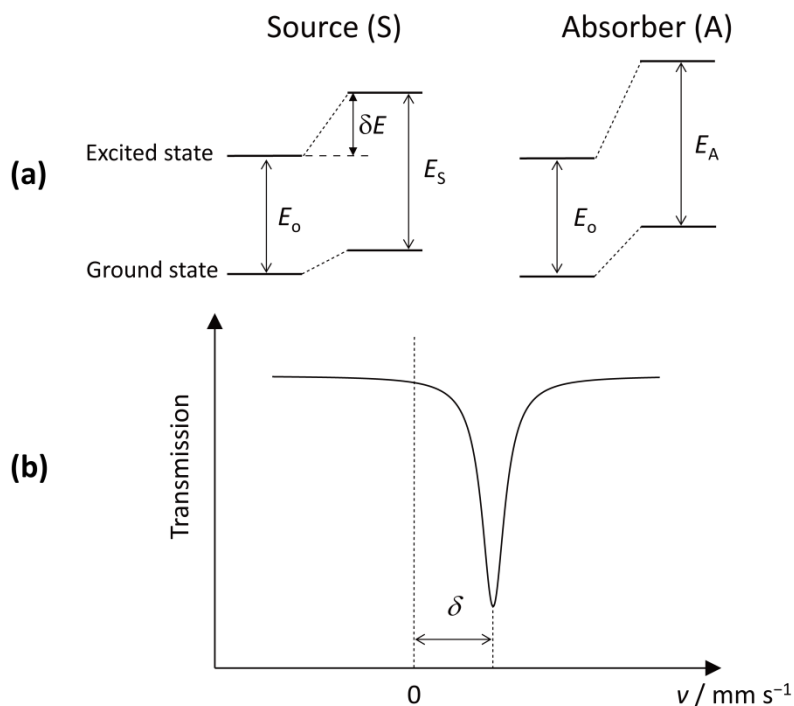


**Figure 2.3.5.** (a) Shift of the energy levels by Coulomb interaction, and (b) shift of the centroid of the absorption spectrum.

$|\phi(0)|^2$  is the total electron density at the nuclear site and s electron is the only electron that has electron density at the nuclear site. However, the information obtained from the isomer shift is not only about the s electron, but also about the p and d electrons that do not have a direct distribution at the nuclear-site change in the  $|\phi(0)|^2$  due to screening effect and influence the isomer shift. For example, in iron compounds, if there is a reduction in the number of 3d electrons, the strength for screening the outer s electrons becomes less and isomer shift reduces. In this way, from the isomer shift, it is possible to determine the oxidation number, d electron configuration (spin state), and bonding in a substance (Figure 2.3.6).

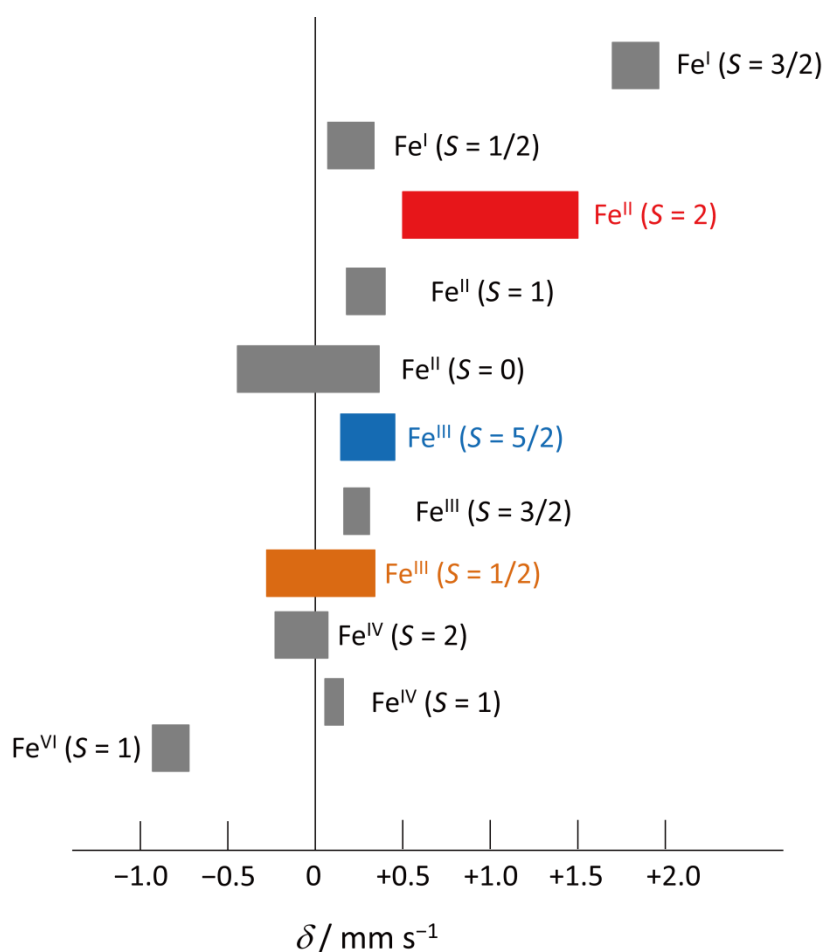


**Figure 2.3.6.** Oxidation numbers and isomer shifts of iron.

### 2.3.2 Quadrupole Splitting

The atomic nucleus has spin angular momentum similar to that of an electron, and nuclear spin moment is denoted by  $I$ . When  $I = 0$ , the nuclear charge distribution is spherically symmetrical and it corresponds to no rotation. When  $I = 1/2$ , the charge distribution is spherically symmetrical and corresponds to rotation. When  $I \geq 1$ , it rotates, but the charge distribution is not spherically symmetrical and has electric quadrupole moment. When the electric quadrupole is placed in the electric field gradient, direction-dependent interaction results and the energy state is determined

according to the direction in which the orientation of the spin inclines with respect to the electric field gradient (Figure 2.3.7). Thus, in case of  $I \geq 1$ , the energy levels of the nucleus split according to the interaction with the distortion in charge distribution of the nuclear site (electric field gradient). For transitions with the levels corresponding to the splitting, several peaks appear in Mössbauer spectrum (Figure 2.3.8). This is called as quadrupole splitting ( $QS$ ) and

$$QS = \frac{1}{2} e^2 q Q \sqrt{1 + \frac{\eta^2}{3}} \quad (2.3.6)$$

Here,  $eq = V_{zz}$  is the electric field gradient when z axis is in the direction of maximum electric field gradient. Further,  $\eta$  is called as asymmetry parameter, and by using electric field gradients  $V_{xx}$  and  $V_{yy}$  in the directions x and y axes, respectively, it is defined as

$$\eta = \frac{V_{xx} - V_{yy}}{V_{zz}} \quad (2.3.7)$$

As the axes are determined so that  $|V_{zz}| \geq |V_{yy}| \geq |V_{xx}|$ , the relation is  $0 \leq \eta \leq 1$ . Since Q is determined according to the nucleus, it is possible to determine the electric field gradient at the nuclear site by measuring the quadrupole splitting.

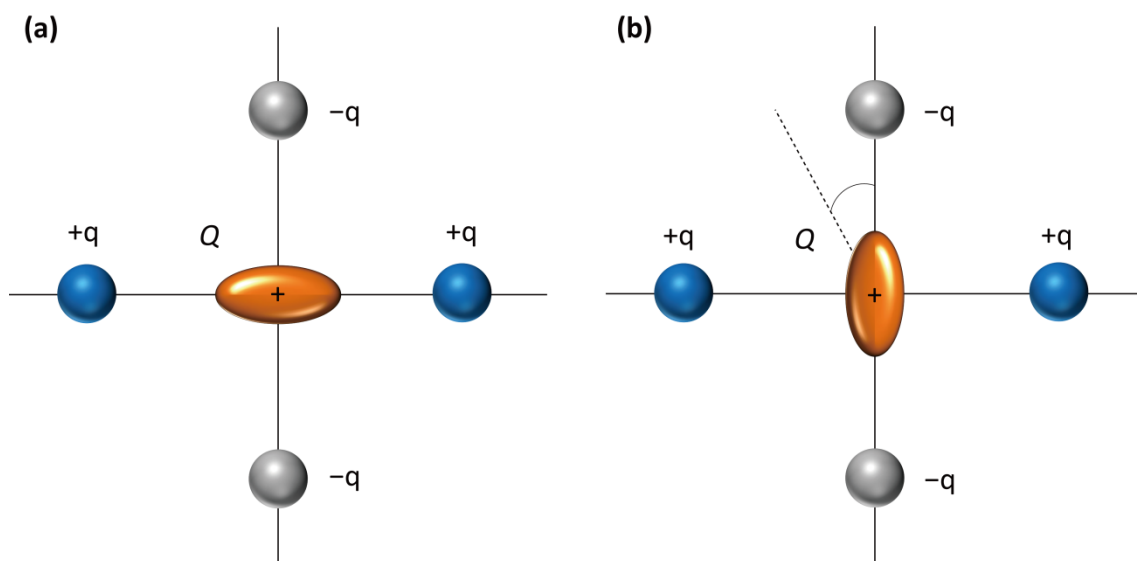


**Figure 2.3.7.** Electric quadrupole moment ( $Q$ ) at the midpoint between two positive charges ( $+q$ ) and two negative charges ( $-q$ ).

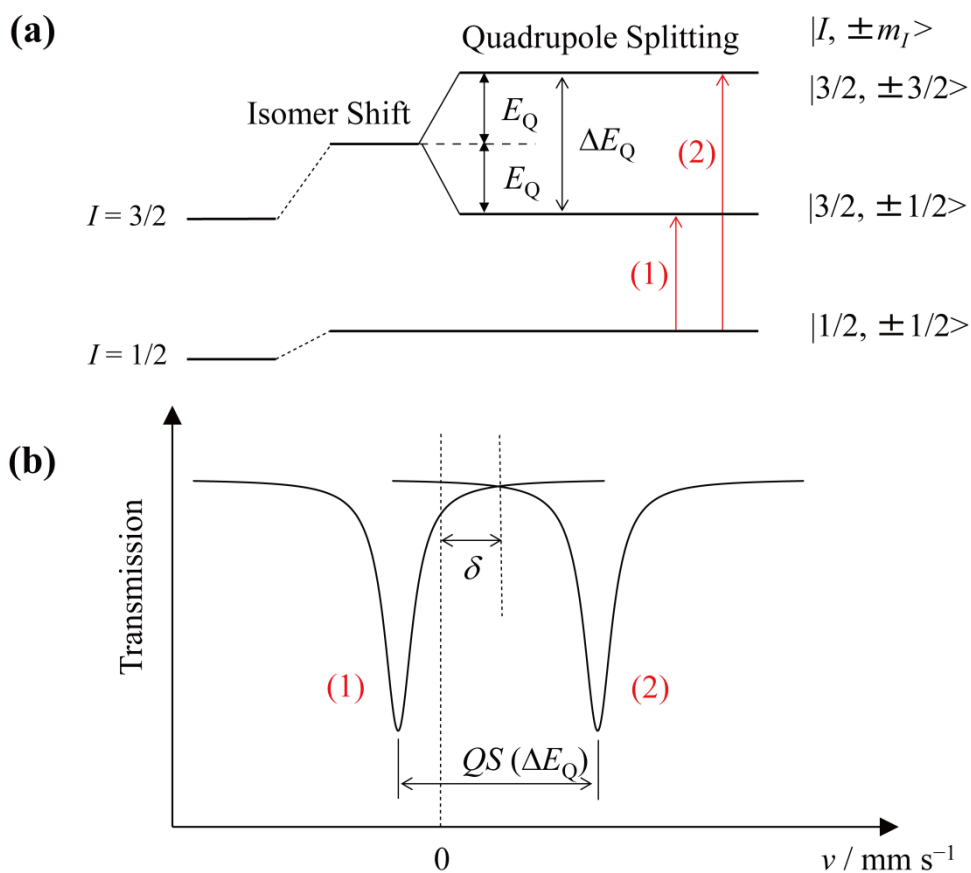


**Figure 2.3.8.** (a) The first excited level being split by the interaction between quadrupole moment and electric field gradient, and (b) the absorption spectrum.

## 2.4 Alternative Current Impedance Method<sup>[9]</sup>

As the electric conductance is the reciprocal of resistance, it can be evaluated by using Ohm's law

$$\sigma = \frac{l I}{S V} \quad (2.4.1)$$

Here,  $\sigma$  is electrical conductance,  $l$  is distance between the electrodes,  $S$  is the cross sectional area of the sample,  $I$  is electric current, and  $V$  is the applied voltage. Thus, by applying a voltage to the sample and measuring the current flowing at that time, the electrical conductance of the sample can be calculated from the values of cross-sectional area of the sample and the distance between the electrodes. However, in case of measurement of conductance of an ionic conductor, often, the ions contribute to the conduction, or ionic conduction is predominant. In such cases, measured conductance includes not only the characteristic conductance of the material (bulk conductance) but also conductance corresponding to the polarization resistance at the electrodes (interface conductance). Furthermore, in case of a polycrystalline sample, it often includes conductance at the grain boundaries (grain boundary conductance) that cannot be neglected. Measurement by using alternating voltage-current is simple for the evaluation of such multi-step conductance by isolating the steps. In the alternating current method, frequency sweeping is carried out and the impedance at each frequency is measured. In the measurement of electrical conductance of a solid, usually frequencies from 10 Hz to 1 MHz are used. In general, the stage involving electrode reaction involves relatively long relaxation time, and therefore, the measurement is made without the influence of polarization occurring at the electrodes by using a frequency greater than this.

Impedance  $Z$  is a complex number, and it is composed of the real component  $Z'$  and imaginary component  $Z''$ .

$$Z = Z' - jZ'' \quad (2.4.2)$$

The impedance plot where  $Z'$  and  $Z''$  are plotted along the horizontal axis and vertical axis, respectively, is called as Nyquist plot. Figure 2.4.1 shows a parallel circuit of  $R$  and  $C$  with impedance spectrum.

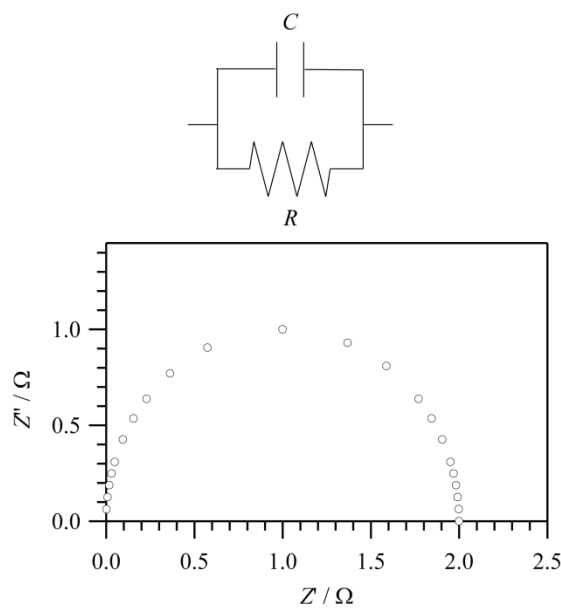


**Figure 2.4.1.** The RC circuit and the Nyquist plot.

$Z'$  and  $Z''$  of the impedance derived from this equivalent circuit are as follows.

$$Z' = \frac{R}{1 + (2\pi f)^2 R^2 C^2} \quad (2.4.3)$$

$$Z'' = \frac{(2\pi f) R^2 C}{1 + (2\pi f)^2 R^2 C^2} \quad (2.4.4)$$

Furthermore, after eliminating  $f$  from equations (2.4.3) and (2.4.4), the following relation is obtained.

$$\left(Z' - \frac{R}{2}\right)^2 + Z''^2 = \left(\frac{R}{2}\right)^2 \quad (2.4.5)$$

The Nyquist plot obtained using equations (2.4.3) and (2.4.5) gives a semicircular locus represented by equation (2.4.5). The semicircle obtained from the parallel RC circuit is called the capacitive semicircle of the time constant RC. The center of the semicircle is  $(R/2, 0)$  and the diameter is  $R$ . The locus of impedance meets the real axis at zero and  $R$  at the high-frequency and low-frequency limits, respectively.

The results of the alternating current method are obtained by assuming a physically suitable equivalent circuit for the actual system and quantifying it. Generally, in case of polycrystalline solid samples with ionic conduction, it is a common practice to carry out the analysis by using a simple equivalent circuit as shown in Figure 2.4.2(a) by considering the effect of grains constituting the sample (bulk), grain boundary, and sample/electrode interface. In such cases, the impedance of each RC parallel circuit is expressed as

$$Z_i = \frac{1}{\frac{1}{R_i} + j\omega C_i} = \frac{R_i}{1 + \omega^2 R_i^2 C_i^2} - j \frac{\omega R_i^2 C_i}{1 + \omega^2 R_i^2 C_i^2} \quad (2.4.6)$$

(suffix  $i = g$  (bulk),  $gb$  (grain boundary),  $if$  (interface))

Here,  $R_i$  is the resistance and  $C_i$  is capacitance,  $\omega$  is the angular frequency ( $=1/2\pi f$  where  $f$  is the frequency). Figure 2.4.2 shows typical impedance spectrum (Nyquist plot) for the equivalent circuit of Figure 2.4.2(a). In general, the relaxation time of each step constituting the equivalent circuit of Figure 2.4.2 increases in the order of the bulk, grain boundary, and electrode interface. Thus, the three semicircles seen in Figure 2.4.2(b) from the high-frequency side (left hand side of the figure) are the responses from bulk, grain boundary, and electrode interface, respectively. According to

each semicircle. In this manner, it is possible in principle to evaluate each component by isolating it by using the alternating current method. In general, the characteristic conductivity of a sample is considered to be the one obtained from its bulk resistance  $R_b$ .

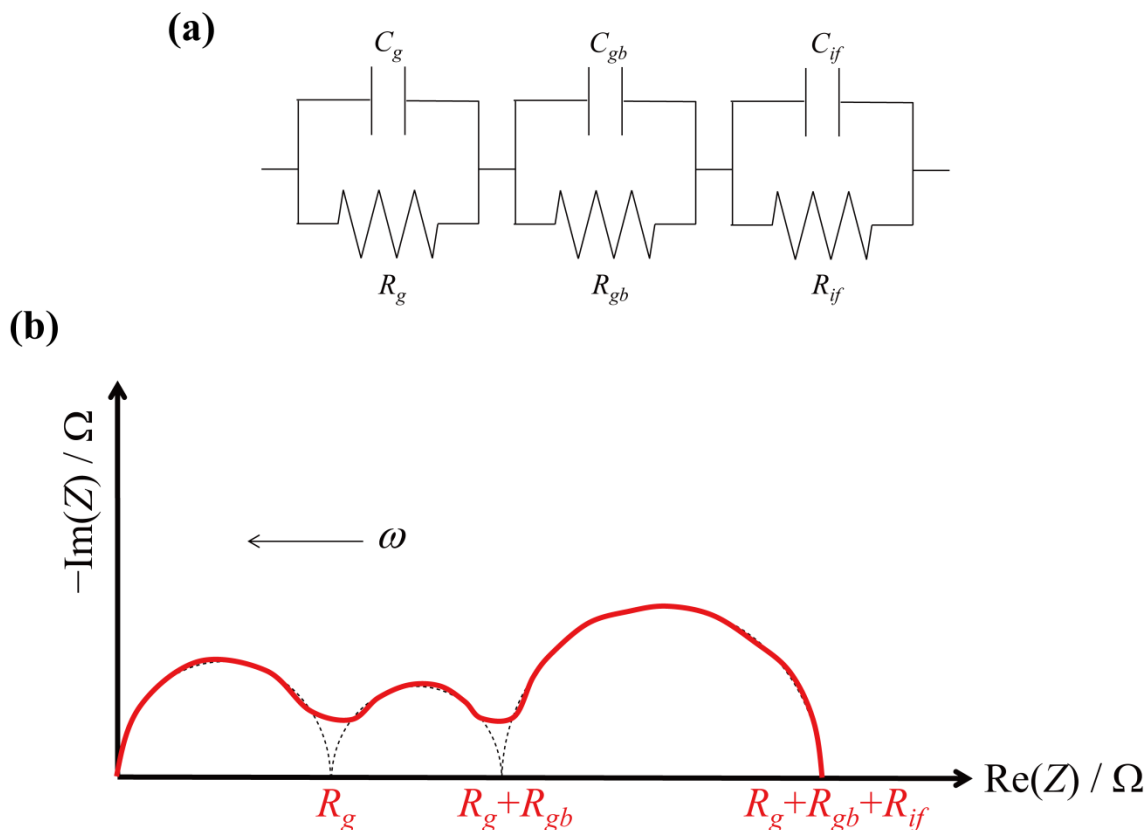


**Figure 2.4.2.** Representative example in a result of conductivity measurement for an ion conductor by means of alternating current method. (a) The equivalent circuit, and (b) the impedance spectrum.

Furthermore, in actual measurement, in many cases, there is a possibility of the spectrum being extremely complicated because of overlapping of several relaxation zones and involvement of some conduction-reaction steps. For example, although a plot like Figure 2.4.2(b) is obtained, there are multiple impedance components and there are many instances when the arcs are not exactly circular. Moreover, depending upon the instrument used, there may be restrictions on the usable frequency

region, and therefore, it may be possible to measure only a part of the arc. Even in the analysis of such a complicated spectrum, electrical conductance is calculated by assuming appropriate equivalent circuits and fitting the data using their theoretical formulas. It is, however, not possible to avoid slight errors or arbitrariness.

## 2.5 Solid State NMR Spectroscopy<sup>[10]</sup>

### 2.5.1 Nuclear Dipole Interactions

In the classical sense, a nuclear spin is much like a small magnet that creates a local magnetic field in its vicinity. When other nuclear spins exist near that, they are mutually affected by the others' magnetic fields. This is referred to as nuclear magnetic dipolar interaction. The magnitude of the effects that the energy level of a spin is subjected to the nuclear magnetic dipolar interaction when the two nuclear spins  $I_1$  and  $I_2$  are separated by a distance of  $r$  (Figure 2.5.1) can be expressed by

$$\mathbf{H}_d = \hbar^2 \gamma_1 \cdot \gamma_2 \left\{ \frac{3(\mathbf{r} \cdot \mathbf{I}_1)(\mathbf{r} \cdot \mathbf{I}_2)}{r^5} - \frac{\mathbf{I}_1 \cdot \mathbf{I}_2}{r^3} \right\} \quad (2.5.1)$$

where  $(\mathbf{r} \cdot \mathbf{I}_1)$ ,  $(\mathbf{r} \cdot \mathbf{I}_2)$ , and  $(\mathbf{I}_1 \cdot \mathbf{I}_2)$  are inner products of the vector. Therefore, the magnitude of the nuclear magnetic dipolar interactions is sensitive to the differences in the internuclear distances; the internuclear distances within a solid can be determined from the nuclear magnetic resonance (NMR) spectrum. Equation (2.5.1) should also be considered for cases where multiple nuclear spins are affected by mutual magnetic dipolar interactions between pairs of all spins and taking their sum. Such nuclear magnetic dipolar interactions affect the shape of the NMR spectrum.

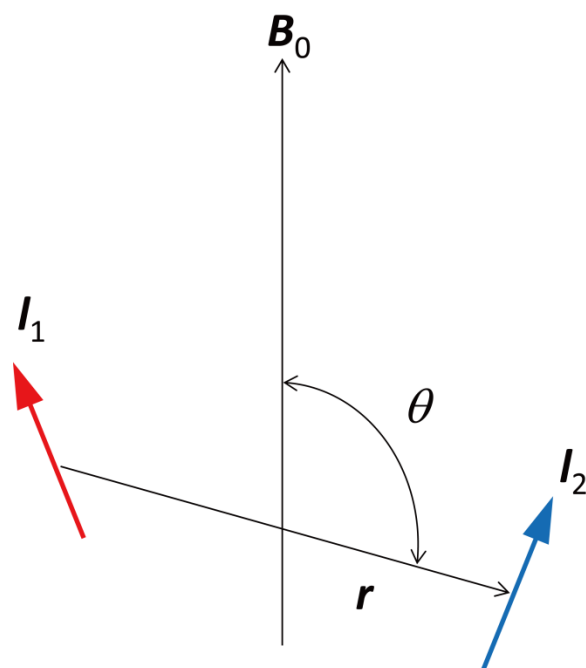


**Figure 2.5.1.** Dipolar interaction between two nuclear spins.

Now, let us consider two proton spins ( $^1\text{H}$ ) as a simple example. When these interact with each other, total nuclear spin  $I$  becomes 1, and the Zeeman energy level in the static magnetic field under such conditions has three types with magnetic quantum numbers  $m_I$  of  $-1$ ,  $0$ , and  $+1$ . Considering the effects on the shape of the NMR spectrum means looking into the slight shift in the Zeeman energy level due to nuclear magnetic dipolar interactions. The frequency  $\nu_D$  that represents the amplitude of this shift is given by

$$\nu_D = \frac{1}{2}D(3\cos^2\theta - 1) \quad (2.5.2a)$$

$$D = \frac{\mu_0 h \gamma_H^2}{4\pi r^3} \quad (2.5.2b)$$

where  $\theta$  is the angle formed by the internuclear vector  $\mathbf{r}$  and the static magnetic field  $B_0$ , and  $\mu_0$  is the absolute permeability of the vacuum. The selection rule for the NMR transition is  $\Delta m_I = \pm 1$ ; if no interaction expressed by Equation (2.5.2) exists, then the observed NMR spectrum has a single line with the frequency of  $\omega_0/2\pi$ . Two lines in the spectrum are observed when the interaction expressed by Equation (2.5.2) is added. As the molecular motion becomes more vigorous because of thermal energy, such spectra composed of two lines cease to be observed (as is the case with the  $^1\text{H}$  NMR spectrum in a solution). This is because the portion of Equation (2.5.2) that is dependent on the angle (*i.e.*,  $3\cos^2\theta - 1$ ) is averaged and becomes zero. The amplitude of the nuclear magnetic dipolar interaction expressed by Equation (2.5.2) is a few tens of kilohertz and is averaged when the molecules and ions are engaged in spinning motions with much higher rates. Conversely, when molecules in a solid start spinning motions, these can be quickly distinguished in the solid NMR spectrum.

### 2.5.2 Magic Angle Spinning (MAS)

Consider a case where an NMR specimen container filled with powdered crystal specimens is artificially spun. Let the angle formed by the orientation of the static magnetic field and the rotational axis of the specimen container be  $\alpha$  and the angle formed by this rotational axis and the internuclear vector to be  $\beta$ . When the specimen container is spun at a sufficiently fast rate, the angle-dependent term of Equation (2.5.2) is partially averaged and can be expressed as

nuclear spins with a large gyromagnetic ratio  $\gamma$ , it is sufficient to rotate at 5-10 kHz for  $^2\text{H}$ ,  $^{13}\text{C}$ ,  $^{15}\text{N}$ , *etc.* with smaller  $\gamma$ . Furthermore, while it is not possible to manipulate the angle formed by the internuclear vector  $\beta$ , the angle  $\alpha$  formed by the orientation of the static magnetic field and the axis about which the specimen container is rotating can be changed arbitrarily. Therefore, the nuclear magnetic bipolar interaction should disappear if the angle  $\alpha$  is set so that  $(1 - 3\cos^2\alpha)$  becomes zero.

In other words, we should get

$$\cos\alpha = \sqrt{\frac{1}{3}}, \alpha = 54.74^\circ \quad (2.5.4)$$

Because the nuclear magnetic bipolar interaction disappears as if by magic, this angle is referred to as the “magic angle.” Rotating the specimen container at the angle  $\alpha$  of  $54.74^\circ$  is referred to as magic angle spinning (MAS). A spinning sideband appears when the MAS frequency is slower than the line width coming from the first-order quadrupolar interaction in an isotope with an integer spin.

### 2.5.3 Nuclear Quadrupolar Interactions and Detection of Molecular Motion

Nuclear quadrupolar interaction is caused by a charge density distribution inside an atomic nucleus from the presence of positive-charge protons and no-charge neutrons. Atomic nuclei generally have a charge density distribution; atomic nuclei in a molecule or ion interact with the electrostatic potential created by their surrounding electrons and other atomic nuclei. When the nuclear spin is  $I \geq 1$ , then this electrostatic interaction affects the energy state of the nuclear spin, and a characteristic shape of the NMR spectrum is formed.

The nuclear quadrupole moment can be expressed by a  $3 \times 3$  matrix (tensor):

$$\begin{bmatrix} V_{xx} & V_{xy} & V_{xz} \\ V_{yx} & V_{yy} & V_{yz} \\ V_{zx} & V_{zy} & V_{zz} \end{bmatrix} \quad (2.5.5)$$

Setting an appropriate coordinate axis that considers the molecular or crystal structure and symmetry around the nucleus makes it possible to set a new coordinate system where the tensor of Equation (2.5.5) only has diagonal components. This is expressed by Equation (2.5.6):

$$\begin{bmatrix} V_{x'x'} & 0 & 0 \\ 0 & V_{y'y'} & 0 \\ 0 & 0 & V_{z'z'} \end{bmatrix} \quad (2.5.6)$$

Furthermore, Equation (2.5.7) can be established based on the properties of the electric field gradient:

$$V_{x'x'} + V_{y'y'} + V_{z'z'} \quad (2.5.7)$$

Because the value of the electric field gradient is related to the quantity of the charge, the  $z'$  component can be expressed by the following equation using the elementary charge  $e$ :

$$V_{z'z'} = eq \quad (2.5.8)$$

The other components can be expressed by defining the asymmetric factor  $0 \leq \eta \leq 1$  as shown in Equation (2.5.9):

$$\eta = \frac{V_{x'x'} - V_{y'y'}}{V_{z'z'}} \quad (2.5.9)$$

For instance, in heavy water ( $D_2O$ ), the influence of the O–D bond is large. However, the influence of the unshared electron pairs is also relatively large, and  $\eta$  often becomes approximately 0.2 when there is no or a weak hydrogen bond. When the O–D–O distance becomes  $R_{O-O} \leq 0.25$  nm, like for an ionized hydrogen bond, the electric field gradient becomes largest in the vicinity of  $^2H$  in the two directions that orthogonally intersect with the O–D–O coupling axis; the amplitude of these two components of the electric field gradient become roughly the same. In such an instance,  $\eta$  becomes

approximately 1. Such characteristics of the electric field gradient in the vicinity of  $^2\text{H}$  sensitively affect the spectrum shape of the solid  $^2\text{H}$  NMR. The amplitude of the energy shift from this nuclear quadrupole interaction acting on the energy level of the  $^2\text{H}$  nucleus can be expressed by  $eq$  of Equation (2.5.8) and the amplitude of the nuclear quadrupole moment  $eQ$ . The frequency  $\nu_Q$  that represents such an energy shift is expressed by

$$\nu_Q = \frac{3}{4}C_Q(3\cos^2\theta - 1) \quad (2.5.10)$$

and derived as

$$C_Q = \frac{e^2qQ}{h} \quad (2.5.11)$$

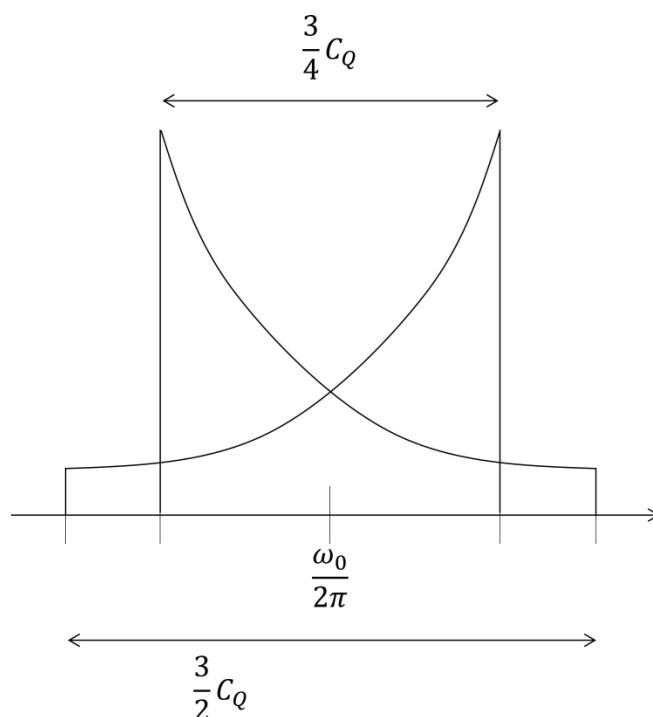


**Figure 2.5.2.** Powder pattern in  $^2\text{H}$ -NMR spectrum: Pake-type doublet.

$C_Q$  represents the nuclear quadrupole coupling constant and varies according to the type of bonds. Because the two resonance lines depicted in Figure 2.5.2 (*i.e.*,  $\hbar\omega_0 + 1/2h\nu_Q$  and  $\hbar\omega_0 - 1/2h\nu_Q$ ) change with  $\theta$ , as shown in Equation (2.5.2), the shape of the spectrum of the powdered crystal specimen becomes as shown in Figure 2.5.2 when  $\eta = 0$ . This split becomes averaged as the molecular motion in the solid intensifies, and the shape of the  $^2\text{H}$  NMR spectrum changes. It is possible to determine what kinds of motions are occurring at what rates in detail through further investigation. A much more detailed investigation than that from using the nuclear dipolar interaction described above is feasible.

## References

- [1] a) O. Kahn, *Molecular Magnetism*, Wiley-VCH, New York, **1993**; b) 大川尚士、『磁性の化学』、朝倉書店、2004; c) 『金属錯体の機器分析 (下)』(大塩寛紀 編)、三共出版、pp.1-69、**2012**.
- [2] a) P. Pascal, *Ann. Chim. Physique* **1910**, 19, 5; b) A. Pacault, *Rev. Sci.* **1948**, 86, 38; c) W. Haberditzl, *Angew. Chem. Int. Ed.* **1966**, 5, 288.
- [3] a) *X-ray Spectroscopy*, ed. by L. V. Azároff, McGraw-Hill, Inc., New York, **1974**; b) B. K. Agarwal, *X-Ray Spectroscopy*, Springer-Verlag, Berlin, Heidelberg, New York, **1979**; c) *X-Ray Spectroscopy in Atomic and Solid State Physics*, ed. by J. G. Ferreira, M. T. Ramos, Plenum Press, New York, **1988**; d) *X-Ray Absorption: Principles, Applications, Techniques of EXAFS, SEXAFS and XANES*, ed. D. C. Koningsberger, R. Prins, Wiley-VCH, New York, **1988**; e) G. Bunker, *Introduction to XAFS*, Cambridge University Press, Cambridge, **2010**.
- [4] [http://133.50.165.193/catdb/index.php?action=xafs\\_login\\_form&opnid=2](http://133.50.165.193/catdb/index.php?action=xafs_login_form&opnid=2)
- [5] A. Corrias, G. Ennas, G. Mountjoy, G. Paschina, *Phys. Chem. Chem. Phys.* **2000**, 2, 1045.
- [6] P. Gütllich, R. Link, and A. Trautwein, *Mössbauer Spectroscopy and Transition Metal Chemistry*, Springer-Verlag, Berlin Heidelberg New York, **1978**.
- [7] (a) R. L. Mössbauer, *Z. Physik* **1958**, 151, 124; b) R. L. Mössbauer, *Naturwissenschaften* 1958, **45**, 538; c) R. L. Mössbauer, *Z. Naturforsch* **1959**, 14a, 211.
- [8] P. Gütllich, E. Bill, and A. X. Trautwein, *Mössbauer Spectroscopy and Transition Metal Chemistry*, Springer, New York, **2010**.
- [9] a) *Impedance Spectroscopy*, ed. by E. Barsoukov, and J. R. Macdonald, John Wiley & Sons, New Jersey, **2005**; b) M. E. Orazem, B. Tribollet, *Electrochemical Impedance Spectroscopy*, John Wiley & Sons, New Jersey, **2008**.
- [10] a) M. H. Levitt, *Spin Dynamics: Basics of Nuclear Magnetic Resonance*, John Wiley & Sons,

2008; b) 荒田洋治、『NMR の書』、丸善、**2000**; c) 『金属錯体の機器分析 (下)』(大塩寛紀編)、三共出版、pp.105-172、**2012**.

### 3. Development of a Proton Responsive Spin-Crossover Complex Film and Its Control of the Spin State Accompanied by Proton Flow

#### Abstract

The hexa-amine cage ligand, sarcophagine, and its derivatives encapsulate transition metal ions, whose coordination compounds with iron(II) exhibit a spin equilibrium between  $t_{2g}^4 e_g^2$  ( $S = 2$ ,  $^5T_{2g}$ ) and  $t_{2g}^6$  ( $S = 0$ ,  $^1A_{1g}$ ). In particular,  $[\text{Fe}^{\text{II}}(\text{diAMsar})]$  (diAMsar = 1,8-diaminosarcophagine) is known as a proton responsive spin-crossover complex. It has yellow colored high-spin (HS) state in acidic conditions, whereas it has blue colored low-spin (LS) state in basic conditions. Recently, transparent films incorporating the pH-sensitive complex,  $[\text{Fe}^{\text{II}}(\text{diAMsar})]@\text{Nafion}$ , have been prepared, which shows different colors originating in the spin states under the synthetic conditions of pH 4, 7 and 10. In the XANES spectra, the energy position of the absorption edge and the main peak of pH 10 were shifted to a higher energy side by 3.5 eV compared with those of pH 4 and 7. This feature is consistent with the spin-crossover transition of  $\text{Fe}^{\text{II}}\text{-N}_6$  complexes. From the analysis of EXAFS, it is clarified that Fe-N bond was shortened as the sample environment changes from pH 4 and 7 to pH 10. The change in Fe-N distance between the HS state (pH 4 and 7) and the LS state (pH 10) was estimated as *ca.* 0.17 Å which is close to that for typical  $\text{Fe}^{\text{II}}$  spin-crossover complexes. Based on these results, an attempt to control the spin state of  $[\text{Fe}^{\text{II}}(\text{diAMsar})]$  by electric-field-induced gradient of proton concentration has been done. As the voltage was applied, the dynamic spin-crossover behavior with time-variable and reversible color change was successfully observed in  $[\text{Fe}^{\text{II}}(\text{diAMsar})]@\text{Nafion}$  at pH 4 with the proton conductivity of  $2.16 \times 10^{-7}$  (S cm<sup>-1</sup>). Meanwhile, the film at pH 10 did not exhibit the color change under the applied voltage with the proton conductivity of  $4.52 \times 10^{-9}$  (S cm<sup>-1</sup>). The results described above imply the direct observation of proton flow in Nafion using proton-responsive spin-crossover complex as a visual indicator.

### 3.1 Introduction

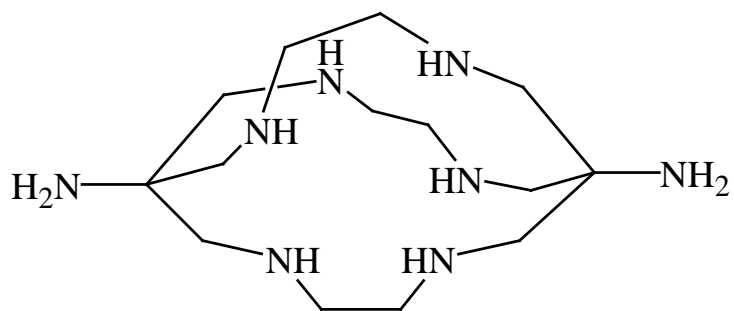
There are a lot of reports on spin-crossover Fe<sup>II</sup> complexes with octahedral FeN<sub>6</sub> geometry.<sup>[1]</sup> Almost all spin-crossover Fe<sup>II</sup> complexes have a  $\pi$ -conjugated ligand with a low-lying  $\pi^*$  orbital (such as pyridine, bipyridine, phenanthroline, *etc.*) which induces the stabilization of  $t_{2g}$  orbitals through  $\pi$ -back donation. As a rare case, Martin *et al.* reported that the spin equilibrium between  $t_{2g}^6$  (<sup>1</sup>A<sub>1g</sub>) and  $t_{2g}^4e_g^2$  (<sup>5</sup>T<sub>2g</sub>) took place in the Fe<sup>II</sup> complexes coordinated by a hexaamine cage ligand, sarcophagine (sar) and its derivatives.<sup>[2]</sup> They investigated the magnetic behavior of [Fe<sup>II</sup>(sar)] complexes in detail and clarified that spin-crossover phenomena took place in solution, not in the solid state.<sup>[3,4]</sup> It should be noted that their complexes consist of the  $\sigma$ -donating ligand without  $\pi$ -back donation. In particular, the spin-transition temperature and the color change of [Fe<sup>II</sup>(diAMsar)] (diAMsar = 1,8-diaminosarcophagine; Scheme 3.1) complex in the solution is dependent on pH ( $T_{1/2}$  = 290 K; pH 4.5,  $T_{1/2}$  = 370 K; pH 8.5) due to the protonation/deprotonation of the terminal amino groups (Figure 3.1).<sup>[4]</sup> As shown in Figure 3.1, [Fe<sup>II</sup>(diAMsar)]@Nafion also has different colors depending on proton concentration controlled by buffer solution (pH 4, 7 and 10). This property indicates that [Fe<sup>II</sup>(diAMsar)] has potential as a molecular device responding to proton concentration as an external stimuli, though nonliquid conditions are unacceptable for such devices.

Pioneering works for related researches have been reported as studies on [Fe<sup>II</sup>(2-mephen)<sub>3</sub>] (2-mephen: 2-methyl-1,10-phenanthroline) and [Fe<sup>II</sup>(R-trz)<sub>3</sub>] (R = H, NH<sub>2</sub>; trz: 1,2,4-triazole) in Nafion, which are transparent films showing spin-crossover transition.<sup>[5-9]</sup> Regarding [Fe<sup>II</sup>(R-trz)<sub>3</sub>], Kröber *et al.* reported the spin-crossover transition with wide thermal hysteresis around RT for [Fe<sup>II</sup>(H-trz)<sub>2.85</sub>(NH<sub>2</sub>-trz)<sub>0.15</sub>](ClO<sub>4</sub>)<sub>2</sub> (trz = 1,2,4-triazole).<sup>[10]</sup> Since then, a number of researchers have investigated triazole-bridged Fe<sup>II</sup> complexes, [Fe<sup>II</sup>(R-trz)<sub>3</sub>] (R = H, NH<sub>2</sub>), from the viewpoint of molecular devices at RT.<sup>[11-13]</sup> For molecular devices, single crystals or thin films are much

preferable to powdered crystals or solution. However,  $[\text{Fe}^{\text{II}}(\text{R-trz})_3]$  complexes hardly crystallize as a single crystal suitable for X-ray crystallography due to its rapid precipitation. Hence, Kojima *et al.* have synthesized the  $[\text{Fe}^{\text{II}}(\text{R-trz})_3]$  complex in Nafion membrane and successfully observed the thermally- and photo-induced spin transition of the transparent spin-crossover complex film:  $[\text{Fe}^{\text{II}}(\text{R-trz})_3]@\text{Nafion}$ .<sup>[14-17]</sup> In  $[\text{Fe}^{\text{II}}(\text{R-trz})_3]@\text{Nafion}$ , the oligomer of  $[\text{Fe}(\text{R-trz})_3]_n^{2n+}$  is embedded in the cavity, and the side chain terminated by  $\text{SO}_3\text{H}$  groups in Nafion behaves as a counter-anion.<sup>[15]</sup>

Nafion, which was developed by DuPont Co. in 1960s, is an ionexchange resin consisting of a linear polymer of fluorocarbon and sulfonic acid or carboxylic acid groups and applied to fuel cells,<sup>[18]</sup> sensors,<sup>[19]</sup> and catalysts<sup>[20]</sup> due to its durability, chemical and thermal stability, and permselectivity. In the case of Nafion 117, reverse micelles consisting of perfluoroalkylether groups with hydrophilic  $\text{SO}_3\text{H}$  groups form clusters of *ca.* 4 nm diameter separated by a distance of *ca.* 5 nm and interconnected through channels of *ca.* 1 nm when they are swollen with water,<sup>[21,22]</sup> and the side chain terminated by  $\text{SO}_3\text{H}$  groups behaves as a counter-anion as well as transparent substrate (Figure 3.2). By achievement of intermediate cooperation in a medium between liquid and solid, it is expected to realize spin-crossover complex films and manipulate the spin state by proton concentration.

In this chapter, efforts to develop transparent films incorporating the pH-sensitive SCO complex using Nafion and to control the spin state electrically through the gradient of proton concentration induced by applied voltage are reported; the concept of this study is summarized in Figure 3.3.



**Scheme 3.1.** Molecular structure of diAMsar.

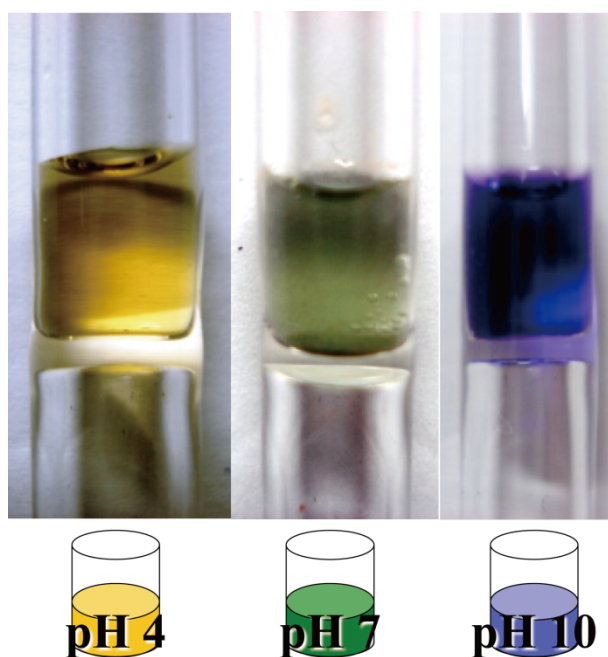


**Figure 3.1.** Photographs of aqueous solutions of [Fe<sup>II</sup>(diAMsar)] at various pH conditions.

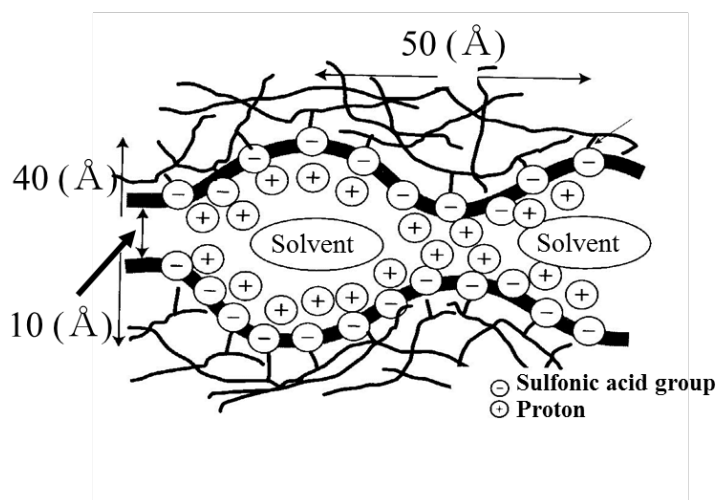


**Figure 3.2.** Inner structural model of Nafion when they are swollen with water.

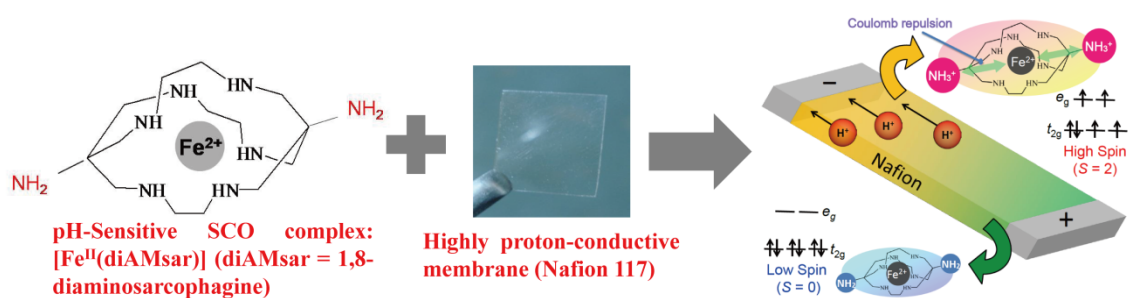


**Figure 3.3.** Concept of this study.

## 3.2 Materials and Methods

### Sample preparation

Nafion 117 was purchased from DuPont Company. The cage ligand, diAMsar, was synthesized according to the literature.<sup>[23]</sup> Distilled water was deoxygenized by inspiring  $N_2$  gas for several days. Nafion 117 was pretreated by immersing in 10% aqueous solution of  $HNO_3$  for 12 h. The acid form of Nafion was immersed in 5% aqueous solution of  $FeSO_4 \cdot 7H_2O$  for 12 h, leading to absorption of  $Fe^{II}$  ions into Nafion. The membrane,  $Fe@Nafion$ , was rinsed with distilled water and subsequently immersed in buffer solution (pH 4, 7, and 10) dissolving diAMsar ligand for 12 h. The film was immersed in an aqueous solution of  $KCl$  ( $2.0 \text{ mol cm}^{-3}$ ) in order to remove excessive free  $Fe^{II}$  ion. This process is schematically shown in Figure 3.4. All operations were carried out under inert atmosphere.

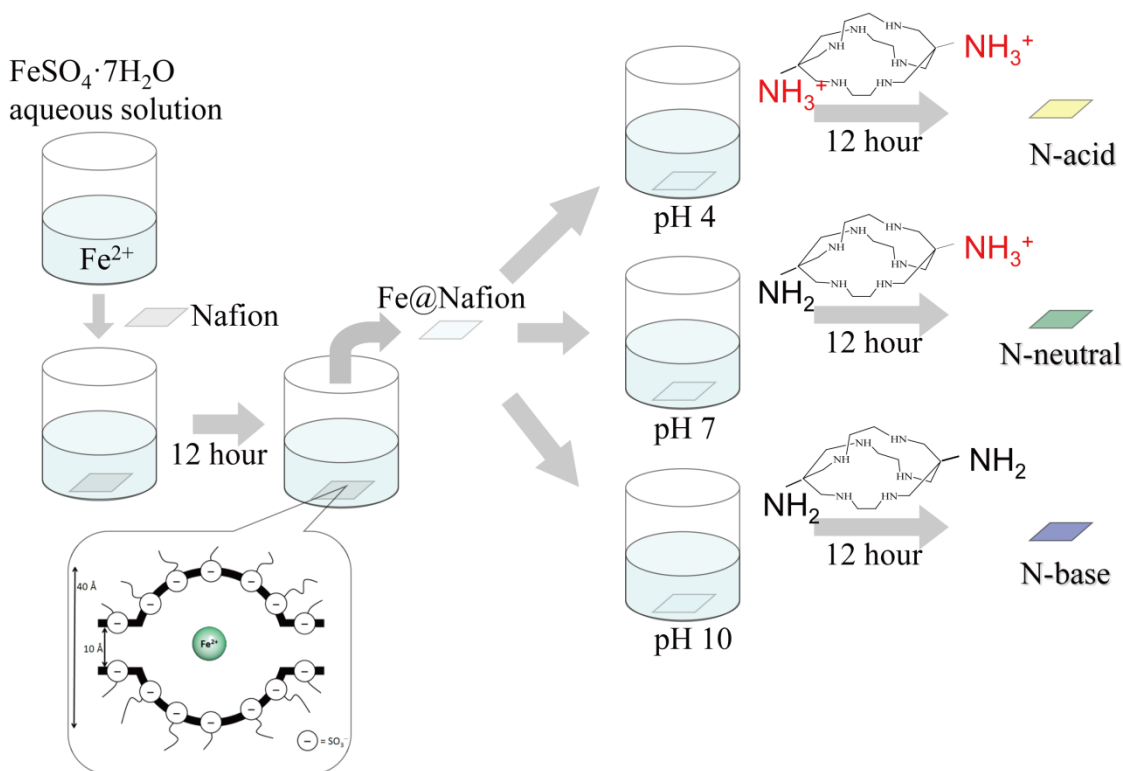


**Figure 3.4.** Schematic illustration of the preparation method of  $[Fe^{II}(\text{diAMsar})]@Nafion$ .

### **UV-vis absorption spectroscopy**

The optical absorption spectra were measured on a JASCO MSV-370 spectrometer under inert atmosphere.

### **<sup>57</sup>Fe Mössbauer spectroscopic measurement**

For <sup>57</sup>Fe Mössbauer spectroscopic measurement, <sup>57</sup>Co in Rh matrix was used as a Mössbauer source. The spectra were calibrated by using the six lines of a body-centered cubic iron foil ( $\alpha$ -Fe), the center of which was taken as zero isomer shift.

### **Fe K-edge XAFS measurement**

Fe K-edge XAFS (X-ray absorption fine structure) spectra were taken at beamlines 9A and 12C of the Photon Factory (operation energy of 2.5 GeV and stored current of 450 mA) in Institute of Materials Structure Science (KEK-PF), using double-crystal Si(111) monochromators. pH 4 and pH 7 samples were measured at around 50 K in the quick-scan transmission mode which took about a minute to collect the whole data while pH 10 sample was measured for 15 minutes in the fluorescence mode using Lytle-type detector at room temperature. The five films of pH 4 sample were piled up for the measurement. Epoxy resin (STYCAST 1266) and fluorinert were used for encapsulating the samples.

### **Applying voltage**

Voltage was applied at 20 V for *ca.* 1 h by using 2400 SourceMeter (Keithley Instruments Company) as a voltage supply.

### **Computational methods**

Density functional theory (DFT) calculations were implemented in the Gaussian 09 package,<sup>[24]</sup> by employing Becke's 3-parameter hybrid functional<sup>[25]</sup> and the Lee-Yang-Parr correlation functional<sup>[26]</sup> (B3LYP). The electronic structures of [Fe<sup>II</sup>(diAMsar)] were determined using a general basis set with the Los Alamos effective core potential LanL2DZ basis set<sup>[27]</sup> for iron and 6-31G(d,p) for other atoms in the vacuum.

### **Proton conductivity**

Gold electrodes were mounted on both sides of the emissive film with carbon paste. The conductivity measurement was performed with Model 1260 Impedance/Gain-Phase Analyzer (Solatron Analytical Co.) equipped with Model 1296 Dielectric Interface (Solatron Analytical Co.) in the frequency range of 1 Hz to 1MHz.

## 3.3 Results and Discussion

### Synthesis

The transparent films,  $[\text{Fe}^{\text{II}}(\text{diAMsar})]@\text{Nafion}$  (Figure 3.5), were prepared according to the following sequential procedure: (i) Loading iron(II) ions into Nafion; (ii) Complexation with diAMsar ligands in the film; (iii) Removing uncoordinated iron(II) ions. Three different types of the complex films were obtained using buffer solutions. The pH dependence of the film color is shown in Figure 3.6. The colors of  $[\text{Fe}^{\text{II}}(\text{diAMsar})]@\text{Nafion}$  films in pH 4, 7, and 10 were yellow, green, and blue, respectively, reflecting the spin states of  $[\text{Fe}^{\text{II}}(\text{diAMsar})]$  complex. The films at pH 4 and 10 were estimated to have the HS and the LS states, respectively, as well as  $[\text{Fe}^{\text{II}}(\text{diAMsar})]$  in water. Besides, the film at pH 7 was assumed to have both the HS and the LS components because the blend of yellow and blue colors becomes green; this was confirmed by  $^{57}\text{Fe}$  Mössbauer spectroscopy as described below.

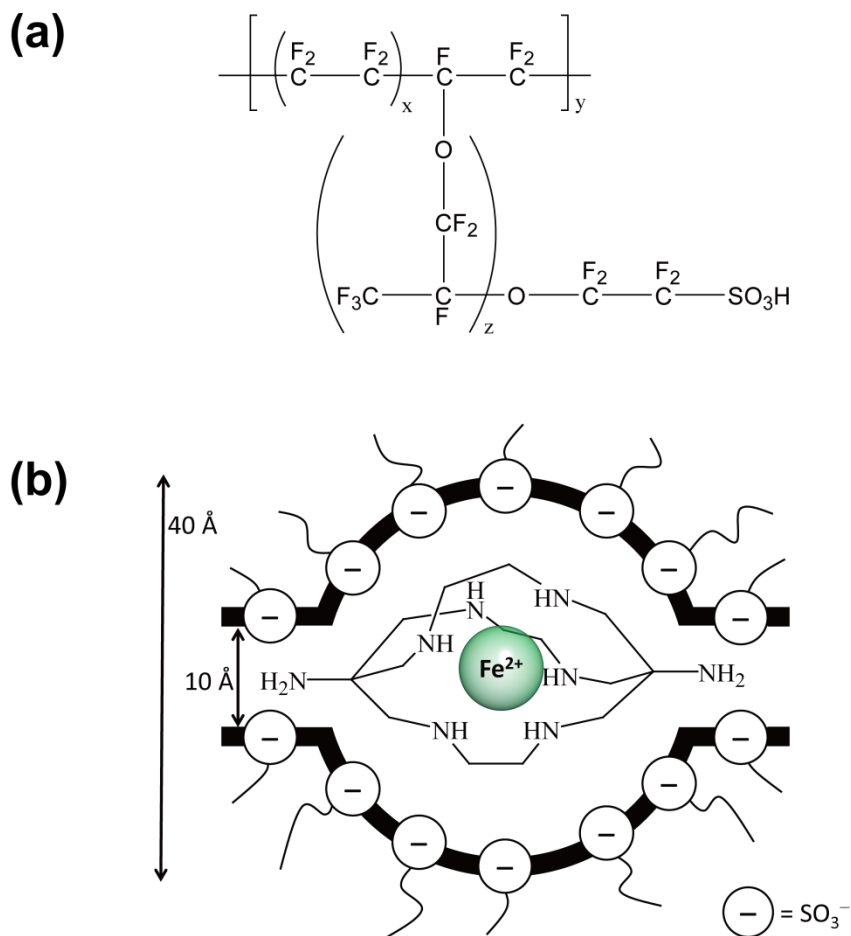


**Figure 3.5.** (a) Structural formula of Nafion. (b) Schematic representation of  $[\text{Fe}^{\text{II}}(\text{diAMsar})]$  embedded in Nafion. Perfluoroalkylether with pendant  $\text{SO}_3^-$  groups forms cavities of ca. 40 Å diameter when Nafion 117 is swollen with water. Nafion behaves as a counter-anion as well as transparent substrate.

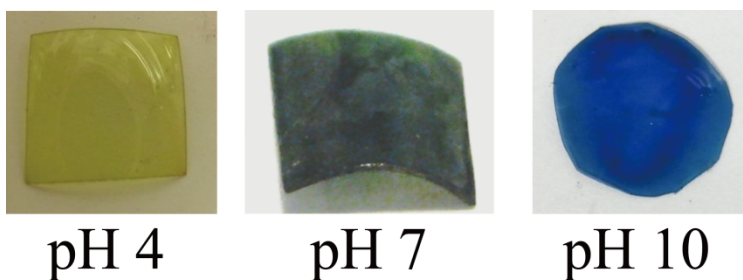


**Figure 3.6.** Photographs of  $[\text{Fe}^{\text{II}}(\text{diAMsar})]$ @Nafion has different colors depending on proton concentration controlled by buffer solutions (pH 4, 7 and 10).

### UV-vis absorption spectroscopy

In the case of pH 7, the optical absorption spectrum shows a broad band at around  $13000\text{ cm}^{-1}$  corresponding to the  ${}^5T_{2g} \rightarrow {}^5E_g$  transition in the HS ( $S = 2$ ) state, while it shows a broad band at around  $18000\text{ cm}^{-1}$  corresponding to the  ${}^1A_{1g} \rightarrow {}^1T_{1g}$  transition in the LS ( $S = 0$ ) state at pH 10 as shown in Figure 3.7. As for the case of pH 4, the band corresponding to the  ${}^5T_{2g} \rightarrow {}^5E_g$  transition is hardly observed due to the desorption of  $\text{Fe}^{\text{II}}$  ions by ion exchange with  $\text{H}^+$  in the acid buffer. The optical results indicate that the amino group becomes protonated with increasing proton concentration, leading to weaker ligand field by the volume expansion of the cage ligand due to the electrostatic repulsion between the  $\text{Fe}^{\text{II}}$  ion and  $\text{NH}_3^+$  group. As a result, the fraction of the HS state in spin equilibrium increases. In contrast, the LS state is dominant in lower proton concentration due to the absence of such a volume expansion. This concept was confirmed by DFT calculation and XAFS spectroscopy.

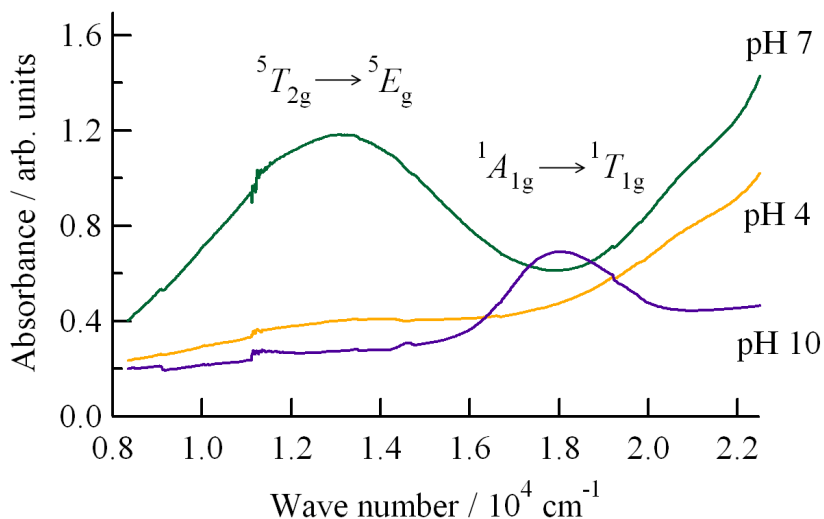


**Figure 3.7.** UV-vis absorption spectra of  $[\text{Fe}^{\text{II}}(\text{diAMsar})]@\text{Nafion}$  films at room temperature.

### <sup>57</sup>Fe Mössbauer spectroscopy

In order to investigate microscopically the electronic state of [Fe<sup>II</sup>(diAMsar)]@Nafion, <sup>57</sup>Fe Mössbauer spectroscopy was carried out at 300 K. <sup>57</sup>Fe Mössbauer spectroscopy, which is based on recoilless resonant absorption of  $\gamma$ -radiation by atomic nuclei, is one of the most efficient and powerful methods to clarify the valence and spin states of iron ions.<sup>[28,29]</sup> The electric monopole interaction alters the position of the resonance lines on the energy scale in units of the Doppler velocity and gives rise to isomer shift ( $\delta$ ).  $\delta$  depends on various chemical parameters, such as oxidation numbers or electron configurations of iron ions, the  $\sigma$ -donor and  $\pi$ -acceptor strengths of the ligands. In addition, the electric quadrupole interaction splits the degenerate nuclear spin energy levels, leading to quadrupole splitting ( $\Delta E_Q$ ) corresponding to the transition from the ground state to the excited state.  $\Delta E_Q$  provides the information about bond properties and the local symmetry of an iron site. Hence, various kinds of valuable informations with respect to the chemical characteristics can be extracted from these nuclear hyperfine interactions.

Figure 3.8 is the <sup>57</sup>Fe Mössbauer spectra of [Fe<sup>II</sup>(diAMsar)]@Nafion at pH 7, whose Mössbauer parameters were summarized in Table 3.1. As can be seen in Figure 3.8, two doublets coexist; the doublet with a larger quadrupole splitting (red line;  $\delta = 1.119 \text{ mm s}^{-1}$ ,  $\Delta E_Q = 2.323 \text{ mm s}^{-1}$ ) can be assigned to the HS state of the Fe<sup>II</sup> ion, whereas that with a smaller  $\Delta E_Q$  (blue line;  $\delta = 0.324 \text{ mm s}^{-1}$ ,  $\Delta E_Q = 0.207 \text{ mm s}^{-1}$ ) can be assigned to the LS state of the Fe<sup>II</sup> ion. In addition, the ratio of the intensity was HS : LS = 76.9 : 23.1. In this manner, coexistence of the HS and the LS states in [Fe<sup>II</sup>(diAMsar)]@Nafion at pH 7 was confirmed. However, the Mössbauer measurement for the films at pH 4 and 10 could not be performed. Possible causes include that the film contains few [Fe<sup>II</sup>(diAMsar)] complexes, namely, few complexes remain at Nafion due to cation exchange between Fe<sup>II</sup> and H<sup>+</sup> ions at pH 4. As for the film at pH 10, the ion-exchange amount of diAMsar ligand may be small because diAMsar is electrically neutral in the basic conditions, and thus the

amount of  $[\text{Fe}^{\text{II}}(\text{diAMsar})]$  complex in Nafion may be quite small from the first. For such reasons,  $[\text{Fe}^{\text{II}}(\text{diAMsar})]$ @Nafion at pH 4 and 10 does not contain the sufficient  $\text{Fe}^{\text{II}}$  amounts of  $\text{Fe}^{\text{II}}$  ions suitable for the  $^{57}\text{Fe}$  Mössbauer spectroscopic measurement.

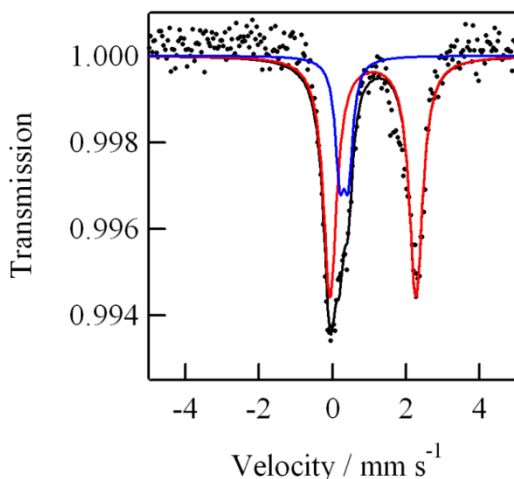


**Figure 3.8.** The  $^{57}\text{Fe}$  Mössbauer spectra of  $[\text{Fe}^{\text{II}}(\text{diAMsar})]$ @Nafion at 300 K, where the HS and LS components coexist with the ratio of 76.9% / 23.1%.

**Table 3.1.** Mössbauer parameters for  $[\text{Fe}^{\text{II}}(\text{diAMsar})]$ @Nafion (pH 7) at room temperature.

	$\delta$ (mm s <sup>-1</sup> )	$\Delta E_{\text{Q}}$ (mm s <sup>-1</sup> )	$\Gamma$ (mm s <sup>-1</sup> )	Relative Area (%)
HS	1.119	2.323	0.409	76.9
LS	0.324	0.207	0.249	23.1

$\delta$ : Isomer Shift,  $\Delta E_{\text{Q}}$ : Quadrupole Splitting,  $\Gamma$ : Line Width, HS: The high-spin state of  $\text{Fe}^{\text{II}}$ , LS: The low-spin state of  $\text{Fe}^{\text{II}}$ .

### Mechanism of the pH dependent spin state

Such a pH-dependent color change originates in proton dissociation equilibrium (Figure 3.9). In acidic condition, the volume of  $\text{diAMsarH}_2^{2+}$  would be expanded due to the electrostatic repulsion between the  $\text{Fe}^{\text{II}}$  ion and the  $\text{NH}_3^+$  groups in diAMsar derived from the protonation of terminal amino groups, and thus the strength of ligand field becomes weak, leading to the predominant HS

component of  $t_{2g}^4 e_g^2$  ( ${}^5T_{2g}$ ,  $S = 2$ ) for  $Fe^{II}$ . On the other hand, in basic condition, the LS component of  $t_{2g}^6$  ( ${}^1A_{1g}$ ,  $S = 0$ ) is predominant because such a volume expansion is absent due to the deprotonation of the  $NH_3^+$  groups in diAMsar.

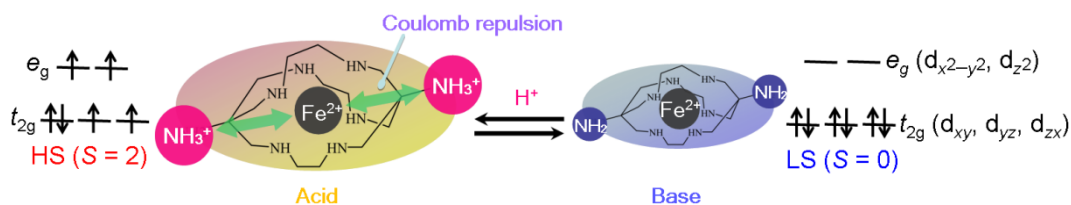
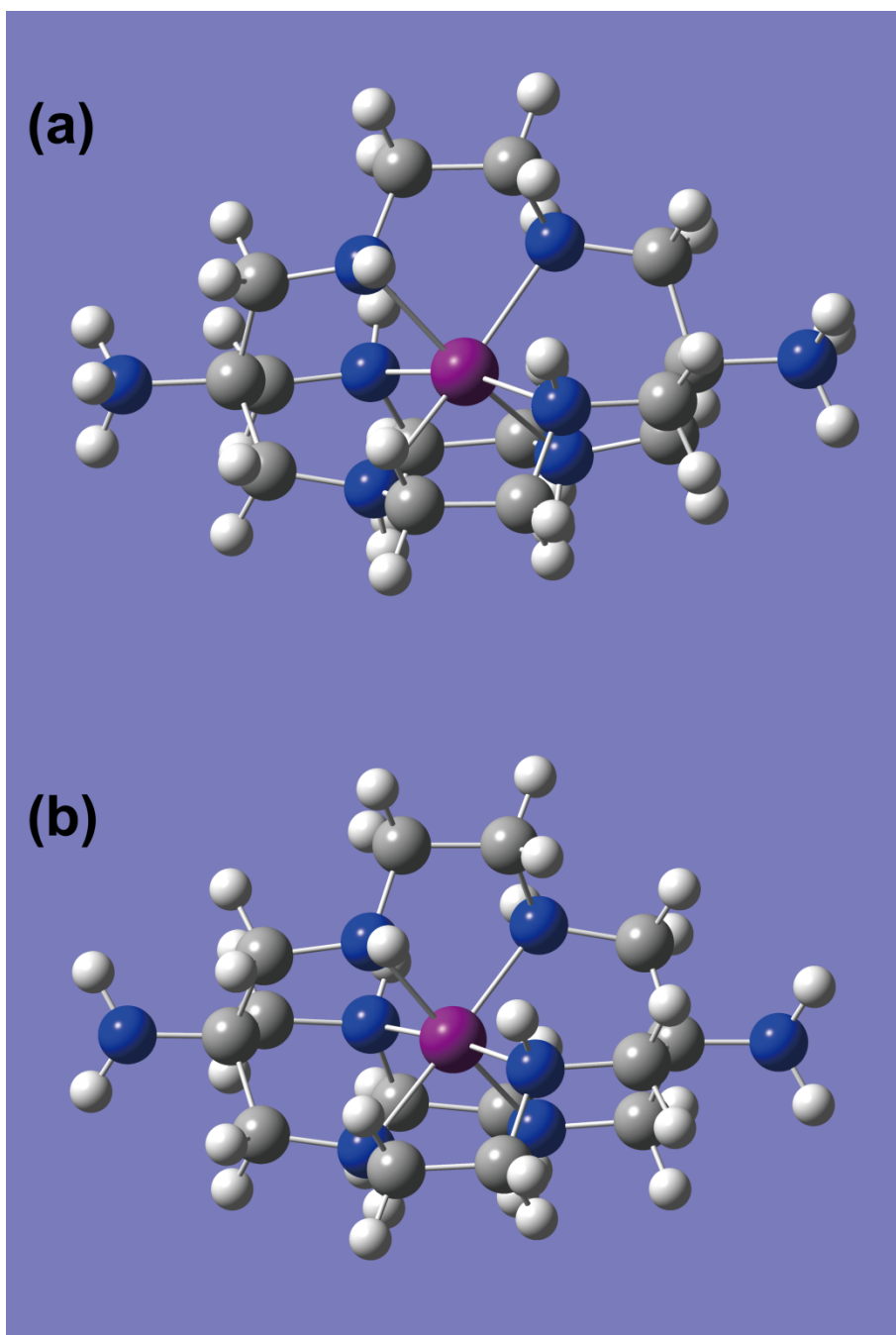


**Figure 3.9.** Schematic representation of the pH dependence for  $[Fe^{II}(diAMsar)]@Nafion$ . In acidic condition, protonation of the terminal amino groups induces the volume expansion of  $diAMsarH_2^+$ , leading to the HS state of  $Fe^{II}$  due to a weaker ligand field derived from the elongated Fe–N distances compared with  $[Fe^{II}(diAMsar)]@Nafion$  in basic condition.

In order to bear out the assumption, DFT calculations were performed for  $[Fe^{II}(diAMsar)]$  on the B3LYP/LanL2DZ/6-31G(d,p) level of theory, although a single crystal of  $[Fe^{II}(diAMsar)]$  suitable for X-ray crystallography has never been obtained. Optimization and energy calculations were performed for the HS ( $S = 2$ ) and the LS ( $S = 0$ ) states of both  $[Fe(diAMsarH_2)]^{4+}$  (diprotonated form) and  $[Fe(diAMsar)]^{2+}$  (deprotonated form). The optimized structures were depicted in Figure 3.10. As summarized in Table 3.2, the energy difference between the HS and the LS states ( $\Delta E_{HS-LS} = E_{HS} - E_{LS}$ ) of  $[Fe(diAMsarH_2)]^{4+}$  was  $-0.25$  kcal/mol, whereas that of  $[Fe(diAMsar)]^{2+}$  was  $\Delta E_{HS-LS} = +1.1$  kcal/mol. Accordingly,  $[Fe(diAMsarH_2)]^{4+}$  in the HS states and  $[Fe(diAMsar)]^{2+}$  in the LS states are more stable than each counterpart. Besides, the average Fe–N coordination bond lengths were  $2.24 \text{ \AA}$  for  $[Fe(diAMsarH_2)]^{4+}$  ( $S = 2$ ) and  $2.08 \text{ \AA}$  for  $[Fe(diAMsar)]^{2+}$  ( $S = 0$ ). Hence the difference of bond distance ( $\Delta r_{HS-LS}$ ) was  $\Delta r_{HS-LS} = 0.16 \text{ \AA}$ , which has good agreement for typical  $Fe^{II}$  spin-crossover complexes. Furthermore, the distances between the terminal amino groups ( $r_{N-N}$ )

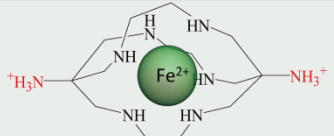
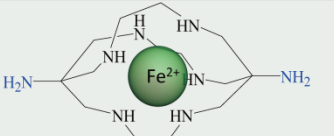
were  $r_{\text{N-N}} = 9.52 \text{ \AA}$  for  $[\text{Fe}(\text{diAMsarH}_2)]^{4+}$  ( $S = 2$ ) and  $r_{\text{N-N}} = 9.20 \text{ \AA}$  for  $[\text{Fe}(\text{diAMsar})]^{2+}$  ( $S = 0$ ).

In this manner, the expansion of the cage was confirmed, so that the DFT calculations strongly support the concept described above,



**Figure 3.10.** Optimized structure of (a) the diprotonated form and (b) the deprotonated form of  $[\text{Fe}^{\text{II}}(\text{diAMsar})]$  by DFT calculations on the B3LYP/LanL2DZ/6-31G(d,p) level of theory.

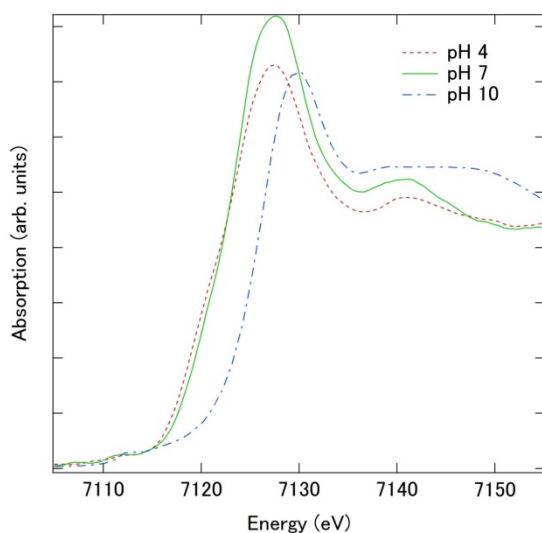
**Table 3.2.** Total energies of protonated and deprotonated forms of [Fe<sup>II</sup>(diAMsar)]@Nafion obtained by B3LYP/LANL2DZ (kcal/mol).

			
Spin state	Total energy	Spin state	Total energy
$S = 0$	-699734.68839	$S = 0$	-699576.43525
$S = 2$	-699734.93497	$S = 2$	-699575.37201
$\Delta E_{\text{HS-LS}} = -0.25$ kcal/mol		$\Delta E_{\text{HS-LS}} = 1.1$ kcal/mol	

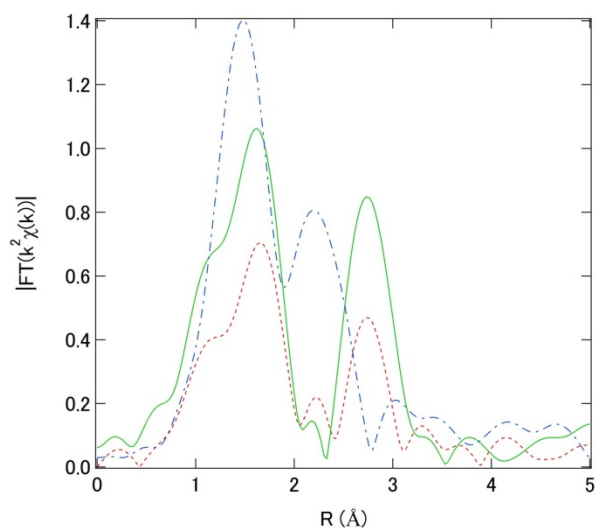
### Fe-K edge XAFS spectroscopy

Figure 3.11 shows the XANES spectra of pH 4, 7, and 10 of [Fe(diAMsar)]@Nafion film. The energy position of the absorption edge and the main peak of pH 10 are shifted to higher energy compared with those of pH 4 and 7. This feature is consistent with the spectral change from the high-spin state to the low-spin state of Fe<sup>II</sup> complex where six nitrogen atoms are coordinated in  $O_h$  symmetry.<sup>[30]</sup> Therefore, XAFS result supports the pH-induced Fe<sup>II</sup> spin-state transition together with the Mössbauer spectroscopy result. Fourier transforms between the  $k$  range of 2.2–9.8  $\text{\AA}^{-1}$  of EXAFS  $k^2\chi(k)$  obtained by the Autobk algorithm<sup>[31]</sup> are shown in Figure 3.12. The first peaks seen at around 1.6  $\text{\AA}$  are assigned to the Fe–N single scattering. According to Figure 3.12, it is revealed that the Fe–N bond is shortened as the sample environment changes from pH 4 or 7 to pH 10, or in other words, from high-spin state to low-spin state. In order to estimate the Fe–N distances, the Fe–N peaks of  $\text{FT}(k^2\chi(k))$  were analyzed with an ab initio calculation of FEFF6 program.<sup>[32]</sup> A curve-fitting analysis was conducted in the back Fourier-transformed  $k$ -space for the  $R$  ranges of 0.1–0.2 nm (for pH 4 and 7) and 0.1–0.19 nm (for pH 10). The total coordination numbers  $N$  were fixed at six with the same Fe–N distance. The intrinsic loss factors  $S_0^2$  were set to 0.6 and the edge energy shifts  $\Delta E_0$  were set

to  $-1$  eV for pH 4 and 7, and to  $1$  eV for pH 10. The result is summarized in Table 3.3. The Fe–N distance difference between Fe<sup>II</sup> high-spin state (pH 4 and 7) and Fe<sup>II</sup> low-spin state (pH 10) is estimated as  $0.17$  Å which is consistent with other Fe nitrogen complexes showing spin-state transition.<sup>[33]</sup> Although the Fe–N peaks in Figure 3.12 gave the bond distance change concomitant with the Fe<sup>II</sup> spin-state change, the assignment of the second peaks of pH 4 and 7 located at  $2.8$  Å remains as a question. Their intensities are too strong to be assigned as the single scattering of the second shell Fe–C. Focusing effect is a possible reason to enhance those peaks around  $2.8$  Å, which is actually observed in Prussian blue analogues.<sup>[34]</sup> However, further discussion is necessary whether a coordinating structure showing such a focusing effect is allowed for keeping the hexamine cage<sup>1</sup>.



**Figure 3.11.** Fe K-edge XANES spectra of  $[\text{Fe}^{\text{II}}(\text{diAMsar})]@\text{Nafion}$ .



**Figure 3.12.** Fourier transforms of Fe K-edge EXAFS spectra  $k^2\chi(k)$  of  $[\text{Fe}^{\text{II}}(\text{diAMsar})]@\text{Nafion}$ .

**Table 3.3.** Results of the curve-fitting analysis of Fe–N shell.

pH	$R(\text{Fe-N})$ (Å)	$C_2$ (Å <sup>2</sup> )	R-factor (%)
4	2.14(2)	0.014(3)	2
7	2.13(1)	0.0061(8)	0.2
10	1.96(1)	0.0065(8)	0.1

### Applying voltage

Figure 3.13 shows the dynamic spin transition behavior of  $[\text{Fe}^{\text{II}}(\text{diAMsar})]$  (pH 4) under the applied voltage, and these color change can be understood as follows. At static state,  $[\text{Fe}^{\text{II}}(\text{diAMsar})]@\text{Nafion}$  at pH 4 is yellow, reflecting the predominant HS component of  $\text{Fe}^{\text{II}}$ . When a voltage is applied, pH around the positive electrode increases due to attracting proton toward the negative electrode, hence the LS and HS components for  $[\text{Fe}^{\text{II}}(\text{diAMsar})]$  are predominant around the positive and the negative electrodes, respectively (see Figure 3.14). Thus, the propagation behavior of green-colored flow is derived from the proton concentration gradient which increases

with time evolution. Moreover, proton flows into opposite direction being associated with the inversion of green-colored flow when the direction of electric field is reversed. In this way, we successfully observed the reversible dynamic spin-crossover behavior of  $[\text{Fe}^{\text{II}}(\text{diAMsar})]@\text{Nafion}$  by electric field-induced proton conduction at room temperature.

Such a dynamic spin-crossover behavior implies the direct observation of proton flow in Nafion membrane. This work is a landmark because the proton conduction is directly observable by color with eyes although a few reports about visualization of some ions by means of magnetic resonance imaging (MRI) have been reported.<sup>[35,36]</sup> Visualization of a flow not only makes easy physical monitoring of the phenomena in accordance with a streaming movement, but is excellent in helping an understanding of them.

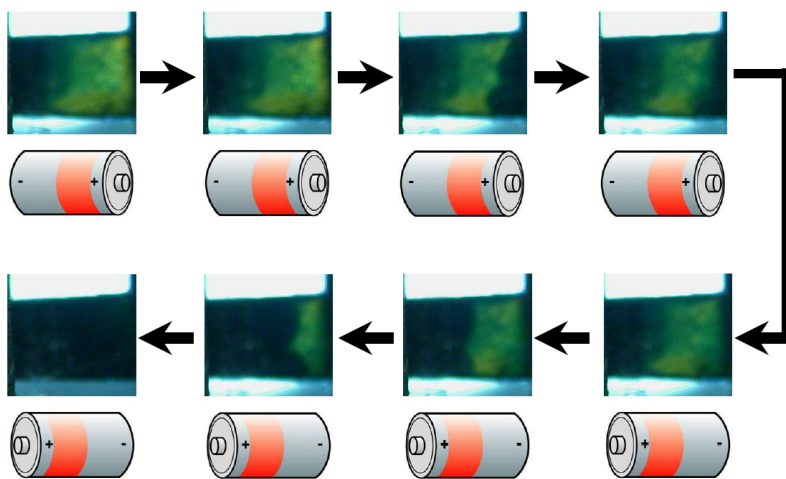


**Figure 3.13.** Color change of  $[\text{Fe}^{\text{II}}(\text{diAMsar})]@\text{Nafion}$  (pH 4) under the applied voltage of 20 V in 15 minutes, which implies the direct observation of proton flow. The illustration of the battery cell represents the direction of electric field. The green-colored flow indicating the increment of LS component of  $\text{Fe}^{\text{II}}$  propagates toward the negative electrode. The dimension of the used film was 0.19 t  $\times$  20 W  $\times$  10 L (mm).

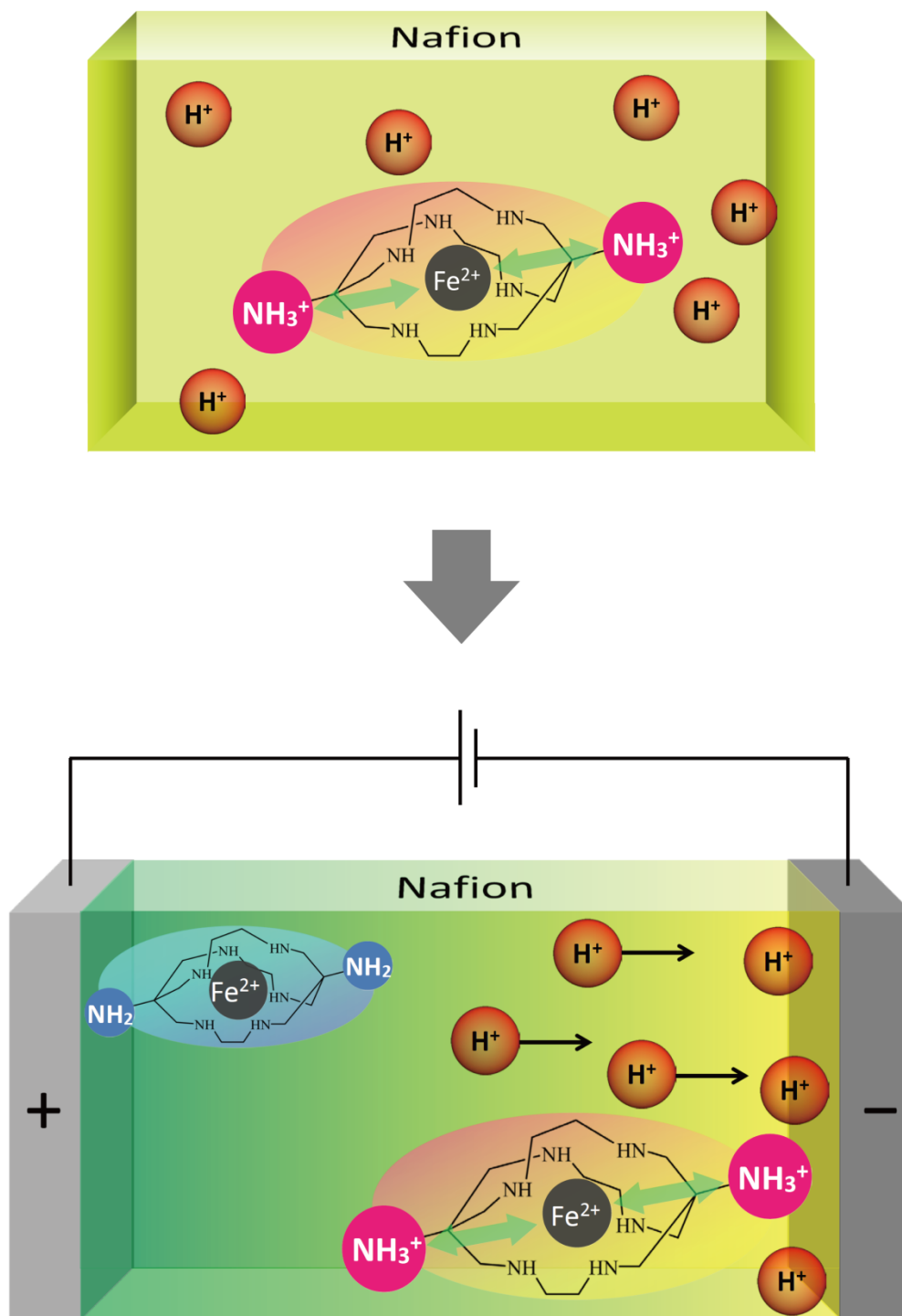


**Figure 3.14.** Schematic representation for visualization of electric field-induced proton flow. Applied voltage generates the gradient of proton concentration due to the attraction of proton by negative electrode. Note: According to the chromium(III) analogue  $[\text{Cr}^{\text{III}}(\text{diMAsar})]$ ,<sup>[37]</sup> the  $\text{p}K_{\text{a}}$  values for the uncoordinated ammonium groups of  $[\text{Fe}^{\text{II}}(\text{diMAsar})]$  are  $\text{p}K_{\text{a}1} = 2.03$  and  $\text{p}K_{\text{a}2} = 4.48$  (298 K). On the other hand, the  $\text{p}K_{\text{a}}$  value of the coordinated amine is 12.0.

**Proton conductivity**

The impedance spectra (Nyquist diagrams) of  $[\text{Fe}^{\text{II}}(\text{diAMsar})]@\text{Nafion}$  at pH 4 and 10 are shown in Figure 3.15. The proton conductivities were estimated as  $2.16 \times 10^{-7} \text{ S cm}^{-1}$  for pH 4 and  $4.52 \times 10^{-9} \text{ S cm}^{-1}$  for pH 10, where several hundred times difference in those was found. Concerning the intrinsic proton conductivity of Nafion at relative humidity of 100% is equal to  $\sim 10^{-2} \text{ S cm}^{-1}$ ,<sup>[38]</sup> it is likely that some incorporated complexes obstruct proton-conducting pathways due to their bulkiness.

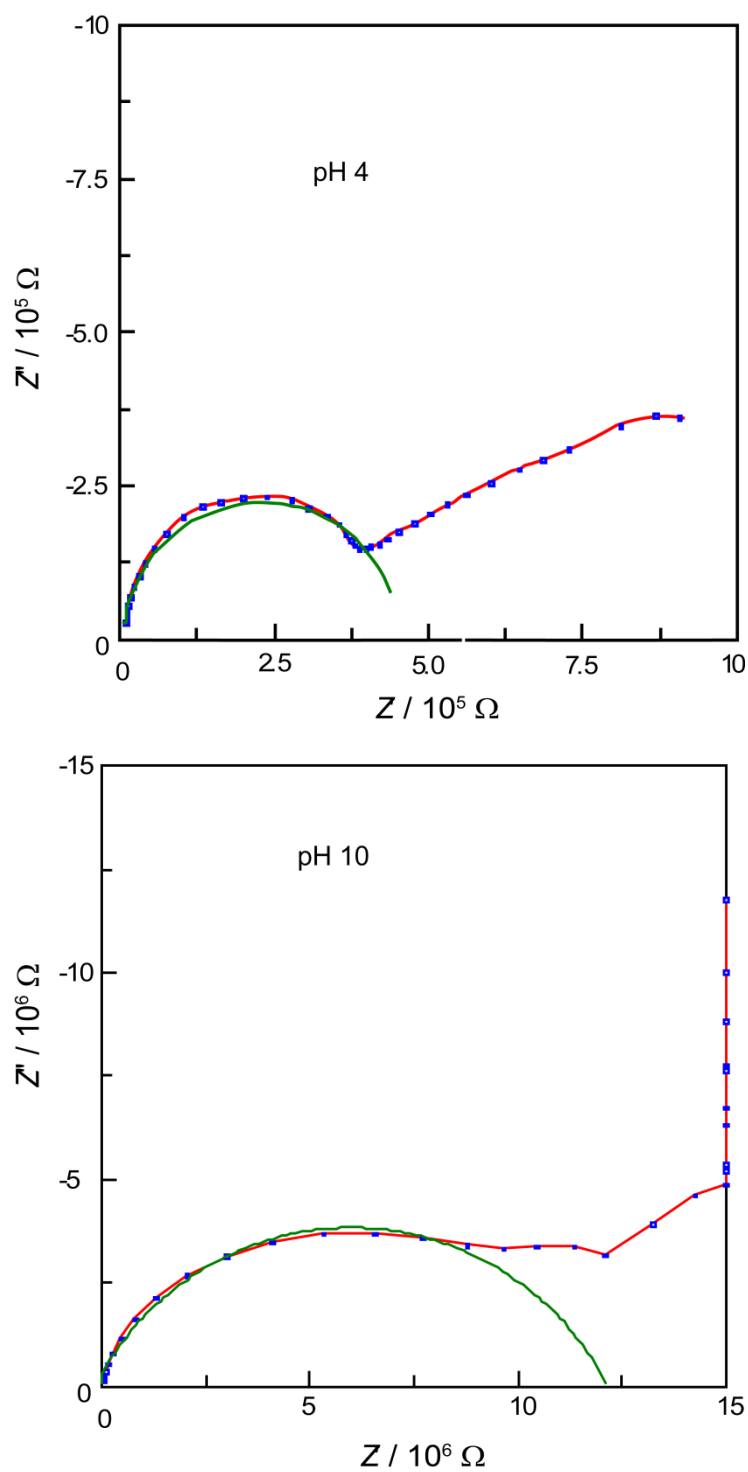


**Figure 3.15.** Nyquist diagrams for  $[\text{Fe}^{\text{II}}(\text{diAMsar})]@\text{Nafion}$  at pH 4 and 10 (room temperature, humidity of ca. 70%).

### 3.4 Conclusion

The transparent films incorporating the pH-responsive SCO complex,  $[\text{Fe}^{\text{II}}(\text{diAMsar})]@\text{Nafion}$ , were newly developed, and its spin state was successfully controlled by differences of pH condition using buffer solutions. The pH-induced spin transition was confirmed by UV-vis and  $^{57}\text{Fe}$  Mössbauer spectroscopy.

XAFS technique is very powerful tool for our system. The protonation-induced SCO transition was demonstrated from the analysis of XANES spectra, and the attendant change of Fe-N bond length was estimated at  $\sim 0.17 \text{ \AA}$ , which is consistent with that of classic  $\text{Fe}^{\text{II}}\text{-N}_6$  SCO complexes. Such a elongation of the coordination bond length was strongly supported DFT calculations.

In conclusion, spatiotemporal manipulation of the spin state of a pH-sensitive spin-crossover complex in highly proton conductive membrane,  $[\text{Fe}^{\text{II}}(\text{diAMsar})]@\text{Nafion}$ , was successfully demonstrated through electric field-induced gradient of proton concentration derived from applied voltage for the first time. Controlling chromism and magnetism by electric field is significant for the development of display materials or information recording medium. Moreover, Nafion enables us to simply prepare any size of homogeneous metal-complex films, undertaking a dual role: “transparent film” and “counter anion”, even if a single crystal cannot be obtained. Thus, multifunctional metal-complexes in Nafion, especially pH-sensitive compounds, are good candidates for the development of molecular devices. This work will be a new breakthrough for the development of transparent film with multifunctionalities from now on.

## References

- [1] *Spin Crossover in Transition Metal Compounds I–III* in *Topics in Current Chemistry*, ed. by P. Gütllich, H. A. Goodwin, Springer, Berlin, **2004**.
- [2] L. L. Martin, K. S. Hagen, A. Hauser, R. L. Martin, A. M. Sargeson, *J. Chem. Soc., Chem. Commun.* **1988**, 1313.
- [3] D. F. Evans, *J. Chem. Soc.* **1959**, 2003.
- [4] L. L. Martin, R. L. Martin, A. M. Sargeson, *Polyhedron* **1994**, *13*, 1969.
- [5] A. Hauser, J. Adler, P. Gütllich, *Chem. Phys. Lett.* **1988**, *152*, 468.
- [6] X. Liu, Y. Moritomo, A. Nakamura, T. Hirao, S. Toyazaki, N. Kojima, *J. Phys. Soc. Jpn.* **2001**, *70*, 2521.
- [7] N. Kojima, S. Toyazaki, M. Itoi, Y. Ono, W. Aoki, Y. Kobayashi, M. Seto, T. Yokoyama, *Mol. Cryst. Liq. Cryst.* **2002**, *376*, 567.
- [8] A. Nakamoto, Y. Ono, N. Kojima, D. Matsumura, T. Yokoyama, *Chem. Lett.* **2003**, *32*, 336.
- [9] A. Nakamoto, N. Kojima, L. X. Jun, Y. Moritomo, A. Nakamura, *Polyhedron* **2005**, *24*, 2909.
- [10] J. Kröber, E. Coddjovi, O. Kahn, F. Grolère, C. Jay, *J. Am. Chem. Soc.* **1993**, *115*, 9810-9811.
- [11] O. Kahn, E. Coddjovi, *Phil. Trans. Royal Soc. London. A* **1996**, *354*, 359-379.
- [12] O. Kahn, L. Sommier, E. Coddjovi, *Chem. Mater.* **1997**, *9*, 3199-3205.
- [13] O. Kahn, C. J. Martinez, *Science* **1998**, *279*, 44-48.
- [14] X.-J. Liu, Y. Moritomo, A. Nakamura, T. Hirao, S. Toyazaki, N. Kojima, *J. Phys. Soc. Jpn.* **2001**, *70*, 2521-2524.
- [15] A. Nakamoto, Y. Ono, N. Kojima, D. Matsumura, T. Yokoyama, *Chem. Lett.* **2003**, *32*, 336-337.
- [16] A. Nakamoto, N. Kojima, X.-J. Liu, Y. Moritomo, A. Nakamura, *Polyhedron* **2005**, *24*, 2909-2912.

- [17] A. Nakamoto, H. Kamebuchi, M. Enomoto, N. Kojima, *Hyperfine Interact.* **2012**, *205*, 41-45.
- [18] V. D. Noto, E. Negro, J.-Y. Sanchez, C. Iojoiu, *J. Am. Chem. Soc.* **2010**, *132*, 2183.
- [19] X. Yu, B. Munge, V. Patel, G. Jensen, A. Bhirde, J. D. Gong, S. N. Kim, J. Gillespie, J. S. Gutkind, F. Papadimitrakopoulos, J. F. Rusling, *J. Am. Chem. Soc.* **2006**, *128*, 11199.
- [20] G. A. Olah, P. S. Iyer, G. K. S. Prakash, *Synthesis* **1986**, 513.
- [21] T. D. Gierke, G. E. Munn, F. C. Wilson, *J. Polym. Sci., Polym. Phys. Ed.* **1981**, *19*, 1687.
- [22] C. Heitner-Wirguin, *J. Membr. Sci.* **1996**, *120*, 1.
- [23] G. A. Bottomley, I. J. Clark, I. I. Creaser, L. M. Engelhardt, R. J. Geue, K. S. Hagen, J. M. Harrowfield, G. A. Lawrance, P. A. Lay, A. M. Sargeson, A. J. See, B. W. Skelton, A. H. White, F. R. Wilner, *Aust. J. Chem.* **1994**, *47*, 143.
- [24] M. J. Frisch, G. W. Trucks, H. B. Schlegel, G. E. Scuseria, M. A. Robb, J. R. Cheeseman, G. Scalmani, V. Barone, B. Mennucci, G. A. Petersson, H. Nakatsuji, M. Caricato, X. Li, H. P. Hratchian, A. F. Izmaylov, J. Bloino, G. Zheng, J. L. Sonnenberg, M. Hada, M. Ehara, K. Toyota, R. Fukuda, J. Hasegawa, M. Ishida, T. Nakajima, Y. Honda, O. Kitao, H. Nakai, T. Vreven, J. A. Montgomery, Jr., J. E. Peralta, F. Ogliaro, M. Bearpark, J. J. Heyd, E. Brothers, K. N. Kudin, V. N. Staroverov, T. Keith, R. Kobayashi, J. Normand, K. Raghavachari, A. Rendell, J. C. Burant, S. S. Iyengar, J. Tomasi, M. Cossi, N. Rega, J. M. Millam, M. Klene, J. E. Knox, J. B. Cross, V. Bakken, C. Adamo, J. Jaramillo, R. Gomperts, R. E. Stratmann, O. Yazyev, A. J. Austin, R. Cammi, C. Pomelli, J. W. Ochterski, R. L. Martin, K. Morokuma, V. G. Zakrzewski, G. A. Voth, P. Salvador, J. J. Dannenberg, S. Dapprich, A. D. Daniels, O. Farkas, J. B. Foresman, J. V. Ortiz, J. Cioslowski, D. J. Fox, *Gaussian 09*, Revision D.01, Gaussian, Inc., Wallingford CT, 2013.
- [25] A. D. Becke, *J. Chem. Phys.* **1993**, *98*, 5648.
- [26] C. Lee, W. Yang, R.G. Parr, *Phys. Rev. B.* **1998**, *37*, 785.
- [27] a) T. H. Dunning, P. J. Hay, *In Modern Theoretical Chemistry*; H. F. Schaefer, Ed.; Plenum:

- New York, **1976**; Vol. 3, p 1; b) P. J. Hay, W. R. Wadt, *J. Chem. Phys.* **1985**, 82, 270; c) W. R. Wadt, P. J. Hay, *J. Chem. Phys.* **1985**, 82, 284.; d) P. J. Hay, W. R. Wadt, *J. Chem. Phys.* **1985**, 82, 299.
- [28] a) R. L. Mössbauer, *Z. Physik* **1958**, 151, 124; b) R. L. Mössbauer, *Naturwissenschaften* **1958**, 45, 538; c) R. L. Mössbauer, *Z. Naturforsch* **1959**, 14a, 211.
- [29] P. Gütllich, R. Link, A. Trautwein, *Mössbauer Spectroscopy and Transition Metal Chemistry*; Springer-Verlag: Berlin Heidelberg, New York, 1978.
- [30] T. E. Westre, P. Kennepohl, J. G. DeWitt, B. Hedman, K. O. Hodgson, and E. I. Solomon, *J. Am. Chem. Soc.* **1997**, 119, 6297.
- [31] M. Newville, P. Livins, Y. Yacoby, E. A. stern, and J. J. Rehr, *Phys. Rev. B* **1993**, 47, 14126.
- [32] S. I. Zabinsky, J. J. Rehr, A. Ankudinov, R. C. Albers, and M. J. Eller, *Phys. Rev. B* **1995**, 52, 2995.
- [33] For example K. Okamoto, K. Nagai, J. Miyawaki, H. Kondoh, and T. Ohta, *Chem. Phys. Lett.* **2003**, 371, 707.
- [34] For example W. A. Steen, S.-W. Han, Q. Yu, R. A. Gordon, J. O. Cross, E. A. Stern, G. T. Seidler, K. M. Jeerage, and D. T. Schwartz, *Langmuir* **2002**, 18, 7714.
- [35] L. Naji, J. A. Chudek, R. T. Baker, *Soft Matter* **2008**, 4, 1879-1886.
- [36] M. Wang, K. W. Feindel, S. H. Bergens, R. E. Wasylshen, *J. Pow. Sour.* **2010**, 195, 7316-7322.
- [37] P. Comba, I. I. Creaser, L. R. Gahan, J. M. Harrowfield, G. A. Lawrance, L. L. Martin, A. W. H. Mau, A. M. Sargeson, W. H. F. Sasse, M. R. Snow, *Inorg. Chem.* **1986**, 25, 384-389.
- [38] T. A. Zawodzinski, Jr., M. Neeman, L. O. Sillerud, S. Gottesfeld, *J. Phys. Chem.* **1991**, 95, 6040-6044.

## 4. Development of the Transparent Films with pH-Sensitive Emission Properties

### Abstract

This work aims to develop a Nafion membrane incorporating pH-sensitive luminescent complexes,  $[(\text{bpy})_2\text{Ru}^{\text{II}}(\text{H}_4\text{bpib})\text{Ru}^{\text{II}}(\text{bpy})_2]$  (bpy = 2,2'-bipyridine,  $\text{H}_4\text{bpib}$  = 1,4-bis([1,10]phenanthroline[5,6-*d*]-imidazol-2-yl)benzene) and  $[\text{Ir}^{\text{III}}(\text{H}_2\text{bip})(\text{Me}_2\text{bib})]$  ( $\text{H}_2\text{bip}$  = 2,6-bis(2-benzimidazolyl)pyridine,  $\text{Me}_2\text{bib}$  = 1,3-bis(1-methylbenzimidazol-2-yl)benzene), whose proton responsivity originates from pH-dependent energy transfer induced by protonation and deprotonation of the imidazole moiety in the ligands. Transparent films with pH-sensitive emission were successfully obtained, and their emission properties were also successfully controlled by external pH conditions by immersing them into Britton-Robinson buffer. Based on this result, electrical control of the emission properties of the films was tried by applied voltage induced proton flow.

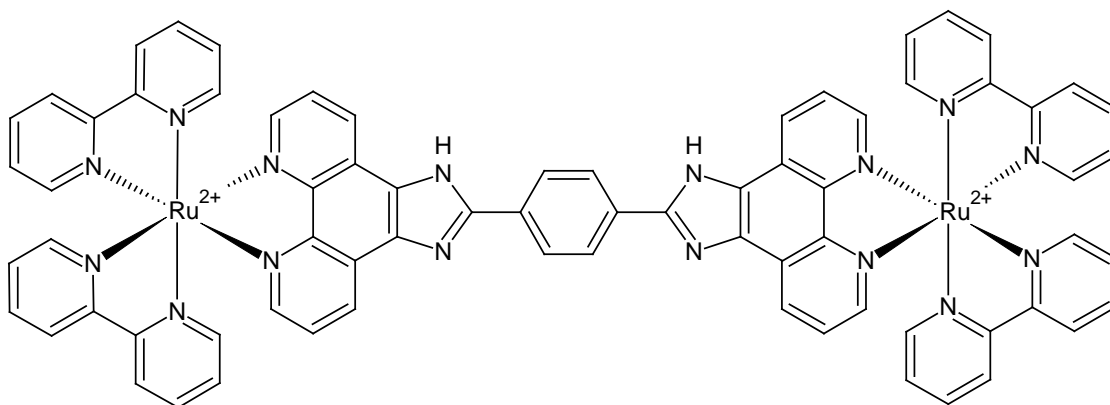
## 4.1 Introduction

As described in Chapter 3, we have developed the transparent film incorporating the pH-sensitive spin-crossover complex,  $[\text{Fe}^{\text{II}}(\text{diAMsar})]@\text{Nafion}$ , at various pH conditions. The film shows different colors reflected in the spin states under the synthetic conditions of pH 4, 7, and 10. Based on this result, we have successfully controlled the spin state of  $[\text{Fe}^{\text{II}}(\text{diAMsar})]$  spatiotemporally by electric field-induced proton concentration gradient. In order to evolve this research, we newly developed transparent films incorporating some proton-responsive emissive complexes.

Emitting materials are widely applied to sensors, electronic devices, chemical analysis, cell markers, *etc.*, which are based on various chemical and physical principles. In particular, considerable attention has been paid to the research of pH-sensitive compounds. For example, pH-sensitive luminescence materials are useful for detecting cancer cells because a pH condition in cancer cells is lower than that of normal cells. For the purpose of this, a great number of pH-sensitive organic molecules, metal complexes, and polymers have been reported. As is clear from this one example, emission of visible light is a direct probe to perceive something, and technical developments of visualization by emission remain a major challenge in various fields of study. Taking the existing state of affairs into consideration, we tried to develop new pH sensors and establish a control method of emission properties in some metal complexes immobilized inside of Nafion by proton concentration and proton flow.

## 4.2 pH-Sensitive Emission in Metal Complexes

In the first place, the dinuclear ruthenium(II) complex in Scheme 4.1 was adopted, whose general formula is  $[(\text{bpy})_2\text{Ru}^{\text{II}}(\text{H}_4\text{bpib})\text{Ru}^{\text{II}}(\text{bpy})_2]$  (**1**; bpy = 2,2'-bipyridine,  $\text{H}_4\text{bpib}$  = 1,4-bis([1,10]phenanthroline[5,6-d]-imidazol-2-yl)benzene).<sup>[1]</sup> The emission properties of ruthenium(II) complexes with polypyridyl ligands are well-documented in previous literatures.<sup>[2]</sup> Among them, the complexes with imidazole-containing ligands show pH-dependent emission properties due to reversible acid/base interconversion originating from a large energy perturbation by protonation/deprotonation. In particular, **1** exhibits ‘off-on-off’ switching in luminescence by changing from low pH to high pH. The emission intensity versus pH profile is shown in Figure 4.1, being like a bell-shape curve. The pH dependency results comes from proton dissociation equilibrium on imidazole moiety in the bridging ligand,  $\text{H}_4\text{bpib}$ , as shown in Scheme 4.2. Thus, the Nafion film containing **1** is expected to be a transparent solid material with pH-responsive luminescence properties. In addition, the complex film is also expected to show a luminous stripe under the applied voltage according to the ‘off-on-off’ switching property.



**Scheme 4.1.** The molecular structure of cationic **1**.

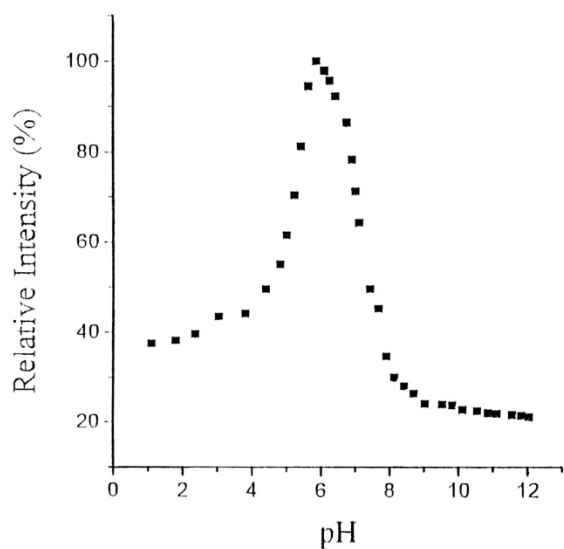
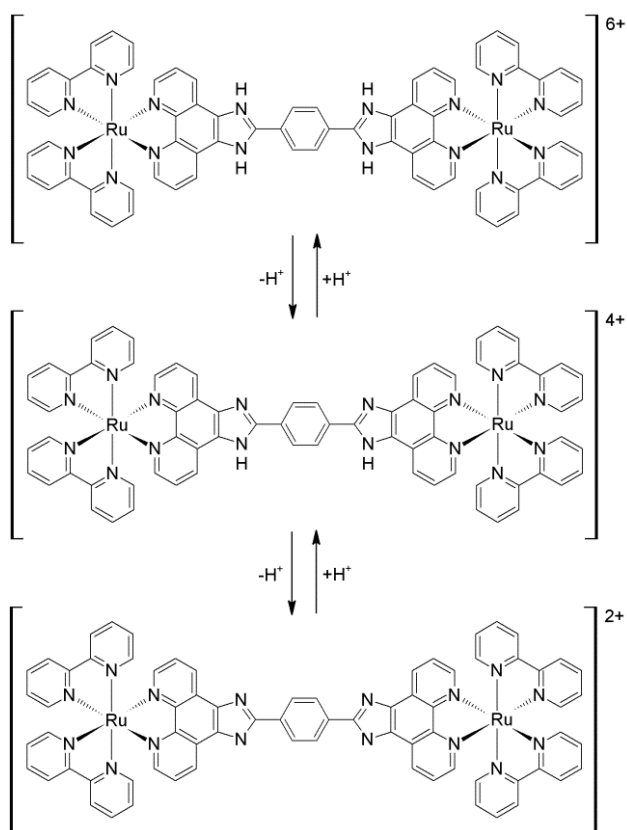
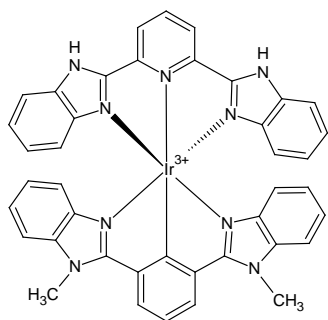


**Figure 4.1.** The pH dependence of the relative emission intensity of **1** in MeOH-H<sub>2</sub>O (1:1 v/v) solution at  $\lambda_{\text{ex}} = 469$  nm at room temperature.<sup>[1]</sup>

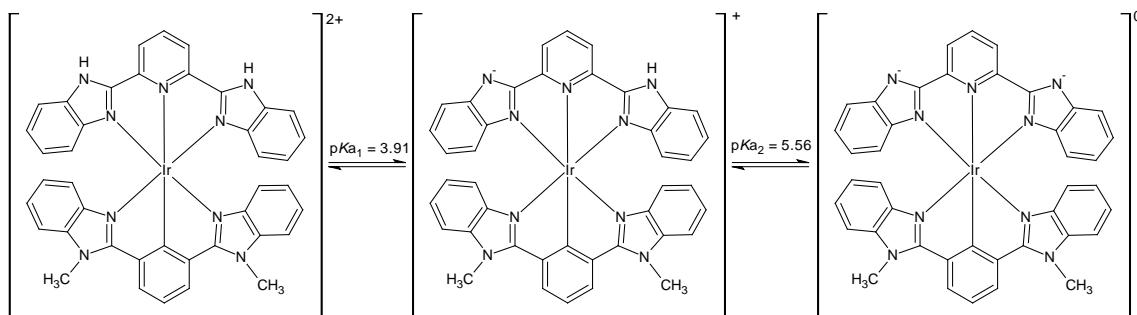


**Scheme 4.2.** Representation of the proton dissociation equilibria of **1** in low-, mid-, and high pH conditions.

In the second place, the mononuclear iridium(III) complex,  $[\text{Ir}^{\text{III}}(\text{H}_2\text{bip})(\text{Me}_2\text{bib})]$  (**2**, Scheme 4.3;  $\text{H}_2\text{bip}$  = 2,6-bis(2-benzimidazolyl)pyridine,  $\text{Me}_2\text{bib}$  = 1,3-bis(1-methylbenzimidazol-2-yl)benzene),<sup>[3]</sup> was adopted to the development of the transparent emission films. Emissive iridium(III) complexes with tridentate ligands are relatively rare in comparison with a huge number of those with bidentate ligands.<sup>[4]</sup> The complex **2** has the imidazole moiety on  $\text{H}_2\text{bip}$  playing the role of pH dependency (Scheme 4.4), and the emission intensity of **2** increases in solution with increasing pH. Therefore, it is expected likewise for **1** to obtain an emissive film whose emission property can be controlled by external pH and proton flow under the applied voltage. To the best of the author's knowledge, the report of the synthesis and the physical properties of **2** has not been published as a peer-reviewed article. Hence, the author synthesized **2** according to the literature method of a derivative<sup>[4f]</sup> and investigated the emission properties of **2** in both solution and film states.



**Scheme 4.3.** The molecular structure of **2**.

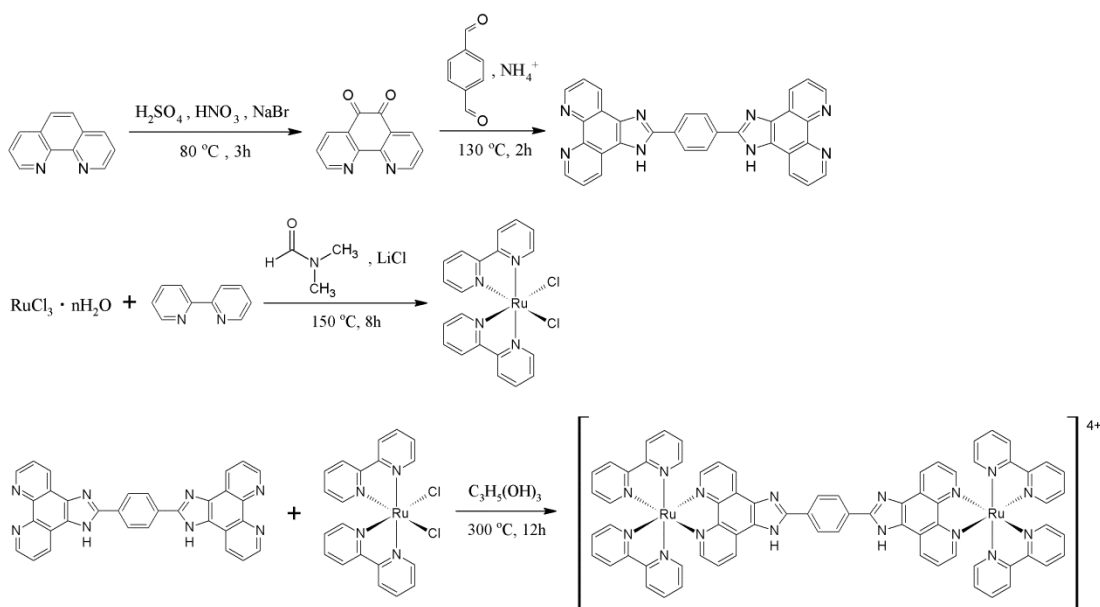


**Scheme 4.4.** Representation of proton dissociation equilibria of **2**.

## 4.3 Materials and Methods

### 4.3.1 Synthesis of $[(\text{bpy})_2\text{Ru}^{\text{II}}(\text{H}_4\text{bpib})\text{Ru}^{\text{II}}(\text{bpy})_2](\text{ClO}_4)_4 \cdot 3\text{H}_2\text{O}$ (**1**)

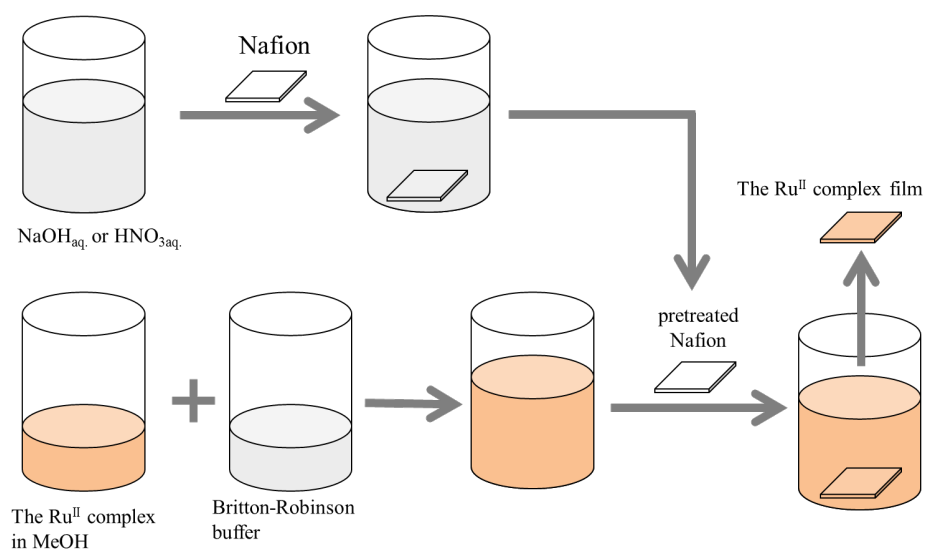
The dinuclear ruthenium(II) complex **1** was synthesized according to the previous literature procedure (Scheme 5).<sup>[5]</sup> Note that the reference written by Sullivan *et al.* has an error in a quantity of reagent for a synthesis of intermediate *cis*- $[(\text{bpy})_2\text{RuCl}_2] \cdot 2\text{H}_2\text{O}$ .<sup>[6]</sup> They described in reference as follows: “Commercial  $\text{RuCl}_3 \cdot 3\text{H}_2\text{O}$  (7.8 g, 29.8 mmol), bipyridine (9.36 g, 60.0 mmol), and LiCl (8.4 g, 2 mmol) were heated at reflux in reagent grade dimethylformamide (50 mL) for 8 h”. However, the molar amount of 8.4 g of LiCl (42.39 g/mol) is 0.20 mol, which is correct. In fact, the author could not obtain *cis*- $[(\text{bpy})_2\text{RuCl}_2] \cdot 2\text{H}_2\text{O}$  by 2 mmol of LiCl (0.085 g) at all. (**Caution!** Perchlorate salts of metal complexes are potentially explosive and should be handled in small quantity with care.)



**Scheme 4.5.** Summary of the synthesis for **1**.

### 4.3.2 Preparation of 1@Nafion

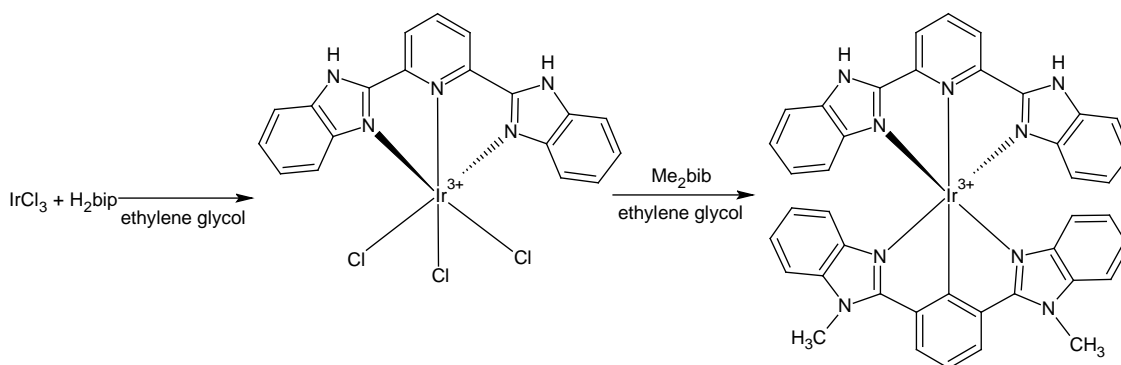
Commercial Nafion 117, which has been formed a film, was immersed in an aqueous solution of 10%  $\text{HNO}_3$  for several hours to replace cations of Nafion with  $\text{H}^+$ , affording H-form. On the other hand, Na-form was prepared by treating with an aqueous solution of  $\text{NaOH}$  (2 mol/L), replacing cations in Nafion with  $\text{Na}^+$ . The dimension was  $0.19\text{t} \times 10\text{W} \times 10\text{L}$  (mm). The pretreated Nafion was immersed in the methanolic solutions of **1** (*ca.* 1 mg) with Britton-Robinson buffer<sup>[7]</sup> (MeOH:buffer = 1:1 v/v) at room temperature, and **1** was then naturally taken into Nafion by the cation exchange (Scheme 4.6). The transparent films, **1**@Nafion, were prepared at the various pH of 2-12. The films prepared from H-form were used for voltage applying experiment, whereas those from Na-form were used for other experiments.



**Scheme 4.6.** Preparation of **1**@Nafion.

### 4.3.3 Synthesis of $[\text{Ir}^{\text{III}}(\text{H}_2\text{bip})(\text{Me}_2\text{bib})](\text{PF}_6)_2$ (**2**)

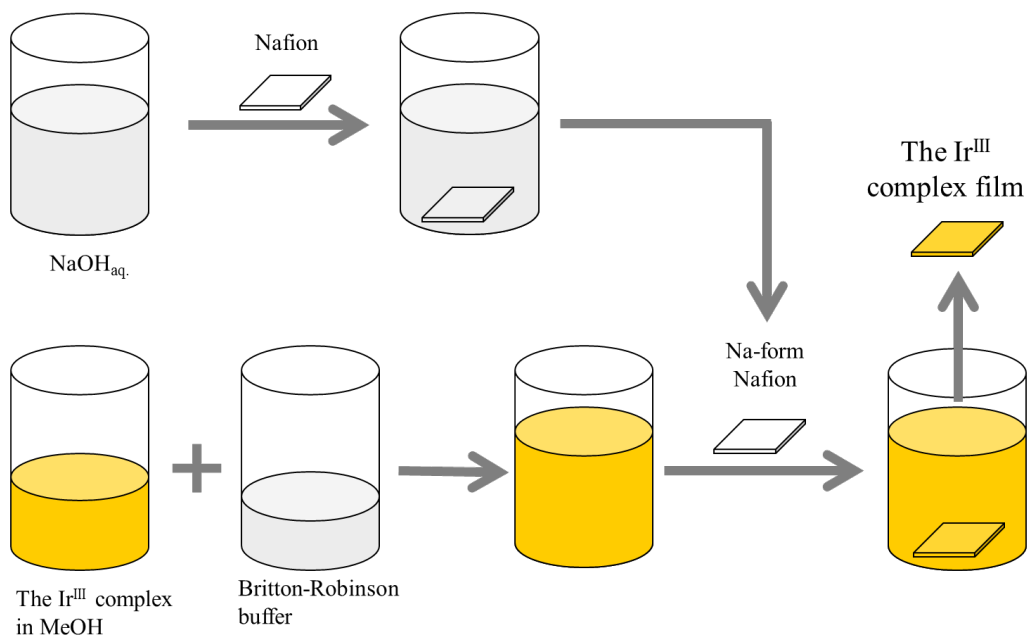
The tridentate ligands  $\text{H}_2\text{bip}$ <sup>[8]</sup> and  $\text{Me}_2\text{bib}$ <sup>[4f]</sup> were synthesized in the same way as the previous literature procedures. The iridium(III) complex **2** was synthesized by a procedure similar to that reported for  $[\text{Ir}^{\text{III}}(\text{H}_2\text{bip})(\text{Me}_2\text{bib})](\text{PF}_6)_2$  as summarized in Scheme 4.7.<sup>[4f]</sup>



**Scheme 4.7.** Summary of the synthesis for **2**.

### 4.3.4 Preparation of **2**@Nafion

The pretreated Nafion (Na-form,  $0.19\text{t} \times 15\text{W} \times 40\text{L}$  (mm)) was immersed in the methanolic solutions of **2** (ca. 7.9 mg) with Britton-Robinson buffer (MeOH:buffer = 4:3 v/v) at room temperature (Scheme 4.8). The transparent films were obtained at pH 2, 4.8, 6, and 10.



**Scheme 4.8.** Preparation of 2@Nafion.

### 4.3.5 Optical spectroscopy

The UV-Visible absorption spectra were measured by V-530 UV-vis Spectrometer (JACSO). The excitation and emission spectra were measured by F-4500 Fluorescence Spectrometer (Hitachi High-Technologies Co.). In measuring optical spectra for the films, they were immersed in the inert fluid, Fluorinert<sup>TM</sup> FC-77 (Sumitomo 3M Limited, Tokyo, Japan), to maintain a smooth surface of them.

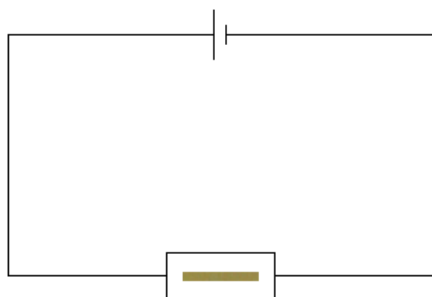
### 4.3.6 Quantum yield and lifetime measurements

Quantum yield was measured by absolute PL quantum yields measurement systems: Quantaaurus-QY (Hamamatsu Photonics Co.). Emission lifetime was measured by compact fluorescence lifetime spectrometer: Quantaaurus-Tau (Hamamatsu Photonics Co.).

### 4.3.7 Applying voltage to the emissive films

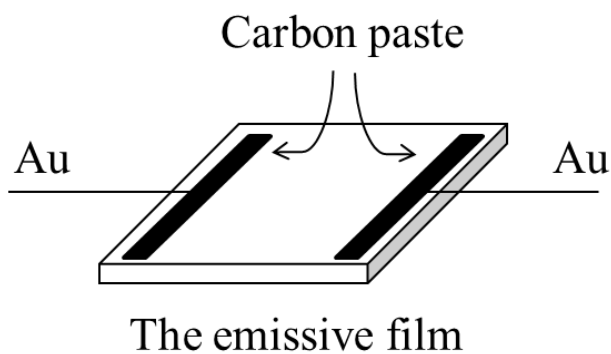
The experiment of applying voltage was performed by three methods as follows:

(a) Agarose 900 (2.4 g) and aqueous KCl (1 mol/L, 4 mL) were stirred in distilled water (200 mL), and then heated by microwave. After the mixture was cooled to 50-55°C, it was poured into a tray as a mold. The emissive film was mounted on the agarose gel and subsequently hot agarose was poured onto it. The agarose gel including the film was soaked in electrolyte (0.25 mol/L of KCl) in an electrophoresis apparatus. The voltage was applied up to 200 V (Scheme 4.9), where the emission was monitored under UV light ( $\lambda = 313$  nm) with a Xe lamp LAX-101 (Asahi Spectra Co.) as a light source using a band pass filter.



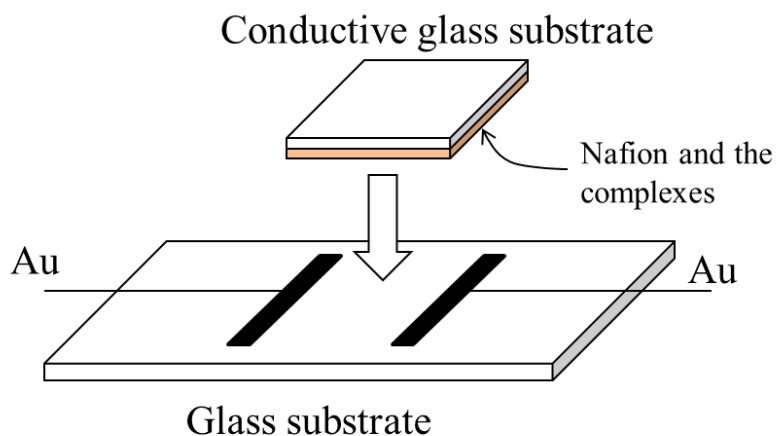
**Scheme 4.9.** The agarose gel including **1@Nafion** or **2@Nafion**.

(b) Gold electrodes were directly mounted on the both ends of the film, and the voltage was then applied up to 200 V (Scheme 4.10).



**Scheme 4.10.** The gold electrodes mounted film.

(c) A 3 mL of ethanolic solution of **1** or **2** (0.2 mM) was poured into an ethanolic solution of 1.25% of Nafion dispersion liquid (4 mL). The mixture was spread all over the surface on a conductive glass substrate being coated by SnO<sub>2</sub>. After the air drying, the glass was soaked in the buffer at pH 2 for 1 h to inject protons into Nafion. The glass was mounted on a glass substrate with Au electrodes, and the voltage was then applied up to 200 V (Scheme 4.11).



**Scheme 4.11.** Nafion and the metal complexes on the conductive glass substrate.

### **4.3.8 Proton conductivity**

Gold electrodes were mounted on both sides of the emissive film with carbon paste. The conductivity measurement was performed with Model 1260 Impedance/Gain-Phase Analyzer (Solatron Analytical Co.) equipped with Model 1296 Dielectric Interface (Solatron Analytical Co.) in the frequency range of 1 Hz to 1MHz.

## 4.4 Results and Discussion

### 4.4.1 $[(\text{bpy})_2\text{Ru}^{\text{II}}(\text{H}_4\text{bpib})\text{Ru}^{\text{II}}(\text{bpy})_2]@\text{Nafion}$ (**1**@Nafion)

#### Incorporated quantity of **1** into Nafion

Exact calculations cannot be performed in calculating with the absorbance of the films incorporating metal complexes due to unknown  $\varepsilon$  and  $c$  values in the Lambert-Beer law ( $A = \varepsilon cl$ ), where  $\varepsilon$  may depend on pH. On the other hand, UV-vis spectra in solutions enable us to calculate the incorporated quantity of metal complexes from the analysis of changes in absorbance before and after immersing Nafion. That is to say that the decrement of **1** in solution is equal to the incorporated quantity of **1** into Nafion, which can be calculated by Lambert-Beer law.

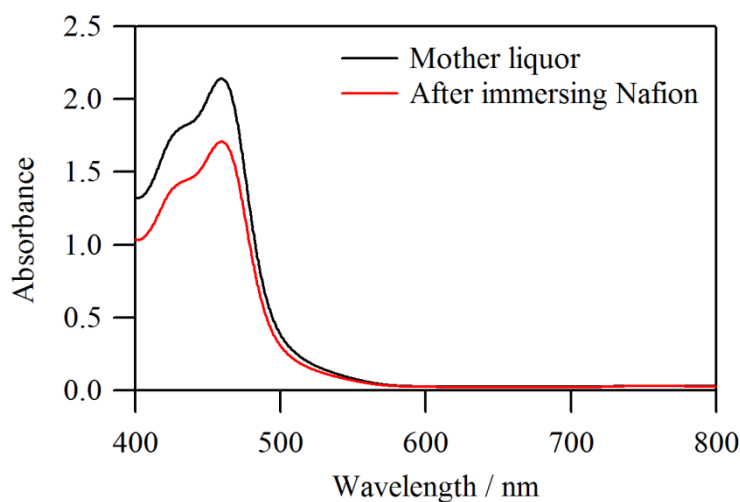


**Figure 4.2.** UV-vis absorption spectra of **1** in the solutions before and after immersing Nafion at pH 2.

**Table 4.1.** Summary of the incorporated quantity of **1** into Nafion.

pH	Incorporated quantity [mol/g(Nafion)]
2	$4.43 \times 10^{-7}$
5	$1.33 \times 10^{-7}$
8	$1.72 \times 10^{-7}$
11	–

As an example, the absorption of the solutions at pH 2 decreased by immersing Nafion (Figure 4.2): the maximum intensity at  $\lambda = 459.5$  nm was changed from  $A = 2.140$  to  $1.708$ . In this way, the incorporated quantities were calculated and summarized in Table 4.1. Among the complex films prepared at various pH conditions, **1**@Nafion(pH 2) incorporated the complex into Nafion in the highest concentration because the complexes has the hexavalent state at pH 2. The incorporated concentrations for **1**@Nafion(pH 5) and **1**@Nafion(pH 8) are similar values, while the value at pH 11 could not be calculated due to low solubility of **1** in this condition.

### UV-vis spectra of **1**@Nafion

The UV-Vis spectra of **1**@Nafion were shown in Figure 4.3. The spectra of the films at various pH conditions have a profile similar to those in aqueous Britton-Robinson buffer in reference[1]. The absorption bands at  $\sim 200$  and  $287$  nm are assigned to ligand-centered (LC)  $\pi \rightarrow \pi^*$  transitions. The two bands at  $240$  and  $460$  nm are assigned to metal-to-ligand charge transfer (MLCT)  $d \rightarrow \pi^*$  transitions with triplet state ( $^3$ MLCT). The presence of long-wavelength tail in the MLCT band around  $460$  nm is suggestive of a triplet character.<sup>[9]</sup> The remaining band at  $355$  nm is assigned to a metal-centered (MC)  $d \rightarrow d$  transition.

The absorption intensity of **1**@Nafion(pH 2) was much stronger than those of the others.

Figure 4.4 shows the plots of intensity at 460 nm in UV-vis spectra for the complex films, superimposed on the values of the incorporated concentration according to the pH conditions (Table 4.1). The result indicates that the absorption intensity dominated by the incorporated concentration of the complex in Nafion.

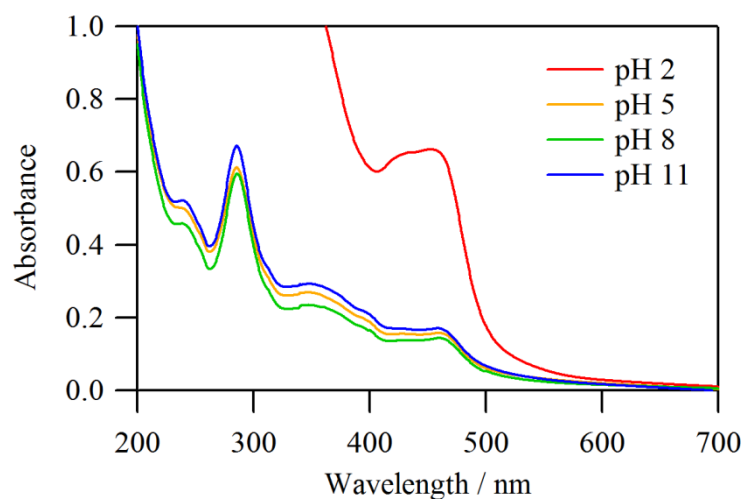


**Figure 4.3.** UV-vis absorption spectra for **1**@Nafion at various pH conditions.

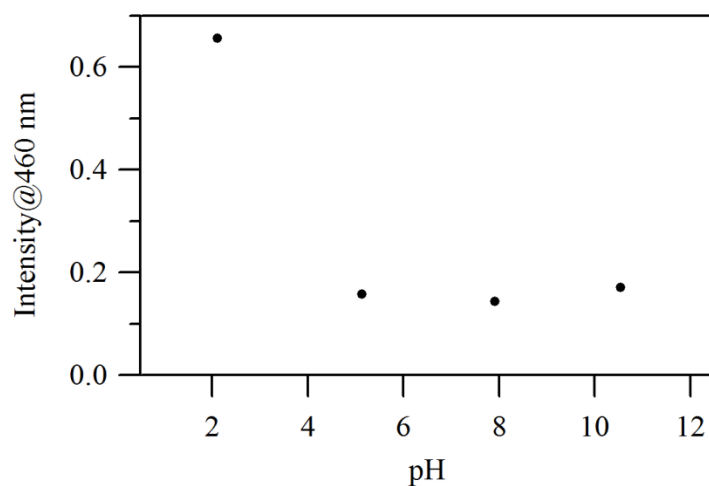


**Figure 4.4.** The maximum absorption intensity of **1**@Nafion at  $\lambda = 460$  nm.

### **Emission property of **1**@Nafion**

The yellow films, **1**@Nafion, showed fluorescence under UV irradiation ( $\lambda = 365$  nm) as can be seen in Figure 4.5. The emission color is orange which is also clear from the emission spectra as shown in Figure 4.6, where the main peaks were observed around 600 nm. Note that the emission spectra were normalized by the ratio of the incorporated quantity of **1** into Nafion. The maximal emission peaks showed a slight blue shift according to the increment of pH. The emission intensity has a significant pH dependence., The emission intensity of **1**@Nafion increases with increasing the pH value from 2 to 5, while the emission was gradually quenched with in the pH range from 5 to 11. Thus, **1**@Nafion acts as an ‘off-on-off’ switch depending on pH as illustrated in Figure 4.7, which is consistent with the behavior of **1** in solution.

The compound **1** has acid dissociation constants,  $pK_a(\text{base}) = 4.11$  and  $pK_a(\text{acid}) = 7.84$ , as reported in reference[1]. In lower pH condition, the non-emissive behavior can be explained as follows. It is known that protonated imidazole rings quench emissions because they are better electron acceptors than  $[\text{Ru}^{\text{II}}(\text{bpy})_3]$  itself.<sup>[10]</sup> On the other hand, the decrease of the emission intensity at higher pH may be attributed to the energy level change of the MC excited state which is responsible for radiationless decay.<sup>[11]</sup> If MC is the lowest excited state, fast radiationless deactivation to the ground state would be dominant, and thus luminescence cannot usually be observed at room temperature. In this case, a lifetime of  $^3\text{MLCT}$  is shortened by activated surface crossing to a short lived MC excited state, whose energy level depends on the ligand field strength. At higher pH, the imidazole ring has the negative charge. As a consequence, it increases  $\sigma$ -donor and decreases  $\pi$ -acceptor capability of the  $\text{bpib}^{2-}$ , resulting in a weakened ligand field strength. For this reason, radiationless deactivation of the emissive MLCT state via MC state is enhanced. In this way, the positive ( $\text{H}_4\text{bpib}^{2+}$ ) and negative ( $\text{bpib}^{2-}$ ) charges on the bridging ligand quench the luminescence, and consequently, **1**@Nafion behaves as an ‘off-on-off’ switch.

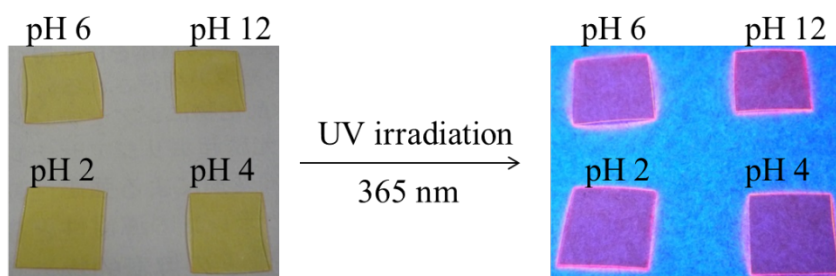


**Figure 4.5.** Photographs of **1@Nafion** at various pH conditions under UV irradiation (365 nm) at room temperature.

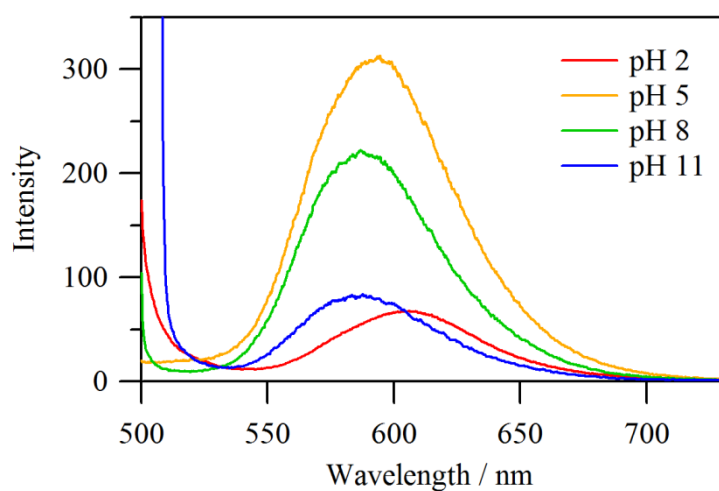


**Figure 4.6.** Emission spectra of **1@Nafion** at various pH conditions at room temperature.

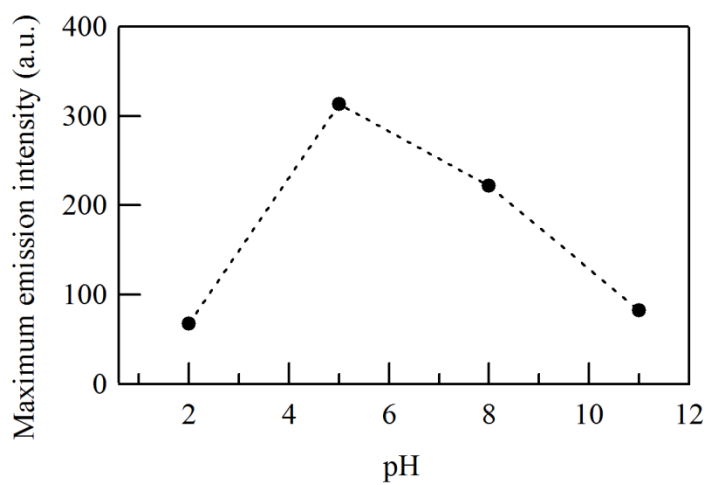


**Figure 4.7.** Maximum emission intensities of **1@Nafion** as a function of pH.

### **Proton conductivity and applying voltage**

The impedance spectra (Nyquist diagrams) of **1**@Nafion at pH 2, 4, and 12 are shown in Figure 4.8, and the values of the proton conductivity estimated from the fittings to the Nyquist diagrams are summarized in Table 4.2. The resistance values of the films exceeded several megaohm as seen in Figure 4.8, resulting in the very low proton conductivities of  $10^{-9}$ ~ $10^{-10}$  S cm<sup>-1</sup>. It was expected that the films at pH 2 and 4 have higher conductivities than that of pH 12, but in actuality there were no pH dependences in proton conductivity. Concerning the intrinsic proton conductivity of Nafion at relative humidity of 100% is equal to  $\sim 10^{-2}$  S cm<sup>-1</sup>,<sup>[12]</sup> it is likely that some incorporated complexes obstruct proton-conducting pathways due to their bulkiness.

As described in experimental section, the three methods were adopted to apply voltage to **1**@Nafion. In the first place, the direct electric voltage was increased 5 V every 10 minutes from 0 to 20 V, where little change in emission property was observed. After that, 20 V was retained and fixed point observation was run on, however, little change was also observed. Finally, the applied voltage was further increased up to 200 V which is the instrument limitation, but no change was seen after all.

Consequently, the electrical control of emission property of **1**@Nafion by proton conduction has been failed to demonstrate due to the very low conductivity. In order to achieve our purpose, there are two possible improvements. The first one is to use a proton responsive complex with lower  $pK_a$  values than **1**, which enables to dissociate and accept protons more easily under the gradient of proton concentration induced by electric field. The other is to choose a smaller complex than **1** because of maintaining the proton conductive pathway in Nafion. According to above discussion, better results will be provided by **2**@Nafion because the complex **2** has a lower  $pK_a$  value and smaller size than **1**.

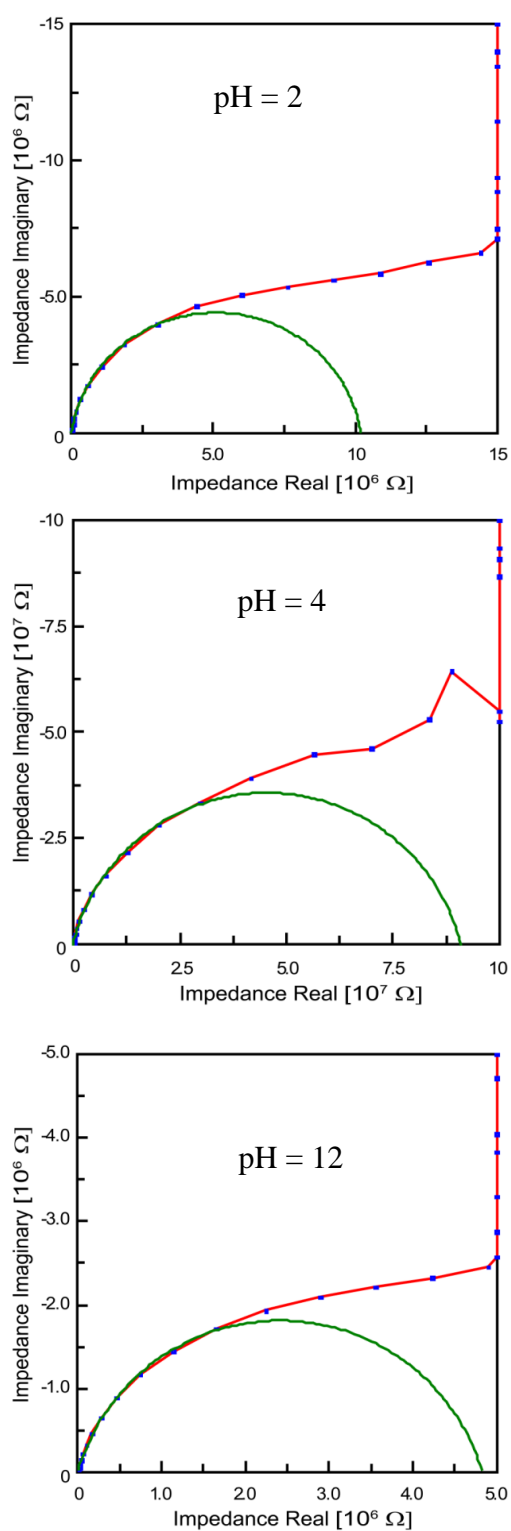


**Figure 4.8.** Nyquist diagrams of 1@Nafion at pH 2, 4, and 12 at room temperature.

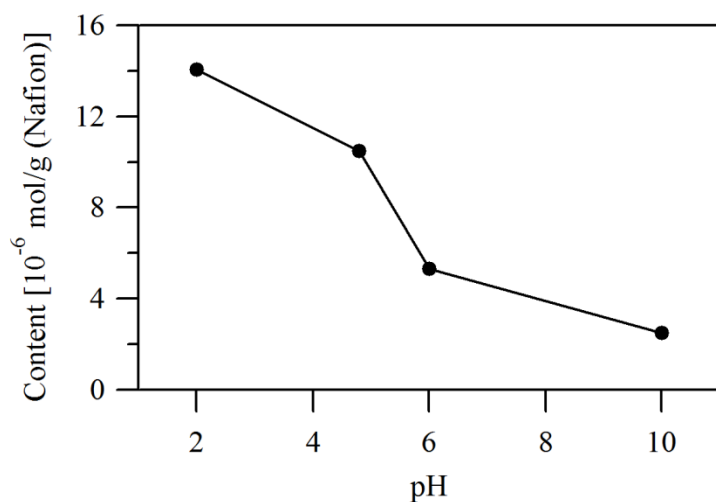
**Table 4.2.** Summary of the proton conductivity of **1@Nafion** at pH 2, 4, and 12.

pH	Conductivity: $\sigma$ [ $\text{S cm}^{-1}$ ]
2	$2.37 \times 10^{-9}$
4	$2.65 \times 10^{-10}$
12	$5.01 \times 10^{-9}$

#### 4.4.2 [Ir<sup>III</sup>(H<sub>2</sub>bip)(Me<sub>2</sub>bib)]@Nafion (**2@Nafion**)

##### Incorporated quantity

The incorporated quantity of the complex **2** into Nafion was estimated by the same way described in subsection 4.4.1. Figure 4.9 shows the content of **2** into Nafion at various pH conditions. In the same tendency as **1@Nafion**, the incorporated quantity of **2@Nafion**(pH 2) is the largest thanks to the positive charge of divalent complexes (see Scheme 4.4) compared with the other complex films. With decreasing pH, the content of **2** per Nafion weight monotonically reduces. At higher pH condition, **2** seems to be incorporated by simple diffusion instead of cation exchange due to its neutral charge.

**Figure 4.9.** The incorporated quantity of **2** into Nafion.

## Optical property

The transparent films, **2**@Nafion, were yellow colored at pH 2 and 4.8, whereas those at pH 6 and 10 are very close to an achromatic color as can be seen in Figure 4.10. As mentioned above, **2**@Nafion at pH 6 and 8 have smaller quantities than that of pH 2 and 4.8, and thus the latter is deep in color. Under UV irradiation ( $\lambda = 365$  nm), the emission of **2**@Nafion was observed as seen in Figure 4.10 (bottom). With increasing pH, the emission color was slightly changed from orange to yellow, and the brightness was gradually increased.

The UV-vis absorption spectra of **2** in solution and film states are shown in Figure 4.11 and Figure 4.12, respectively. Owing to the limitation of the apparatus, the spectra under 400 nm could not be measured. In all the spectra, the absorption was continuously increased with decreasing wavelength below 500 nm with a shoulder around 480 nm. The absorption band around 480 nm is assigned to  $^3\text{MLCT}$  transition. In addition, the ligands of **2**, H<sub>2</sub>bip and Me<sub>2</sub>bib, also exhibit luminescence under the UV irradiation. Thus, LC transition may be observed below 400 nm. As seen in Figure 4.12, **2**@Nafion at pH 2 and 4.8 has higher absorbance than that of pH 6 and 10, which is due to the difference in the incorporated quantity of **2** into Nafion.

Figure 4.13 and Figure 4.15 are the emission spectra of **2** in solution and film states, and in addition, Figure 4.14 and Figure 4.16 show the maximum emission intensity of **2** in solution and film states, respectively. The maximum emission intensities of **2**@Nafion were linearly increased with increasing pH with a slight blue shift. The emission of **2**@Nafion was observed in the range from 500 to 700 nm. The vertical axis of the emission spectra (Figure 4.15) is normalized intensity by the incorporated quantity. At pH 2 and 4.8, the emission maxima were observed at  $\lambda_{\text{max}} = 563$  nm with comparable intensities. Meanwhile, the emission intensity at pH 6 was dramatically increased over twenty times with appearing a new shoulder around 520 nm. The film at pH 10 eventually exhibited the most intense emission which is approximately twice as much as that of pH 6. As

already pointed out, with increasing pH, the light-emitting efficiency increases, and in contrast, the incorporated quantity decreases as seen in Figure 4.9. Therefore, such a remarkable difference appeared after the normalization by the content of **2** in Nafion. Incidentally, the cause of the curious appearance of the shoulder around 520 nm is still unclear, which is the reason why the emission of **2**@Nafion at pH 6 and 10 is a bit yellow colored.

The pH dependence of quantum yield was depicted in Figure 4.17. In methanolic solution of **2**, an upward trend was observed from  $\Phi = 0.029$  at pH 2 to  $\Phi = 0.10$  at pH 10. To append a comment to this, a slight jump was seen between pH 4.8 and 6, which is presumably due to a change in charge of **2**. Likewise, the upward trend was observed in **2**@Nafion with a significant jump between pH 4.8 and 6. It should be noted that the quantum yield of **2**@Nafion was greater than **2** in MeOH on the whole. In general, excitation characteristics of emissive transition metal complexes can be controlled by surrounding media including solvation effect, rigidity, electrostatic interaction, and so forth. For example, an emissive ruthenium(II) complex,  $[\text{Ru}^{\text{II}}(\text{bpy})_3]$ , in polymerized film has an MLCT excited state with comparative long lifetime and high energy due to restraining a relaxation of the excited state in comparison with solution states.<sup>[13, 14]</sup> Metal complexes with the high energy Frank-Condon (FC) excited state in solution are generally stabilized to an excited state in thermal equilibrium by internal conversion, intersystem crossing, solvent reorganization, and so forth. Radiative- and nonradiative deactivation occurs from the stabilized state. In contrast, a relaxation from the FC excited state is restrained in solid states like a polymerized film due to absence of vibrations in surrounding media. As a result, the energy of an emissive excited state is heighten, and moreover, the lifetime of the high energy excited state would be improved thanks to the suppression of the nonradiative deactivation according to the energy-gap law. In the case of **2**@Nafion membrane, Nafion behaves as counter-anion for cationic metal complex **2**. Therefore, the rigid media effect and the electrostatic interaction may certainly affect the emission property of **2**. Taking

above discussion into consideration, the cause of the new appearance of a shoulder around 520 nm in the emission spectra of **2**@Nafion (Figure 4.15) is speculated as a species strongly influenced by the rigid media effect. Such a discussion lends itself well to the data for the emission lifetime.

An analogous analysis was performed to extract the lifetime by fitting to a time resolved decay curve as a multi-exponential decay except for **2** in MeOH at pH 6 and 10. Figure 4.18 and Figure 4.19 are the time resolved decay curve of **2** in MeOH solution and film states, respectively. All the obtained lifetimes were summarized in Table 4.3 with other important parameters of this system. The complex **2** had multiple lifetimes, which seems to be under the influence of a co-presence of  $\text{Ir}^{\text{III}} \rightarrow \text{H}_2\text{bip}$  and  $\text{Ir}^{\text{III}} \rightarrow \text{Me}_2\text{bib}$  MLCT transitions. Moreover, the lifetime had a tendency to increase with increasing pH in both states. This is supposed to be in consequence of an enhancement of  $\text{Ir}^{\text{III}} \rightarrow \text{Me}_2\text{bib}$  MLCT transition due to the negative charge of deprotonated  $\text{bip}^-$ . In addition, the lifetime of **2**@Nafion was longer than **2** in MeOH on the whole. It is worth mentioning again, the excited state of **2** appears to be stabilized thanks to the rigid media effect by Nafion itself. Therefore, possible causes include that the decay with multiple lifetimes comes from changes in stabilization process of FC excited state by the media effect.

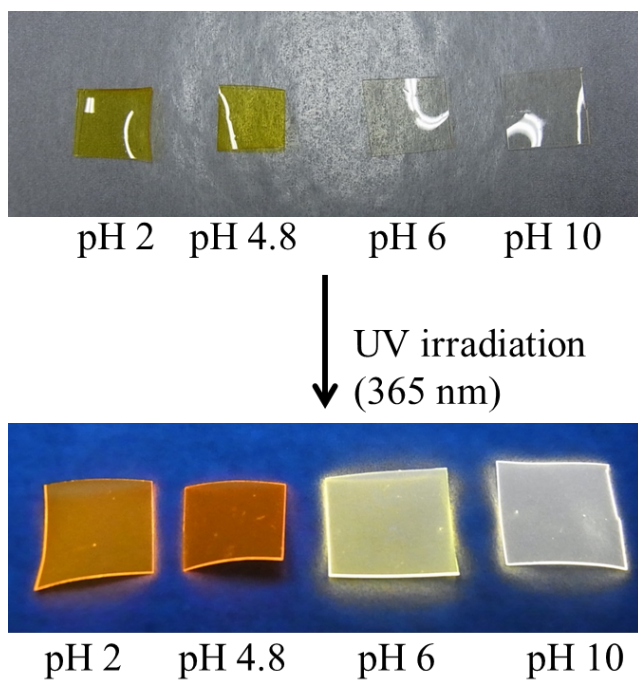


**Figure 4.10.** Photographs of **2**@Nafion prepared at various pH conditions.

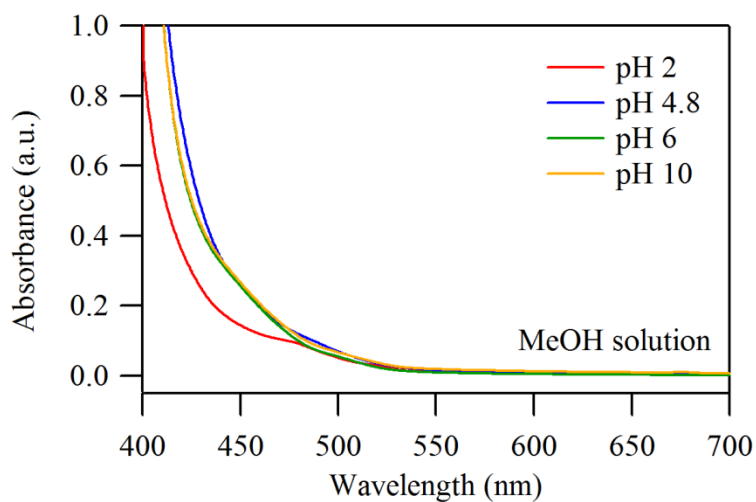


**Figure 4.11.** UV-vis absorption spectra of **2** in MeOH at various pH conditions.

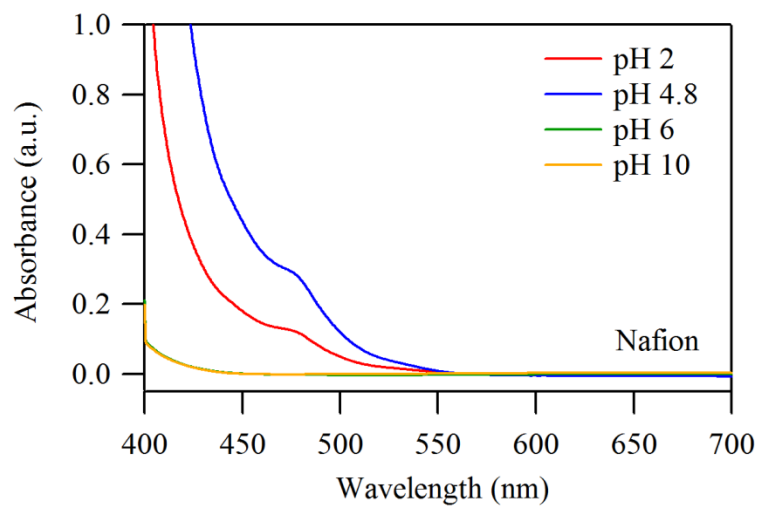


**Figure 4.12.** UV-vis absorption spectra of **2**@Nafion at various pH conditions.

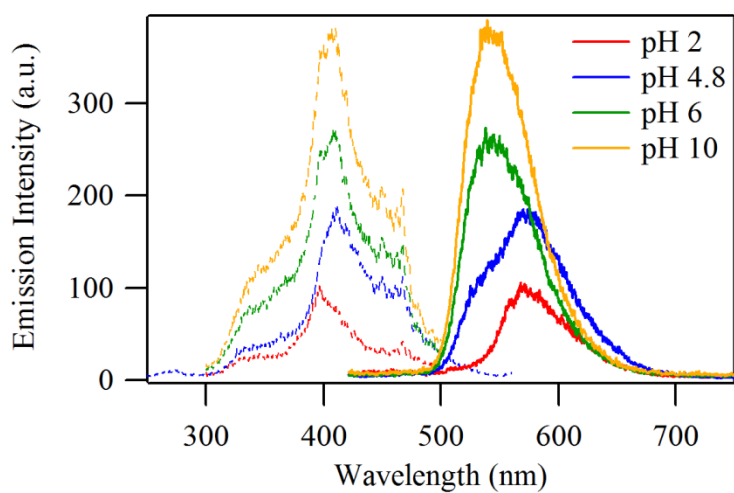


**Figure 4.13.** Excitation (dashed lines) and emission (solid lines) spectra of **2** in MeOH.

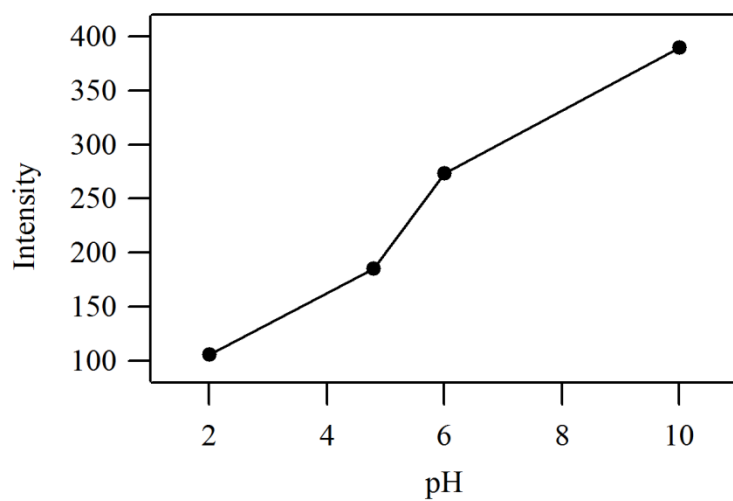


**Figure 4.14.** pH dependence of the emission intensities at maximum peaks for **2** in MeOH.

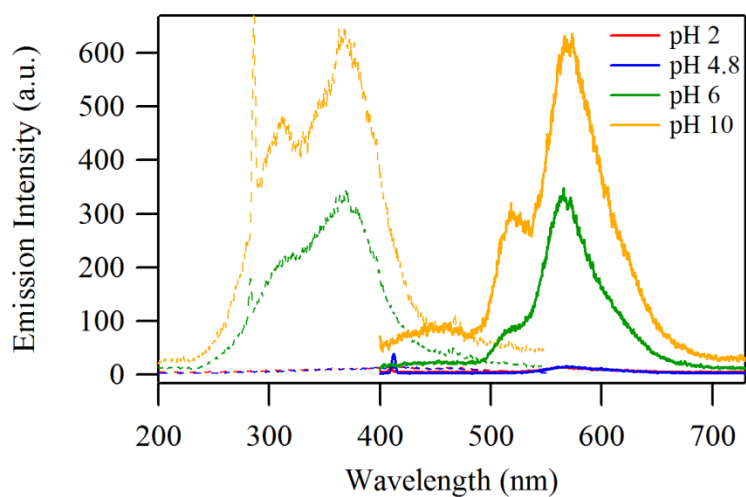


**Figure 4.15.** Excitation (dashed lines) and emission (solid lines) spectra of **2@Nafion**.

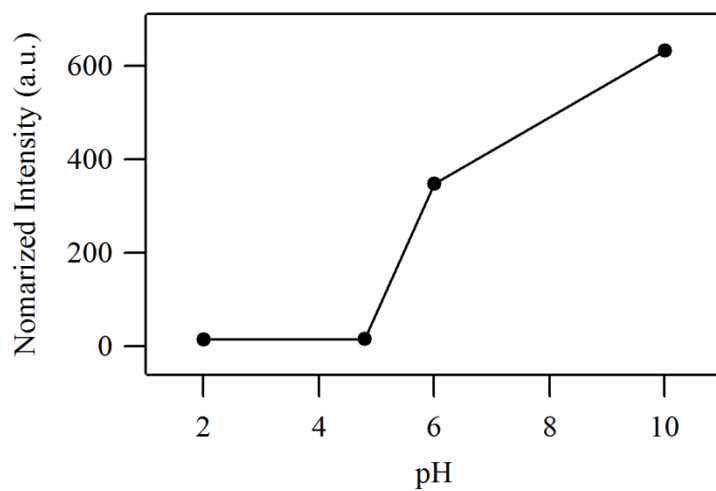


**Figure 4.16.** pH dependence of the emission intensities at maximum peaks for **2**@Nafion.

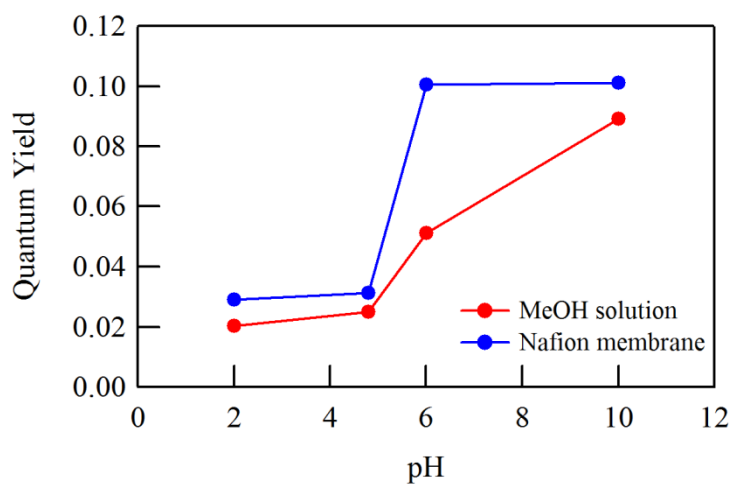


**Figure 4.17.** pH dependence of the luminescence quantum yields of **2** in MeOH (red) and **2**@Nafion (blue). Solid lines are drawn as a guide to the eye.

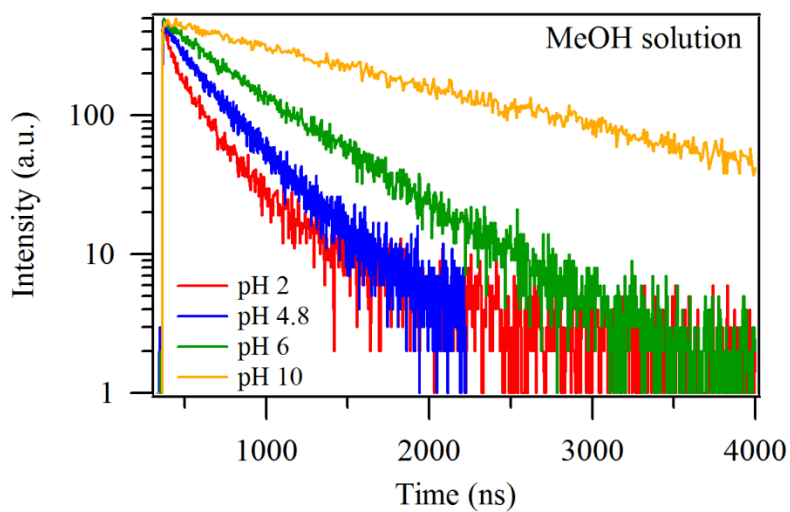


**Figure 4.18.** Emission decay time spectra of **2** in MeOH at various pH conditions. Variation of the emission lifetime of **2** in MeOH with pH.

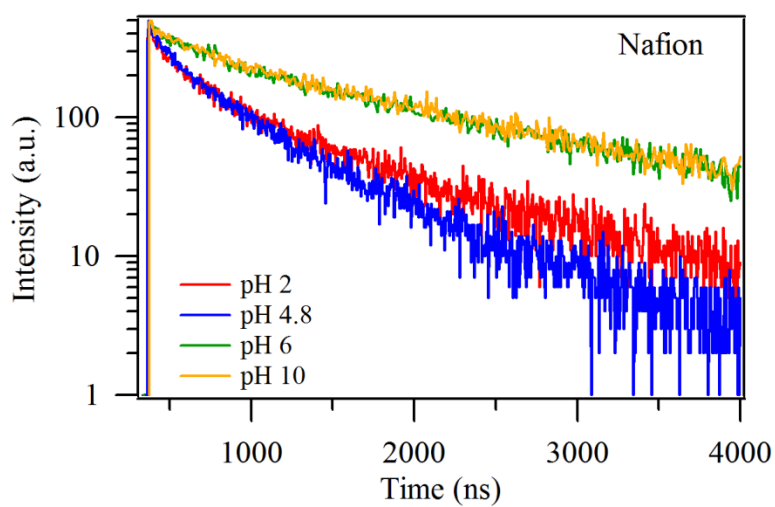


**Figure 4.19.** pH dependence of emission decay time spectra of **2@Nafion** at various pH conditions.

**Table 4.3.** Summary of the incorporated quantity and optical parameters in solution and film states of **2**.

pH	Quantity [ $10^{-6}$ mol/g (Nafion)]	$I_{\max}$ [a.u.]	$\Phi$	$\Phi$ (sol.)	$\tau$ [ns]	$\tau$ (sol.) [ns]
2	14.04	14.1	0.029	0.020	12.2	3.17
					267.3	72.4
					1169	303.8
4.8	10.46	16.1	0.031	0.025	141.5	85.6
					654.1	325.2
6	5.32	348	0.10	0.051	429.3	525.6
					1957	
10	2.48	633	0.10	0.089	462.7	1531
					1989	

$I_{\max}$ : normalized maximum emission intensity,  $\Phi$ : quantum yield,  $\tau$ : emission lifetime.

### Proton conduction and applying voltage

The impedance spectra (Nyquist diagrams) of **2**@Nafion at pH 2, 4.8, 6, and 10 are shown in Figure 4.20, and the values of the proton conductivity estimated from the fittings to the Nyquist diagrams are summarized in Table 4.4. The resistance values estimated from the fitting were several thousand ohm at most. With decreasing pH, the proton conductivity was increased from  $6.21 \times 10^{-6} \text{ S cm}^{-1}$  (pH 10) to  $1.46 \times 10^{-4} \text{ S cm}^{-1}$  (pH 2), which was totally higher than that of **1**@Nafion. The rather small size of **2** than **1** and moisturizing may be the causes of improvement of conductivity.

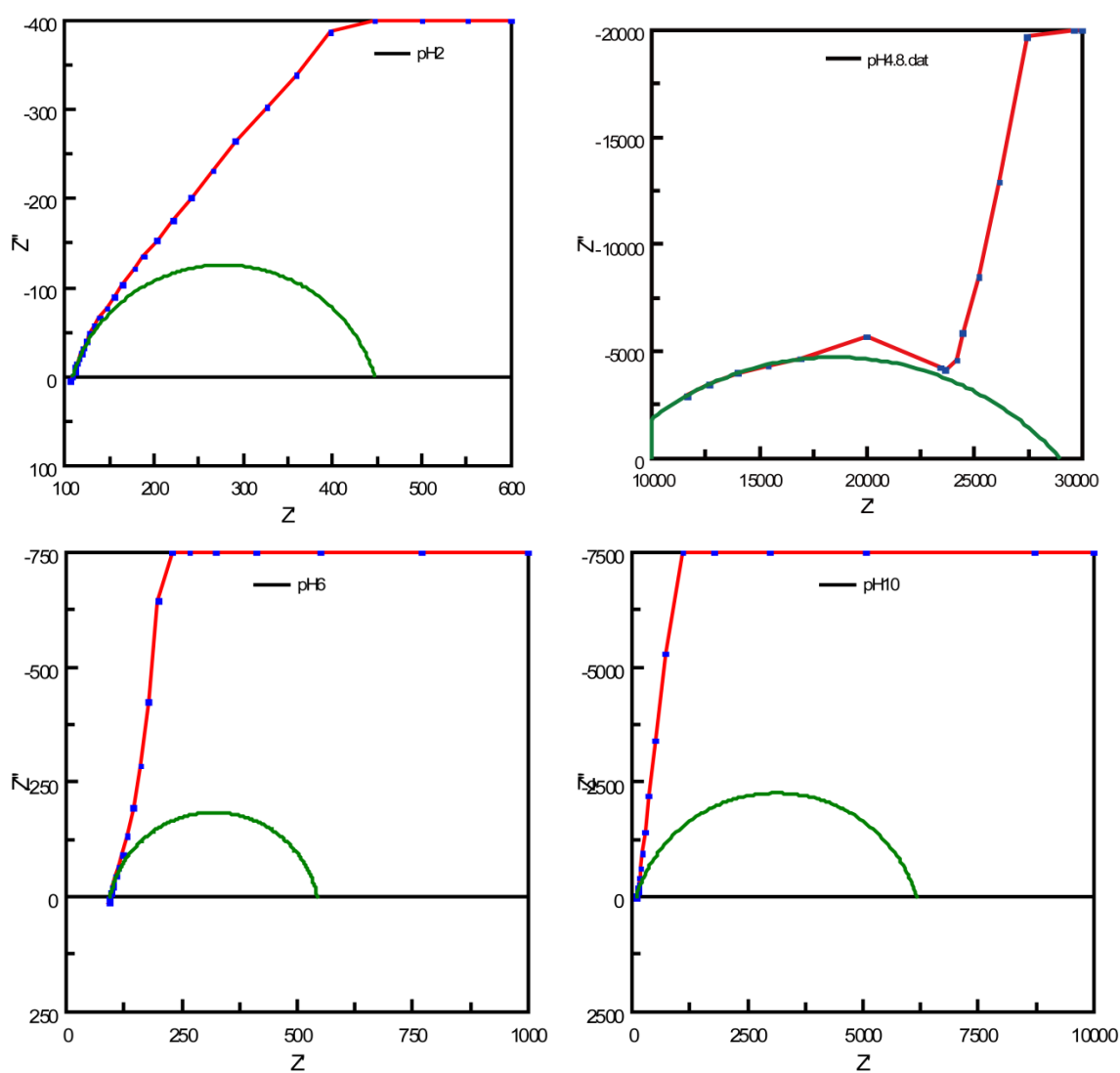


**Figure 4.20.** Impedance spectra (Nyquist diagrams) of **2@Nafion** at various pH conditions. The relative humidity and temperature were maintained at 85% and 25°C, respectively. The green semicircle lines represent the fit result. The red lines are drawn as a guide to the eye.

**Table 4.4.** Summary of proton conductivity of **2@Nafion**.

pH	Proton Conductivity $\sigma$ [ $\text{S cm}^{-1}$ ]
2	$1.46 \times 10^{-4}$
4.8	$8.34 \times 10^{-7}$
6	$8.41 \times 10^{-5}$
10	$6.21 \times 10^{-6}$

## 4.5 Conclusion

Development of the emissive films with transparency and control of their emission properties by external pH were demonstrated in this chapter. The dinuclear ruthenium(II) complex **1** has the fascinating emission property dependent on pH with some difficulties in Nafion. The emission property was failed to control by applied voltage even though it was successfully controlled by external pH conditions. Allowing for some trouble of the experiment for **1**@Nafion, **2**@Nafion was newly developed. In this system, it was clarified that the quantum yield and the emission lifetime of **2** in the film state were greater than that in solution state. Such a “rigid media effect” is a sure merit to create a film using Nafion. Besides, the experiment for controlling the emission property of **2**@Nafion by applied voltage is currently in progress. Much is expected of successful control, however, it should be eventually confirmed by an emission spectroscopic measurement. Accordingly, it is to be desired that a measuring system will be established which can control humidity, apply voltage, and measure emission spectra simultaneously.

Transparent emissive materials are widely developed due to their potential to use in displays, illuminators, and other applications. To provide a transparent emitter, methodologies can be generally classified roughly into two types as follows: (1) Using particulate phosphor like quantum dots or nanocrystals which does not scatter visible light, and (2) dispersing emitters into some media. In comparison to this, Nafion can provide transparent emitter easily thanks to its ion exchange property. This methodology is expected to bring transparent emissive materials to a variety of application fields where the see-through characteristic shall be useful.

## References

- [1] H. Chao, B.-H. Ye, Q.-L. Zhang, L.-N. Ji, *Inorg. Chem. Commun.* **1999**, *2*, 338-340.
- [2] V. Balzani, A. Juris, M. Venturi, *Chem. Rev.* **1996**, *96*, 759-833.
- [3] S. Ogawa *et al.*, The 2005 International Chemical Congress of Pacific Basin Societies, Hawaii, USA, Abstract Inorg 227, **2005**.
- [4] a) J.-P. Collin, I. M. Dixon, J.-P. Sauvage, J. A. G. Williams, F. Barigelletti, L. Flamigni, *J. Am. Chem. Soc.* **1999**, *121*, 5009-5016; b) N. Yoshizawa, T. Matsumura-Inoue, *Anal. Sci.* **2003**, *19*, 761-765; c) M. Polson, S. Fracasso, V. Bertolasi, M. Ravaglia, F. Scandola, *Inorg. Chem.* **2004**, *43*, 1950; d) W. Leslie, A. S. Batsanov, J. A. K. Howard, J. A. G. Williams, *Dalton Trans.* **2004**, 623-631; e) E. Baranoff, I. M. Dixon, J.-P. Collin, J.-P. Sauvage, B. Ventura, L. Flamigni, *Inorg. Chem.* **2004**, *43*, 3057-3066; f) T. Yutaka, S. Obara, S. Ogawa, K. Nozaki, N. Ikeda, T. Ohno, Y. Ishii, K. Sakai, M. Haga, *Inorg. Chem.* **2005**, *44*, 4737-4746; g) M. Ashizawa, L. Yang, K. Kobayashi, H. Sato, A. Yamagishi, F. Okuda, T. Harada, R. Kuroda, M. Haga, *Dalton Trans.* **2009**, 1700-1702; h) J.-L. Chen, Y.-H. Wu, L.-H. He, H.-R. Wen, J. Liao, R. Hong, *Organometallics* **2010**, *29*, 2882-2891; i) J. Kuwabara, T. Namekawa, M. Haga, T. Kanbara, *Dalton Trans.* **2012**, *41*, 44-46; j) L. F. Gildea, A. S. Batsanov, J. A. G. Williams, *Dalton Trans.* **2013**, *42*, 10388-10393; k) Naokazu Y., Shinichi Y., Shigeyoshi S., Nobuko K., Tsuyoshi I., Hiroshi T., *Can. Chem. Trans.* **2014**, *2*, 134-148.
- [5] H. Chao, R.-H. Li, C.-W. Jiang, H. Li, L.-N. Ji, X.-Y. Li, *J. Chem. Soc., Dalton Trans.* **2001**, 1920-1926.
- [6] B. P. Sullivan, D. J. Salmon, T. J. Meyer, *Inorg. Chem.* **1978**, *17*, 3334-3341.
- [7] H. T. S. Britton, R. A. Robinson, *J. Chem. Soc.* **1931**, 1456-1462.
- [8] A. W. Addison, P. J. Burke, *J. Heterocyclic Chem.* **1981**, *18*, 803-805.
- [9] D. M. Klassen, G. A. Crosby, *J. Chem. Phys.* **1968**, *48*, 1853-1858.

- [10] R. Grigg, W. D. J. A. Norbert, *J. Chem. Soc., Chem. Commun.* **1992**, 1300-1302.
- [11] a) R. H. Fabian, D. M. Klassen, R. W. Sonntag, *Inorg. Chem.* **1980**, *19*, 1977-1982; b) J. M. Kelly, C. Long, C. M. O'Connell, J. G. Vos, A. H. A. Tinnemans, *Inorg. Chem.* **1983**, *22*, 2818-2824; c) A. Juris, V. Balzani, F. Barigelletti, S. Campagna, P. Belser, A. von Zelewsky, *Coord. Chem. Rev.* **1988**, *84*, 85-277.
- [12] T. A. Zawodzinski, Jr., M. Neeman, L. O. Sillerud, S. Gottesfeld, *J. Phys. Chem.* **1991**, *95*, 6040-6044.
- [13] a) T. E. Knight, A. P. Goldstein, M. K. Brennaman, T. Cardolaccia, A. Pandya, J. M. DeSimone, T. J. Meyer, *J. Phys. Chem. B* **2011**, *115*, 64-70; b) A. Ito, D. J. Stewart, Z. Fang, M. K. Brennaman, T. J. Meyer, *Proc. Natl. Acad. Sci. USA* **2012**, *109*, 15132-15135; c) A. Ito, D. J. Stewart, T. E. Knight, Z. Fang, M. K. Brennaman, T. J. Meyer, *J. Phys. Chem. B* **2013**, *117*, 3428-3438; d) A. Ito, Z. Fang, M. K. Brennaman, T. J. Meyer, *Phys. Chem. Chem. Phys.* **2014**, *16*, 4880-4891.
- [14] in connection with ref.[13]: A. Ito, T. E. Knight, D. J. Stewart, M. K. Brennaman, T. J. Meyer, *J. Phys. Chem. A* **2014**, *118*, 10326-10332.

## 5. Fastener Effect on Uniaxial Chemical Pressure for One-Dimensional Spin-Crossover System, $[\text{Fe}^{\text{II}}(\text{NH}_2\text{-trz})_3](\text{C}_n\text{H}_{2n+1}\text{SO}_3)_2 \cdot x\text{H}_2\text{O}$ : Magnetostructural Correlation and Ligand Field Analysis

### Abstract

One-dimensional spin-crossover (SCO) polymers of formula  $[\text{Fe}^{\text{II}}(\text{NH}_2\text{-trz})_3](\text{C}_n\text{H}_{2n+1}\text{SO}_3)_2 \cdot x\text{H}_2\text{O}$  (trz = 4-substituted-1,2,4-triazole;  $n = 1-9$ ) have been synthesized. They displayed hysteretic SCO transition around 280-350 K. With increasing alkyl chain length ( $n$ ), the spin transition temperatures ( $T_{1/2}$ ) increased in the heating and cooling processes, and the hysteresis width becomes narrower. From the analysis of EXAFS, the nearest-neighbor Fe-Fe distance decreased with increasing  $n$ , and it had a close relationship with  $T_{1/2}$ . This is highly indicative of the increase of intrachain interaction of  $[\text{Fe}^{\text{II}}(\text{NH}_2\text{-trz})_3]$  with increasing  $n$  being attributed to the uniaxial chemical pressure effect induced by van der Waals force between alkyl chains, so-called “fastener effect”. To elucidate the physicochemical effect on  $T_{1/2}$ , the ligand field and Racah parameter ( $B$ ) were estimated by analysing the pre-edge region in Fe-K edge XANES spectra based on the ligand-field theory.  $B$  decreased with increasing  $n$ , which were closely consistent with the behavior of  $T_{1/2}$  and  $^{57}\text{Fe}$  Mössbauer isomer shift ( $IS$ ). Judging from these results, a covalency between  $\text{Fe}^{\text{II}}$  3d and ligand  $\pi^*$  orbital is enhanced by the fastener effect, leading to the expansion of the 3d orbital, *i.e.* the remarkable decrease of  $B$  and  $IS$ , which is the dominating factor on  $T_{1/2}$  in our system.

## 5.1 Introduction

The five d orbitals of transition metal ions in octahedral symmetry are splitted into  $t_{2g}$  ( $d_{xy}$ ,  $d_{yz}$ ,  $d_{zx}$ ) and  $e_g$  ( $d_{x^2-y^2}$ ,  $d_{z^2}$ ) subsets. In some transition metal complexes with  $3d^4$ - $3d^7$  electronic configurations, either high-spin (HS) states with maximum spin multiplicity or low-spin (LS) states where 3d electrons nicely pair up in the  $t_{2g}$  orbitals are spin ground state due to a conflict between ligand field splitting ( $10Dq$ ) and spin pairing energy ( $P$ ). When  $10Dq$  and  $P$  energetically vie with each other, and besides, the magnitude of energy difference between them is comparable to the thermal energy ( $k_B T$ ), HS and LS states as spin ground state are reversibly switched by temperature, which is referred to as spin-crossover (SCO) phenomenon. Additionally,  $P$ , *i.e.* interelectron interactions, is defined by coulombic and exchange integral. They are described Racah parameters  $A$ ,  $B$  and  $C$  in ligand field theory. Usually  $A$  is ignored because it is roughly the same for any metal ions, and generally  $B$  has an empirical proportionality relation with  $C$ , that is to say  $B \approx 1/4 C$ . Therefore, relative relationships between each spin states are determined by  $10Dq/B$ , which is the dominant parameter how much spin transition temperatures ( $T_{1/2}$ ) reach.

There remains an ever-increasing interest and challenge to investigate multifunctional properties triggered by external stimuli, for instance, heat, light, pressure, magnetic field, X-ray *etc.*<sup>[1]</sup> Among a number of multifunctional materials, SCO complexes are the leading candidates as field-sensitive molecular system.<sup>[2]</sup> Up to now, many kinds of SCO complexes have been reported. Most of them are  $Fe^{II}$  and  $Fe^{III}$  compounds,<sup>[3,4]</sup> and to a lesser extent  $Co^{II}$  compounds.<sup>[5]</sup> As comparatively rare example,  $Cr^{II}$ ,  $Mn^{II}$ ,  $Mn^{III}$ , and  $Co^{III}$  compounds have also been reported.<sup>[6]</sup> Among them, in particular in  $Fe^{II}$  compounds, the transition between high-spin (HS;  ${}^5T_{2g}$ ,  $S = 2$ ) and low-spin (LS;  ${}^1A_{1g}$ ,  $S = 0$ ) is associated with diamagnetic to paramagnetic switching as well as with drastic color change (colorless  $\leftrightarrow$  purple). Owing to the outstanding magnetic and optical properties,

$\text{Fe}^{\text{II}}$  SCO materials are expected to open a large field of molecular devices, including information storage, display, sensor,<sup>[7]</sup> etc. since the discovery of LIESST (Light Induced Excited Spin State Trapping).<sup>[8]</sup>

Over the past two decades, one dimensional (1D)  $\text{Fe}^{\text{II}}$  coordination polymers bridged by 4-substituted-1,2,4-triazole (R-trz) which provides many kinds of the fascinating not only monomers but also extended systems,<sup>[9,10]</sup> whose general formula of the SCO 1D system is  $[\text{Fe}^{\text{II}}(\text{R-trz})_3]\text{Anion} \cdot x\text{H}_2\text{O}$  (Anion = mono- or divalent anion), have been drawing intense research interest because of their potential applications in molecular electronics or as sensors.<sup>[11-14]</sup> The primary reasons for this are their tunable and abrupt SCO behavior, sometimes with associated wide thermal hysteresis around room temperature (RT). The spin transition temperature ( $T_{1/2}$ ) of  $[\text{Fe}^{\text{II}}(\text{R-trz})_3]\text{Anion} \cdot x\text{H}_2\text{O}$  strongly depends on (i) substituents on triazole ligand (R); (ii) counteranions (Anion); and (iii) presence or absence of crystal solvent ( $\text{H}_2\text{O}$ ) located in the space among  $[\text{Fe}^{\text{II}}(\text{R-trz})_3]$  chains,<sup>[15]</sup> all of which are influential on intra- and interchain interactions and cooperative effect. At first, let us take the variations of  $T_{1/2}$  for  $[\text{Fe}^{\text{II}}(\text{H-trz})_{3-3y}(\text{NH}_2\text{-trz})_{3y}](\text{ClO}_4)_2 \cdot \text{H}_2\text{O}$  as an example since this is an ideal experiment demonstrating the very systematic control of  $T_{1/2}$ . In this system,  $T_{1/2}$  is tuned linearly from  $T_{1/2}\uparrow = 319$  K and  $T_{1/2}\downarrow = 304$  K for  $[\text{Fe}^{\text{II}}(\text{H-trz})_3](\text{ClO}_4)_2 \cdot \text{H}_2\text{O}$  ( $y = 0$ ) to  $T_{1/2}\uparrow = 189$  K and  $T_{1/2}\downarrow = 187$  K for  $[\text{Fe}^{\text{II}}(\text{NH}_2\text{-trz})_3](\text{ClO}_4)_2 \cdot \text{H}_2\text{O}$  ( $y = 1$ ), for that, it is the approach called “molecular alloy”.<sup>[11b,16]</sup> It is also worth mentioning that RT falls in the middle of the thermal hysteresis loop for  $[\text{Fe}^{\text{II}}(\text{H-trz})_{2.85}(\text{NH}_2\text{-trz})_{0.15}](\text{ClO}_4)_2 \cdot \text{H}_2\text{O}$  ( $y = 0.05$ ).<sup>[17]</sup> Next, let us take a look at the influence of variation for counteranion on  $T_{1/2}$ . In the complexes  $[\text{Fe}^{\text{II}}(\text{NH}_2\text{-trz})_3](\text{Anion})_2 \cdot x\text{H}_2\text{O}$ , for instance,  $T_{1/2}$  increases with decreasing the size of anions along the series of Anion =  $\text{ClO}_4^-$ ,  $\text{I}^-$ ,  $\text{Br}^-$ ,  $\text{BF}_4^-$ ,  $\text{NO}_3^-$ ,  $\text{Cl}^-$ .<sup>[18]</sup> From the analysis of extended X-ray absorption fine structure (EXAFS) on the LS state of  $[\text{Fe}^{\text{II}}(\text{NH}_2\text{-trz})_3](\text{Anion})_2 \cdot x\text{H}_2\text{O}$ , the nearest neighbor Fe-N distances tend to decrease in the same

series of anions due to the increase of anion-cation interactions, and thereby resulting the increase of chemical or electrostatic pressure, which has been supported by  $^{57}\text{Fe}$  Mössbauer<sup>[18f]</sup> and X-ray fluorescence spectroscopy.<sup>[18a]</sup> These results also point out the importance of interchain spacing, which is influential on the cooperative interaction among  $[\text{Fe}^{\text{II}}(\text{NH}_2\text{-trz})_3]$  chains. A quite similar example was reported by Garcia *et al.* for  $[\text{Fe}^{\text{II}}(\text{hyetrz})_3](\text{Anion})_2 \cdot x\text{H}_2\text{O}$  (hyetrz = 4-(2'-hydroxy-ethyl)-1,2,4-triazole) along the series of Anion =  $\text{PF}_6^-$ ,  $\text{ClO}_4^-$ ,  $\text{BF}_4^-$ ,  $\text{I}^-$ ,  $\text{Br}^-$ ,  $\text{NO}_3^-$ ,  $\text{Cl}^-$ .<sup>[19]</sup> Furthermore, these features are observed for the series of  $[\text{Fe}^{\text{II}}(\text{NH}_2\text{-trz})_3](\text{Anion})_2 \cdot x\text{H}_2\text{O}$  with organic sulfonate anions,<sup>[15a,20-23]</sup> and inorganic mono-<sup>[24]</sup> and divalent anions.<sup>[25-27]</sup>

X-ray absorption near edge structure (XANES) is also useful technique to investigate chemical characteristics of SCO compounds. XANES is a region of X-ray absorption spectrum within ~50 eV of the absorption edge and its features are dominated by multiple-scattering resonance of the photoelectrons ejected at low kinetic energy.<sup>[28]</sup> Naturally, X-ray multiple-scattering is strongly sensitive to the chemical environment, *e.g.* atomic position of neighbors, interatomic distances, site symmetry, valence and spin states, *etc.* In particular, this chapter focused attention on the “pre-edge region” in the K-edge XANES spectra of the first transition metal ions. The features are caused by  $1s \rightarrow 3d$  transitions, which is also sensitive to the chemical environment of the absorbing atoms.<sup>[29]</sup> The relationship between symmetry and pre-edge peak intensity are well-investigated in iron complexes by Westre and co-workers.<sup>[30]</sup> They divided the pre-edge peak intensity and energy in 49 number of iron complexes by valency, spin state, geometry, ligand, and the number of nuclear. Furthermore, they obtained the energy levels of d orbitals by density functional theory (DFT) calculation, and thereby estimated electric dipole- and quadrupole transition intensities in the pre-edge peaks based on group theory. The computational study showed that there is a clear correlation between pre-edge peak intensity and 3d-4p mixing, which is in good agreement with the trend for a series of 28 iron-tyrosinate proteins demonstrated by Roe *et al.*<sup>[31]</sup> In fact, a pre-edge intensity increases with

increasing d-p mixing responsible for the parity allowed electric dipole transition from 1s orbital to p-orbital components.

In this chapter, ligand field analysis for 1D SCO polymer with alkanesulfonate,  $[\text{Fe}^{\text{II}}(\text{NH}_2\text{-trz})_3](\text{C}_n\text{H}_{2n+1}\text{SO}_3)_2 \cdot x\text{H}_2\text{O}$ , is reported.  $T_{1/2}$  of this series of material increases with increasing the number of carbon atoms of the counteranions ( $n$ ) due to an uniaxial chemical pressure effect originating from van der Waals force between the alkyl chains. The self-assembly interaction is called “fastener effect” and plays a crucial role in Fe-Fe distance and  $T_{1/2}$ . This closely-linked magnetostructural correlation was evidenced by EXAFS in which the distances between the neighboring Fe atoms along the chain axis decrease with increasing  $n$ . In order to clarify the origin of the magnetostructural correlation, detailed analysis based on the ligand field theory was performed on a pre-edge region in Fe-K edge XANES spectra. From the analysis of the pre-edge region in a HS state of  $\text{Fe}^{\text{II}}$  complexes,  $10Dq$  and  $B$  can be extracted. Because Racah parameter  $B$  is directly related to the d-electron distribution of central ions, the physico-chemical correlations can be discussed. Additionally as mentioned above,  $10Dq/B$  is the dominant parameter on  $T_{1/2}$ . To the best of our knowledge, this is the first report on the correlation between  $10Dq/B$  and  $T_{1/2}$  for the SCO materials from the analysis of Fe-K edge XANES spectra. Here note that those results have been partially reported as a doctoral thesis in 2006.<sup>[32]</sup> Therefore, a review of the results about X-ray diffraction, magnetometry,  $^{57}\text{Fe}$  Mössbauer spectroscopy, and EXAFS will be provided at first in the next section, in which some of the data were collected by the author. In addition, a preliminary result of ligand field analysis have also been reported in Ref.[32], where the accuracy was not good enough. Therefore, the pre-edge region in XANES spectra was reanalyzed, and the  $^{57}\text{Fe}$  Mössbauer spectra were also measured in order to support the results of ligand field analysis. These informations are provided in the Section 5.4.

## 5.2 Review of the Material

### X-ray Powder Diffraction

XRPD measurements were performed for  $[\text{Fe}^{\text{II}}(\text{NH}_2\text{-trz})_3](\text{C}_n\text{H}_{2n+1}\text{SO}_3)_2 \cdot x\text{H}_2\text{O}$  ( $n = 1-9$ ) at RT and from which the spacing value ( $d$ ) was estimated according to Bragg equation ( $2d\sin\theta = m\lambda$ ). As can be seen in Figures 5.1 and 5.2,  $d$  value increases with increasing  $n$  and are approximately in the linear relationship except for  $n = 1$ . The deviation of  $n = 1$  from the linear relationship appears to be due to the difference of the spin state at RT, *i.e.*  $n = 1$  has the HS state at RT, whereas  $n = 2-9$  have the LS state at RT as described in the later section. As evidenced by Figure 5.2,  $\text{C}_n\text{H}_{2n+1}\text{SO}_3^-$  plays a systematic role as a spacer between  $[\text{Fe}^{\text{II}}(\text{NH}_2\text{-trz})_3]$  chains.

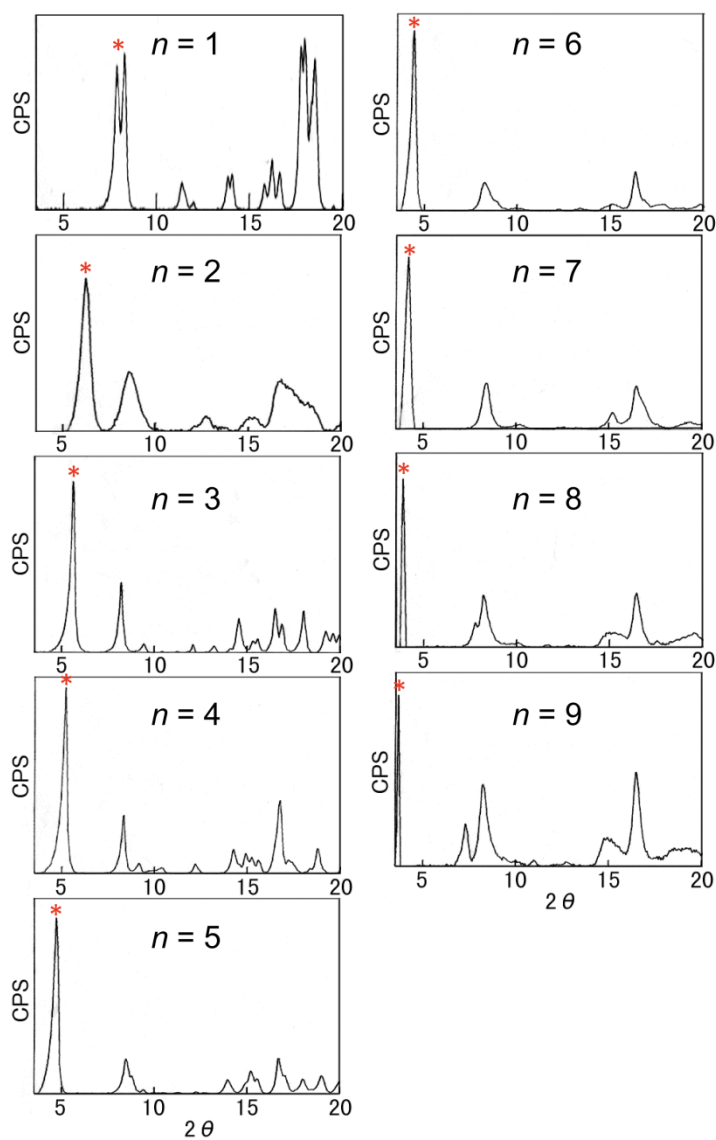


**Figure 5.1.** XRPD patterns for  $[\text{Fe}^{\text{II}}(\text{NH}_2\text{-trz})_3](\text{C}_n\text{H}_{2n+1}\text{SO}_3)_2 \cdot x\text{H}_2\text{O}$  ( $n = 1\text{--}9$ ) at RT.

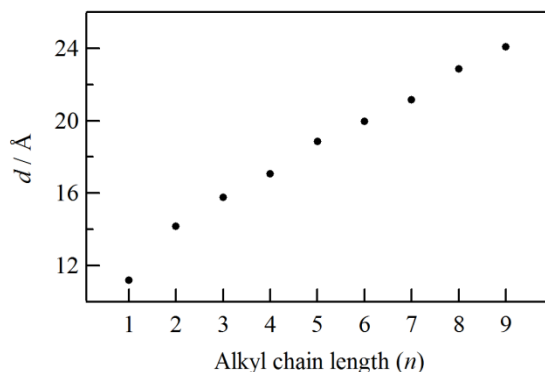


**Figure 5.2.** The spacing value ( $d$ ) as a function of alkyl chain length ( $n$ ) for  $[\text{Fe}^{\text{II}}(\text{NH}_2\text{-trz})_3](\text{C}_n\text{H}_{2n+1}\text{SO}_3)_2 \cdot x\text{H}_2\text{O}$  ( $n = 1-9$ ) at RT.

### Fe K-Edge EXAFS Analysis

The single crystals of  $[\text{Fe}^{\text{II}}(\text{R-trz})_3]$  complexes suitable for X-ray crystallographic analysis have almost never been obtained owing to their rapid precipitation, unfortunately, so that the sufficiently large single crystals of  $[\text{Fe}^{\text{II}}(\text{NH}_2\text{-trz})_3](\text{C}_n\text{H}_{2n+1}\text{SO}_3)_2 \cdot x\text{H}_2\text{O}$  ( $n = 1-9$ ) could not be obtained. Although the crystal structure of 1D  $[\text{Fe}^{\text{II}}(\text{R-trz})_3]\text{Anion} \cdot x\text{H}_2\text{O}$  is becoming clear in the most recent studies,<sup>[33,34]</sup> Fe-K edge EXAFS technique is still highly effective in investigating the local structure around  $\text{Fe}^{\text{II}}$  ions and demonstrating the formation of 1D chains.<sup>[18a,d,e,20a,35]</sup> Besides, changes in the first-nearest-neighbor Fe-N distances between HS and LS states have been elucidated by many previous studies. Figure 5.3 shows the Fourier transforms of  $[\text{Fe}^{\text{II}}(\text{NH}_2\text{-trz})_3](\text{C}_n\text{H}_{2n+1}\text{SO}_3)_2 \cdot x\text{H}_2\text{O}$  ( $n = 1-9$ ) at 35 K and 370 K, corresponding to the LS and the HS states, respectively. In each spin states, no significant differences were observed in the spectral patterns of all the compounds ( $n = 1-9$ ), thus local structures around Fe atoms are similarly formed for all the compounds. At a glance, dominant peaks at 1.6-1.8 Å in Figure 5.3 (a) and (b) are attributed to the N atoms of  $\text{FeN}_6$  core with the six-fold coordination. The peak distance in the HS state is clearly shifted to a longer distance side than that in the LS state. On the other hand, several peaks at the range of 2-4 Å are attributed to

several kinds of coordination such as Fe-N, Fe-C and Fe-Fe shells and some multiple-scattering paths, as illustrated in Scheme 5.1. At the longer distance range ( $> 4 \text{ \AA}$ ), several contributions are still found, suggesting a highly ordered local structure in the crystal structure of the present compounds. Here, as can be seen in the Figure 5.3(a) (LS state), remarkable peaks appeared around  $7 \text{ \AA}$ . Usually in the EXAFS spectra, distinct peaks cannot be observed in this distance range. According to the previous study,<sup>[35]</sup> relatively strong peaks at  $\sim 7 \text{ \AA}$  in the LS state are attributed to the multiple scattering of Fe-Fe-Fe shell. To evaluate the backscattering amplitude and the phase shift, FEFF6 calculations<sup>[36]</sup> were carried out for a virtual chain-like pentanuclear cluster,  $\text{Fe}_5(\text{NH}_2\text{-trz})_{12}$  (Figure 5.4). The intensity is strongly enhanced due to the multiple scattering focusing effect for the collinearly arranged Fe chain as illustrated in Figure 5.4. Consequently, this is the definitive evidence showing the formation of 1D chains with Fe-Fe arrangement at intervals of *ca.*  $3.5 \text{ \AA}$ . Meanwhile in the HS state, even though the intensity of Fe-Fe-Fe multiple scattering is rather weak, it does not mean the deformation of linear chain structure of  $[\text{Fe}^{\text{II}}(\text{NH}_2\text{-trz})_3]$  unit. This is considered to be an influence of the increase of Debye-Waller factor. In connection with this, the following comments should be noted. Yokoyama *et al.* reported the temperature dependence of the Debye-Waller factor of  $[\text{Fe}^{\text{II}}(\text{NH}_2\text{-trz})_3](\text{CH}_3\text{SO}_3)_2$ .<sup>[35b]</sup> The Debye-Waller factor jumps accompanied by the spin transition from the LS state to the HS state, which originates in the 3d electrons occupying in  $e_g$  orbitals in the HS state. The LS state has the electronic configuration of  $(t_{2g})^6(e_g)^0$  in which no 3d electrons occupy the  $\sigma$ -antibonding  $e_g$  orbitals, whereas the HS state has the electronic configuration of  $(t_{2g})^4(e_g)^2$ , leading to a significant weakening of the Fe-N bond. Taken together, the jump of the Debye-Waller factor mentioned above results in the weakening of the intensity of X-ray multiple scattering Fe-Fe-Fe, which leads to the disappearance of the peak around  $7 \text{ \AA}$ .

For the methanesulfonate compound ( $n = 1$ ), the first-nearest neighbor Fe-N distances were estimated as  $1.977\text{-}1.984 \text{ \AA}$  and  $2.153\text{-}2.156 \text{ \AA}$  between 35 and 370 K for the LS and the HS states,

respectively. For the other compounds ( $n = 2-9$ ), the first-nearest neighbor Fe-N distances were estimated as 1.965-1.983 Å (LS) and 2.152-2.156 Å (HS). In all the compounds, *ca.* 0.18 Å elongation was observed in the first-nearest neighbor Fe-N distances accompanied by the spin transition from the LS to the HS state. The other shell distances also showed a similar elongation accompanied by the spin transition. On the other hand,  $[\text{Fe}^{\text{II}}(\text{NH}_2\text{-trz})_3](\text{C}_n\text{H}_{2n+1}\text{SO}_3)_2 \cdot x\text{H}_2\text{O}$  in the LS state (35 K) has a tendency of the decrease of the nearest neighbor Fe-Fe distance accompanied by „even-odd effect“ with increasing  $n$  as shown in Figure 5.5(a). This implies the uniaxial chemical pressure induced by the fastener effect originating from van der Waals force among the alkyl chains. As for the nearest-neighbor Fe-N distances, they remain almost unchanged in the accuracy of EXAFS what though the carbon number of the alkyl chain length increases as illustrated in Figure 5.5(b).

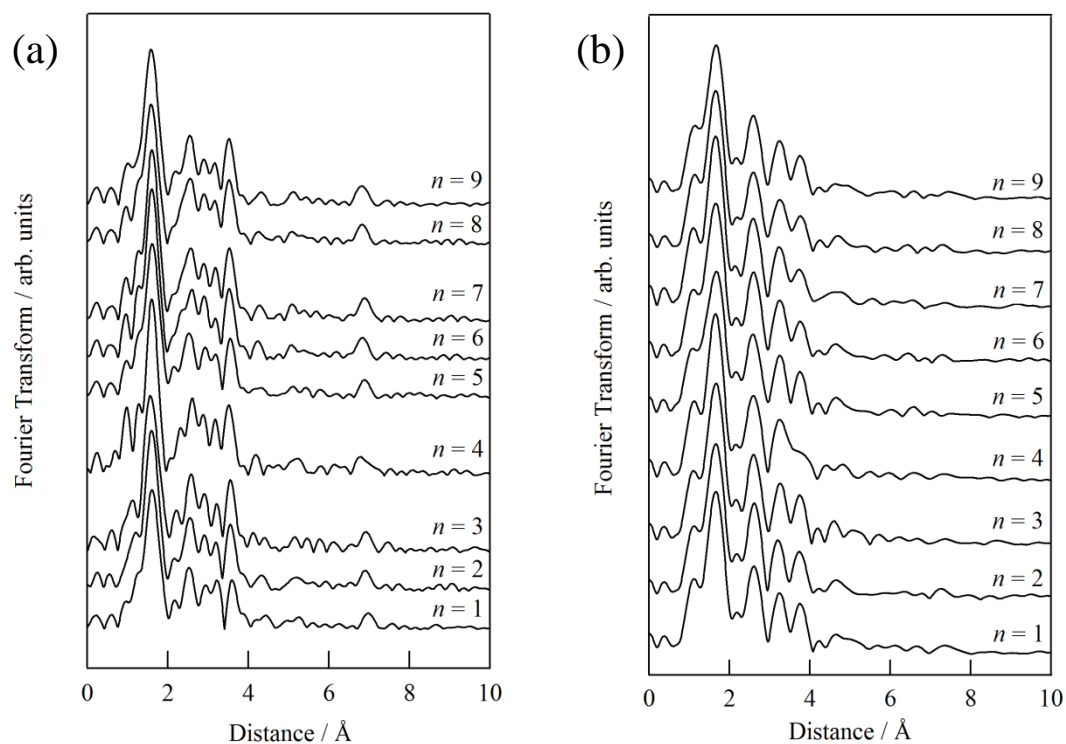
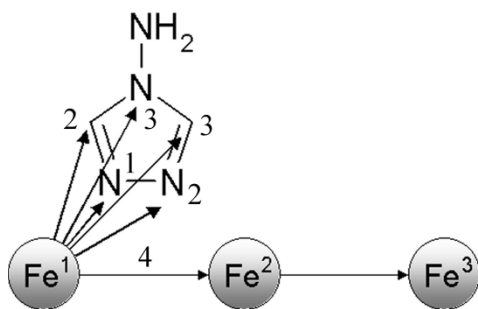


**Figure 5.3.** Fourier transforms of Fe-K-edge EXAFS oscillation functions  $k^3\chi(k)$  for  $[\text{Fe}(\text{NH}_2\text{trz})_3](\text{C}_n\text{H}_{2n+1}\text{SO}_3)_2 \cdot x\text{H}_2\text{O}$  ( $n = 1-9$ ) at (a) 35 K (LS state) and (b) 370 K (HS state).



**Scheme 5.1.** Selected important paths for the EXAFS analysis.

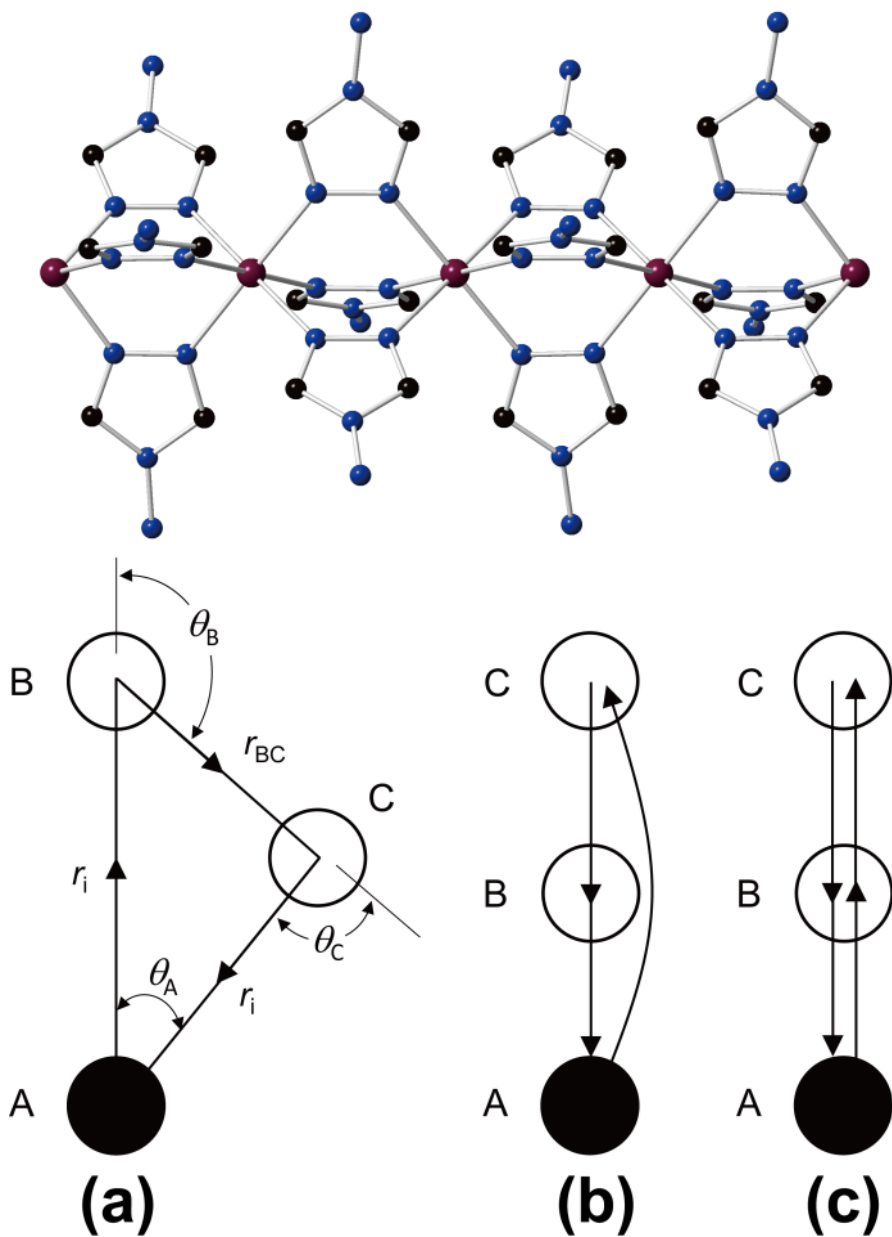


**Figure 5.4.** Molecular structure of a virtual chain-like pentanuclear cluster,  $Fe_5(NH_2-trz)_{12}$ , and schematic illustration of possible backscatterings. (a) A backscattered wave would be produced by double-scattering contribution. Here  $\theta_B$  and  $\theta_C$  are scattering angle by the atom B and C,  $\theta_A$  is the angle between the first and last scattering paths, and  $r$  is the interatomic distances. The backscattering amplitude is expressed as  $\{F(\theta_B)F(\theta_C)\exp[i[k(2r_i+r_{BC})+\delta^{(2)}(k)-\pi/2]]\cos\theta_A/kr_i^2r_{BC}$ , where  $\delta^{(2)}(k)$  is a phase shift,  $F(\theta_B)$  and  $F(\theta_C)$  are the amplitude of the scattering from the atom B and C, respectively.<sup>[28d]</sup> A Fourier transform of the form of backscattering will peak at the larger distance,  $R \approx r_i+(r_{BC}/2)$ . In the case of  $\theta_C \approx 0^\circ$ ,  $F(0)$  peaks and becomes much larger. (b) Double-scattering path and (c) triple-scattering path.

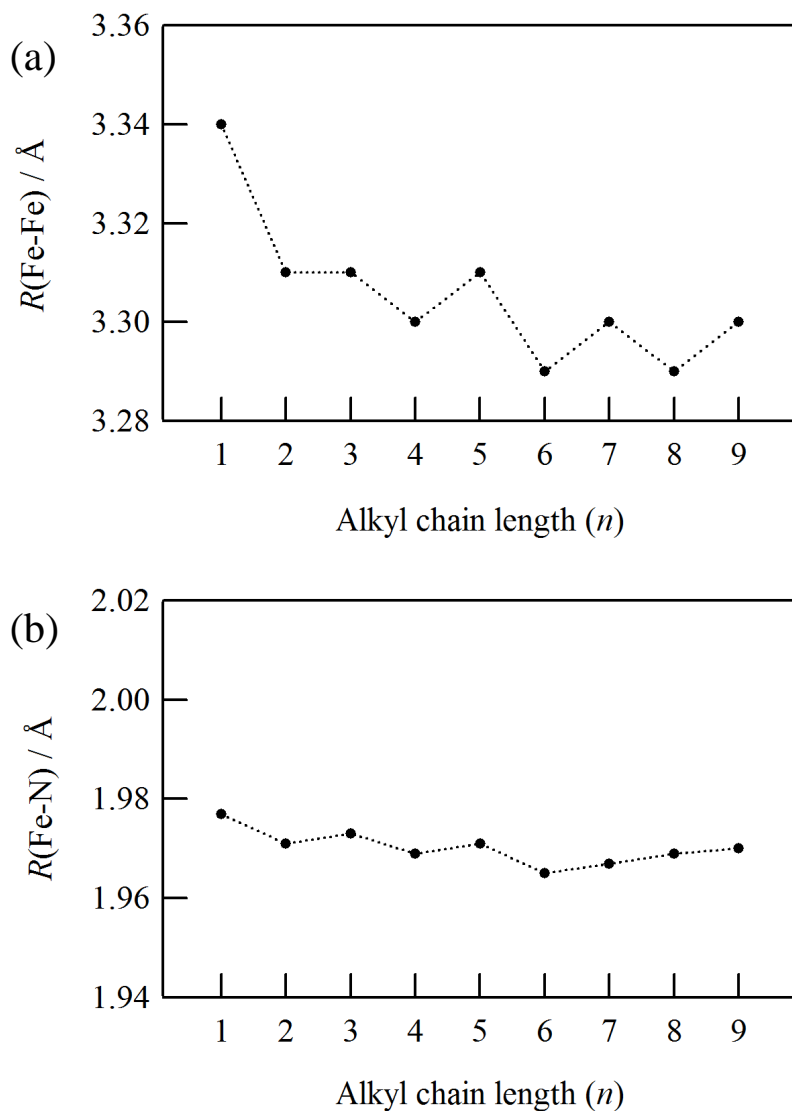


**Figure 5.5.** The nearest-neighbor (a) Fe-Fe and (b) Fe-N distances as a function of the alkyl chain length ( $n$ ) at 35 K.

### SCO Behavior of $[\text{Fe}^{\text{II}}(\text{NH}_2\text{-trz})_3](\text{C}_n\text{H}_{2n+1}\text{SO}_3)_2 \cdot x\text{H}_2\text{O}$

The powdered samples of  $[\text{Fe}^{\text{II}}(\text{NH}_2\text{-trz})_3](\text{C}_n\text{H}_{2n+1}\text{SO}_3)_2 \cdot x\text{H}_2\text{O}$  encapsulated in aluminium capsule were used for the magnetic susceptibility measurements to avoid the loss of crystal water molecules.

Figure 5.6 shows the temperature dependence of molar magnetic susceptibility ( $\chi_M$ ) data collected by using SQUID magnetometer (MPMS-5) in the temperature range of 240-320 K. In the compound

of  $n = 1$ , the  $\chi_M T$  value at 320 K was  $3.42 \text{ cm}^3 \text{ K mol}^{-1}$ , which is approximately equal to the theoretical value expected for the HS state of  $Fe^{II}$  ions. With decreasing temperature on the cooling process, the  $\chi_M T$  values gradually decreased ( $T_{1/2\downarrow} = 276 \text{ K}$ ) and reached the minimum value of  $0.21 \text{ cm}^3 \text{ K mol}^{-1}$ , corresponding to the diamagnetic LS state of  $Fe^{II}$  ions. Subsequently on the heating process, the  $\chi_M T$  values gradually increased ( $T_{1/2\uparrow} = 295 \text{ K}$ ), reaching the maximum value of  $3.41 \text{ cm}^3 \text{ K mol}^{-1}$ . The temperature dependence of  $\chi_M T$  values was reproduced in the second cooling and heating process with the hysteresis width ( $\Delta T_{1/2} = T_{1/2\uparrow} - T_{1/2\downarrow}$ ) of 19 K.

As can be seen in Figure 5.7(a),  $T_{1/2}$  increases in the cooling and heating processes with increasing the alkyl chain length accompanied by even-odd effect.  $T_{1/2}$  becomes higher with increasing  $n$  up to 4, however it remains almost constant for  $n > 5$ . In connection with this, there is a close relationship between  $T_{1/2}$  and the nearest-neighbor Fe-Fe distances ( $R(\text{Fe-Fe})$ ) estimated from the analysis of EXAFS at 35 K. The relationship between  $\Delta T_{1/2}$  and the alkyl chain length is depicted in Figure 5.7(b). An even-odd effect was also observed in the hysteresis width, namely the hysteresis width was slightly wider for even  $n$ , narrower for odd  $n$ .  $\Delta T_{1/2}$  became smaller with increasing the alkyl chain length and saturated over  $n = 5$ .

Figure 5.8(a) shows representative  $^{57}\text{Fe}$  Mössbauer spectra for  $n = 1$  on cooling and heating processes in the temperature range of 77-298 K. All the Mössbauer parameters are listed in Table 5.1. The spectrum at 298 K shows a single quadrupole doublet attributed to the HS state of  $Fe^{II}$  ions, whose Mössbauer parameters are  $IS = 1.028 \text{ mm s}^{-1}$  and  $QS = 2.877 \text{ mm s}^{-1}$  ( $IS$  = isomer shift,  $QS$  = quadrupole splitting). On cooling, a new quadrupole doublet appeared below 280 K, and its intensity was gradually increased with decreasing temperature. Eventually, the HS doublet disappeared at 77 K and only single LS doublet ( $IS = 0.503 \text{ mm s}^{-1}$  and  $QS = 0.245 \text{ mm s}^{-1}$ ) was observed. On heating, the relative intensity of the LS doublet gradually decreased but remained in population of 45.0% at 290 K, which is the evidence of hysteresis effect (Figure 5.8(b)). In this way,  $^{57}\text{Fe}$  Mössbauer

spectroscopy clearly observed the SCO behavior of  $[\text{Fe}^{\text{II}}(\text{NH}_2\text{-trz})_3](\text{C}_n\text{H}_{2n+1}\text{SO}_3)_2 \cdot x\text{H}_2\text{O}$ , which is consistent with the magnetic susceptibility measurements.

In the previous section, the result that the spin transition temperatures in both cooling and heating processes increase with increasing the alkyl chain length was provided. This is contrastive to the results for spherical anion,  $[\text{Fe}^{\text{II}}(\text{NH}_2\text{-trz})_3](\text{Anion})_2 \cdot x\text{H}_2\text{O}$  (Anion =  $\text{ClO}_4^-$ ,  $\Gamma^-$ ,  $\text{Br}^-$ ,  $\text{BF}_4^-$ ,  $\text{NO}_3^-$ ,  $\text{Cl}^-$ ),<sup>[18]</sup> in which the spin transition temperature decreases with increasing the radius of anion as mentioned above. Taking into account that the nearest-neighbor Fe-N distances in the title compounds do not depend on the alkyl chain length, the spin transition temperature is considered to be mainly affected by the nearest-neighbor Fe-Fe distances.  $\text{Fe}^{\text{II}}$  ions in 1D arrangement move on with counteranions due to their self-assembly interaction called “fastener effect” between alkyl chains induced by van der Waals force, leading to the shortening of the neighboring Fe-Fe distances. Consequently, the elevation of the elastic energy of  $[\text{Fe}^{\text{II}}(\text{NH}_2\text{-trz})_3]$  units would be induced. This situation is closely analogous to the effects of hydrostatic pressure on SCO systems.<sup>[37]</sup> Increase of external pressure leads to the narrowing of the hysteresis loop and the increase of  $T_{1/2}$ . Especially in the 1D-SCO system,  $T_{1/2}$  is dominated not only by long-range interaction but also by short-range interaction, *i.e.* the intrachain interaction, and it can be seen that the stability of the LS state and the narrowing of the hysteresis loop are enhanced by pressure when the short-range interaction substantially exceeds the long-range interaction.<sup>[38]</sup> This concept clearly points to the fact that  $T_{1/2}$  increases with increasing the alkyl chain length, which is in harmony with the close relationship between  $T_{1/2}$  and the  $R(\text{Fe-Fe})$  estimated from the analysis of EXAFS at 35 K as shown in Figure 5.7(a). Above  $n \geq 5$ , the saturation of  $T_{1/2} \sim 350$  K corresponds to the limit of fastener effect to shorten Fe-Fe distance. It is worthy of note that this is the first system systematically modifying Fe-Fe in triazole-bridged  $\text{Fe}^{\text{II}}$  SCO compounds, and there is a crucial difference between other systems investigating the counteranion dependences in the SCO behavior as described in references

[18-27] and the title compounds.

As for the hysteresis width, it became narrower with increasing the alkyl chain length, which is the same result for compounds with spherical counteranions. Anions are located among cationic  $\text{Fe}^{\text{II}}$  chains and behave as spacers. Accordingly, the increment of anion size leads to detach from neighboring cationic chains, and thereby interchain interactions, *i.e.* the cooperative effects, decrease. In the title compounds, the hysteresis width does not become zero even though the hysteresis width decreases with increasing the alkyl chain length. For the compounds of  $n \geq 5$  the hysteresis width is almost the same value,  $\Delta T_{1/2} = 6$  K, which is comparable with the value ( $\Delta T_{1/2} = 3$  K) of single  $[\text{Fe}^{\text{II}}(\text{NH}_2\text{-trz})_3]$  chain as oligomer.<sup>[39]</sup>

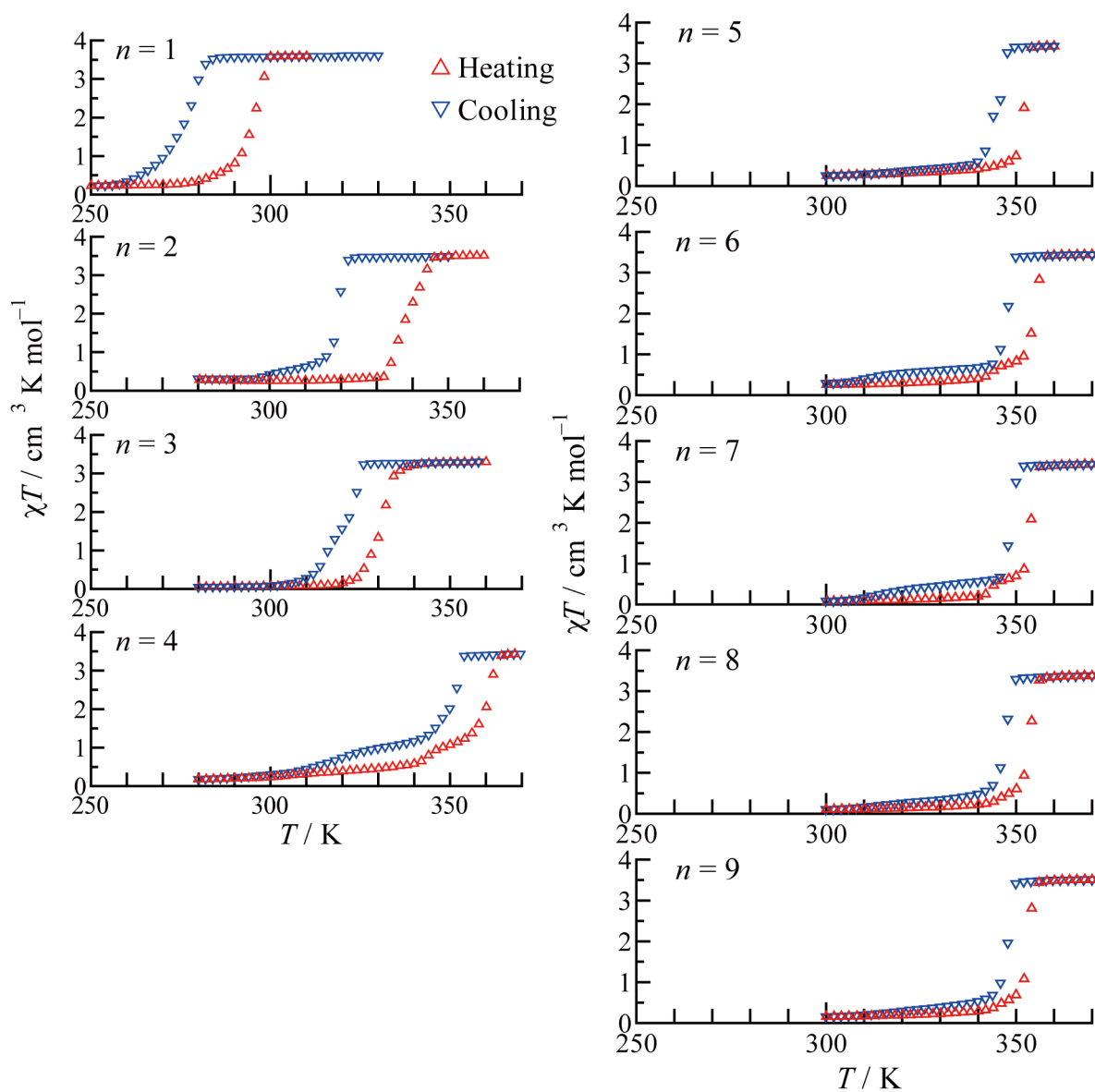


**Figure 5.6.** Temperature dependence of molar magnetic susceptibility multiplied by temperature ( $\chi T$ ) for  $[\text{Fe}^{\text{II}}(\text{NH}_2\text{-trz})_3](\text{C}_n\text{H}_{2n+1}\text{SO}_3)_2 \cdot x\text{H}_2\text{O}$ .

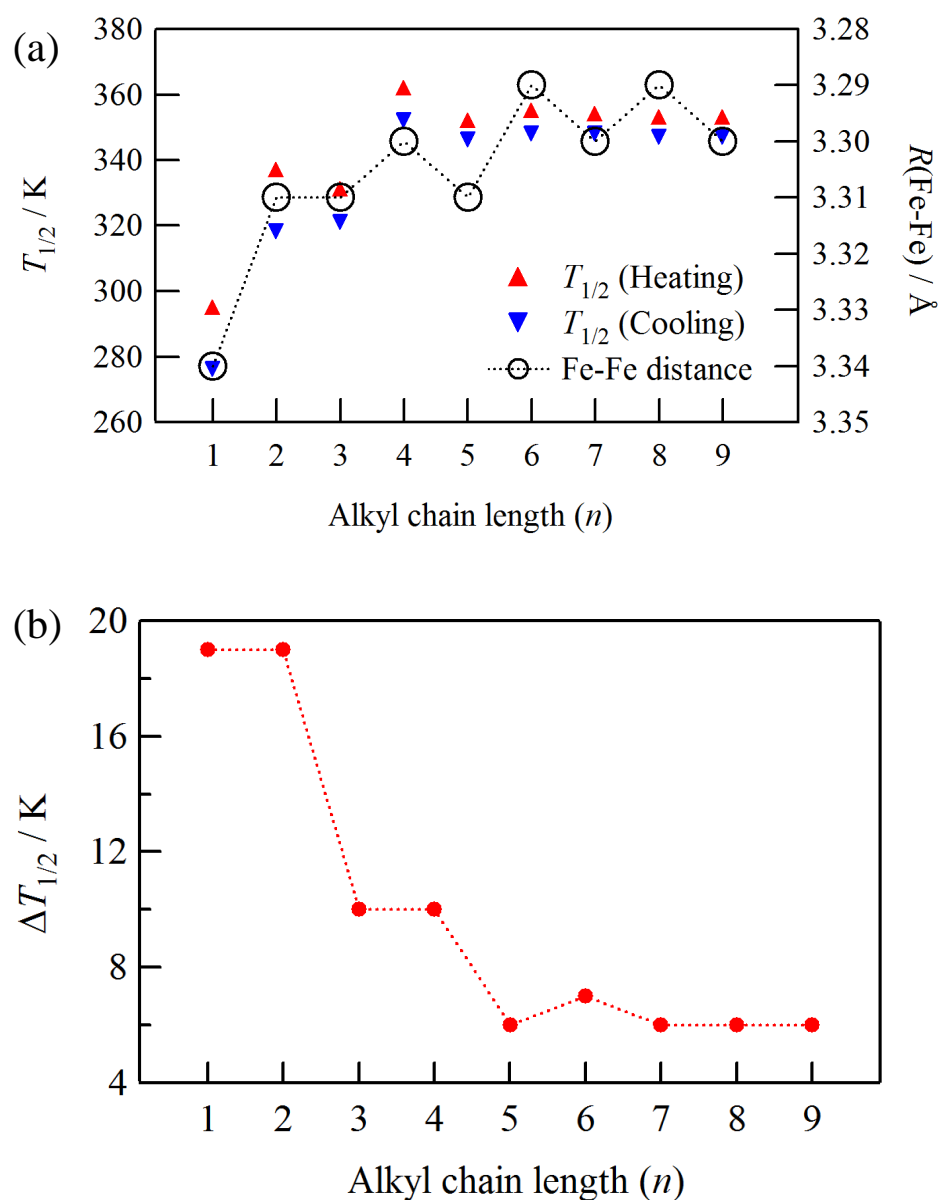


**Figure 5.7.** (a) Correlation between  $T_{1/2}$  and Fe-Fe distance ( $R(\text{Fe-Fe})$ ) at 35 K, (b)  $\Delta T_{1/2}$  as a function of alkyl chain length ( $n$ ).

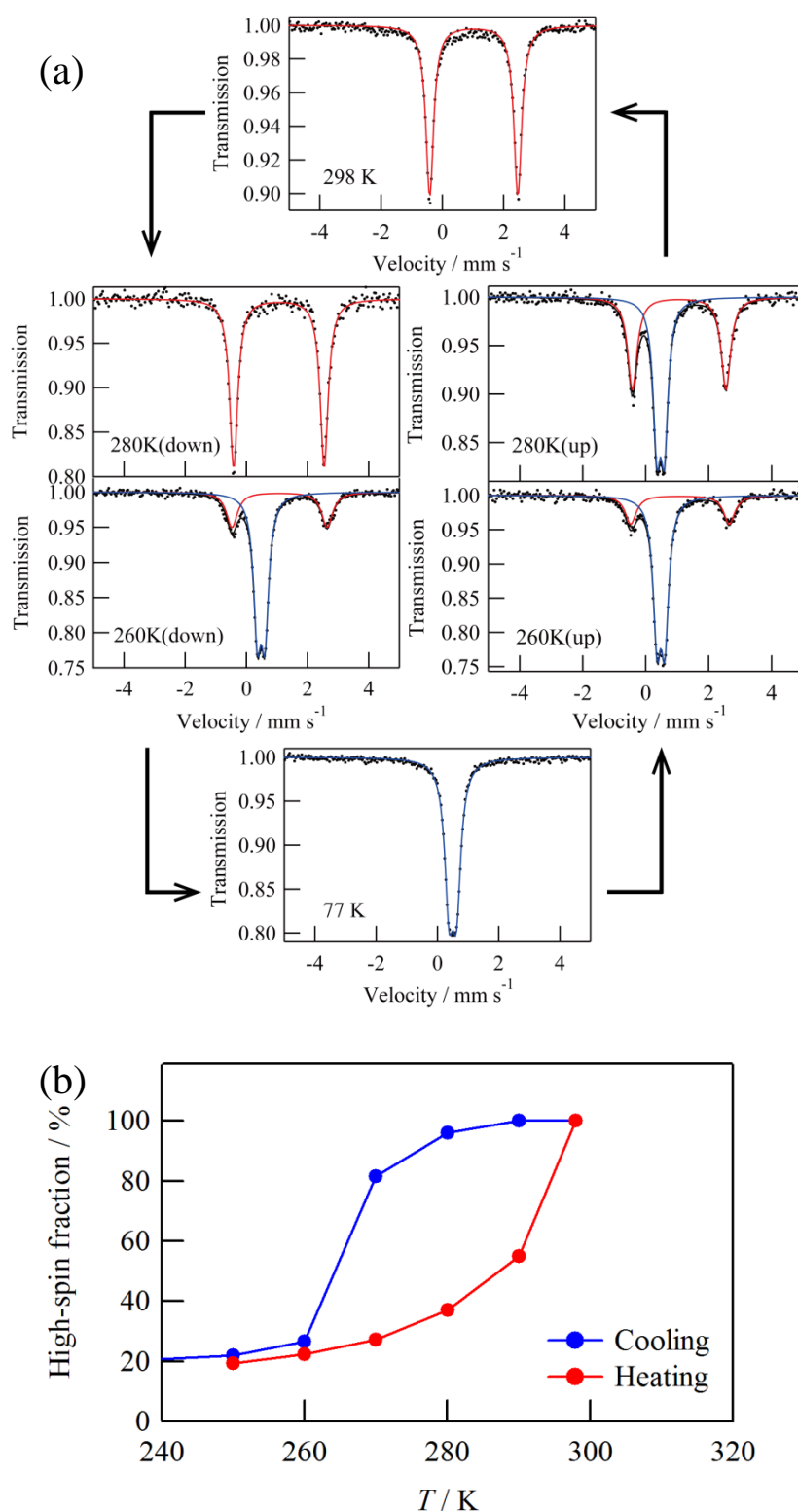


**Figure 5.8.** (a) Temperature dependence of  $^{57}\text{Fe}$  Mössbauer spectra for  $[\text{Fe}^{\text{II}}(\text{NH}_2\text{-trz})_3](\text{CH}_3\text{SO}_3)_2 \cdot \text{H}_2\text{O}$ . Red and blue lines correspond to the doublets for the HS and LS state of  $\text{Fe}^{\text{II}}$  ions, respectively. (b) Temperature dependence of the HS fraction (%) for  $n = 1$ .

**Table 5.1.** Temperature dependence of  $^{57}\text{Fe}$  Mössbauer parameters for  $[\text{Fe}^{\text{II}}(\text{NH}_2\text{-trz})_3](\text{CH}_3\text{SO}_3)_2 \cdot \text{H}_2\text{O}$ .

$T$ (K)	$IS / \text{mm s}^{-1}$		$QS / \text{mm s}^{-1}$		$\Gamma / \text{mm s}^{-1}$		Area / %	
	HS	LS	HS	LS	HS	LS	HS	LS
298↓	1.028	-	2.877	-	0.308	-	100	0
290↓	1.034	-	2.892	-	0.357	-	100	0
280↓	1.038	0.465	2.926	0.240*	0.356	0.333*	96	4
270↓	1.026	0.44	2.961	0.242	0.382	0.333*	81.6	18.4
260↓	1.044	0.445	2.959	0.233	0.457	0.333	26.5	73.5
250↓	1.039	0.453	2.907	0.243	0.681	0.319	22	78
77	-	0.503	-	0.245	-	0.338	0	100
250↑	1.036	0.454	2.946	0.242	0.641	0.323	19.3	80.7
260↑	1.032	0.447	2.953	0.237	0.513	0.34	22.4	77.6
270↑	1.038	0.442	2.928	0.235	0.458	0.333	27.2	72.8
280↑	1.037	0.438	2.903	0.229	0.41	0.345	37	63
290↑	1.013	0.412	2.882	0.221	0.407	0.375	55	45
298↑	1.027	-	2.863	-	0.386	-	100	0

$IS$  = isomer shift,  $QS$  = nuclear quadrupole splitting,  $\Gamma$  = line width, \* = fixed values

## 5.3 Materials and Methods

### Synthesis

The compounds  $[\text{Fe}^{\text{II}}(\text{NH}_2\text{-trz})_3](\text{C}_n\text{H}_{2n+1}\text{SO}_3)_2 \cdot x\text{H}_2\text{O}$  were obtained according to the previous literature procedure.<sup>[20b]</sup>

### Fe K-Edge XAFS Spectroscopy

Fe K-edge XAFS spectra were measured in the conventional transmission mode at BL-10B in Photon Factory (operation energy of 2.5 GeV and stored current of 400-200 mA) in High Energy Accelerator Research organization in Tsukuba, Japan. A water-cooled Si(311) channel-cut crystal was employed as a monochromator. The intensities of the incident and transmitted X-ray were recorded using ionization chambers filled with pure  $\text{N}_2$ . Although the absolute photon energy was not calibrated, the relative photon energies never changed during the measurements within the employed energy step (0.2 eV), judging from several glitches appearing in the  $I_0$  function. The sample was diluted with BN to give a pellet for XAFS measurements. In order to avoid the desorption of crystal water in vacuum, the pellet was completely sealed with an adhesive substrate (STYCAST 1266). The Fe K-edge jump was found to be  $\sim 0.1$ , while the total absorption coefficient was estimated to be less than 4.0, most of which originated from BN and the adhesive substrate. It is established that the effect of higher harmonics can be neglected under these conditions when pure  $\text{N}_2$  is employed as a detection gas for both the ionization chambers. The measurement temperature range was 30-373 K. For the low-temperature measurements, a closed-cycle He refrigerator was used and the temperature was measured with a Si diode placed close to the sample. For higher-temperature measurements ( $>296$  K), a furnace was used, where a Chromel-Alumel thermocouple was inserted for the temperature measurement.

### **$^{57}Fe$ Mössbauer Spectroscopy**

For  $^{57}Fe$  Mössbauer spectroscopic measurement,  $^{57}Co$  in Rh matrix was used as a Mössbauer source. The pellet was completely sealed with STYCAST 1266 as mentioned above. The spectra were calibrated by using the six lines of a body-centered cubic iron foil ( $\alpha$ -Fe), the center of which was taken as zero isomer shift. An Iwatani Co. cryogenic refrigerator set, Cryomini and MiniStat was used in the temperature range between 10 K and 300 K. The spectra were fitted with a MossWinn 3.0 program.<sup>[40]</sup>

## 5.4 Results and Discussion

### Pre-Edge Peaks in XANES Spectra

Figure 5.9 shows the Fe K-edge XANES spectra of the HS and LS states, respectively. Spectral features are clearly different between the LS and HS states, but quite similar among nine compounds ( $n = 1-9$ ). In particular, these compounds have a weak fine structure below the absorption edge. In the Fe K-edge XANES spectra of the title compounds, pre-edge peaks corresponding to the  $1s \rightarrow 3d$  transition and a charge transfer peak from the metal  $1s$  to the ligand  $\pi^*$  can be observed. An expanded view of the pre-edge region of the HS state and the LS state for  $[\text{Fe}^{\text{II}}(\text{NH}_2\text{-trz})_3](\text{CH}_3\text{SO}_3)_2 \cdot \text{H}_2\text{O}$  is shown in Figure 5.10.

The electron excitation from the  $1s$  orbital to the  $3d$  orbital gives  $d^{n+1}$  (in this case:  $3d^7$ ) electronic configuration. In the LS state, the two peaks in the pre-edge region were observed as shown in Figure 5.10(a). The  $1s \rightarrow 3d$  transition gives rise to the electron configuration  $(t_{2g})^6(e_g)^1$ , which gives the  ${}^2E_g$  state (Scheme 5.2). The lowest excited state around 7112 eV is assigned to the  ${}^2E_g$  state. The second excited state around 7116 eV, which cannot be explained by the  $1s \rightarrow 3d$  transition, but can be assigned to a charge transfer transition from the metal  $1s$  orbital to the ligand  $\pi^*$  orbital (metal-to-ligand charge transfer: MLCT). The  $\text{NH}_2\text{-trz}$  ligand has a vacant orbital with  $\pi$  symmetry which interacts with filled metal  $t_{2g}$  orbital, providing a bonding- ( $t_{2g}'$ ) and an antibonding orbital ( $t_{2g}'^*$ ). As a result, the ligand field  $10Dq$  ( $\Delta E_{e_g-t_{2g}'}$ ) increases and the  $1s \rightarrow t_{2g}'^*$  transition would be measurable (Scheme 5.3). As an example, a SCO compound,  $[\text{Zn}^{\text{II}}_{1-z}\text{Fe}^{\text{II}}_z(2\text{-pic})_3]\text{Cl}_2 \cdot \text{EtOH}$  (2-pic = 2-picolylamine), in the LS state shows an intense absorption band around 480 nm which is assigned to the MLCT band.<sup>[41]</sup> It almost disappears, and an absorption band corresponding to  ${}^5T_{2g} \rightarrow {}^5E_g$  transition newly appears around  $12000 \text{ cm}^{-1}$  after the LS  $\rightarrow$  HS conversion by thermal- or photo perturbations. In this way, the spin state can be determined by optical absorption spectra based

on the MLCT band which originates from the stronger overlap between metal and ligand orbitals in the LS state than that in the HS state. However, the analysis of pre-edge region based on the ligand field theory cannot be performed because the LS state has one single peak corresponding to the  $1s \rightarrow 3d$  transition.

In the HS state, the three weak peaks around 7112, 7113, and 7114.5 eV in the pre-edge region can be fitted by the ligand field theory. In the HS state, the  $1s \rightarrow 3d$  transition gives rise to the electron configuration  $(t_{2g})^5(e_g)^2$  and  $(t_{2g})^4(e_g)^3$  (Scheme 5.4). According to the ligand field theory,  $(t_{2g})^5(e_g)^2$  configuration gives  ${}^4\text{T}_{1g}(1)$  and  ${}^4\text{T}_{2g}$  states and  $(t_{2g})^4(e_g)^3$  configuration gives  ${}^4\text{T}_{1g}(2)$  state, from which the pre-edge feature in the HS state requires a three-peak fit. A fit to the pre-edge region of the HS state for  $[\text{Fe}^{\text{II}}(\text{NH}_2\text{-trz})_3](\text{CH}_3\text{SO}_3)_2 \cdot \text{H}_2\text{O}$  is shown in Figure 5.10(b). The relative energy differences on  ${}^4\text{T}_{1g}(1) - {}^4\text{T}_{2g}$  and  ${}^4\text{T}_{2g} - {}^4\text{T}_{1g}(2)$  can be calculated by the central positions of the pre-edge peaks. Based on this deconvolution of fine structure, the energy of the  ${}^4\text{T}_{1g}(1)$ ,  ${}^4\text{T}_{2g}$ , and  ${}^4\text{T}_{1g}(2)$  states can be expressed using only  $10Dq$  and  $B$  by solving the  $3d^7$  Tanabe-Sugano matrices.<sup>[42]</sup> Therefore, the ligand field analysis in XANES pre-edge region can be performed for the HS state. From the  $d^7$  Tanabe-Sugano matrices, the  ${}^4\text{T}_{1g}$  term is given as follows:

$$\begin{array}{cc} |t_{2g}^4 e_g^3\rangle & |t_{2g}^5 e_g^2\rangle \\ \left| \begin{array}{cc} -3B - 2Dq & 6B \\ 6B & -12B + 8Dq \end{array} \right| & (5.1) \end{array}$$

Note that common diagonal component  $21A - 28B + 14C$  is omitted because it does not affect the eigen vector. The eigen equation can be expressed as

$$\varepsilon^2 + (15B - 6Dq)\varepsilon - 16Dq^2 = 0, \quad (5.2)$$

hence, the eigen value is obtained as

$$\varepsilon = \frac{-(15B - 6Dq) \pm \{(15B - 6Dq)^2 + 64Dq^2\}^{1/2}}{2} \quad (5.3)$$

with  $B$  and  $Dq > 0$ . In addition, the energy of the  ${}^4\text{T}_{2g}$  term derived from  ${}^4\text{F}$  is  $-2Dq-15B$ . Therefore, the energy splitting is schematically illustrated as Scheme 5.5, where  $\varepsilon_1$  and  $\varepsilon_2$  are the eigen values ( $\varepsilon_2 > \varepsilon_1$ ).

In the same way described above, the other pre-edge structure of XANES spectra for  $[\text{Fe}^{\text{II}}(\text{NH}_2\text{-trz})_3](\text{C}_n\text{H}_{2n+1}\text{SO}_3)_2 \cdot x\text{H}_2\text{O}$  ( $n = 2-9$ ) is analyzed by ligand field theory. Figure 5.11 shows the energy levels for  ${}^4\text{T}_{1g}(1)$ ,  ${}^4\text{T}_{2g}$  and  ${}^4\text{T}_{1g}(2)$  for  $[\text{Fe}^{\text{II}}(\text{NH}_2\text{-trz})_3](\text{C}_n\text{H}_{2n+1}\text{SO}_3)_2 \cdot x\text{H}_2\text{O}$  in the HS states.

Figure 5.12 (red squares) shows the alkyl chain length ( $n$ ) dependence of Racah parameter  $B$ . It has a tendency to decrease with increasing  $n$ , in which  $B$  was saturated over  $n = 5$ . The decrease of  $B$  is highly indicative of a decrease of Coulomb repulsion among 3d electrons on  $\text{Fe}^{\text{II}}$  ions. It is well known that the value of  $B$  in a ligand field is smaller than the one in free ion state. This fact indicates that complexation makes lower the Coulomb repulsion among d electrons of the central metal ions due to a p-d mixing. C. K. Jørgensen defined this effect as “nephelauxetic effect”.<sup>[43]</sup> In the title compounds, the decrease of  $B$  is suggestive of an expansion of the 3d electrons on central  $\text{Fe}^{\text{II}}$  ions to the ligand  $\pi^*$  orbitals. Such a concept shows a close affinity to a high-pressure chemistry of electronic transitions in crystals. Parameters strongly depending on interatomic distances, *e.g.* mixing of electrons and band width, can be efficiently varied due to a shrink of crystal lattice induced by pressurizing. Particularly, in transition metal compounds referred to as strongly correlated electron system, physical properties depend on delicate balancing of strong interelectronic

interactions and band widths in a large number of cases. Therefore, pressurizing is an effectual manner to control structures and to explore new properties. In the viewpoint of ligand field, Racah parameters also depend on pressure. For examples, ruby ( $Cr^{III}$  ion in  $Al_2O_3$ )<sup>[44]</sup> and  $MnX_2$  ( $Mn^{II}$  ion;  $X = Cl, Br$ )<sup>[45]</sup> show significant decreases of  $B$  and  $C$  with pressure. As the crystal lattice shrinks, the 3d orbital expands due to a reduction of the effective nuclear charge originating from the overlap of the electron cloud on a metal with the electron pair of a ligand. This effect will affect the covalency of coordination bonds around metal ions. The covalency increases the expansion of d orbitals and decreases the repulsion. Now, let us take the following equation related to the covalency and the nephelauxetic effect in the title compounds:<sup>[46]</sup>

$$B/B_0 = (1 - k)h \quad (5.4)$$

where  $B$  and  $B_0$  are Racah parameters of free ions (for  $Fe^{II}$ :  $B = 1058 \text{ cm}^{-1}$ ) and the ions in crystals, respectively. And,  $k$  represents the effect of central metal ions expressed as

$$k = [(Z + 2 - S)/5]^2, \quad (5.5)$$

where  $Z$  is the valence of the ion,  $S$  is the spin. The chemical environmental factor,  $h$ , is defined as follows:

$$h = (\sum \alpha_L^v f_c^v)^{1/2} \quad (5.6)$$

where  $\alpha_L^v$  is the polarizability of the ligand bond and  $f_c^v$  is the covalency in the  $v$ th bond. Based on the above equations, changes in the covalency can be estimated for

$[\text{Fe}^{\text{II}}(\text{NH}_2\text{-trz})_3](\text{C}_n\text{H}_{2n+1}\text{SO}_3)_2 \cdot x\text{H}_2\text{O}$  in the HS state as shown in Figure 5.13. The covalency in the coordination bonds on  $\text{Fe}^{\text{II}}$  ion, that is to say the delocalization of 3d electrons, increases with increasing the alkyl chain length. Besides, we should consider the  $d\pi\text{-}p\pi$  backbonding to the vacant  $\pi^*$  orbitals of the ligand  $\text{NH}_2\text{-trz}$ . This is also an important contribution to the 3d electron delocalization and to the increase of ligand field,  $10Dq$ . The  $\pi^*$  orbital has the appropriate symmetry to interact with the metal  $d\pi$  ( $t_{2g}$ ) orbitals. The  $\text{Fe}^{\text{II}}$  ions will donate electrons into the  $\pi^*$  orbital, and then  $t_{2g}$  orbital will be stabilized. Therefore, Figure 5.12 is also highly suggestive of the increase of the  $d\pi\text{-}p\pi$  backdonation effect with increasing the length of alkyl tails,  $n$ . Consequently, the fact that the Racah parameter  $B$  decreases and the ligand field strength increases as can be seen in the Figures 5.12 and 5.14 with increasing  $n$  can be naturally understood. The ligand field strength parameter  $10Dq$  has an increasing tendency with increasing  $n$ , indicating the interactions between the alkyl chains affect the  $10Dq$ . Likewise,  $10Dq/B$  and  $T_{1/2}$  versus  $n$  are closely linked with each other as can be seen in Figure 5.15, where it has an increasing tendency with increasing  $n$  as well as  $T_{1/2}$ . As mentioned above,  $10Dq/B$  is the dominating parameter on  $T_{1/2}$ . In the title compounds, the remarkable decrease of  $B$  stabilizes the LS state and makes larger the difference in energy between the HS and the LS states, leading to the increase of  $T_{1/2}$ .

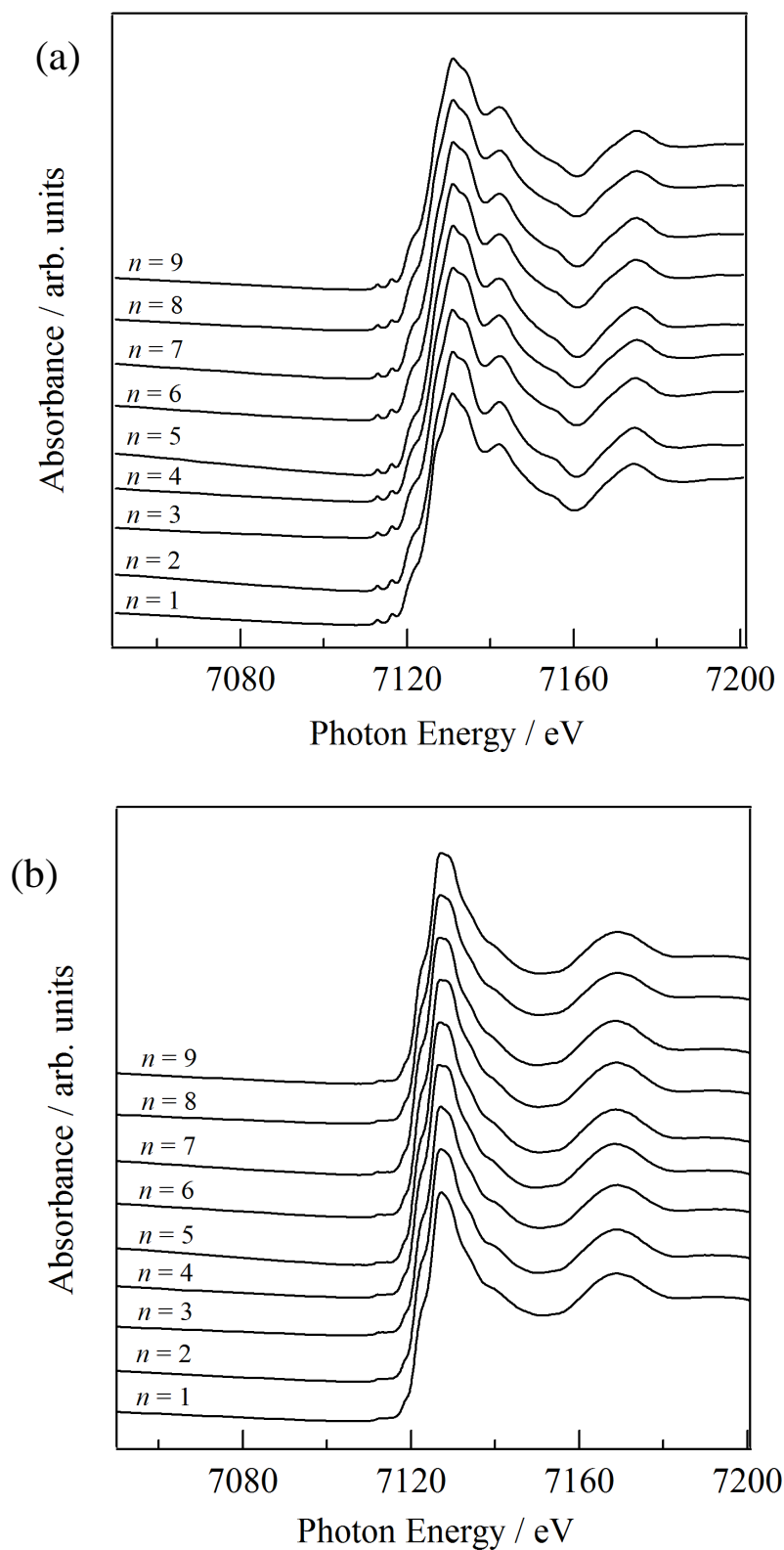


**Figure 5.9.** XANES spectra for  $[\text{Fe}^{\text{II}}(\text{NH}_2\text{-trz})_3](\text{C}_n\text{H}_{2n+1}\text{SO}_3)_2 \cdot x\text{H}_2\text{O}$  in the (a) LS (35 K) and (b) HS (370 K) states.

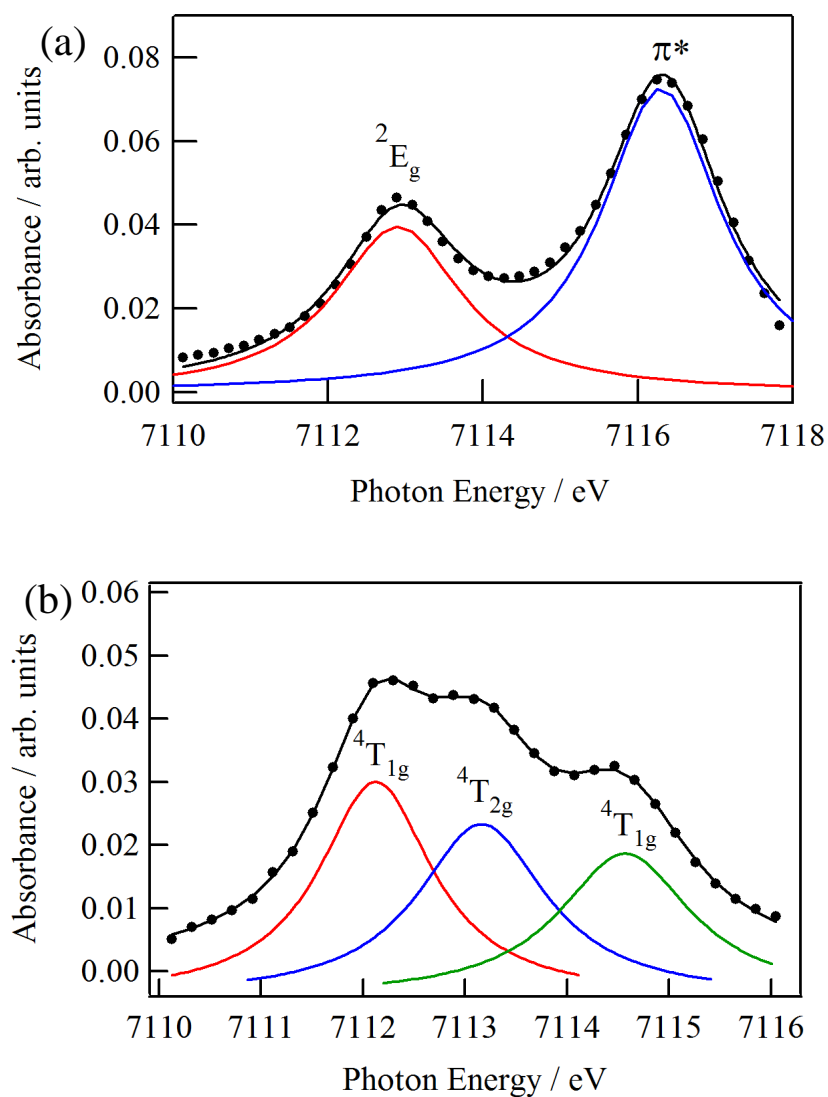
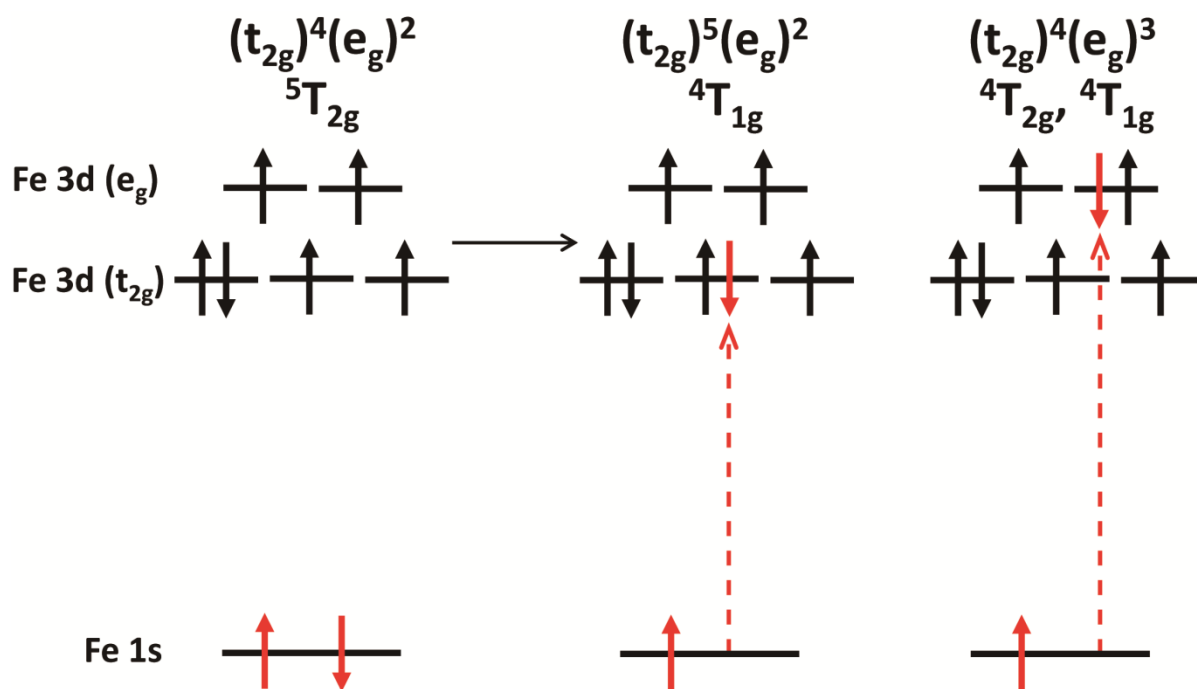
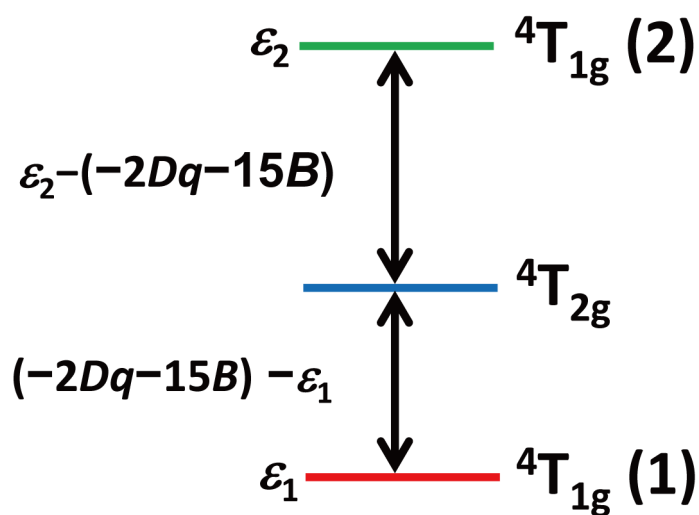


**Figure 5.10.** The expanded view of the XANES pre-edge region for  $[\text{Fe}^{\text{II}}(\text{NH}_2\text{-trz})_3](\text{CH}_3\text{SO}_3)_2 \cdot \text{H}_2\text{O}$  ( $n = 1$ ) in the (a) LS (35 K) and (b) HS (370 K) states.





**Scheme 5.4.** The electron configurations of  $\text{Fe}^{\text{II}}$  induced by the  $1s \rightarrow 3d$  transition in the HS state.



**Scheme 5.5.** The energy splitting of  $4T_{1g}(1)$ ,  $4T_{2g}$ , and  $4T_{1g}(2)$  states.

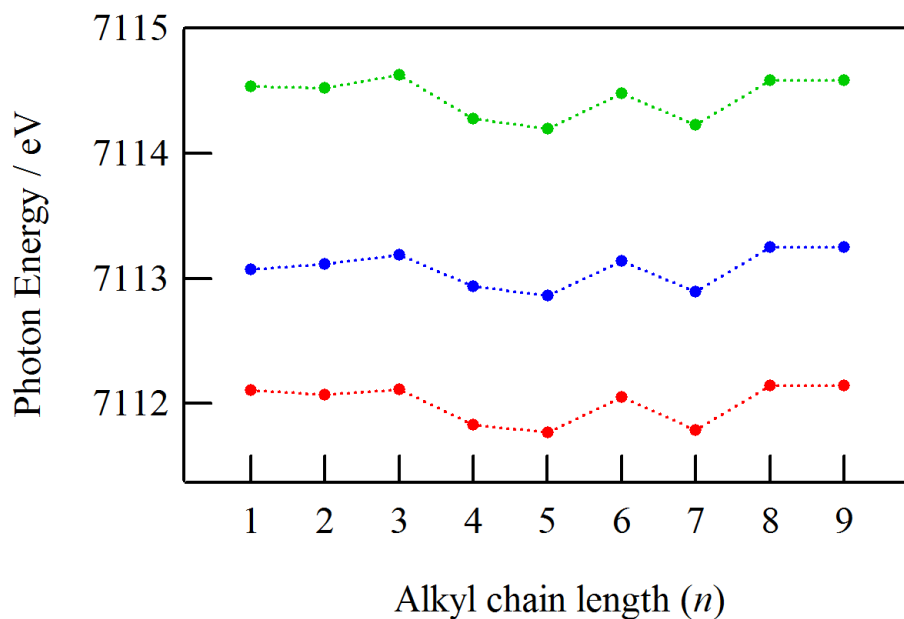


**Figure 5.11.** The energy levels of  ${}^4\text{T}_{1g}(1)$ ,  ${}^4\text{T}_{2g}$  and  ${}^4\text{T}_{1g}(2)$  for  $[\text{Fe}^{\text{II}}(\text{NH}_2\text{-trz})_3](\text{C}_n\text{H}_{2n+1}\text{SO}_3)_2 \cdot x\text{H}_2\text{O}$  in the HS states.

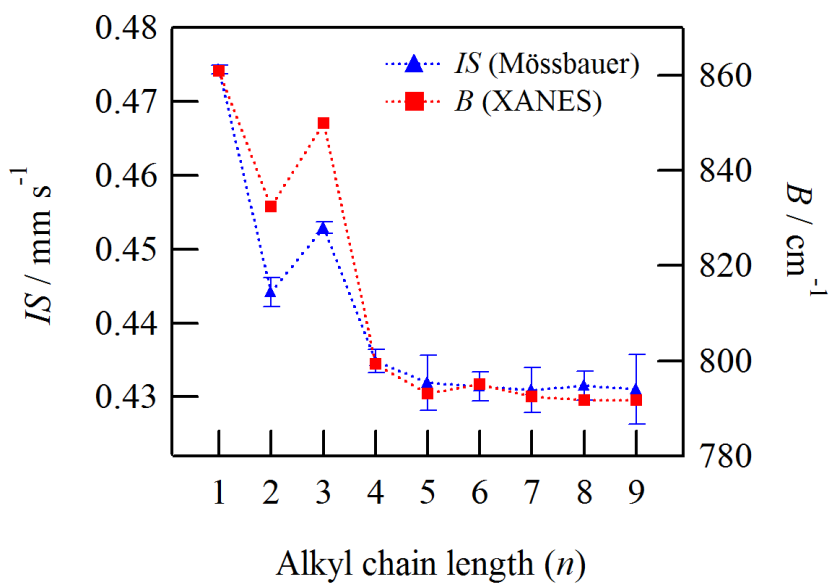


**Figure 5.12.** The correlation between Mössbauer isomer shifts ( $IS$ ) at 200 K and Racah parameter ( $B$ ) at 370 K as a function of alkyl chain length ( $n$ ).

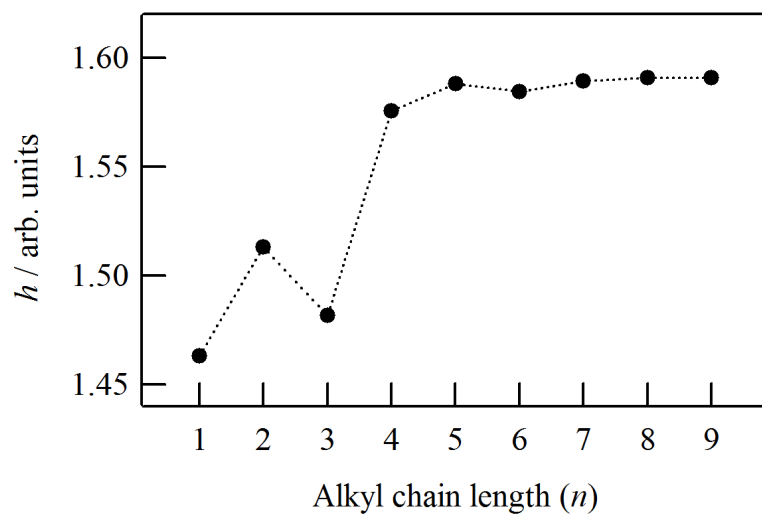


**Figure 5.13.** The alkyl chain length dependence of the chemical environmental factor,  $h$ , which is proportional to the covalency of the bonds,  $f_c$ .

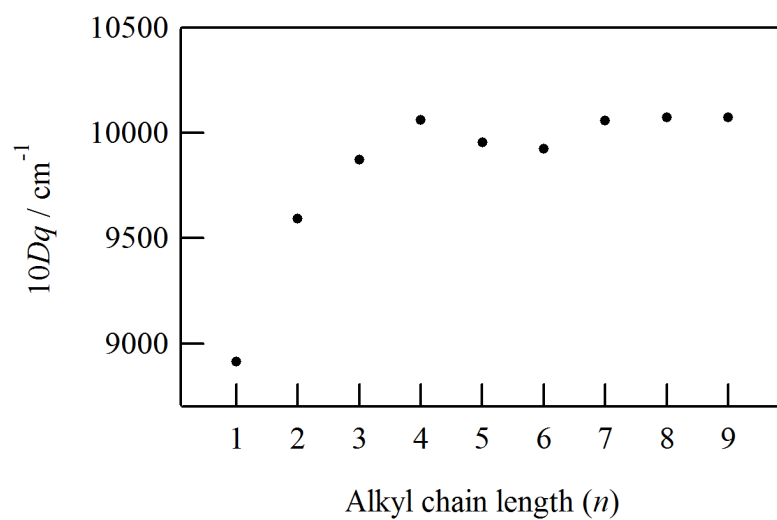


**Figure 5.14.** The alkyl chain length dependence of ligand field,  $10Dq$ .

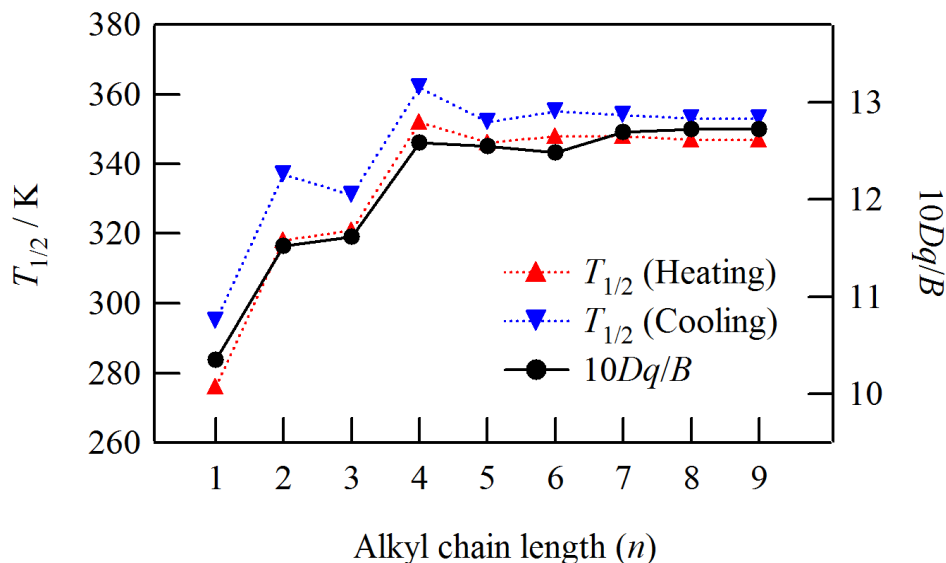


**Figure 5.15.** The correlation between  $10Dq/B$  at 370 K and spin transition temperature ( $T_{1/2}$ ) as a function of alkyl chain length ( $n$ ).

### $^{57}\text{Fe}$ Mössbauer spectroscopy

The relationship between  $T_{1/2}$  and the Racah parameter  $B$  described above can be discussed from the viewpoint of  $^{57}\text{Fe}$  Mössbauer spectroscopy. It is the most powerful tool for iron SCO materials due to clear and direct detections of the electronic states in central iron ions.<sup>[47]</sup> Figure 5.12 (blue triangles) shows the alkyl chain length dependence of Mössbauer isomer shift ( $IS$ ).  $IS$  values are very informative on oxidation states, spin states, and the degree of covalency.  $IS$  can be generally expressed as Eq. (5.7):

$$IS = 4/5 \pi Z S(Z) e_0^2 R^2 (\Delta R/R) \{ |\psi(0)|_A^2 - |\psi(0)|_S^2 \} \quad (5.7)$$

Here,  $Z$  is the nuclear charge of the absorber,  $S(Z)$  is a relativistic correction factor,  $e_0$  is the elementary charge,  $R$  is nuclear radius of the iron atom,  $\Delta R$  is nuclear radius difference between

ground and excited states ( $R_e - R_g$ ),  $|\psi(0)|_A^2$  and  $|\psi(0)|_S^2$  are electron densities on nucleus of absorber and  $\gamma$ -ray source ( $^{57}\text{Co}$  in Rh matrix), respectively. Since the source properties can be replaced by constant (C), it is sufficient for us to consider the following simplified equation:

$$IS = \text{const.} (\Delta R/R) \{ |\psi(0)|_A^2 - C \} \quad (5.8)$$

The 1s and 2s electrons provide electron densities at the nucleus and do not depend on the chemical state. Meanwhile, the 3s electrons are shielded by 3d electrons due to a comparable radial maximum between them. Consequently,  $IS$  of the metal is affected by the filling and the radial extent of the 3d orbitals (*i.e.* spreading of the 3d orbitals). In most Mössbauer nuclear species,  $IS$  increases with decreasing 3d electron density due to an increase of s-electron density at a nuclear in the shielding of iron because of  $\Delta R > 0$ . However, in the case of  $^{57}\text{Fe}$ ,  $IS$  decreases with increasing s-electron density due to  $\Delta R < 0$ . As can be seen in Figure 5.12,  $IS$  of  $[\text{Fe}^{\text{II}}(\text{NH}_2\text{-trz})_3](\text{C}_n\text{H}_{2n+1}\text{SO}_3)_2 \cdot x\text{H}_2\text{O}$  in the LS state at 200 K has a tendency to decrease with increasing  $n$ . A close resemblance can be seen in many ionic compounds<sup>[48]</sup> and SCO materials under high pressure.<sup>[49]</sup> For ionic compounds of  $\text{Fe}^{\text{II}}$  and  $\text{Fe}^{\text{III}}$  as described in ref.[48], the pressure acts to reduce the 3d shielding and increase the delocalization as discussed in the previous section. In the SCO compound  $[\text{Fe}^{\text{II}}(\text{phen})_2(\text{NCS})_2]$  (phen = 1,10-phenanthroline),  $IS$  decreases with pressure over 2 GPa. The decrease of  $IS$  at high pressure is certainly associated with the reduction of 3d shielding, the spreading of the 3d orbital, and the back bonding of the 3d orbital into the  $\pi^*$  orbitals of the ligands. Concerning the above discussions, reducing  $IS$  in Figure 5.12 is suggestive of an expansion of 3d orbital induced by uniaxial chemical pressure effect. Therefore, 3d electron will delocalize through the  $d\pi$  back donation to the vacant ligand  $\pi^*$  orbitals, leading to the decrease of repulsion. In general, a ligand with high  $\pi$  acceptability would withdraw electrons from d orbital to low-lying  $\pi^*$  orbital, causing a reduction in the shielding

of the s-electrons of the iron and the decrease in  $IS$ . Through the hybridization of the  $t_{2g}$  orbital and the  $\pi^*$  orbital, the ligand field splitting  $10Dq$  increases, leading to the increment of spin transition temperature. This is the most important contribution to the ligand field parameters and  $T_{1/2}$ .

## 5.5 Conclusion

In this chapter, the magnetostructural correlation for 1D SCO system,  $[\text{Fe}^{\text{II}}(\text{NH}_2\text{-trz})_3](\text{C}_n\text{H}_{2n+1}\text{SO}_3)_2 \cdot x\text{H}_2\text{O}$ , was investigated.  $R(\text{Fe-Fe})$  estimated from EXAFS decreased with increasing  $n$ , which is highly suggestive of the increase of intra-chain interaction with the alkyl chain length being attributed to the effect on the uniaxial chemical pressure along  $\text{Fe}^{\text{II}}$  chain axis induced by self-assembly interaction between alkyl chains, so-called “fastener effect”. At the same time,  $T_{1/2}$  increased with increasing  $n$ . To elucidate such a closely-linked magnetostructural correlation, detailed analysis of pre-edge structure of XANES spectra based on ligand field theory was also performed. Racah parameter ( $B$ ) and Mössbauer isomer shift ( $IS$ ) decrease with increasing  $n$ , which are also closely consistent with the behavior of  $T_{1/2}$ . In the title compounds, the uniaxial chemical pressure due to the fastener effect of alkanesulfonates induces the changes in the coordination bond angle, subsequently the covalency would be increased. In fact, the overlap the metal 3d orbital with the ligand 2p orbital reduces the shielding effect on 3s orbital and enhances the expansion of the metal 3d orbital. The spread 3d electrons are donated into the vacant  $\pi^*$  orbital through the  $d\pi\text{-}p\pi$  back bonding. This delocalization is a crucial contribution to the reduction of  $B$  and  $IS$  and to the increase of  $10Dq$ . As mentioned in the general introduction (Chapter 1), reducing  $B$  and increasing  $10Dq$  stabilize the LS state. Thus, the required thermal energy on the SCO transition becomes higher. It necessarily follows that  $10Dq/B$  is the key factor determining  $T_{1/2}$  of SCO compounds.

In this way, X-ray absorption spectroscopy can be used to determine the magnitude of the ligand field parameter ( $10Dq$ ) and the Racah parameter ( $B$ ). Applying the methodology in future studies would give better insights into the mechanism of physical properties in various transition metal compounds.

This work provides a new way of controlling spin transition temperatures. The “fastener effect” between alkyl chains is able to apply chemical pressure along the 1D  $\text{Fe}^{\text{II}}$  chains without any changes in Fe-N coordination bond lengths. At the present time, this is the first system directly modifying Fe-Fe distance in 1D SCO system through the uniaxial chemical pressure effect.

## References

- [1] *Multifunctional Molecular Materials*, ed. by L. Ouahab, Pan Stanford Publishing, Singapore, **2013**, and related references therein.
- [2] a) A. Bousseksou, G. Molnár, G. Matouzenko, *Eur. J. Inorg. Chem.* **2004**, 2004, 4353; b) O. Sato, J. Tao, Y.-Z. Zhang, *Angew. Chem. Int. Ed.* **2007**, 46, 2152; c) K. S. Murray, *Eur. J. Inorg. Chem.* **2008**, 2008, 3101; d) P. Gülich, *Eur. J. Inorg. Chem.* **2013**, 2013 (Cluster Issue), 581; e) *Spin Crossover in Transition Metal Compounds I–III*, ed. by P. Gülich, H. A. Goodwin, Springer-Verlag, Berlin, Heidelberg, New York, **2004**; f) *Spin-Crossover Materials: Properties and Applications*, ed. by M. A. Halcrow, Wiley-VCH, Chichester, **2013**.
- [3] for  $\text{Fe}^{\text{II}}$  spin crossover complexes, see a) E. König, G. Ritter, S. K. Kulshreshtha, *Chem. Rev.* **1985**, 85, 219; b) P. Gülich, A. Hauser, H. Spiering, *Angew. Chem. Int. Ed. Engl.* **1994**, 33, 2024; c) P. Gülich, Y. Garcia, H. A. Goodwin, *Chem. Soc. Rev.* **2000**, 29, 419; d) P. Gülich, A. B. Gaspar, Y. Garcia, *Beilstein J. Org. Chem.* **2013**, 9, 342.
- [4] for  $\text{Fe}^{\text{III}}$  spin crossover complexes, see M. Nihei, T. Shiga, Y. Maeda, H. Oshio, *Coord. Chem. Rev.* **2007**, 251, 2060.
- [5] a) I. Krivokapic, M. Zerara, M. Lawson Daku, A. Vargas, C. Enachescu, C. Ambrus, P. Tregenna-Piggott, N. Amstutz, E. Krausz, A. Hauser, *Coord. Chem. Rev.* **2007**, 251, 364; b) S. Hayami, Y. Komatsu, T. Shimizu, H. Kamihata, Y.-H. Lee, *Coord. Chem. Rev.* **2011**, 255, 1981.
- [6] Y. Garcia, P. Gülich in *Spin Crossover in Transition Metal Compounds II*, ed. by P. Gülich, H. A. Goodwin, Springer-Verlag, Berlin, Heidelberg, New York, **2004**, vol. 234, pp. 49–62.
- [7] A. Bousseksou, G. Molnár, L. Salmon, W. Nicolazzi, *Chem. Soc. Rev.* **2011**, 40, 3313.
- [8] a) S. Decurtins, P. Gülich, C. P. Köhler, H. Spiering, A. Hauser, *Chem. Phys. Lett.* **1984**, 105, 1; b) S. Decurtins, P. Gülich, K. M. Hasselbach, A. Hauser, H. Spiering, *Inorg. Chem.* **1985**, 24, 2174.

- [9] J. G. Haasnoot, *Coord. Chem. Rev.* **2000**, 200-202, 131.
- [10] G. Aromí, L. A. Barrios, O. Roubeau, P. Gamez, *Coord. Chem. Rev.* **2011**, 255, 485.
- [11] a) O. Kahn, J. Kröber, C. Jay, *Adv. Mater.* **1992**, 4, 718; b) O. Kahn, C. Jay Martinez, *Science* **1998**, 279, 44; c) J.-F. Létard, P. Guionneau, L. Goux-Capes in *Spin Crossover in Transition Metal Compounds III*, ed. by P. Gülich, H. A. Goodwin, Springer-Verlag, Berlin, Heidelberg, New York, **2004**, vol. 235, pp. 221–249.
- [12] a) Y. Garcia, V. Ksenofontov, P. Gülich, *Hyperfine Interact.* **2002**, 139/140, 543; b) M. M. Dîrtu, F. Schmit, A. D. Naik, A. Rotaru, J. Marchand-Brynaert, Y. Garcia, *Int. J. Mol. Sci.* **2011**, 12, 5339; c) J. Linares, E. Codjovi, Y. Garcia, *Sensors* **2012**, 12, 4479.
- [13] T. Q. Hung, F. Terki, S. Kamara, M. Dehbaoui, S. Charar, B. Sinha, C. Kim, P. Gandit, I. A. Gural'skiy, G. Molnar, L. Salmon, H. J. Shepherd, A. Bousseksou, *Angew. Chem. Int. Ed.* **2013**, 52, 1185.
- [14] a) O. Kahn, E. Codjovi, *Phil. Trans. R. Soc. Lond. A* **1996**, 354, 359; b) O. Roubeau, *Chem. Eur. J.* **2012**, 18, 15230.
- [15] a) S. Toyazaki, Y. Murakami, T. Komatsu, N. Kojima, T. Yokoyama, *Mol. Cryst. Liq. Cryst.* **2000**, 343, 175; b) O. Roubeau, J. G. Haasnoot, E. Codjovi, F. Varret, J. Reedijk, *Chem. Mater.* **2002**, 14, 2559.
- [16] O. Kahn, L. Sommier, E. Codjovi, *Chem. Mater.* **1997**, 9, 3199.
- [17] J. Kröber, E. Codjovi, O. Kahn, F. Grolière, C. Jay, *J. Am. Chem. Soc.* **1993**, 115, 9810.
- [18] a) N. V. Bausk, S. B. Erenburg, L. N. Mazalov, L. G. Lavrenova, V. N. Ikorskii, *J. Struct. Chem.* **1994**, 35, 509; b) L. G. Lavrenova, N. G. Yudina, V. N. Ikorskii, V. A. Varnek, I. M. Oglezneva, S. V. Larionov, *Polyhedron* **1995**, 14, 1333; c) V. A. Varnek, L. G. Lavrenova, *J. Struct. Chem.* **1995**, 36, 104; d) N. V. Bausk, S. B. Erenburg, L. G. Lavrenova, L. N. Mazalov, *J. Struct. Chem.* **1995**, 36, 925; e) S. B. Erenburg, N. V. Bausk, V. A. Varnek, L. G. Lavrenova, *J. Magn. Magn. Mater.* **1996**,

157/158, 595; f) S. B. Erenburg, N. V. Bausk, L. G. Lavrenova, V. A. Varnek, L. N. Mazalov, *Solid State Ionics* **1997**, 101-103, 571;

[19] Y. Garcia, P. J. van Koningsbruggen, R. Lapouyade, L. Rabardel, O. Kahn, M. Wieczorek, R. Bronisz, Z. Ciunik, M. F. Rudolf, *C. R. Acad. Sci. Paris* **1998**, II c, 523.

[20] a) N. Kojima, Y. Murakami, T. Komatsu, T. Yokoyama, *Synth. Met.* **1999**, 103, 2154; b) Y. Murakami, T. Komatsu, N. Kojima, *Synth. Met.* **1999**, 103, 2157; c) N. Kojima, S. Toyazaki, M. Itoi, Y. Ono, W. Aoki, Y. Kobayashi, M. Seto, T. Yokoyama, *Mol. Cryst. Liq. Cryst.* **2002**, 376, 567.

[21] S. Toyazaki, M. Nakanishi, T. Komatsu, N. Kojima, D. Matsumura, T. Yokoyama, *Synth. Met.* **2001**, 121, 1794.

[22] A. Sugahara, M. Enomoto, N. Kojima, *J. Phys.: Conf. Ser.* **2010**, 217, 012128.

[23] P. J. van Koningsbruggen, Y. Garcia, E. Codjovi, R. Lapouyade, O. Kahn, L. Fournès, L. Rabardel, *J. Mater. Chem.* **1997**, 7, 2069.

[24] G. A. Berezovskii, O. G. Shakirova, Y. G. Shvedenkov, L. G. Lavrenova, *Russ. J. Phys. Chem. A* **2003**, 77, 1054.

[25] M. B. Bushuev, L. G. Lavrenova, Yu. G. Shvedenkov, V. A. Varnek, L. A. Sheludyakova, V. V. Volkov, S. V. Larionov, *Russ. J. Coord. Chem.* **2008**, 34, 190.

[26] L. G. Lavrenova, O. G. Shakirova, V. N. Ikorskii, V. A. Varnek, L. A. Sheludyakova, S. V. Larionov, *Russ. J. Coord. Chem.* **2003**, 29, 22.

[27] M. M. Dîrtu, A. Rotaru, D. Gillard, J. Linares, E. Codjovi, B. Tinant, Y. Garcia, *Inorg. Chem.* **2009**, 48, 7838.

[28] a) *X-ray Spectroscopy*, ed. by L. V. Azároff, McGraw-Hill, Inc., New York, **1974**; b) B. K. Agarwal, *X-Ray Spectroscopy*, Springer-Verlag, Berlin, Heidelberg, New York, **1979**; c) *X-Ray Spectroscopy in Atomic and Solid State Physics*, ed. by J. G. Ferreira, M. T. Ramos, Plenum Press, New York, **1988**; d) *X-Ray Absorption: Principles, Applications, Techniques of EXAFS, SEXAFS and*

- XANES, ed. D. C. Koningsberger, R. Prins, Wiley-VCH, New York, **1988**; e) R. S. von Bordewehr, *Ann. Phys. Fr.* **1989**, *14*, 377.
- [29] U. C. Srivastava, H. L. Nigam, *Coord. Chem. Rev.* **1972-1973**, *9*, 275.
- [30] T. E. Westre, P. Kennepohl, J. G. DeWitt, B. Hedman, K. O. Hodgson, E. I. Solomon, *J. Am. Chem. Soc.* **1997**, *119*, 6297.
- [31] A. L. Roe, D. J. Schneider, R. J. Mayer, J. W. Pyrz, J. Widom, L. Que, Jr., *J. Am. Chem. Soc.* **1984**, *106*, 1676.
- [32] A. Nakamoto, Doctoral Thesis, The University of Tokyo, **2006**.
- [33] A. Grosjean, N. Daro, B. Kauffmann, A. Kaiba, J.-F. Létard, P. Guionneau, *Chem. Commun.* **2011**, *47*, 12382.
- [34] a) A. Urakawa, W. V. Beek, M. Monrabal-Capilla, J. R. Galán-Mascarós, L. Palin, M. Milanesio, *J. Phys. Chem. C* **2011**, *115*, 1323; b) A. Grosjean, P. Négrier, P. Bordet, C. Etrillard, D. Mondieig, S. Pechev, E. Lebraud, J.-F. Létard, P. Guionneau, *Eur. J. Inorg. Chem.* **2013**, *2013 (Cluster Issue)*, 796.
- [35] a) A. Michalowicz, J. Moscovici, B. Ducourant, D. Cracco, O. Kahn, *Chem. Mater.* **1995**, *7*, 1833; b) T. Yokoyama, Y. Murakami, M. Kiguchi, T. Komatsu, N. Kojima, *Phys. Rev. B* **1998**, *58*, 14238; c) A. Michalowicz, J. Moscovici, Y. Garcia, O. Kahn, *J. Synchrotron Rad.* **1999**, *6*, 231; d) S. B. Erenburg, N. V. Bausk, L. G. Lavrenova, L. N. Mazalov, *J. Synchrotron Rad.* **1999**, *6*, 576; e) S. B. Erenburg, N. V. Bausk, L. G. Lavrenova, L. N. Mazalov, *Nucl. Inst. Method Phys. Res. A* **2000**, *448*, 351; f) A. Michalowicz, J. Moscovici, J. Charton, F. Sandid, F. Benamrane, Y. Garcia, *J. Synchrotron Rad.* **2001**, *8*, 701; g) Y. Garcia, J. Moscovici, A. Michalowicz, V. Ksenofontov, G. Levchenko, G. Bravic, D. Bravic, D. Chasseau, P. Gütllich, *Chem. Eur. J.* **2002**, *8*, 4992; h) A. Nakamoto, Y. Ono, N. Kojima, D. Matsumura, T. Yokoyama, *Chem. Lett.* **2003**, *32*, 336.
- [36] S. I. Zabinsky, J. J. Rehr, A. Ankudinov, R. C. Albers, M. J. Eller, *Phys. Rev. B* **1995**, *52*, 2995.
- [37] a) P. Gütllich, A. B. Gaspar, V. Ksenofontov, Y. Garcia, *J. Phys.: Condens. Matter* **2004**, *16*,

- S1087; b) P. Gütllich, V. Ksenofontov, A. B. Gaspar *Coord. Chem. Rev.* **2005**, *249*, 1811; c) P. Gütllich, A. B. Gaspar, Y. Garcia, V. Ksenofontov, *C. R. Chimie* **2007**, *10*, 21.
- [38] S. Klokishner, J. Linares, F. Varret, *Chem. Phys.* **2000**, *255*, 317.
- [39] a) A. Nakamoto, Y. Ono, N. Kojima, D. Matsumura, T. Yokoyama, *Chem. Lett.* **2003**, *32*, 336; b) A. Nakamoto, N. Kojima, X.-J. Liu, Y. Moritomo, A. Nakamura, *Polyhedron* **2005**, *24*, 2909.
- [40] MossWinn – Mössbauer spectrum analysis and database software. <http://www.mosswinn.com/>.
- [41] a) A. Vef, U. Manthe, P. Gütllich, A. Hauser, *J. Chem. Phys.* **1994**, *101*, 9326; b) H. Romsted, A. Hauser, H. Spiering, *J. Phys. Chem. Solids* **1998**, *59*, 265.
- [42] a) S. Sugano, Y. Tanabe, H. Kamimura, *Multiplets of Transition-Metal Ions in Crystals*, Academic Press, New York, **1970**; b) B. N. Figgis, M. A. Hitchman, *Ligand Field Theory and Its Applications*, Wiley-VCH, New York, **2000**.
- [43] a) C. K. Jørgensen, *Absorption Spectra and Chemical Bonding in Complexes*, Addison-Wesley Publishing, Reading, Massachusetts, **1962** ; b) C. K. Jørgensen, *Prog. Inorg. Chem.* **1962**, *4*, 73.
- [44] D. R. Stephens, H. G. Drickamer, *J. Chem. Phys.* **1961**, *35*, 427.
- [45] J. C. Zahner, H. G. Drickamer, *J. Chem. Phys.* **1961**, *35*, 1483.
- [46] F.-M. Gao, *J. Phys.: Condens. Matter* **2003**, *15*, L637.
- [47] a) *Chemical Applications of Mössbauer Spectroscopy*, ed. by V. I. Goldanskii, R. H. Herber, Academic Press, New York, **1968**; b) N. N. Greenwood, T. C. Gibb, *Mössbauer Spectroscopy*, Chapman and Hall, London, **1971**; c) *Mössbauer Spectroscopy and Its Chemical Applications*, ed. by J. G. Stevens, G. K. Shenoy, American Chemical Society, Washington, D. C., **1981**; d) P. Gütllich, E. Bill, A. X. Trautwein, *Mössbauer Spectroscopy and Transition Metal Chemistry*, Springer-Verlag, Berlin, Heidelberg, New York, **2011**.
- [48] a) A. R. Champion, R. W. Vaughan, H. G. Drickamer, *J. Chem. Phys.* **1967**, *47*, 2583; b) A. R. Champion, H. G. Drickamer, *J. Chem. Phys.* **1967**, *47*, 2591.

## Chapter 5

---

*Fastener Effect on Uniaxial Chemical Pressure for One-Dimensional Spin-Crossover System,  $[Fe^{II}(NH_2-trz)_3](C_nH_{2n+1}SO_3)_2 \cdot xH_2O$*

[49] a) D. C. Fisher, H. G. Drickamer, *J. Chem. Phys.* **1971**, *54*, 4825; b) J. Pebler, *Inorg. Chem.* **1983**, *22*, 4125.

## 6. Magnetic Switching by Photo-Irradiation in the Spin-Crossover Iron(III) Complex with Photoisomerizable Counteranion

### Abstract

Iron(III) complexes coordinated by planar Schiff bases with extended  $\pi$ -electron system,  $[\text{Fe}^{\text{III}}(\text{qsal})_2]$ -Anion (Hqsal = *N*-(8-quinoly)salicylaldimine), are known to exhibit the spin-crossover (SCO) behavior which is strongly affected by counter-anions. This work aims at synthesis of an  $\text{Fe}^{\text{III}}$  complex with photochromic counter-anion,  $[\text{Fe}^{\text{III}}(\text{qsal})_2]\text{SPSO}_3$  ( $\text{SPSO}_3^-$  = spiropyran sulfonate) and achievement of the spin conversion by light irradiation. The compound  $[\text{Fe}^{\text{III}}(\text{qsal})_2]\text{SPSO}_3$  crystallized in the *P*-1 space group and showed a SCO behavior with the spin-transition temperature ( $T_{1/2}$ ) of 182 K. Irradiating UV light ( $\lambda = 350$  nm,  $10$  mW  $\text{cm}^{-1}$ ) for 21 h at room temperature produced a remarkable change in the  $\chi_{\text{mol}}T$ - $T$  profile below 200 K with  $T_{1/2} = 148$  K (photo-induced state I). Based on the  $\chi_{\text{mol}}T$  values at 60 K for a UV-irradiated and unirradiated samples, it can be estimated that 13.2% of the LS components were converted to the HS state. Subsequently, green light ( $\lambda = 550$  nm,  $50$  mW  $\text{cm}^{-1}$ ) irradiation for 23 h at room temperature induced a further change in the  $\chi_{\text{mol}}T$ - $T$  profile with  $T_{1/2} = 151$  K (photo-induced state II), resulting in the photoconversion ratio of 11.8% from the LS state to the HS one. The photoinduced state II can revert to the photoinduced state I according to the additional UV irradiation. In this way, the reversible photoconversion of the spin state of  $[\text{Fe}^{\text{III}}(\text{qsal})_2]\text{SPSO}_3$  was successfully performed. Such magnetic switching behaviors are presumably due to the photoisomerization of  $\text{SPSO}_3^-$ , which appears to influence on  $\pi$ - $\pi$  stackings between adjacent  $\text{qsal}^-$  ligands of  $[\text{Fe}^{\text{III}}(\text{qsal})_2]^+$  units, leading to the changes in intermolecular interactions and/or ligand field strengths.

## 6.1 Introduction

Spin-crossover (SCO) materials are the best known as molecular bistable systems, in which optical, magnetic, and other physicochemical properties can be reversibly switched between a high-spin (HS) and a low-spin (LS) states by changing the temperature, applied pressure, electric and magnetic fields (Figure 6.1). Photoswitchable magnetism between a HS and a LS states was first observed in the solid state by Gütlich *et al.* in 1984,<sup>[1]</sup> which is called light-induced excited spin state trapping (LIESST). The LIESST effect is usually operative at low temperatures, and thereby the phenomenon possesses a serious limitation for application in photodevices. Another approach to achieve photoswitching in SCO systems was proposed by Roux *et al.* in 1994 as ligand-driven light-induced spin-change (LD-LISC) effect.<sup>[2]</sup> In the LD-LISC effect, photoisomerization of a photoactive ligand induces a conversion of the spin state of coordinated metal ions due to modifying a ligand field, operating at higher temperature ranges (Figure 6.2). However, at the present time, there have been few reports on the LD-LISC of SCO complexes *in the solid state* owing to little accessible space of the structural change by photoisomerization. In this work, to accomplish the development of SCO materials with room-temperature photoresponsibility, the following concept is adopted: counterion-driven light-induced spin-change (CID-LISC). In the CID-LISC systems, spin-transition units and photoresponsive molecules are separated from each other in a crystal lattice, which affords an enough space for the counteranions to photoisomerize (Figure 6.3). Therefore, it is expected to achieve a photoconversion of the spin states at higher temperature ranges in the solid state through modifying the cooperative effects of SCO complexes due to a chemical pressure accompanied by the photoisomerization.

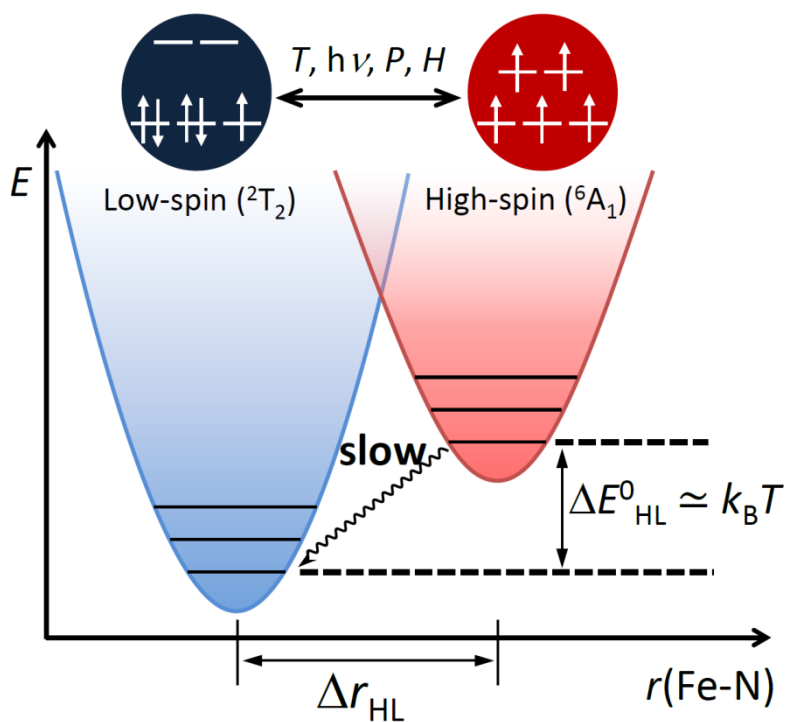


**Figure 6.1.** Adiabatic potentials for the HS and LS states along with the most important reaction coordinate for Fe<sup>III</sup> SCO phenomenon, where the typical mean metal-to-ligand bond length change,  $\Delta r_{\text{HL}}$ , is around 0.15 Å.

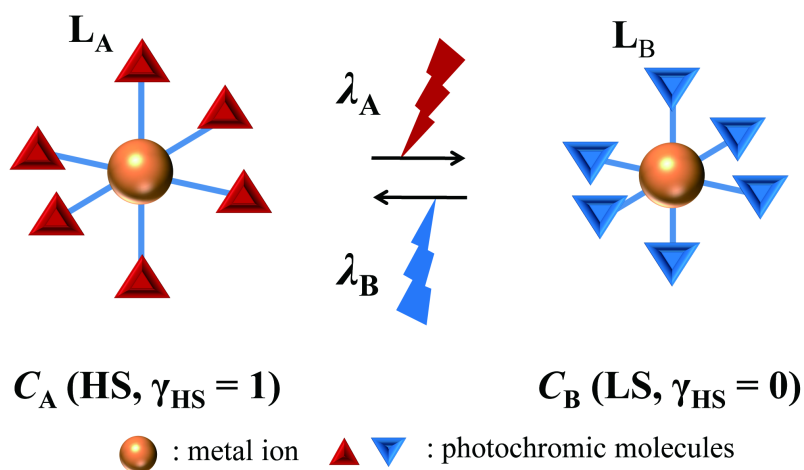


**Figure 6.2.** Schematic representation of the concept of LS-LISC.

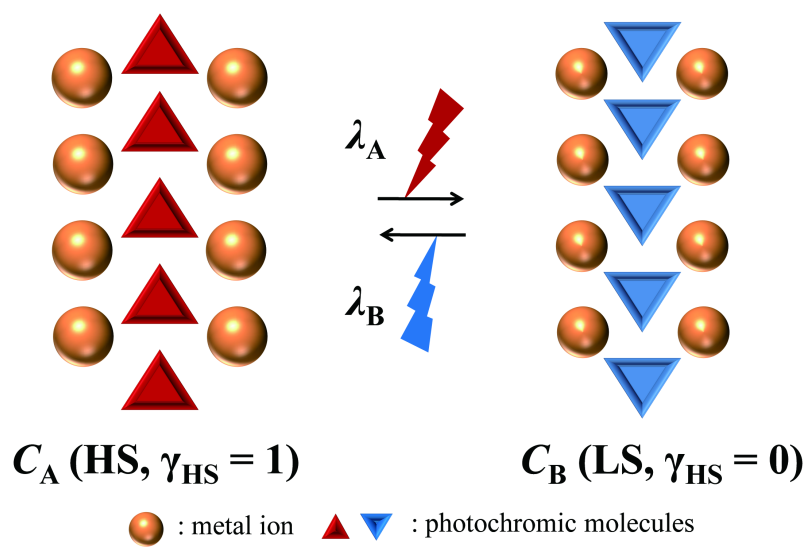


**Figure 6.3.** Schematic representation of concept of CID-LISC.

## 6.2 Counteranion Dependence of Magnetism in $[\text{Fe}^{\text{III}}(\text{qsal})_2]\text{X}$

Iron(III) complexes, which are represented as  $[\text{Fe}^{\text{III}}(\text{qsal})_2]\text{X}$ , are known to exhibit SCO transition between the HS ( $S = 5/2$ ) and the LS ( $S = 1/2$ ) states with a thermal hysteresis (Figure 6.4). Monovalent counter-anions in the compounds are located in the space among  $[\text{Fe}^{\text{III}}(\text{qsal})_2]^+$  units and play a crucial role in  $\pi$ - $\pi$  stacking between adjacent qsal ligands and in intermolecular magnetic interactions as follows. For  $\text{X} = \text{Cl}$  and  $\text{Br}$ , the complexes show the paramagnetic HS states in the whole temperature ranges (Figure 6.5). Note that a drop of the magnetic moment below 10 K for  $\text{X} = \text{Cl}$  is due to a zero-field splitting. In contrast,  $[\text{Fe}^{\text{III}}(\text{qsal})_2]\text{I}$  remains the LS state up to 300 K (Figure 6.5).<sup>[3a]</sup> In the case of  $\text{X} = \text{NCS}$ , the complex exhibits the SCO transition as can be seen in Figure 6.5, which was confirmed by means of  $^{57}\text{Fe}$  Mössbauer spectroscopy (Figure 6.6).<sup>[3a,b]</sup> Furthermore, the SCO transition strongly depends on crystal solvents as well as counter-ions.  $[\text{Fe}^{\text{III}}(\text{qsal})_2]\text{NCS}\cdot\text{MeOH}$  exhibits remarkable SCO behavior with wide thermal hysteresis in the first heating and cooling cycles because of the removal of the MeOH molecules (Figure 6.7).<sup>[3c]</sup> Based on such a counter-anion dependent magnetic property, a qsal-coordinated iron(III) complex with a photoisomerizable organic molecule as a counter-anion was synthesized for the development of photoresponsive SCO materials.  $[\text{Fe}^{\text{III}}(\text{qsal})_2]^+$  are cationic, and hence the anionic photochromic molecule, 1',3',3'-trimethyl-6-nitrospiro[2H-1-benzopyran-2,2'-indoline]-5'-sulfonate ( $\text{SPSO}_3^-$ ), was employed. The potassium salt,  $\text{SPSO}_3\text{K}$ , shows photoisomerization at room temperature between a spiropyran (SP) and a merocyanin (MC) forms in the solid state (Figure 6.8(a)).<sup>[4]</sup> UV-Vis absorption spectra for  $\text{SPSO}_3\text{K}$  in a KBr disc at 300 K are shown in Figure 6.8(b). A broad band around 550 nm demonstrates the photoisomerization from the SP form to the MC form after the UV irradiation ( $\lambda = 350$  nm). Therefore, it is expected to realize a conversion of SCO behavior of

$[\text{Fe}^{\text{III}}(\text{qsal})_2]\text{SPSO}_3$  by photoisomerization of the counter-anion because the intermolecular interaction of  $[\text{Fe}^{\text{III}}(\text{qsal})_2]^+$  units through the  $\pi$ - $\pi$  stackings may be affected by the shape variation of  $\text{SPSO}_3^-$  (Figure 6.9).

During the past two decades, several studies have been devoted to the combination between paramagnetic transition-metal complexes with photochromic materials.<sup>[5]</sup> As an example, a photochromic unit, nitroprussiate  $[\text{Fe}(\text{CN})_5(\text{NO})]^{2-}$ , is useful to build polynuclear networks.  $[\text{Ni}(\text{en})_2][\text{Fe}(\text{CN})_5(\text{NO})] \cdot 3\text{H}_2\text{O}$  and  $[\text{Ni}(\text{en})_2]_4[\text{Fe}(\text{CN})_5(\text{NO})][\text{Fe}(\text{CN})_6] \cdot 5\text{H}_2\text{O}$  are typical three-dimensional networks exhibiting paramagnetic properties.  $[\text{Ru}(\text{NH}_3)_5(\text{NO})]^+$  is a nitrosyl-coordinated transition-metal complex like nitroprusside and is also useful as a photochromic unit. A combination of two discrete entities  $[\text{Ru}(\text{NH}_3)_5(\text{NO})][\text{Cr}(\text{CN})_6]$  is a first example of a synergy between optical and magnetic properties.<sup>[6]</sup> It shows a weak reversible increment of  $\chi_{\text{mol}}T$  values under the light irradiation ( $\lambda = 406\text{-}415$  nm) at low temperature. In the irradiated compound, the NO ligand on ruthenium ion was rotated by *ca.*  $180^\circ$ , and then the electron density distribution in  $[\text{Cr}(\text{CN})_6]$  is induced by the attractive Coulombic force between the inverted  $\text{NO}^+$  and  $\text{CN}^-$ .

As for the compounds containing SCO complexes, very few studies have been reported except for materials with nitroprusside and the related ruthenium complex.  $[\text{Fe}(\text{3-bpp})_2][\text{Fe}(\text{CN})_5(\text{NO})]$  (3-bpp = 2,6-bis(pyrazol-3-yl)pyridine) undergoes an abrupt SCO transition associated with a narrow hysteresis loop ( $T_{1/2} \downarrow = 181$  K,  $T_{1/2} \uparrow = 184$  K).<sup>[7a]</sup> The nitroprussiate are linked with  $[\text{Fe}(\text{3-bpp})_2]^+$  ions through a hydrogen bonding between CN nitrogen on equatorial position and pyrazole HN, resulting in a two-dimensional network. The axial CN and NO groups are free from hydrogen bonding. Thanks to this structure, the complex cation is very effectively accommodated by that of the anion. As an another example, trinuclear complex  $[\text{Fe}^{\text{III}}(\text{salpet})\{\text{Fe}^{\text{II}}(\text{CN})_5(\text{NO})\}\text{Fe}^{\text{III}}(\text{salpet})] \cdot 0.5\text{MeOH} \cdot 3.75\text{H}_2\text{O}$  (salpet = a nonsymmetrical pentadentate ligands, 1,6-diamino-4-azahexane, yielded from Schiff-condensed with (X-substituted)

*o*-salicylaldehyde) was reported.<sup>[7b]</sup> However, none of them has been investigated a photomagnetism.

Very recently, several combinations of SCO cations and photochromic anions were reported with the formula  $[\text{Fe}(\text{qsal})_2]_2[\text{Fe}(\text{CN})_5(\text{NO})]$ -solvent,  $[\text{Fe}(\text{salEen})_2]_2[\text{Fe}(\text{CN})_5(\text{NO})]$  (HsalEen = *N*-[(2-ethylamino)ethyl]salicylaldimine) and  $[\text{Fe}(\text{qsal})_2]_2[\text{Ru}(\text{CN})_5(\text{NO})] \cdot 2.5\text{H}_2\text{O}$ , where the SCO transition and LIESST effect were adequately characterized.<sup>[8]</sup> Unfortunately, no photochromic effect coming from anion units was detected in those systems. According to these previously reported studies,  $[\text{Fe}^{\text{III}}(\text{qsal})_2]\text{SPSO}_3$  will be the first photomagnetic system based on photoisomerizable molecule if the photochromic effect on SCO behavior is successfully observed.

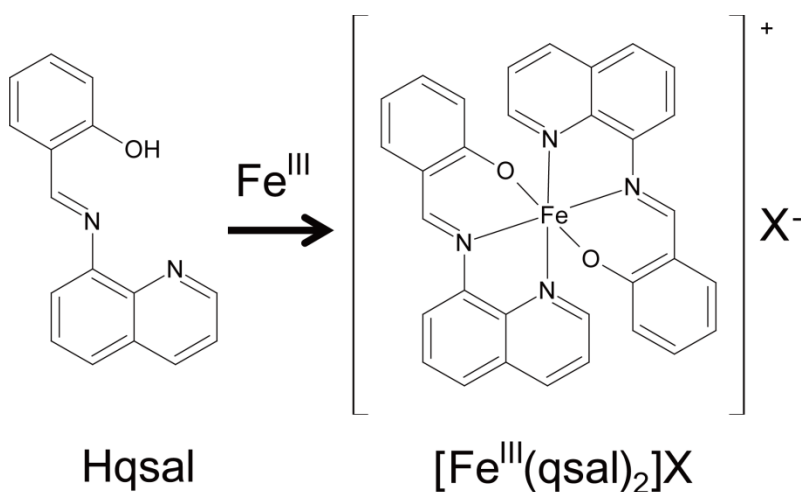


**Figure 6.4.** The molecular structures of Hqsal and  $[\text{Fe}^{\text{III}}(\text{qsal})_2]\text{X}$ .

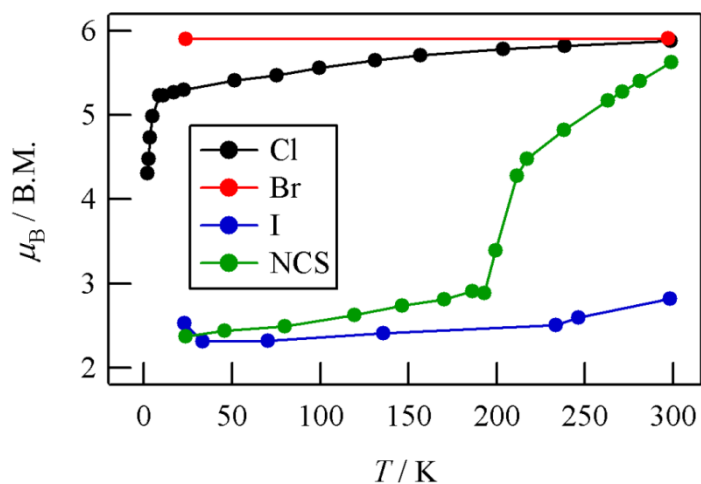


**Figure 6.5.** Temperature dependence of the effective magnetic moment ( $\mu_{\text{eff}}$ ) for  $[\text{Fe}^{\text{III}}(\text{qsal})_2]\text{X}$  ( $\text{X} = \text{Cl}$ , Br, I, NCS).<sup>[3a]</sup>

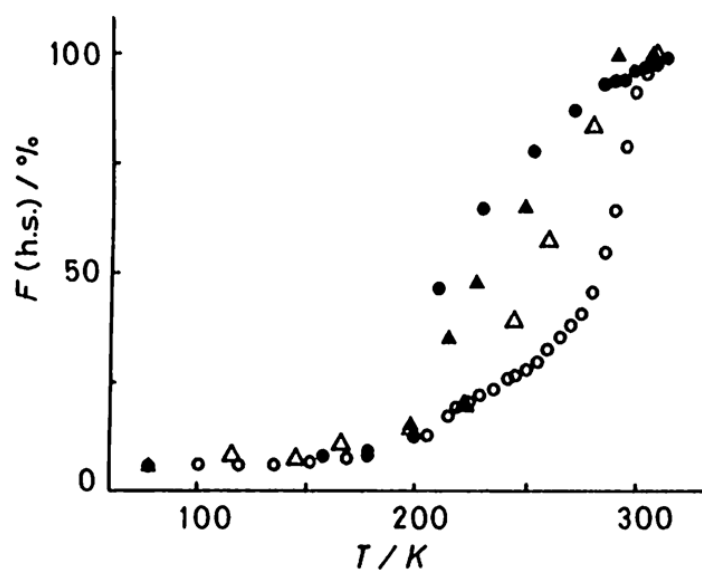


**Figure 6.6.** Temperature dependence of the HS fraction obtained from magnetic susceptibility (filled and open circles) and  $^{57}\text{Fe}$  Mössbauer spectra (filled and open triangles) for  $[\text{Fe}^{\text{III}}(\text{qsal})_2]\text{NCS}$ .<sup>[3b]</sup>

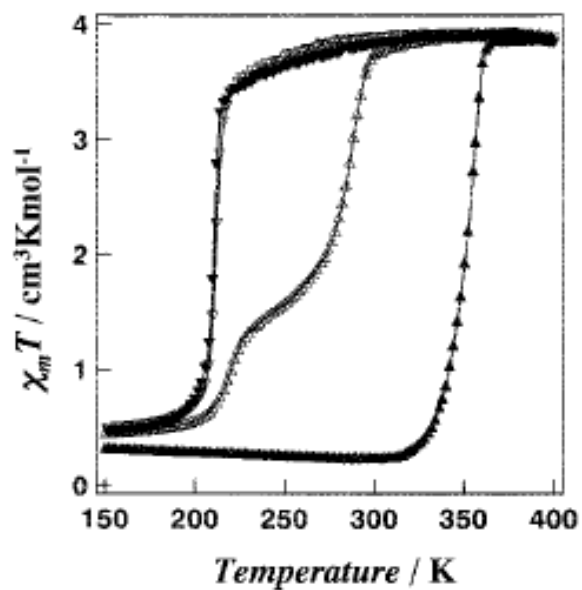


**Figure 6.7.** Temperature dependence of the magnetic susceptibility multiplied by temperature ( $\chi_{\text{mol}}T$ ) for  $[\text{Fe}^{\text{III}}(\text{qsal})_2]\text{NCSe}$ .<sup>[3c]</sup> ▲ and ▼ are the first heating- and cooling processes, respectively.

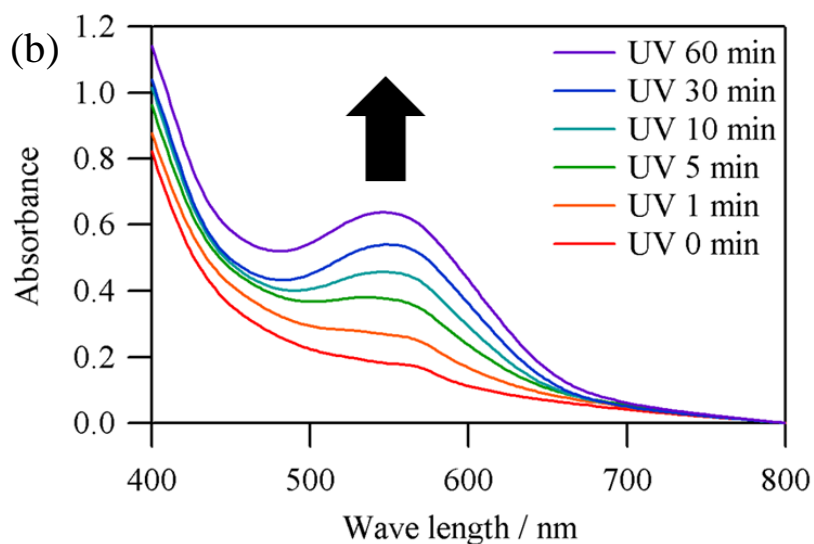
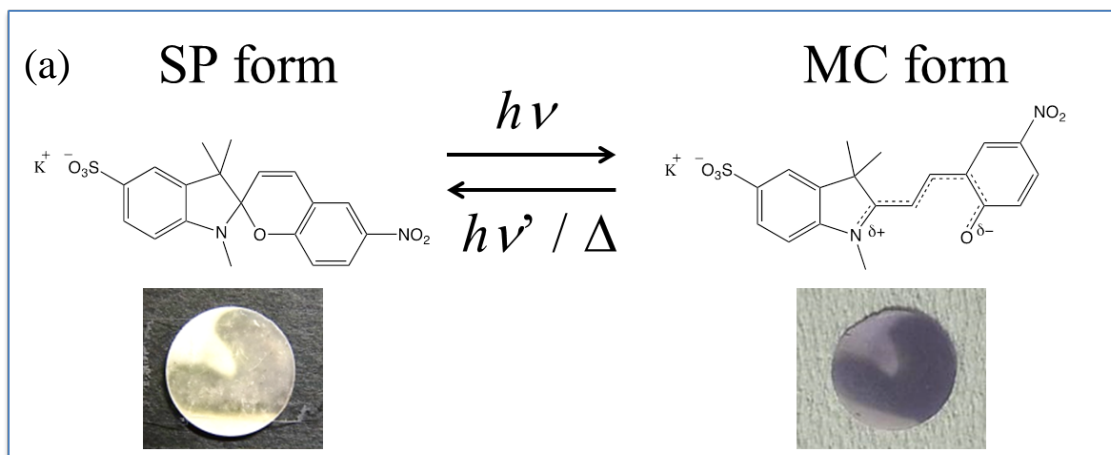


**Figure 6.8.** (a) Photoisomerization of SPSO<sub>3</sub>K from SP form to MC form. (b) UV-vis absorption spectra for SP·K before and after UV irradiation ( $\lambda = 350$  nm) at room temperature.

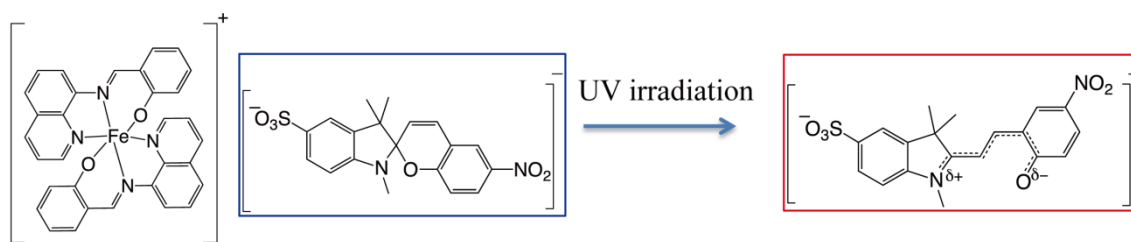


**Figure 6.9.** Schematic representation of concept of this work.

## 6.3 Materials and Methods

### Synthesis

The potassium salt of anionic spiropyran, SPSO<sub>3</sub>K, and [Fe<sup>III</sup>(qsal)<sub>2</sub>]Cl were obtained according to the previous literature procedures.<sup>[4,3a]</sup> SPSO<sub>3</sub>K (201 mg, 0.457 mmol) was added to a solution of 18-crown-6 (193 mg, 0.731 mmol) in MeOH of 300 mL. [Fe<sup>III</sup>(qsal)<sub>2</sub>]Cl (254 mg, 0.435 mmol) was then added to the solution. After the filtration to remove some insoluble impurities, the reaction mixture was stirred at 60°C for 1.5 h. The mixture was allowed to stand in open air. Black block single crystals suitable for X-ray crystallography were obtained within 2 days as [Fe<sup>III</sup>(qsal)<sub>2</sub>]SPSO<sub>3</sub>·2H<sub>2</sub>O·MeOH. The yield was 300 mg (67.6%). Anal. calcd for C, 61.24; H, 4.65; N, 8.24; S, 3.14. Found: C, 59.92; H, 4.66; N, 8.50; S, 3.20%.

### Single crystal X-ray diffraction and structure analysis

The single-crystal X-ray diffraction data were collected on a Rigaku VariMax Dual with Saturn diffractometer using multi-layer mirror monochromated Mo K $\alpha$  irradiation ( $\lambda = 0.71075 \text{ \AA}$ ). An empirical absorption correction was performed with the CrystalClear-SM 1.4.0 software. The structure was solved by direct methods and expanded using Fourier techniques in CRYSTALSTRUCTURE program package.<sup>[9]</sup> Full-matrix least-squares methods on  $F^2$  were applied using all of the unique reflection data. All of the atoms except H were refined anisotropically, whereas H atoms were refined isotropically. The crystal and experimental data are summarized in Tables 6.1 and 6.2.

### **Magnetic measurements**

The magnetic susceptibilities were measured on a Quantum Design MPMS-5S SQUID magnetometer down to 2 K in an applied magnetic field of 5000 Oe. The polycrystalline specimen was wrapped in polyethylene film. The magnetic response was corrected for the background of the sample holder and the diamagnetic contribution of the sample itself was estimated from Pascal's constants.

### **Light irradiation**

The UV ( $\lambda = 350$  nm,  $10$  mW cm<sup>-2</sup>) and green light ( $\lambda = 550$  nm,  $50$  mW cm<sup>-2</sup>) were directly irradiated through a quartz-based optical fiber to a powdered sample. A Xe lamp LAX-101 (Asahi Spectra Co.) with band pass filters (half bandwidth: 10 nm) was employed as a light source.

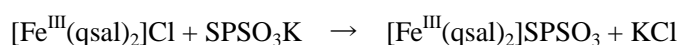
### **<sup>57</sup>Fe Mössbauer measurements**

<sup>57</sup>Co in the Rh matrix was used as a <sup>57</sup>Fe Mössbauer source. The spectra were calibrated by using the six lines of a body-centered cubic iron foil ( $\alpha$ -Fe), the center of which was taken as a zero isomer shift. A cryogenic refrigerator set, Cryomini and MiniStat (Iwatani Co.), was used in the temperature range between 5 K and 300 K. The spectra were fitted using the MossWinn 3.0 program.<sup>[10]</sup>

## 6.4 Results and Discussion

### Synthesis

[Fe<sup>III</sup>(qsal)<sub>2</sub>]SPSO<sub>3</sub> was synthesized by an ion exchange reaction between [Fe<sup>III</sup>(qsal)<sub>2</sub>]Cl and SPSO<sub>3</sub>K as follows:



[Fe(qsal)<sub>2</sub>]-based complexes often crystallize with some solvents. Owing to the bulkiness of the components in [Fe<sup>III</sup>(qsal)<sub>2</sub>]SPSO<sub>3</sub>, two H<sub>2</sub>O and one MeOH molecules as crystal solvents were located in the space among [Fe<sup>III</sup>(qsal)<sub>2</sub>]<sup>+</sup> units without exception as described in the next section. Therefore, this system has the formula of [Fe<sup>III</sup>(qsal)<sub>2</sub>]SPSO<sub>3</sub>·2H<sub>2</sub>O·MeOH, but this compound is abbreviated to [Fe<sup>III</sup>(qsal)<sub>2</sub>]SPSO<sub>3</sub> for convenience hereafter.

### Crystal structure

The compound [Fe<sup>III</sup>(qsal)<sub>2</sub>]SPSO<sub>3</sub> crystallized with crystal solvents in the *P*-1 space group, where the counteranion lies in the space among [Fe<sup>III</sup>(qsal)<sub>2</sub>]<sup>+</sup> units in the SP form (Figure 6.10). One water molecule was linked with the phenoxide oxygen atom (O2) on the qsal ligand through a hydrogen bonding, and the other H<sub>2</sub>O (H<sub>2</sub>O(2)) was linked with the oxygen atom on the MeOH molecule. Owing to the loosely packed H<sub>2</sub>O(2) forming a column along with the *a* axis, a positional disorder of H<sub>2</sub>O(2) and the attendant orientational disorder of MeOH molecules were seen in the middle of structural analysis. Hence, the crystal structure is poorly resolved on the whole; nevertheless the information obtained from this experiment effectively allows to discuss the structure of [Fe<sup>III</sup>(qsal)<sub>2</sub>]<sup>+</sup>

units.

The iron(III) ion had an octahedral  $N_4O_2$  coordination sphere, whose oxygen atoms were occupied in a *cis* position. One of the qsal ligand (qsal<sup>A</sup>) had a certain distortion between the 8-aminoquinoline (Quin) and the salicylaldehyde (Sal) moieties, and their dihedral angle was  $25.5^\circ$  at 250 K. The other qsal ligand (qsal<sup>B</sup>) had a high planarity with the dihedral angle of  $4.2^\circ$ . As for the information of structural changes accompanied by SCO transition, remarkable changes in coordination bond lengths were observed. In the HS state at 250 K, the average Fe-O and Fe-N distances ( $r_{Fe-O}$  and  $r_{Fe-N}$ ) were 1.91 Å and 2.13 Å, respectively. In the LS state at 93 K, the coordination bond lengths shortened;  $r_{Fe-O} = 1.88$  Å and  $r_{Fe-N} = 1.98$  Å. The average differences,  $\Delta r_{Fe-O}$  and  $\Delta r_{Fe-N}$ , of the bond lengths between the HS and the LS states are 0.03 Å and 0.15 Å, respectively. The  $\Delta r_{Fe-N}$  value of 0.15 Å is typical of Fe<sup>III</sup> SCO complexes, while  $\Delta r_{Fe-O}$  is rather small.

In the crystal packing, two kinds of  $\pi$ - $\pi$  stackings were observed between adjacent qsal<sup>B</sup> ligands, whereas no  $\pi$ - $\pi$  stackings was found in qsal<sup>A</sup>. The stacking distance of  $R(\text{Sal-Quin}) = 3.266$  Å is slightly shorter than that of  $R(\text{Sal-Sal}) = 3.306$  Å at 250 K. Thanks to these  $\pi$ - $\pi$  stackings,  $[\text{Fe}^{\text{III}}(\text{qsal})_2]^+$  units were nicely accommodated side by side along with a one-dimensional cation array as shown in Figure 6.11. The Quin rings are stacked on both sides of the Sal-Sal stacking as Quin-Sal-Sal-Quin. At the present time,  $[\text{Fe}^{\text{III}}(\text{qsal})_2]\text{SPSO}_3$  is the first SCO system in qsal coordinated Fe complexes with such a side-by-side linked  $[\text{Fe}^{\text{III}}(\text{qsal})_2]^+$  array.

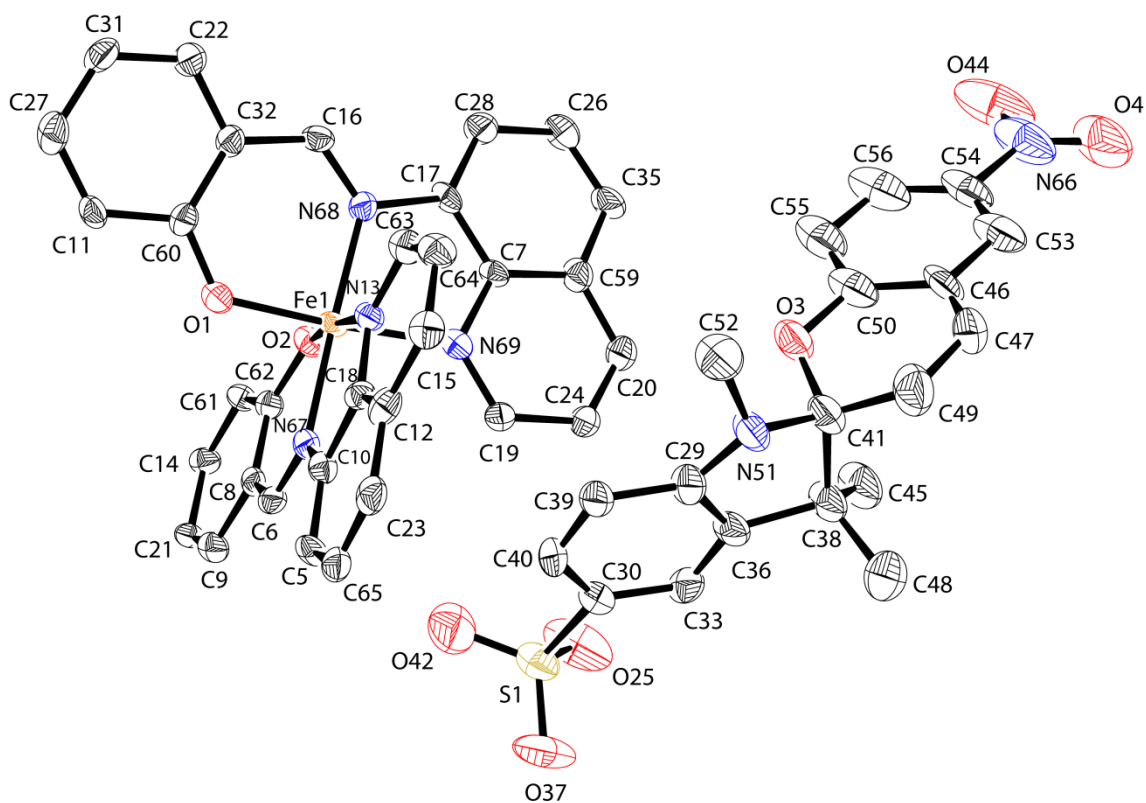


**Figure 6.10.** ORTEP view of  $[\text{Fe}^{\text{III}}(\text{qsal})_2]\text{SPSO}_3$  in the LS state at 93 K showing 50% probability displacement ellipsoids. Hydrogen atoms and crystal solvent molecules are omitted for clarity.

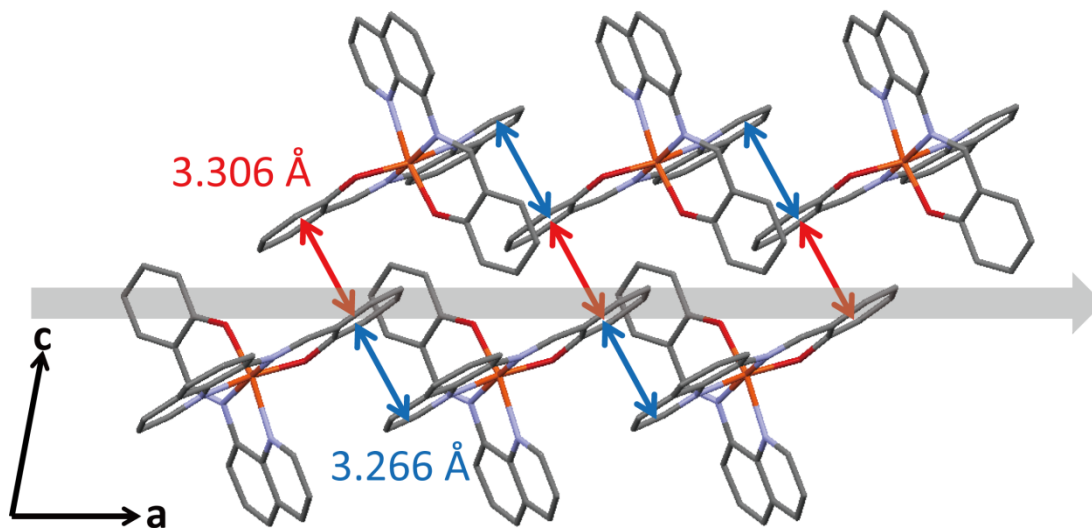


**Figure 6.11.** Structure of the  $\pi$ - $\pi$  stacking between  $[\text{Fe}^{\text{III}}(\text{qsal})_2]^+$  units at 250 K. Hydrogen atoms and crystal solvent molecules are omitted for clarity.

**Table 6.1.** Selected crystallographic data for [Fe<sup>III</sup>(qsal)<sub>2</sub>]SPSO<sub>3</sub>.

<i>T</i> / K	250	190	170	93
Crystal system	Triclinic			
Space group	<i>P</i> -1			
<i>a</i> / Å	8.400(2)	8.4085(19)	8.401(2)	8.383(3)
<i>b</i> / Å	10.904(3)	10.861(3)	10.852(3)	10.939(5)
<i>c</i> / Å	27.005(7)	26.897(6)	26.871(7)	26.865(10)
$\alpha$ / °	79.382(11)	79.438(10)	79.432(11)	101.671(6)
$\beta$ / °	81.345(11)	81.420(10)	81.424(11)	90.480(4)
$\gamma$ / °	71.555(8)	71.554(7)	71.491(8)	110.953(5)
<i>V</i> / Å <sup>3</sup>	2305.87	2279.7	2272.76	2244.3
<i>Z</i>	2	2	2	2
<i>R</i>	0.117	0.1303	0.1015	0.121

**Table 6.2.** Coordination bond lengths around the Fe atom in [Fe<sup>III</sup>(qsal)<sub>2</sub>]SPSO<sub>3</sub>.

<i>T</i> / K	250	190	170	93
Fe-O(1) / Å	1.904(4)	1.899(8)	1.900(3)	1.874(4)
Fe-O(2) / Å	1.925(4)	1.919(9)	1.924(4)	1.890(5)
Fe-N(1) / Å	2.148(5)	2.137(8)	2.139(3)	2.009(4)
Fe-N(2) / Å	2.105(5)	2.093(8)	2.093(4)	1.965(5)
Fe-N(3) / Å	2.166(6)	2.158(1)	2.149(5)	1.998(6)
Fe-N(4) / Å	2.099(5)	2.089(8)	2.080(4)	1.939(5)

The single crystal X-ray diffraction data for  $[\text{Fe}^{\text{III}}(\text{qsal})_2]\text{SPSO}_3$  were collected not only at 250 K and 93 K, but also 190 K and 170 K because the compound exhibited three-step SCO transition before light irradiation in a single crystal state as described in the next section. However, none of remarkable structural changes such as symmetry breaking were obtained unfortunately.  $[\text{Fe}^{\text{III}}(\text{qsal})_2]\text{SPSO}_3$  had the crystallographically independent  $\text{Fe}^{\text{III}}$  site in the whole temperature range. Therefore, the relationship between intermediate states in the  $\chi_{\text{mol}}T$ - $T$  profile and crystal structures at 190 and 170 K remains to be elucidated.

### Magnetic properties and effect of photo-irradiation

The temperature dependence of the molar magnetic susceptibility ( $\chi_{\text{mol}}$ ) multiplied by temperature,  $\chi_{\text{mol}}T$ , is shown in Figure 6.12. At 300 K, the  $\chi_{\text{mol}}T$  value was  $4.32 \text{ cm}^3 \text{ K mol}^{-1}$ , which is in good agreement with the spin-only value ( $4.375 \text{ cm}^3 \text{ K mol}^{-1}$ ;  $S = 5/2$ ) expected for an  $\text{Fe}^{\text{III}}$  ion in the HS state. On cooling, the  $\chi_{\text{mol}}T$  product stepwisely dropped from *ca.* 200 K to *ca.* 150 K, and then approached  $0.628 \text{ cm}^3 \text{ K mol}^{-1}$  at 10 K. The SCO transition seems to take place via two plateaus around 190 K and 170 K, where the  $\chi_{\text{mol}}T$  values are  $3.03 \text{ cm}^3 \text{ K mol}^{-1}$  and  $1.64 \text{ cm}^3 \text{ K mol}^{-1}$ , respectively. The additional decrement of  $\chi_{\text{mol}}T$  below 10 K is due to zero-field splitting of the  $\text{Fe}^{\text{III}}$  ion in the LS state. The  $\chi_{\text{mol}}T$  values were nicely reproduced without thermal hysteresis in the heating process, which is not shown in Figure 12. It can be concluded that the spin transition is due to  $S = 5/2 \leftrightarrow S = 1/2$  ( ${}^6\text{A}_{1g} \leftrightarrow {}^2\text{T}_{2g}$ ) SCO behavior with three steps.

Such a multistep spin conversion process can be divided into two types: (i) a symmetry breaking of crystal structures and (ii) a synergistic effect between intra- and intermolecular interactions. As an example for the former,  $[\text{Fe}^{\text{III}}(\text{H-5-Br-thsa})(5\text{-Br-thsa})]\cdot\text{H}_2\text{O}$  (H<sub>2</sub>-5-Br-thsa = 5-bromosalicylaldehyde thiosemicarbazone) amazingly shows five- and six-step SCO transition in

heating and cooling processes, respectively.<sup>[11]</sup> Some of the multisteps are attributable to an intermolecular hydrogen bonding and a proton transfer, but they are nonetheless partially attributable to changes in space group symmetry. The complex crystallizes in  $P2_1/n$  space group both at 303 K (HS state; before the first step in the cooling process) and 123 K (LS state; after the final step), but the screw axis  $2_1$  is vanished and thereby it crystallizes in  $Pn$  space group without any unit cell multiplication in the intermediate states. As a result, two crystallographically independent  $\text{Fe}^{\text{III}}$  sites coexist in the unit cell. Thus, the two step symmetry breaking such as  $P2_1/n \rightarrow Pn \rightarrow P2_1/n$  appears to be ascribed to the multistability in the SCO compound. As mentioned in the previous section, however, none of remarkable change in the crystal structure of  $[\text{Fe}^{\text{III}}(\text{qsal})_2]\text{SPSO}_3$  including the symmetry breaking was observed. Therefore, the concept of symmetry breaking is not applicable to  $[\text{Fe}^{\text{III}}(\text{qsal})_2]\text{SPSO}_3$ . Switching the subject to the other explanation for a multistep SCO behavior, the dinuclear iron(II) compound  $[\text{Fe}^{\text{II}}(\text{bt})(\text{NCS})_2]_2\text{bpym}$  (bt = 2,2'-bi-2-thiazoline, bpym = 2,2'-bipyrimidine) is the first and the most famous example exhibiting two step  $S = 2 \leftrightarrow S = 0$  ( ${}^5\text{T}_{2g} \leftrightarrow {}^1\text{A}_{1g}$ ) SCO transition.<sup>[12]</sup> The  $\chi_{\text{mol}}T$  value of  $[\text{Fe}^{\text{II}}(\text{bt})(\text{NCS})_2]_2\text{bpym}$  gradually decreases on cooling from room temperature, and then the intermediate point appears around 175 K, where the proportion of the HS  $\text{Fe}^{\text{II}}$  ions is found to be *ca.* 51%. Accordingly, the SCO transition of this compound occurs in the two steps such as  $[\text{HS-HS}] \leftrightarrow [\text{HS-LS}] \leftrightarrow [\text{LS-LS}]$ . The enthalpy of mixed-spin species,  $H_{\text{HS-LS}}$ , can be written as  $H_{\text{HS-LS}} = (H_{\text{HS-HS}}/H_{\text{LS-LS}})2 + W$ , where the value of  $W$  is determined by contributions of electrostatic and vibronic effects, *i.e.* a cooperativity within the crystal lattice. In the case of  $W < 0$ , the system shows two-step SCO transition. In fact, the two-step transition is ascribed to a synergistic effect between intermolecular interactions favoring the  $[\text{HS-HS}]$  or the  $[\text{LS-LS}]$  states and intramolecular interactions favoring the  $[\text{HS-LS}]$  state. However,  $[\text{Fe}^{\text{III}}(\text{qsal})_2]\text{SPSO}_3$  has the crystallographically unique  $\text{Fe}^{\text{III}}$  site even in the intermediate states at 190 K and 170 K. Furthermore, the reason why “three” steps appear in the middle of SCO transition

is still unclear even if effective intermolecular interactions are taken into consideration. Accordingly, the argument about the three-step transition still has not met a clear explanation to shed light on the cause of that.

The light irradiation brought about significant changes in  $\chi_{\text{mol}}T$ - $T$  profile, and the proportions of the HS and the LS states before and after the light irradiation were summarized in Table 6.3. After the UV ( $\lambda = 350$  nm,  $10$  mW  $\text{cm}^{-2}$ ) irradiation for 21 h at room temperature, SCO behavior with  $T_{1/2} = 148$  K was observed, and the  $\chi_{\text{mol}}T$ - $T$  profile below 200 K was remarkably changed (photo-induced state I). At 60 K, the  $\chi_{\text{mol}}T$  value was  $1.14$   $\text{cm}^3$   $\text{K mol}^{-1}$ , where the proportion of the HS  $\text{Fe}^{\text{III}}$  ions was 19.1%. Meanwhile, the proportion of the HS  $\text{Fe}^{\text{III}}$  ions at 60 K was 5.88% before the UV irradiation, that is, 13.2% of the LS  $\text{Fe}^{\text{III}}$  ions were converted to the HS state below 60 K. Photoisomerization of SP may be influential on  $\pi$ - $\pi$  stackings between  $\text{qsal}^-$  ligands, leading to the changes in intermolecular interactions and/or ligand field strengths. However, the proportion of photo-converted MC isomer is still unclear because the UV-vis absorption spectra of  $[\text{Fe}^{\text{III}}(\text{qsal})_2]^+$  based compounds are hardly measurable in many cases. Besides, an intermediate state was seen between 190 K and 150 K, resulting in two-step SCO transition. This is also a difficult issue which should be resolved in the future, but the crystal structure of  $[\text{Fe}^{\text{III}}(\text{qsal})_2]\text{SPSO}_3$  after the UV irradiation can be hardly determined because the irradiation experiment was carried out for the powdered sample, which was the unavoidable circumstance. In addition to this, the very dark black colored single crystal of  $[\text{Fe}^{\text{III}}(\text{qsal})_2]\text{SPSO}_3$  cannot let UV and green lights permeate therethrough; there is no help for detection of precise changes in crystal structures of the irradiated samples.

The green light ( $\lambda = 550$  nm,  $50$  mW  $\text{cm}^{-2}$ ) irradiation induced a further changes in the  $\chi_{\text{mol}}T$ - $T$  profile below 200 K with  $T_{1/2} = 151$  K (photo-induced state II). At 60 K, the  $\chi_{\text{mol}}T$  value was  $1.61$   $\text{cm}^3$   $\text{K mol}^{-1}$ , where the proportion of the HS  $\text{Fe}^{\text{III}}$  ions was 30.9%. Thus, 11.8% of the LS component was ascribed to be newly photo-converted to the HS state. These results are beyond

expectation because a green light can reconvert the MC isomer to the original SP form. Besides, none of the intermediate state could be seen in the middle of  $S = 5/2 \leftrightarrow S = 1/2$  conversion. Furthermore, after the UV irradiation again, the  $\chi_{\text{mol}}T$ - $T$  profile reverted to the behavior plotted by the blue circles in Figure 6.12. In this way, reversible photo-conversion of the spin state of  $[\text{Fe}^{\text{III}}(\text{qsal})_2]\text{SPSO}_3$  was successfully demonstrated.

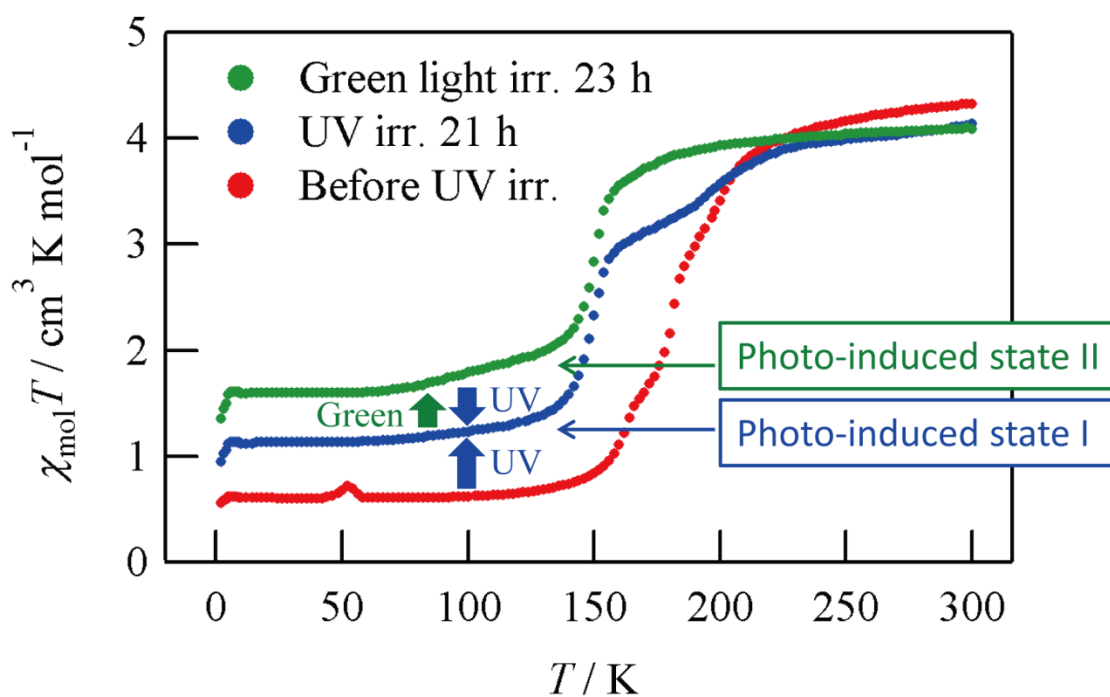


**Figure 6.12.** The  $\chi_{\text{mol}}T$  products as a function of temperature for  $[\text{Fe}^{\text{III}}(\text{qsal})_2]\text{SPSO}_3$ .

**Table 6.3.** Proportions of the HS and the LS states at 60 K before and after the light irradiation for  $[\text{Fe}^{\text{III}}(\text{qsal})_2]\text{SPSO}_3$ .

	HS (%)	LS (%)
Before UV irradiation	5.88	94.1
Photo-induced state I	19.1	80.9
Photo-induced state II	30.9	69.1

### $^{57}\text{Fe}$ Mössbauer spectroscopy

The SCO behavior before light irradiation was confirmed by temperature dependence of  $^{57}\text{Fe}$  Mössbauer spectra (Figure 6.13) as well as the magnetic properties by SQUID magnetometry. The spectrum at 300 K showed only one broad doublet with the isomer shift ( $\delta$ ) of  $0.312 \text{ mm s}^{-1}$  and the quadrupole splitting ( $\Delta E_{\text{Q}}$ ) of  $0.550 \text{ mm s}^{-1}$ , which agree with the values expected for the HS  $\text{Fe}^{\text{III}}$  ion. On cooling, a new doublet with large  $\Delta E_{\text{Q}}$  appeared as expected for the LS iron(III) ion. The relative intensity of the HS doublet was continuously reduced with decreasing temperature, and it reached 4.5% at 5 K. The LS doublet at 5 K had the Mössbauer parameters of  $\delta = 0.189 \text{ mm s}^{-1}$  and  $\Delta E_{\text{Q}} = 2.845 \text{ mm s}^{-1}$ . Besides, concerning the intermediate states at 190 K and 170 K, any noticeable anomaly was observed in the Mössbauer spectra.

The asymmetry of the doublet appears to be traceable to a difference in interaction between nuclear spin and electron spin of  $^{57}\text{Fe}$  nucleus, which is a sort of relaxation phenomenon.<sup>[13]</sup> The HS iron(III) ion with  $S = 5/2$  has six electronic states (the  ${}^6\text{S}_{5/2}$  ground state) with different magnetic hyperfine interactions. The direction of the nuclear spin precession with the magnetic quantum number ( $m_I$ ) of  $m_I = \pm 3/2$  is parallel to the fluctuating hyperfine magnetic field, whereas that of  $m_I = \pm 1/2$  is perpendicular to the field. Hence, the precession frequency corresponding to  $m_I = \pm 1/2$  is

lower than  $m_I = \pm 3/2$ , and thereby the nuclear with  $m_I = \pm 1/2$  takes in an averaged hyperfine magnetic field, whereas that of  $m_I = \pm 3/2$  is exposed to incompletely averaged field. Therefore, the line corresponding to  $(I = 1/2, m_I = \pm 1/2) \leftrightarrow (I = 3/2, m_I = \pm 3/2)$  becomes to be broadened than that of  $(I = 1/2, m_I = \pm 1/2) \leftrightarrow (I = 3/2, m_I = \pm 1/2, \mp 1/2)$  transitions. In this manner, the line shape of Mössbauer spectra results in an asymmetrical broadened doublet owing to the fluctuating hyperfine magnetic field between the six different values, whose relaxation time is  $10^{-11} \sim 10^{-9}$  s.

The photo-induced states, unfortunately, could not be detected due to an underlying problem of the refrigerator system. It requires *ca.* 12 h for beginning to cool off. In process of that, the MC form and photo-induced states are thermally deactivated.

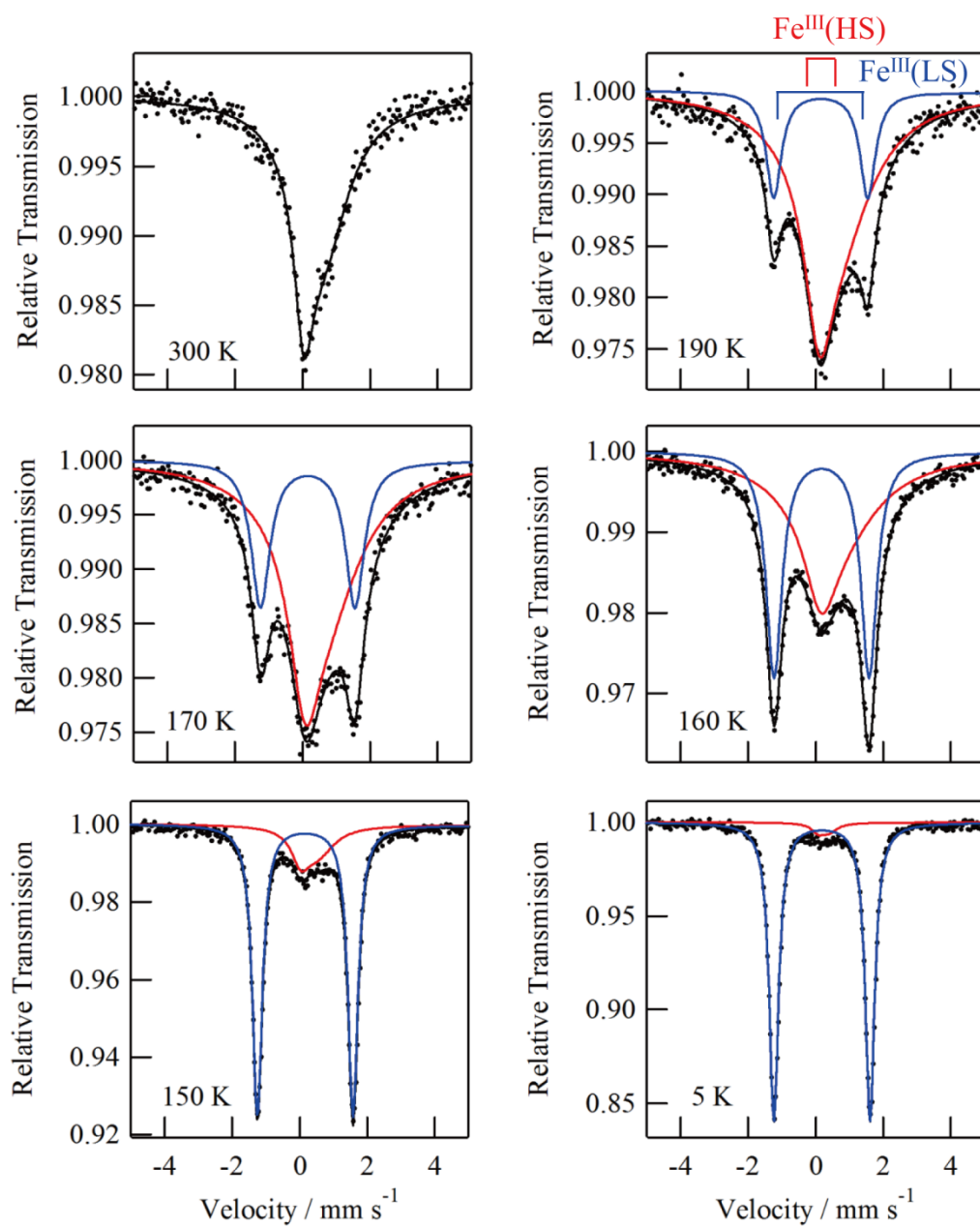


**Figure 6.13.** Selected temperature dependence of  $^{57}\text{Fe}$  Mössbauer spectra for  $[\text{Fe}^{\text{III}}(\text{qsal})_2]\text{SPSO}_3$ .

**Table 6.4.** Temperature dependence of Mössbauer parameters for  $[\text{Fe}^{\text{III}}(\text{qsal})_2]\text{SPSO}_3$ .

$T / \text{K}$	$\delta / \text{mm s}^{-1}$		$\Delta E_{\text{Q}} / \text{mm s}^{-1}$		$\Gamma / \text{mm s}^{-1}$			Area %	
	HS	LS	HS	LS	HS ( <i>l</i> )	HS ( <i>h</i> )	LS	HS	LS
300	0.312	–	0.550	–	0.676	1.898	–	100.0	0.0
210	0.344	0.106	0.502	2.692	0.954	2.831	0.560	88.3	11.7
190	0.360	0.155	0.506	2.784	0.974	2.581	0.549	81.2	18.8
170	0.354	0.156	0.558	2.795	1.067	2.692	0.673	73.1	26.1
160	0.361	0.178	0.395	2.814	1.141	3.105	0.571	58.0	42.0
150	0.277	0.165	0.497	2.831	0.630	1.213	0.357	20.5	79.5
125	0.282	0.173	0.436	2.836	0.391	0.895	0.356	9.0	91.0
100	0.248	0.199	0.481	2.833	0.454	0.573	0.358	6.9	93.1
5	0.243	0.189	0.335	2.845	0.466	0.596	0.334	4.5	95.5

$\delta$  = isomer shift,  $\Delta E_{\text{Q}}$  = quadrupole splitting,  $\Gamma$  = line width, HS (*l*) = HS fraction at low velocity, HS (*h*) = HS fraction at high velocity.

### Photoisomerization in the crystalline state

As mentioned above, the precise structural information can be hardly obtained; nevertheless, reflectance spectra and X-ray powder diffraction can provide useful information to a certain extent. Reflectance spectra before and after UV irradiation for the single crystal of  $[\text{Fe}^{\text{III}}(\text{qsal})_2]\text{SPSO}_3$  are shown in Figure 6.14. The peak around 460 nm is ascribed to be assigned to a ligand-to-metal charge transfer (LMCT) band. Under the UV irradiation, the reflectance of the LMCT band was decreased, whereas that around 550 nm was increased with the progress of irradiation time. In addition, the reflection intensity around 700 nm was remained largely unchanged under the UV irradiation. The increase of reflectance around 550 nm is suggestive of photoisomerization of counteranion from the SP form to the MC form.

X-ray powder diffraction patterns before and after UV irradiation were shown in Figure 6.15 in the range of  $2\theta = 3^\circ$ – $25^\circ$ . Beyond  $2\theta = 25^\circ$ , no distinct diffraction peaks appeared. UV irradiation effect on a change in the X-ray diffraction can be slightly seen in Figure 6.15. It may imply a

structural change accompanied by photoisomerization of the counteranion,  $\text{SPSO}_3^-$ .

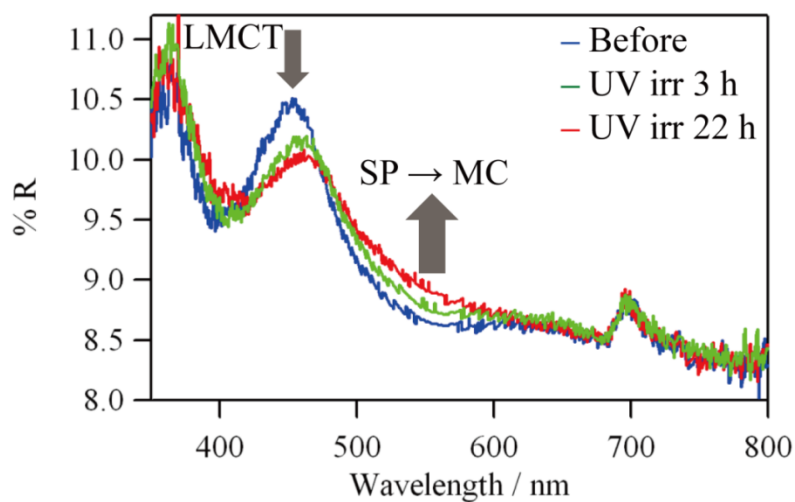


**Figure 6.14.** Reflectance spectra for the single crystal of  $[\text{Fe}^{\text{III}}(\text{qsal})_2]\text{SPSO}_3$  before and after the UV irradiation at room temperature.

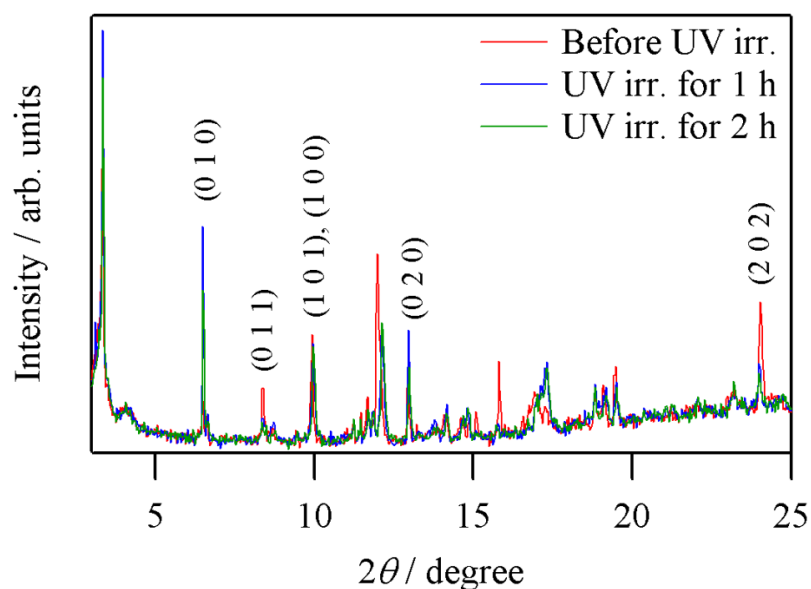


**Figure 6.15.** X-ray powder diffraction patterns of  $[\text{Fe}^{\text{III}}(\text{qsal})_2]\text{SPSO}_3$  before and after UV irradiation at room temperature.

## 6.5 Conclusion

The iron(III) SCO complex possessing photoisomerizable counter-anion,  $[\text{Fe}^{\text{III}}(\text{qsal})_2]\text{SPSO}_3$ , was successfully synthesized, and its crystal structure and magnetic properties were investigated.  $[\text{Fe}^{\text{III}}(\text{qsal})_2]^+$  units were linked by  $\pi$ - $\pi$  stackings side by side, forming a one-dimensional cation array. The counter-anion,  $\text{SPSO}_3^-$ , was located along the one-dimensional array of  $[\text{Fe}^{\text{III}}(\text{qsal})_2]^+$  as the SP form. By photo-irradiation, the SCO behavior of  $[\text{Fe}^{\text{III}}(\text{qsal})_2]\text{SPSO}_3$  was remarkably changed especially below 200 K. Though the green light irradiation could not reproduce the  $\chi_{\text{mol}}T$ - $T$  profile before UV irradiation, the Photo-Induced States I and II were reversibly controlled by UV and green lights. The photoconverted spin state is wished to be confirmed by  $^{57}\text{Fe}$  Mössbauer spectroscopy. Furthermore, a LIESST experiment is also desired to be conducted in the future. Anyhow, the possibility to realize the CID-LISC effect on the SCO behavior was demonstrated in this study.

## References

- [1] S. Decurtins, P. Gütllich, C. P. Köhler, H. Spiering, A. Hauser, *Chem. Phys. Lett.* **1984**, *105*, 1.
- [2] C. Roux, J. Zarembowitch, B. Gallois, T. Granier, R. Claude, *Inorg. Chem.* **1994**, *33*, 2273.
- [3] a) R. C. Dickson, W. A. Baker, Jr., R. L. Collins, *J. Inorg. Nucl. Chem.* **1977**, *39*, 1531; b) H. Oshio, K. Kitazaki, J. Mishiro, N. Kato, Y. Maeda, Y. Takashima, *J. Chem. Soc., Dalton Trans.* **1987**, 1341; c) S. Hayami, Z.-Z. Gu, H. Yoshiki, A. Fujishima, O. Sato, *J. Am. Chem. Soc.* **2001**, *123*, 11644.
- [4] A. Sugahara, N. Tanaka, A. Okazawa, N. Kojima, *Chem. Lett.* **2014**, *43*, 281.
- [5] a) Z. Z. Gu, O. Sato, T. Iyoda, K. Hashimoto, A. Fujishima, *Chem. Mater.* **1997**, *9*, 1092–1097; b) H. L. Shyu, H. H. Wei, Y. Wang, *Inorg. Chim. Acta* **1997**, *258*, 81–86; c) L. Kushch, L. Buravov, V. Tkacheva, E. Yagubskii, L. Zorina, S. Khasanov, R. Shibaeva, *Synth. Met.* **1999**, *102*, 1646–1649; d) M. Clemente-León, E. Coronado, J. R. Galán-Mascaras, C. Giménez-Saiz, C. J. Gómez-García, J. M. Fabre, *Synth. Met.* **1999**, *103*, 2279–2282; e) M. Clemente-León, E. Coronado, J. R. Galán-Mascarós, C. J. Gómez-García, T. Woike, J. M. Clemente-Juan, *Inorg. Chem.* **2000**, *39*, 87–94; f) S. Bénard, E. Rivière, P. Yu, K. Nakatani, J. F. Delouis, *Chem. Mater.* **2001**, *13*, 159–162; g) F. Bellouard, M. Clemente-León, E. Coronado, J. R. Galán-Mascarós, C. Giménez-Saiz, C. J. Gómez-García, T. Woike, *Polyhedron* **2001**, *20*, 1615–1619; h) M. Clemente-León, E. Coronado, J. R. Galán-Mascarós, C. J. Gómez-García, Th. Woike, J. M. Clemente-Juan, *Inorg. Chem.* **2001**, *40*, 87–94; i) K. Ueda, M. Takahashi, H. Tomizawa, E. Miki, C. Faulmann, *J. Mol. Struct.* **2005**, *751*, 12–16; j) S. Bonhommeau, P. G. Lacroix, D. Talaga, A. Bousseksou, M. Seredyuk, I. O. Fritsky, V. Rodriguez, *J. Phys. Chem. C* **2012**, *116*, 11251–11255.
- [6] L. A. Kushch, L. S. Kurochkina, E. B. Yagubskii, G. V. Shilov, S. M. Aldoshin, V. A. Emel'yanov, Y. N. Shvachko, V. S. Mironov, D. Schaniel, T. Woike, C. Carbonera, C. Mathonière, *Eur. J. Inorg.*

*Chem.* **2006**, 4074-4085.

[7] a) K. H. Sugiyarto, W.-A. McHale, D. C. Craig, A. D. Rae, M. L. Scudder, H. A. Goodwin, *Dalton Trans.* **2003**, 2443-2448; b) I. Šalitroš, R. Boča, L. Dlháň, M. Gembický, J. Kožíšek, J. Linares, J. Moncol', I. Nemeč, L. Perašínová, F. Renz, I. Svoboda, H. Fuess, *Eur. J. Inorg. Chem.* **2009**, 3141-3154.

[8] C. Faulmann, J. Chahine, L. Valade, G. Chastanet, J.-F. Létard, D. de Caro, *Eur. J. Inorg. Chem.* **2013**, 1058-1067.

[9] G. M. Sheldrick, *Acta Crystallogr., Sect. A: Found. Crystallogr.* **2008**, *64*, 112.

[10] MossWinn – Mössbauer spectrum analysis and database software, <http://www.mosswinn.com/>.

[11] Z.-Y. Li, J.-W. Dai, Y. Shiota, K. Yoshizawa, S. Kanegawa, O. Sato, *Chem. Eur. J.* **2013**, *19*, 12948-12952.

[12] J.-A. Real, H. Bolvin, A. Bousseksou, A. Dworkin, O. Kahn, F. Varret, J. Zarembowitch, *J. Am. Chem. Soc.* **1992**, *114*, 4650-4658.

[13] a) M. Blume, *Phys. Rev. Lett.* **1965**, *14*, 96; b) M. Blume, *Phys. Rev. Lett.* **1967**, *18*, 305; c) N. Thrane, G. Trumphy, *Phys. Rev. B* **1970**, *1*, 153; d) P. Gülich, E. Bill, A. X. Trautwein, *Mössbauer Spectroscopy and Transition Metal Chemistry*, Springer-Verlag, Berlin, Heidelberg, **2011**, pp. 205-210.

# 7. A Tricky Water Molecule Coordinated to a Verdazyl Radical–Iron(II) Complex: A Multitechnique Approach

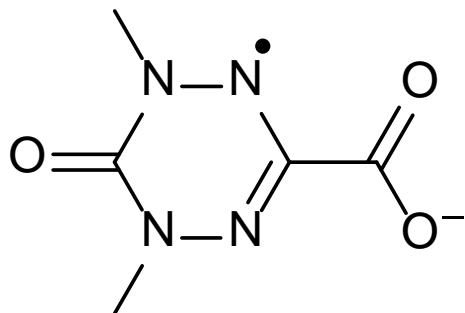
## Abstract

The first iron complexes of high-spin (HS) iron(II) species directly coordinated to verdazyl radicals,  $[\text{Fe}^{\text{II}}(\text{vdCOO})_2(\text{H}_2\text{O})_2] \cdot 2\text{H}_2\text{O}$  (**1**;  $\text{vdCOO}^- = 1,5\text{-dimethyl-6-oxo-verdazyl-3-carboxylate}$ ) and  $[\text{Fe}^{\text{II}}(\text{vdCOO})_2(\text{D}_2\text{O})_2] \cdot 2\text{D}_2\text{O}$  (**2**), were synthesized. The crystal structure of **1** was investigated by single-crystal X-ray diffraction at room temperature and at 90 K. The compound crystallizes in the  $P-1$  space group with no phase transition between 300 and 90 K. The crystals are composed of discrete  $[\text{Fe}^{\text{II}}(\text{vdCOO})_2(\text{H}_2\text{O})_2]$  complexes and crystallization water molecules. In the complex, two  $\text{vdCOO}^-$  ligands coordinate to the iron(II) ion in a head-to-tail arrangement and two water molecules complete the coordination sphere. The Fe-X (X = O, N) distances vary in the 2.069–2.213 Å range at 300 K and in the 2.0679–2.2111 Å range at 90 K, indicating that the iron(II) ion is in its HS state at both temperatures. At 300 K, one of the coordinated water molecules is H-bonded to two crystallization water molecules whereas the second one appears as loosely H-bonded to the two oxygen atoms of the carboxylate group of two neighboring complexes. At 90 K, the former H-bonds remain essentially the same whereas the second coordinated water molecule reveals a complicated behavior appearing simultaneously as tightly H-bonded to two oxygen atoms and non-H-bonded. The  $^{57}\text{Fe}$  Mössbauer spectra, recorded between 300 K and 10 K, give a clue to this situation. They show two sets of doublets typical of HS iron(II) species whose intensity ratio varies smoothly with temperature. It demonstrates the existence of an equilibrium between the high temperature and low temperature forms of the compounds. The solid-state magic angle spinning  $^2\text{H}$  NMR spectra of **2** were recorded between 310 K and 193 K. The spectra suggest the existence of a strongly temperature-dependent motion of one of the coordinated water molecules in the whole temperature range. Variable-temperature magnetic susceptibility measurements indicate an antiferromagnetic interaction ( $J_{\text{Fe-vd}} = -27.1 \text{ cm}^{-1}$ ;  $\mathbf{H} = -J_{ij}\mathbf{S}_i\mathbf{S}_j$ ) of the HS iron(II) ion and the radical spins with high  $g_{\text{Fe}}$  and  $D_{\text{Fe}}$  values ( $g_{\text{Fe}} = 2.25$ ,  $D_{\text{Fe}} = +3.37 \text{ cm}^{-1}$ ) for the HS iron(II) ion. Moreover, the radicals are strongly antiferromagnetically coupled through the iron(II) center ( $J_{\text{vd-vd}} = -42.8 \text{ cm}^{-1}$ ). These last results are analyzed based on the framework of the magnetic orbitals formalism.

## 7.1 Introduction

Molecular magnetism based on transition-metal complexes has blossomed with essentially diamagnetic ligands.<sup>[1]</sup> In the early years of molecular magnetism, the nitroxide-based radicals fiercely competed against the diamagnetic ligands.<sup>[2]</sup> Though still of interest, studies on nitroxide-based ligands started declining at the turn of the century.<sup>[3]</sup> Other stable radicals have been recently introduced to build up metal–radical architectures and take advantage of the potentially strong exchange interaction between the spin bearers.<sup>[4,5]</sup> Understanding the chemistry and the exchange interaction involving these new actors is a prerequisite for spreading their use. For verdazyl radicals, this has been undertaken by reacting these radicals with  $[M^x(\text{hfac})_x(\text{H}_2\text{O})_y]$  (Hhfac = 1,1,1,5,5,5-hexafluoro-2,4-pentanedione) complexes where the hfac<sup>−</sup> ligand both plays a blocking role and enhances the acidity of the metal ion.<sup>[6]</sup> To go towards more complex and hence more interesting architectures, it is important to restrict the use of blocking ligands. An important step in this direction is the description of  $[M(\text{vdCOO})_2(\text{H}_2\text{O})_2]$  complexes (M = Co, Ni; vdCOO<sup>−</sup> = 1,5-dimethyl-6-oxo-verdazyl-3-carboxylate; Scheme 7.1) which are synthesized in water<sup>[7]</sup> and where the radical is available for bridging metal ions. In this chapter, this series is extended to the iron(II) derivatives synthesized either in H<sub>2</sub>O leading to  $[\text{Fe}(\text{vdCOO})_2(\text{H}_2\text{O})_2] \cdot 2\text{H}_2\text{O}$  (**1**) or in D<sub>2</sub>O leading to  $[\text{Fe}(\text{vdCOO})_2(\text{D}_2\text{O})_2] \cdot 2\text{D}_2\text{O}$  (**2**). The crystal structures of **1** and **2** are investigated by single-crystal X-ray diffraction at room temperature and at 90 K. In the complex, one coordinated water molecule has a rather abnormal behavior. To tackle this phenomenon, a multi-technique approach is used relying on the simultaneous analysis of X-ray crystallographic data, <sup>57</sup>Fe Mössbauer spectroscopy, and solid state <sup>2</sup>H-NMR spectroscopy. Moreover, the magnetic properties are investigated by variable-temperature magnetic susceptibility measurements between 300 K and 2

K. The exchange interaction parameters of the whole series of complexes (M = Fe, Co, Ni) are analyzed and discussed.



**Scheme 7.1.** Structural formula of 1,5-dimethyl-6-oxo-verdazyl-3-carboxylate (vdCOO<sup>-</sup>).

## 7.2 Materials and Methods

### Synthesis

The tetrazane precursor of the verdazyl radical ligand, H<sub>3</sub>vdCOOH, was obtained according to the previous literature procedure.<sup>[8]</sup>

**[Fe(vdCOO)<sub>2</sub>(H<sub>2</sub>O)<sub>2</sub>]·2H<sub>2</sub>O (1):** FeSO<sub>4</sub>·7H<sub>2</sub>O (230 mg, 0.828 mmol) was added to a solution (20 mL) of H<sub>3</sub>vdCOOH in distilled water (405 mg, 2.33 mmol). Sodium hydroxide (100 mg, 2.50 mmol) was then added resulting in a pale yellow solution. The mixture was allowed to stand in open air. Black block single crystals were obtained after 4 days, yield was 154 mg (40%). Mp.: >300 °C. Anal. calcd for C<sub>10</sub>H<sub>20</sub>N<sub>8</sub>FeO<sub>10</sub>: C, 25.66; H, 4.31; N, 23.94. Found: C, 25.42; H, 4.53; N, 23.71%. IR (KBr disk):  $\nu(\text{O-H})$  3390, 3170,  $\nu(\text{C-H})$  2950 (w),  $\nu(\text{C=O})$  1680 (s),  $\nu(\text{C=O})_{\text{carbox}}$  1640, 1420 (s) cm<sup>-1</sup>.  $\lambda_{\text{max}}/\text{nm}$  ( $\epsilon/\text{M}^{-1} \text{cm}^{-1}$ ) (1-propanol): 399 ( $2.3 \times 10^3$ ), 676 ( $1.1 \times 10^3$ ), 769 ( $1.1 \times 10^3$ ).

**[Fe(vdCOO)<sub>2</sub>(D<sub>2</sub>O)<sub>2</sub>]·2D<sub>2</sub>O (2):** FeSO<sub>4</sub>·H<sub>2</sub>O (141mg, 0.828 mmol) was obtained by heating FeSO<sub>4</sub>·7H<sub>2</sub>O (230 mg, 0.828 mmol) in vacuo for 30 min at 373 K. It was then added, together with sodium hydroxide (100 mg, 2.5 mmol) to a deuterated aqueous solution (20 mL) of H<sub>3</sub>vdCOOH (405 mg, 2.33 mmol). The mixture was put on a dry desiccator with silica gel where single crystals were grown by slow evaporation. The yield was 83.12 mg (21.1%). Mp.: >300 °C. IR (KBr disk):  $\nu(\text{O-D})$  2500, 2360,  $\nu(\text{C-H})$  2950 (w),  $\nu(\text{C=O})$  1680 (s),  $\nu(\text{C=O})_{\text{carbox}}$  1640, 1420 (s) cm<sup>-1</sup>.  $\lambda_{\text{max}}/\text{nm}$  ( $\epsilon/\text{M}^{-1} \text{cm}^{-1}$ ) (1-propanol): 399 ( $2.3 \times 10^3$ ), 676 ( $1.1 \times 10^3$ ), 769 ( $1.1 \times 10^3$ ).

### X-ray crystallographic analysis

The single-crystal X-ray diffraction data were recorded using a Bruker SMART 1000 CCD area detector system with graphite-monochromated Mo K $\alpha$  radiation ( $\lambda = 0.71073 \text{ \AA}$ ). Data frames were integrated using Bruker SAINT V6.45A ( $2\theta_{\max} = 60.0^\circ$ ). The intensities were corrected for Lorentz and polarization effects. Semi-empirical absorption correction was performed using the SADABS program. The structure was solved by direct methods and refined by full-matrix least squares on  $F^2$  using SHELXLTL.<sup>[9]</sup> All of the atoms except H and D were refined anisotropically. H and D atoms of the water molecules were refined isotropically, whereas the other H atoms were refined according to riding models. The crystal and experimental data are summarized in Table 7.1 and Table 7.2 for **1** and **2** respectively.

### <sup>57</sup>Fe Mössbauer measurements

<sup>57</sup>Co in the Rh matrix was used as a <sup>57</sup>Fe Mössbauer source. The spectra were calibrated by using the six lines of a body-centered cubic iron foil ( $\alpha$ -Fe), the center of which was taken as a zero isomer shift. The cryogenic refrigerator sets, Cryomini and MiniStat, Iwatani Co. were used in the temperature range between 10 K and 300 K. The spectra were fitted using the MossWinn 3.0 program.<sup>[10]</sup>

### Solid-state <sup>2</sup>H-MAS-NMR

The solid-state high-resolution magic angle spinning (MAS) <sup>2</sup>H NMR spectra of the polycrystalline sample were recorded between 193 K and 310 K at *ca.* 9 and 12 kHz, with a rotation synchronized spin-echo pulse sequence  $\pi/2-\tau-\pi$  ( $\tau = 111$  and  $83 \mu\text{s}$ ) and a resonance frequency of 46.1 MHz, provided by a Bruker DSX300 spectrometer. The polycrystalline sample was packed into the center

of a zirconia rotor of 4 mm diameter and a length of *ca.* 6 mm to minimize the temperature gradient of the sample. The thermometer of the MAS NMR probe was carefully calibrated.<sup>[11]</sup> The shifts of <sup>2</sup>H NMR lines were measured from an external CDCl<sub>3</sub> reference (7.26 ppm).

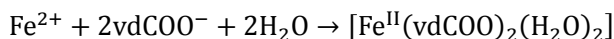
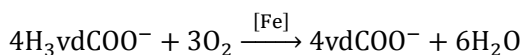
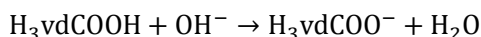
### **Magnetic measurements**

The magnetic susceptibility was measured on a Quantum Design MPMS-5 SQUID magnetometer down to 2 K in an applied magnetic field of 5000 Oe. The polycrystalline specimen was wrapped in polyethylene film. The experimental magnetic susceptibility was corrected for the background and the diamagnetism of the sample was estimated from Pascal's constants. Simulation of the experimental magnetic data was performed using the julX program (version 1.4.1) written by E. Bill through full-matrix diagonalization of the spin Hamiltonian.<sup>[12]</sup>

## 7.3 Results

### Synthesis

Complex **1** was synthesized by reacting iron(II) with the tetrazane precursor of the radical H<sub>3</sub>vdCOOH. The oxidation of H<sub>3</sub>vdCOOH and the reaction between iron(II) and the radical were carried out in a one-pot synthesis by metal-catalyzed air oxidation of the tetrazane<sup>[6,7,13]</sup> in basic medium involving the following reactions:



The *in situ* oxidation of the tetrazane appears as an efficient way to avoid the precipitation of the product and to favor the formation of single crystals.<sup>[6,7,13]</sup> In the present case, one could expect that the oxidation of the iron(II) species and of the tetrazane would occur at the same time. It appears that the oxidation of the latter and the crystallization of the complex are rapid enough to prevent the oxidation of the iron(II) species. In the case of **2**, it is necessary to dehydrate the iron(II) salt and to perform the crystal growth in a dessicator to avoid the contamination of the compound by non-deuterated water molecules from the initial hydrated salt or from moist air.

### Single crystal X-ray diffraction

The crystal structures of **1** and **2** were determined by single crystal X-ray diffraction analysis at 300 K and at 90 K. The two compounds are isostructural and crystallize in the *P*-1 space group with no

phase transition between 300 and 90 K (Table 7.1 for **1** and Table 7.2 for **2**). Hereafter, the description of the structure of **1** is provided. The crystals contain discrete  $[\text{Fe}^{\text{II}}(\text{vdCOO})_2(\text{H}_2\text{O})_2]$  complexes (Figure 7.1). The  $\text{vdCOO}^-$  moieties are essentially planar, in particular, the  $\text{C}_2\text{N}_4$  heterocycle, which thus corresponds to the oxidized radical form.<sup>[14]</sup> The iron atom is surrounded by two  $\text{vdCOO}^-$  radical ligands in an *N,O*-chelating mode. The two ligands are in a head-to-tail arrangement around the iron atom which sits in the  $\text{N}_2\text{O}_2$  plane. Two  $\text{H}_2\text{O}$  molecules complete the coordination sphere of the metal ion in *trans* positions above and below the Fe  $\text{N}_2\text{O}_2$  plane. With four short Fe–O distances in the range 2.07–2.12 Å and two longer Fe–N distances close to 2.21 Å, the iron(II) ion is in an elongated octahedral environment. The observed distances (Table 7.3) are in line with a high-spin (HS) iron(II) ion. Each complex is well isolated from the neighboring complexes (no  $\pi$ – $\pi$  interactions, and shortest contacts around and beyond van der Waals distances).

At both temperatures, the two coordinated water molecules in **1** are non-equivalent. This is obvious at first sight from the difference in the isotropic displacement parameters of their respective hydrogen atoms at room temperature (Figure 7.1(a)). This indeed corresponds to the difference in the electronic density found around O1 and O2 at this temperature (Figures 7.2(a) and 7.3(a), and Figures 7.4(a) and 7.5(a) for **2**). The huge values found for H2A and H2B atoms compared to any other in the structure could be the signature of a disorder rather than mere thermal effects though it is not possible to explore this possibility at 300 K. Nevertheless, since the H atoms on the coordinated water molecules have been refined, it is possible to reveal the existence of H-bonds by scrutinizing the distance between the hydrogen and the donor atoms and the O–H...O angle.<sup>[15]</sup> The coordinated water molecule I (H1A–O1–H1B) establishes H-bonds with the two crystallization water molecules with H...O distances of 1.831 Å (O9) and 1.901 Å (O10) and O–H...O angles of 178.11° (O9) and 176.21° (O10) at 300 K. At 90 K, H...O distances are 1.871 Å (O9) and 1.763 Å (O10) and O–H...O angles are 168.31° (O9) and 174.01° (O10). These values are characteristic of short H-bonds

with good alignment of the three involved atoms.<sup>[15]</sup> The two crystallization water molecules are further H-bonded to the oxygen atom of the carboxyl groups of two neighboring complexes. The situation for the coordinated water molecule II (H2A–O2–H2B) is dramatically different (Figure 7.6). In particular, it is strongly temperature-dependent. At 300 K, the H···O distances are 2.429 Å (O4), 2.456 Å (O3), 2.396 Å (O7) and 2.808 Å (O6) and O–H···O angles are 150.41° (O4), 119.51° (O3) 156.31° (O7) and 110.51° (O6). The low values of the angles for O3 and O6 rule out the presence of H-bonds<sup>[15]</sup> whereas the long H···O distances observed for O4 and O7 indicate the presence of rather loose H-bonds (Figure 7.6(a)). At 90 K, we found an explicit disorder of the hydrogen atoms of the coordinated water molecule II – there are more than two sites occupied by the hydrogen atoms in the electron density difference map at 90 K. At this temperature, all the O–H···O angles involving H2C and H2D are below 130° and can be as low as 90.1° (O2–H2D···O6) indicating that these two atoms are not involved in H-bonds. Accordingly, as shown in Figure 7.6(b), the H-bonds are solely between H2B and O3 (H2B···O3 = 1.990 Å; O2–H2B···O3 = 160.7°) and between H2A and O7 (H2A···O7 = 2.041 Å; O2–H2A···O7 = 167.0°). They are considerably shortened compared to the situation encountered at 300 K.

The analysis of the single crystal X-ray diffraction data does not allow reaching a full understanding of the status of the coordinated water molecule II. In order to clarify this point, complementary spectroscopic information was used. In an iron containing system, the use of Mössbauer spectroscopy appears as much natural.

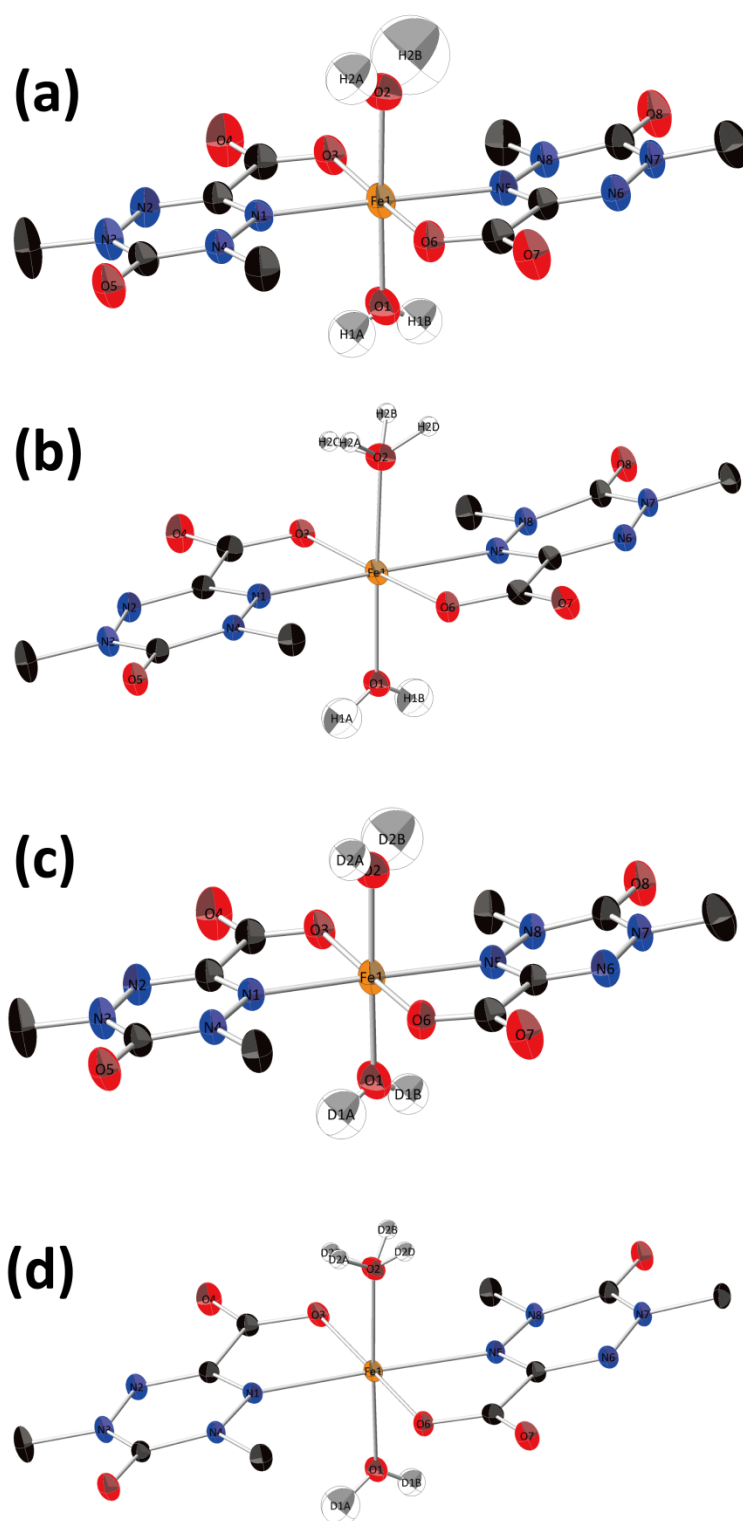


**Figure 7.1.** Molecular structure of  $[\text{Fe}^{\text{II}}(\text{vdCOO})_2(\text{H}_2\text{O})_2]$  at 300 K (a) and at 90 K (b) and that of  $[\text{Fe}^{\text{II}}(\text{vdCOO})_2(\text{D}_2\text{O})_2]$  at 300 K (c) and at 90 K (d) with thermal ellipsoids at the 50% probability level. Atom numbering is shown whereas the non-coordinated water molecules and the hydrogen atoms of the methyl groups are omitted for clarity.

**Table 7.1.** Selected Crystallographic Data for **1** at 300 K and 90 K.

compound	<b>1</b>	
formula	C <sub>10</sub> H <sub>20</sub> FeN <sub>8</sub> O <sub>10</sub>	
formula weight	468.19	
crystal system	triclinic	
space group	<i>P</i> -1	
<i>T</i> /K	300	90
<i>a</i> /Å	9.1837(11)	9.2092(8)
<i>b</i> /Å	9.5706(11)	9.2785(8)
<i>c</i> /Å	10.6018(13)	10.6971(10)
<i>α</i> /deg	84.936(2)	84.406(2)
<i>β</i> /deg	83.959(2)	84.601(2)
<i>γ</i> /deg	79.849(2)	79.076(2)
<i>V</i> /Å <sup>3</sup>	909.83(19)	890.53(14)
<i>Z</i>	2	2
<i>R</i> <sub>1</sub> ( <i>I</i> > 2σ( <i>I</i> ))	0.0468	0.0397
<i>wR</i> <sub>2</sub> (all data)	0.1354	0.1132
G.O.F.	1.007	1.058

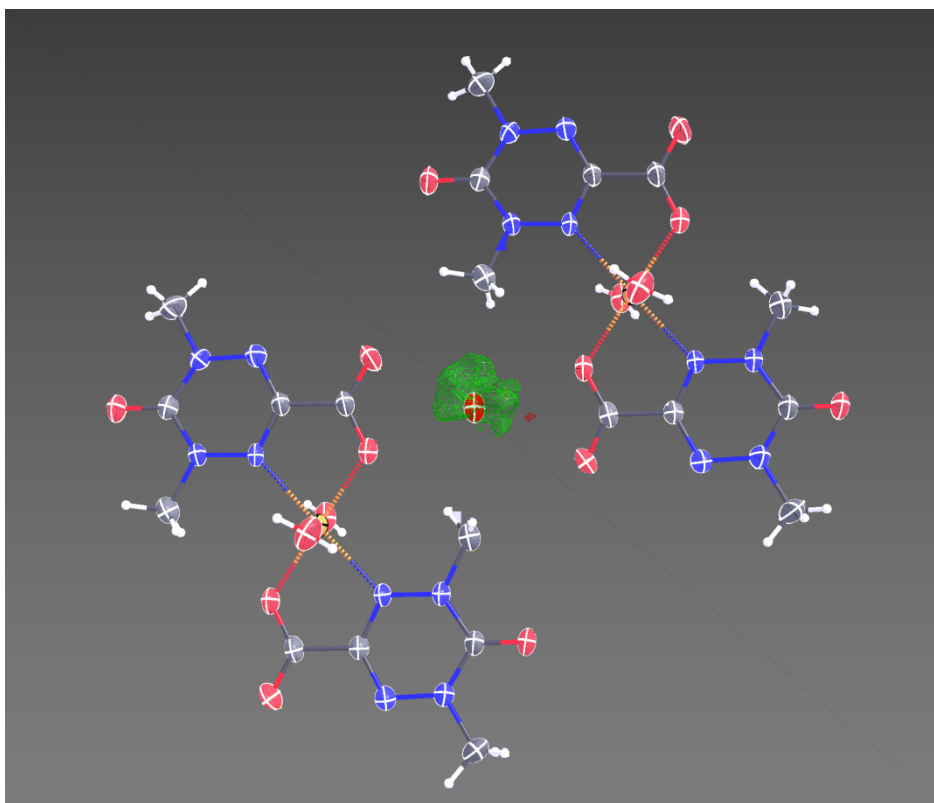
**Table 7.2.** Selected Crystallographic Data for **2** at 300 K and 90 K.

compound	<b>2</b>	
formula	C <sub>10</sub> H <sub>12</sub> D <sub>8</sub> FeN <sub>8</sub> O <sub>10</sub>	
formula weight	476.21	
crystal system	triclinic	
space group	P-1	
<i>a</i> /Å	9.1722(7)	9.1747(6)
<i>b</i> /Å	9.5972(7)	9.2567(6)
<i>c</i> /Å	10.5527(8)	10.6372(7)
<i>α</i> /deg	84.837(2)	84.2890(10)
<i>β</i> /deg	83.709(2)	84.4090(10)
<i>γ</i> /deg	80.095(2)	79.2460(10)
<i>V</i> /Å <sup>3</sup>	907.17(12)	880.24(10)
<i>Z</i>	2	2
<i>R</i> <sub>1</sub> ( <i>I</i> > 2σ( <i>I</i> ))	0.0408	0.0341
<i>wR</i> <sub>2</sub> (all data)	0.1206	0.0911
G.O.F.	1.045	1.073
<i>T</i> /K	300	90

**Table 7.3.** Distances around the Fe atoms in **1**(RT) compared with Co and Ni derivatives.

Distances / Å	<i>Fe</i> (this work)	<i>Co</i> <sup>[7]</sup>	<i>Ni</i> <sup>[7]</sup>
MO1(H <sub>2</sub> O)	2.069	2.023	2.037
MO2(H <sub>2</sub> O)	2.121	2.060	2.097
MO3(vd)	2.098	2.035	2.055
MO6(vd)	2.092	2.025	2.043
MN1(vd)	2.208	2.127	2.185
MN5(vd)	2.213	2.141	2.192

(a)



(b)

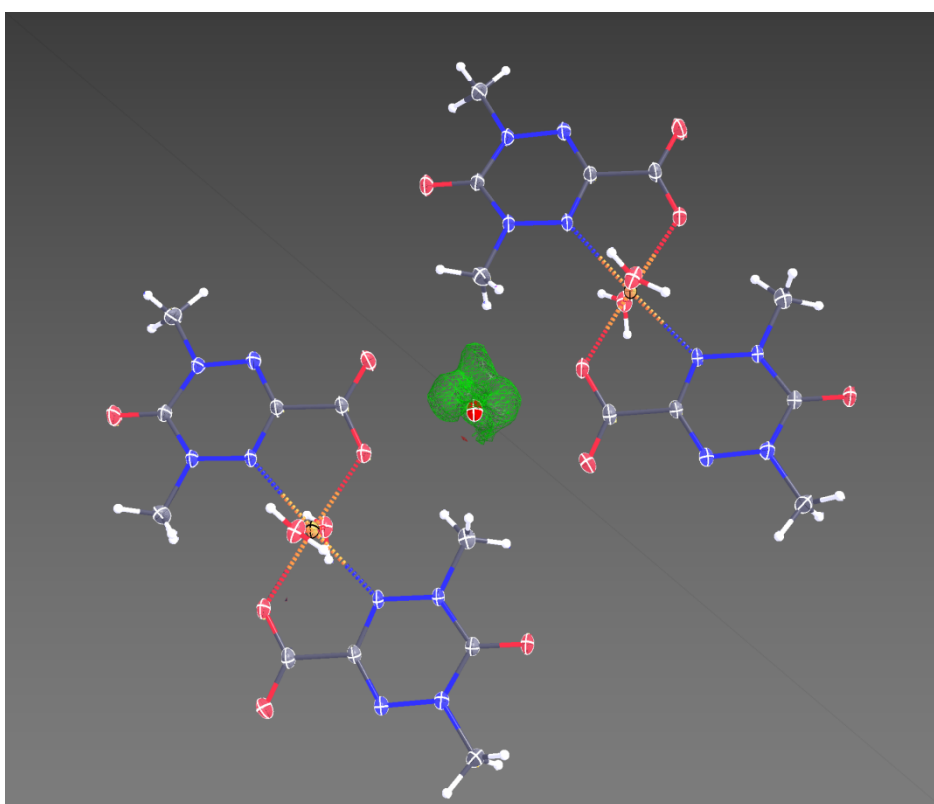


**Figure 7.2.** Electron density difference map for hydrogen atoms of coordinated water II (around O2) in **1** at (a) 300 K and (b) 90 K.

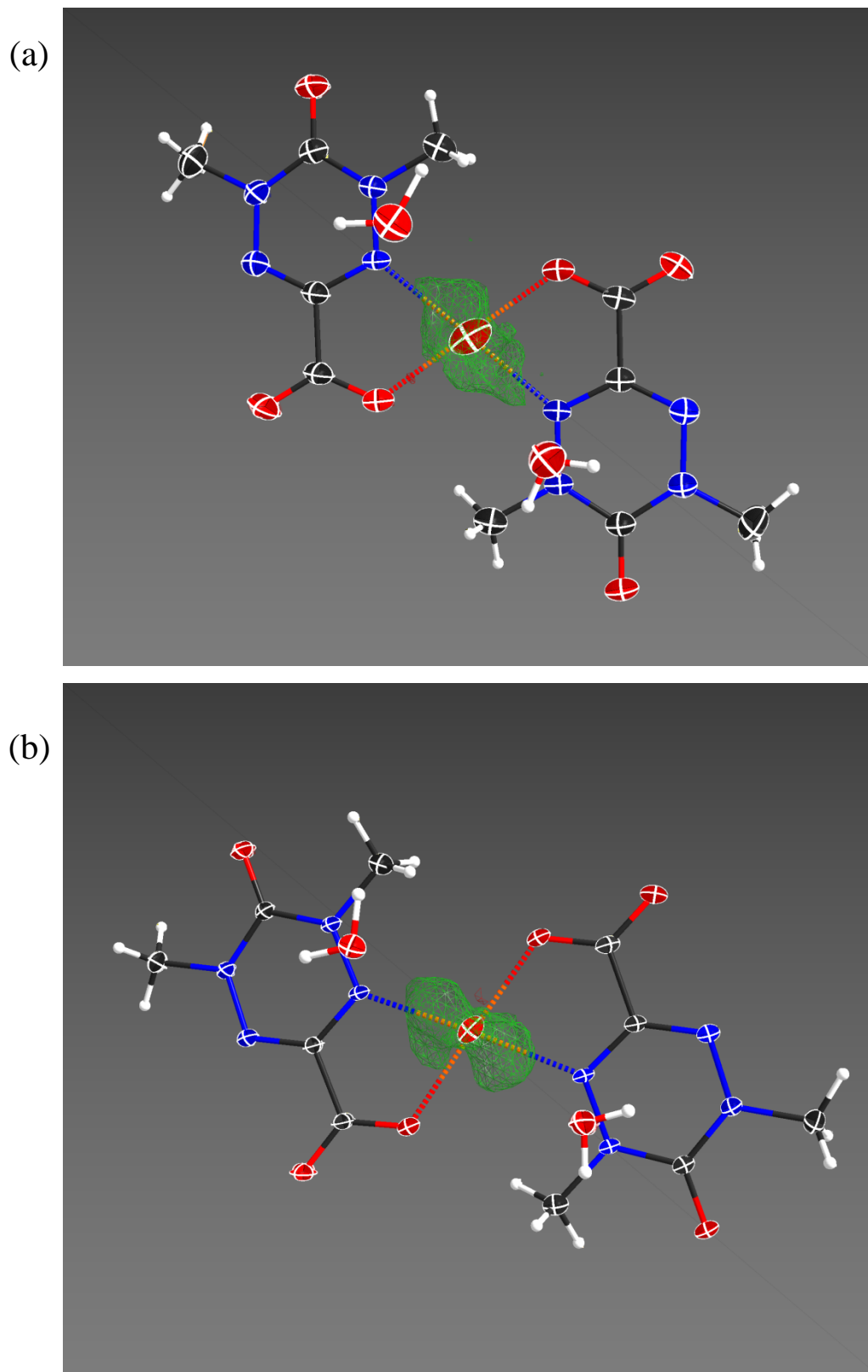


**Figure 7.3.** Electron density difference map for hydrogen atoms of the coordinated water I (around O1) in **1** at (a) 300 K and (b) 90 K.

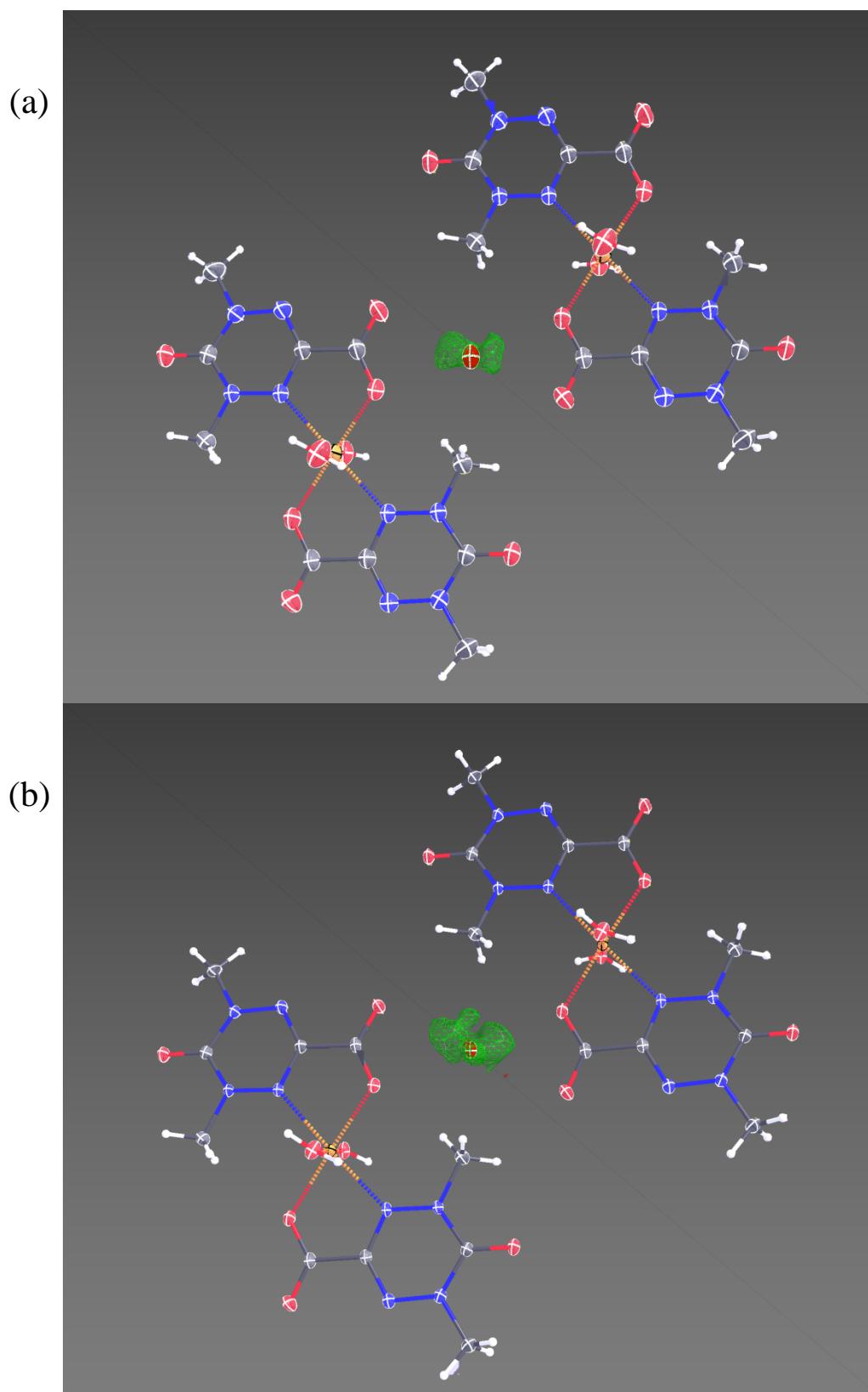


**Figure 7.4.** Electron density difference map for deuterium atoms of the coordinated water II (around O2) in **2** at (a) 300 K and (b) 90 K.

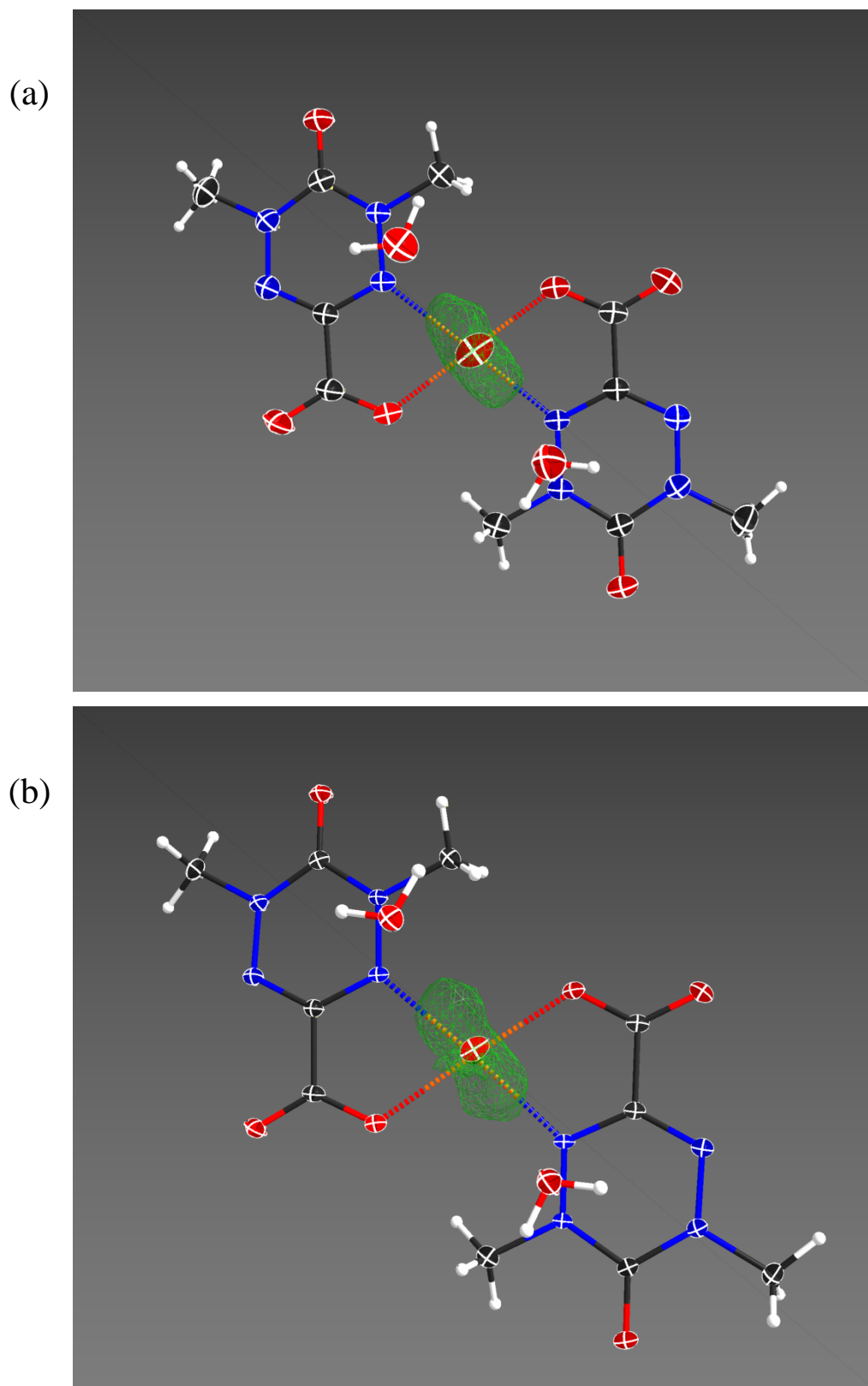


**Figure 7.5.** Electron density difference map for deuterium atoms of the coordinated water I (around O1) in **2** at (a) 300 K and (b) 90 K.

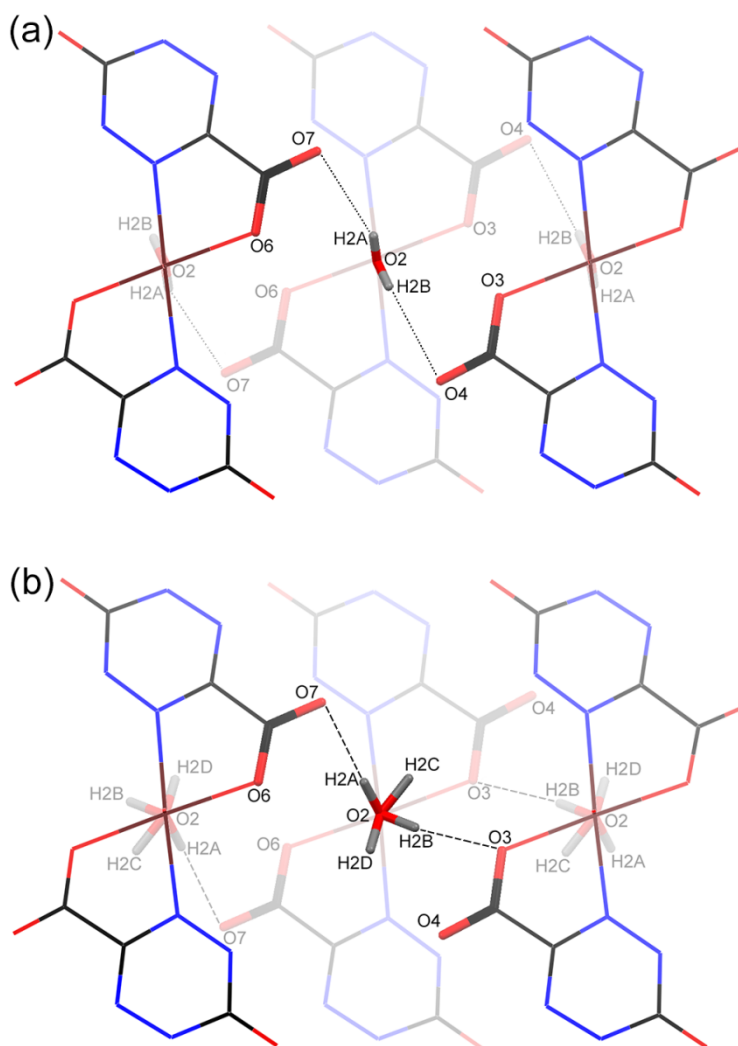


**Figure 7.6.** H-bonds implying coordinated water II in **1** at (a) 300 K and (b) 90 K. Methyl groups, coordinated water I, and crystallization water molecules are omitted for clarity. Long H-bonds at 300 K are denoted by the dotted lines whereas short H-bonds at 90 K are denoted by the dashed lines.

### <sup>57</sup>Fe Mössbauer spectroscopy

Figure 7.7 shows the <sup>57</sup>Fe Mössbauer spectra of **1** and **2** at various temperatures. In the whole temperature range between 10 K and 300 K, in both compounds, two kinds of doublets were observed, which have almost the same value of isomer shift ( $\delta$ ) but slightly different values of quadrupole splitting ( $\Delta E_Q$ ) (Table 7.4 for **1** and Table 7.5 for **2**). The  $\delta$  values (1.12–1.28 mm s<sup>-1</sup>) of both doublets are much comparable to one another and are larger by *ca.* 0.5 mm s<sup>-1</sup> compared to that

of a typical iron(III) ion.<sup>[16]</sup> Moreover, the  $\Delta E_Q$  values in the two species are typical values of the HS state ( $S = 2$ ) iron(II) species.<sup>[17]</sup> Both species appearing in the Mössbauer spectra are thus HS-iron(II) species, ruling out the possibility of valence tautomerism<sup>[18]</sup> between  $\text{Fe}^{\text{II}}$  and the verdazyl radical or the occurrence of iron-based spin crossover (SCO). Accordingly, the two set of signals are attributed to different structural forms of the HS-iron(II) compound referred as HT for the one which predominates at high temperature and LT for the one dominating at low temperature.

The intensity ratio of the two doublets varies dramatically with temperature. At 300 K, the inner doublet with smaller  $\Delta E_Q$  is dominant with a relative area of 75.3% for **1** then its intensity gradually decreases with decreasing temperature. The outer doublet with larger  $\Delta E_Q$  undergoes the reverse evolution and it eventually becomes the dominant part of the spectrum below 60 K for **1** and 80 K for **2**. The evolution of the relative intensities of the two doublets is very smooth and continuous (Figure 7.8).

The continuous change in the intensity ratio of the two doublets in the whole temperature range and their coexistence without thermal hysteresis rules out the existence of a phase transition in favor of an equilibrium phenomenon. This is consistent with the specific heat measurement performed on **1** by a relaxation method, where no anomaly was observed (Figure 7.9). Therefore, the abundance ratio of HT and LT species changes as a function of temperature under the control of Gibbs energy ( $\Delta G = \Delta H - T\Delta S$ ). It is possible to relate the LT and HT species fractions,  $f_{\text{LT}}$  and  $f_{\text{HT}}$ , to the thermodynamic quantities associated with this equilibrium by the following expression:

$$f_{\text{LT}} = \frac{\exp\left(-\frac{\Delta S}{R} + \frac{\Delta H}{RT}\right)}{1 + \exp\left(-\frac{\Delta S}{R} + \frac{\Delta H}{RT}\right)}, \quad f_{\text{HT}} = \frac{1}{1 + \exp\left(-\frac{\Delta S}{R} + \frac{\Delta H}{RT}\right)} \quad (7.1)$$

Eq. (7.1) was used to fit the thermal evolution of the relative area of the two doublets observed in the  $^{57}\text{Fe}$  Mössbauer spectra of **1** and **2** (Figure 7.8). This gives  $\Delta H_1 = 0.68(4) \text{ kJ mol}^{-1}$ ,  $\Delta S_1 = 11.6(5) \text{ J K}^{-1} \text{ mol}^{-1}$  for **1**, and  $\Delta H_2 = 0.84(6) \text{ kJ mol}^{-1}$ ,  $\Delta S_2 = 10.3(7) \text{ J K}^{-1} \text{ mol}^{-1}$  for **2**. The values of the thermodynamic constants extracted from the fit are smaller by at least one order of magnitude than those encountered in valence tautomerism or SCO transitions determined by specific heat measurements, for example.<sup>[18]</sup> The differences observed between **1** and **2** confirms quantitatively the influence of the deuterium isotopic effect on the equilibrium between the HT and LT forms anticipated by the 20 K difference in the temperature where the two forms are equiprobable (Figure 7.8). This strong deuterium isotope effect indicates that hydrogen atoms close to the iron(II) center, *e.g.* able to affect the electric field gradient at the iron nucleus, evolve when the dominant form shifts from the HT form to the LT form. Those of the coordinated water molecules are good candidates all the more that the isotopic effect affects the hydrogen bonding and hence the total Gibbs energy. The existence of two forms of the complex and the isotopic effect are compatible with the explicit disorder of the H atoms of coordinated water molecule II found in the X-ray diffraction analysis at 90 K. These observations indeed indicate that this water molecule is engaged in the equilibrium between the two forms. In order to investigate the effect of dynamical motion of water molecules, we performed solid-state high-resolution  $^2\text{H}$ -MAS-NMR measurements for **2**.

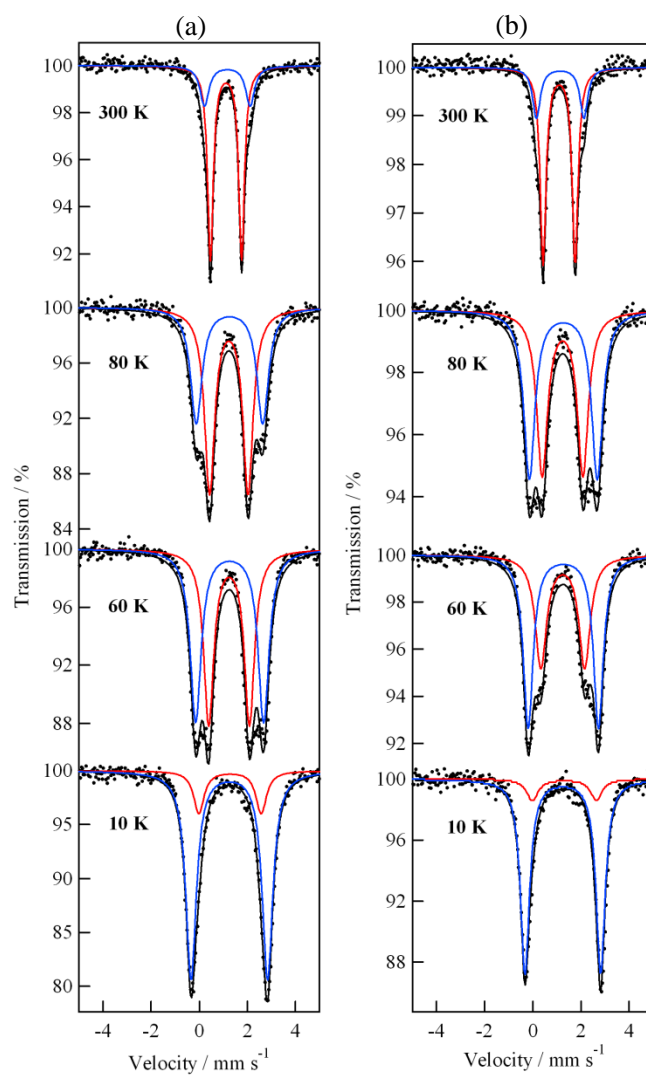


**Figure 7.7.**  $^{57}\text{Fe}$  Mössbauer spectra at various temperatures for (a) **1** and (b) **2**. The solid lines are best fits to the data points.

**Table 7.4.** Temperature Dependence of Mössbauer Parameters for **1**.

$T$ (K)	$\delta$ (mm s <sup>-1</sup> )		$\Delta E_Q$ (mm s <sup>-1</sup> )		$\Gamma$ (mm s <sup>-1</sup> )		Relative area	
	HT	LT	HT	LT	HT	LT	HT	LT
300	1.116	1.169	1.299	1.901	0.284	0.446	0.753	0.247
250	1.142	1.198	1.335	2.022	0.391	0.543	0.760	0.240
200	1.167	1.196	1.441	2.250	0.445	0.563	0.726	0.274
150	1.196	1.236	1.436	2.465	0.445	0.581	0.704	0.296
100	1.221	1.253	1.530	2.694	0.464	0.568	0.634	0.366
80	1.234	1.260	1.599	2.765	0.511	0.575	0.585	0.415
70	1.234	1.260	1.644	2.811	0.505	0.555	0.545	0.455
60	1.245	1.266	1.695	2.828	0.506	0.546	0.483	0.517
50	1.232	1.249	1.833	2.903	0.562	0.487	0.469	0.531
40	1.260	1.268	1.996	2.946	0.612	0.530	0.373	0.627
30	1.244	1.250	2.233	3.047	0.659	0.425	0.338	0.662
20	1.250	1.250	2.357	3.143	0.583	0.492	0.259	0.741
10	1.282	1.251	2.594	3.181	0.529	0.530	0.170	0.830

$\delta$ : Isomer shift,  $\Delta E_Q$ : Quadrupole splitting,  $\Gamma$ : Line width, HT: Predominant species at high temperature, LT: Predominant species at low temperature.

**Table 7.5.** Temperature Dependence of Mössbauer Parameters for **2**.

$T$ (K)	$\delta$ (mm s <sup>-1</sup> )		$\Delta E_Q$ (mm s <sup>-1</sup> )		$\Gamma$ (mm s <sup>-1</sup> )		Relative area	
	HT	LT	HT	LT	HT	LT	HT	LT
300	1.096	1.139	1.328	1.968	0.290	0.390	0.742	0.258
250	1.137	1.180	1.364	2.012	0.418	0.503	0.707	0.293
200	1.174	1.228	1.440	2.302	0.447	0.595	0.673	0.327
150	1.181	1.221	1.497	2.470	0.487	0.577	0.630	0.370
100	1.224	1.250	1.609	2.720	0.493	0.573	0.530	0.470
90	1.228	1.257	1.676	2.762	0.578	0.620	0.514	0.486
80	1.238	1.270	1.688	2.819	0.548	0.559	0.487	0.513
70	1.240	1.269	1.725	2.858	0.545	0.540	0.446	0.554
60	1.247	1.272	1.816	2.917	0.570	0.493	0.428	0.572
50	1.227	1.244	1.950	2.973	0.613	0.507	0.383	0.617
40	1.259	1.271	2.121	3.020	0.640	0.457	0.361	0.639
30	1.250	1.250	2.063	3.045	0.582	0.409	0.291	0.709
20	1.313	1.250	2.357	3.143	0.511	0.465	0.202	0.798
10	1.313	1.250	2.652	3.143	0.572	0.456	0.122	0.878

$\delta$ : Isomer shift,  $\Delta E_Q$ : Quadrupole splitting,  $\Gamma$ : Line width, HT: Predominant species at high temperature, LT: Predominant species at low temperature.

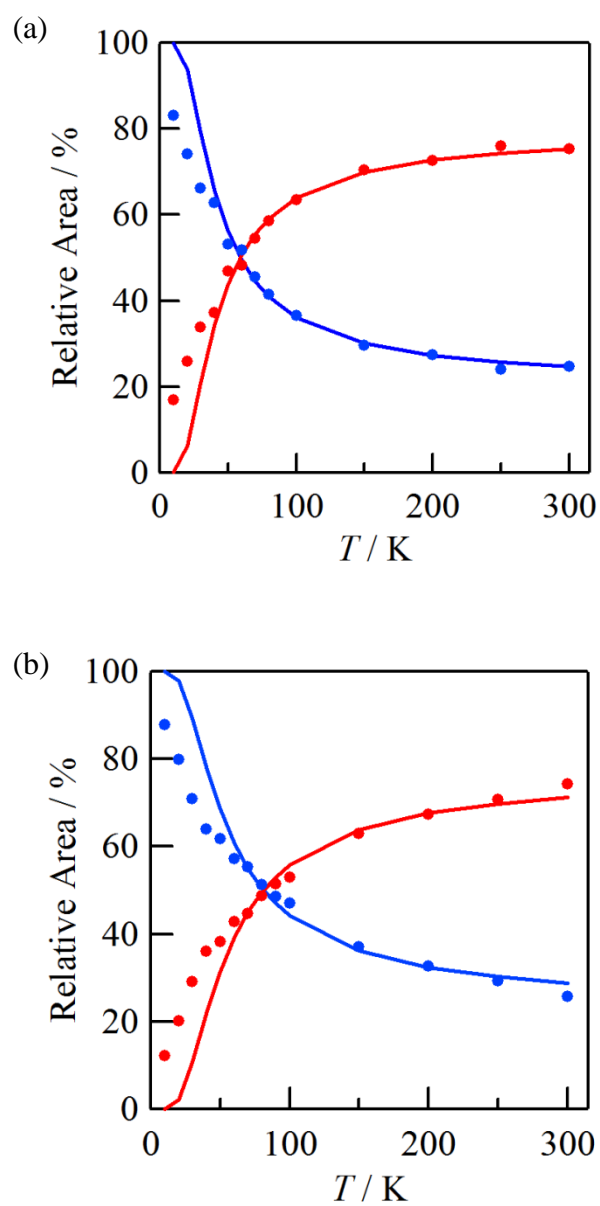


**Figure 7.8.** Experimental (filled circles) and calculated (solid lines) relative area of the Mössbauer signals of the HT (red) and LT (blue) forms of (a) **1** and (b) **2**.

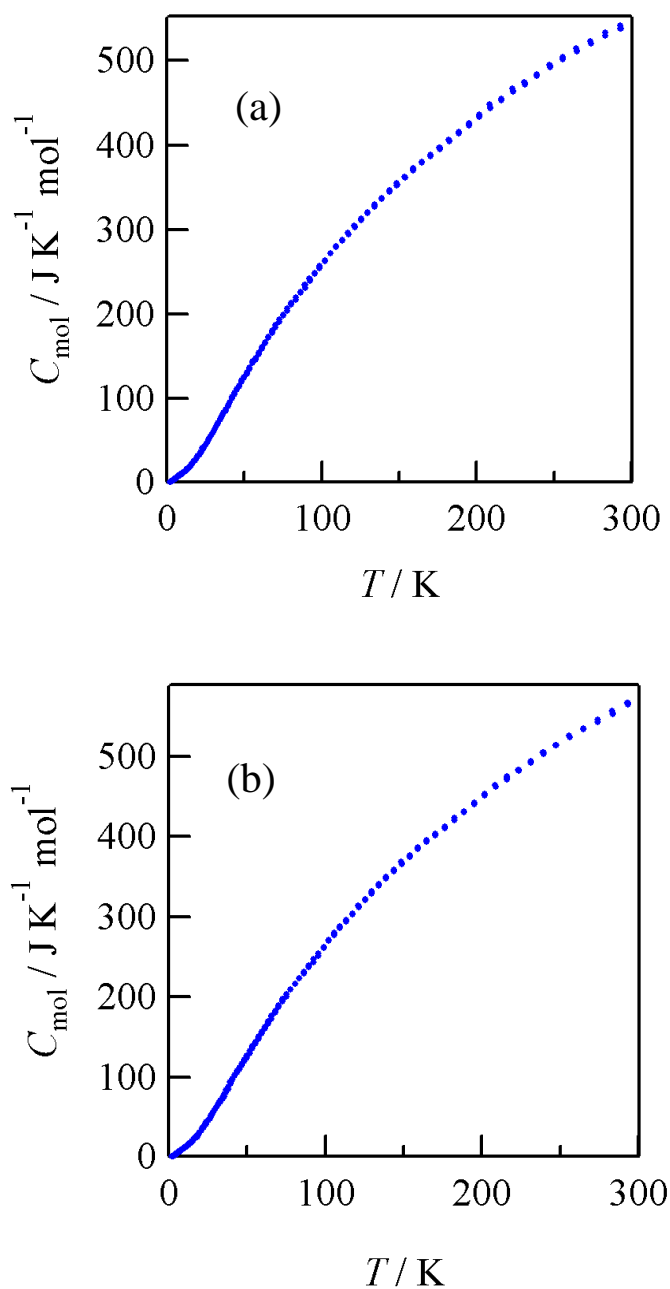


**Figure 7.9.** Temperature dependence of molar heat capacity measured by relaxation method. (a) **1**, (b) **2**.

### Solid state $^2\text{H}$ -MAS-NMR

Because the deuterium nucleus has a nuclear spin  $I$  equal to 1,  $^2\text{H}$  NMR line shapes of powdered samples depend on the quadrupole interaction and are thus sensitive to local molecular motion

between ~100 kHz and a few MHz.<sup>[19]</sup>

At room temperature, the total  $^2\text{H}$ -MAS-NMR spectra of **2** can be deconvolved into three components related to three different  $\text{D}_2\text{O}$  molecules (Figure 7.10). This is consistent with the structural analysis of **1** and **2** where crystallization and two types of coordinated water molecules were identified. The signal at  $\delta_{\text{iso}} = +16$  ppm (Figure 7.10(d)) has the smallest paramagnetic shift among the three components. It can thus be assigned to the deuterium atoms that are the farthest from the paramagnetic center, *e.g.* the two crystallization water molecules. Accordingly, the linewidth of the peaks are small compared to that of the two other signals, and the integral intensity reaches almost 50%. The signals centered at  $\delta_{\text{iso}} = +46$  ppm have a Pake doublet-type shape (Figure 7.10(b)). This is indicative of deuterium atoms that have a low mobility.<sup>[19]</sup> In the present case, it can be attributed to those engaged in strong H-bonds. According to the X-ray diffraction structural analysis at 90 and 300 K, this set of signals arises from the deuterium atoms of coordinated water molecule I. In contrast, the signals centered at  $\delta_{\text{iso}} = -22$  ppm have a Bell-type shape (Figure 7.10(c)). This is indicative of deuterium atoms exhibiting a high mobility.<sup>[19]</sup> Following the structural analysis at 300 K, they are attributed to the highly agitated deuterium atoms, that is, those of coordinated water molecule II. Moreover, the spinning sideband pattern suggests that the coordinated water molecule II experiences a  $180^\circ$  flip-flop motion.<sup>[19]</sup>

By varying the temperature, it is possible to vary the frequency of the moving nucleus. Recording the  $^2\text{H}$ -MAS-NMR spectra of **2** in a wide range of temperatures (310–193 K) opens the opportunity to probe these variations (Figure 7.11). The bell-shape of the total spectrum remained down to 193 K. In addition, complicated peaks appear below 278 K. This feature is a result of different paramagnetic coupling with electron spin for different deuterium atoms. Eventually, deconvolution to each component is impossible. The conservation of the overall shape indicates that molecular motions of the water molecules, in particular, the  $180^\circ$  flip-flop motions of the

coordinated water molecule II are still active down to 193 K, although their rates decrease as temperature decreased as commonly expected.

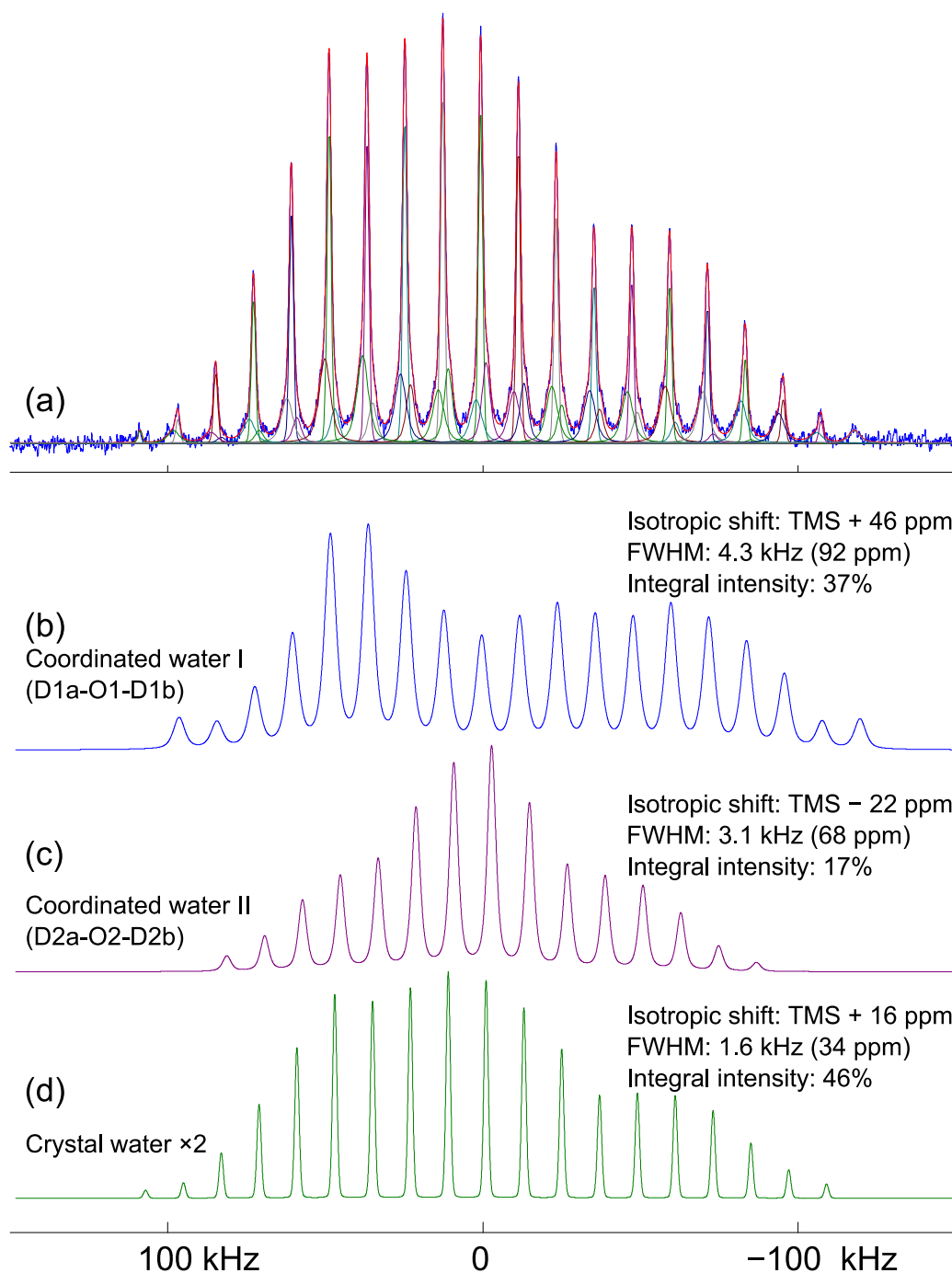


**Figure 7.10.** (a) Experimental solid-state  $^2\text{H}$ -MAS-NMR spectra of **2** measured at a MAS speed of 12 kHz at room temperature. It can be deconvoluted into three components attributed to the three types of water molecules identified by X-ray diffraction: (b) coordinated water molecule I (D1a-O1-D1b), (c) coordinated water molecule II (D2a-O2-D2b), and (d) crystallization water molecules. The integrated intensities of the components (c) and (d) are underestimated due to the motional processes.

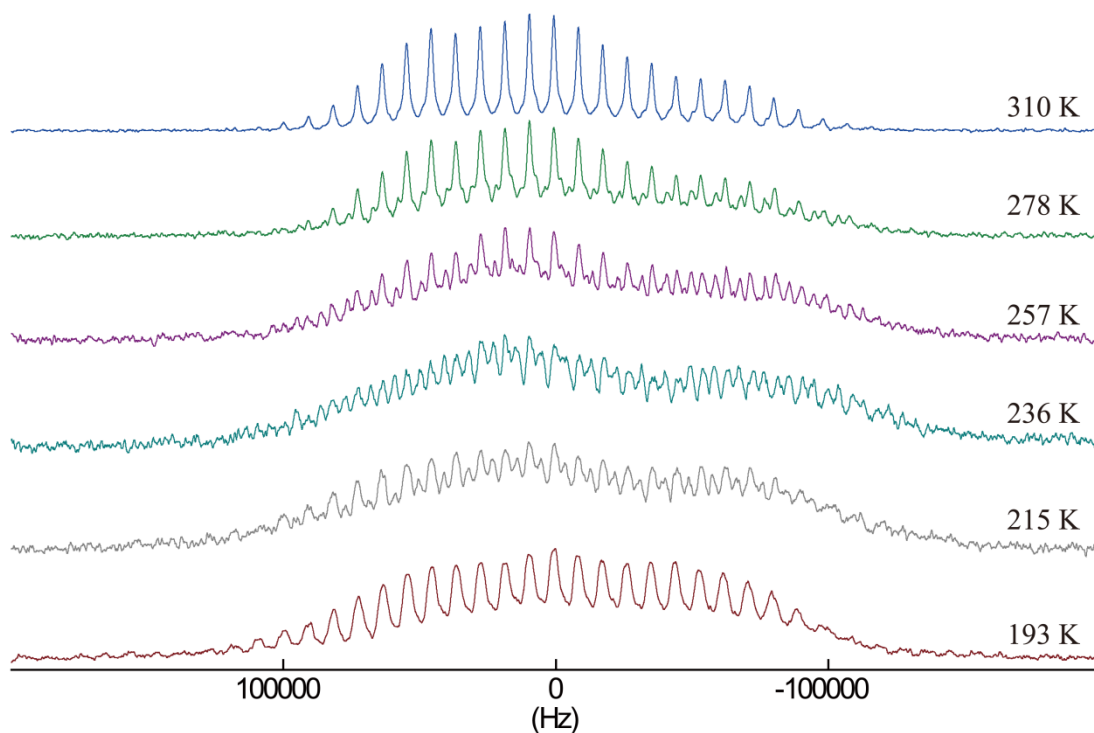


**Figure 7.11.** Temperature dependence of solid-state  $^2\text{H}$ -MAS-NMR spectra measured at MAS speed of 9 kHz between 310 K (top) and 193 K (bottom) for **2**.

### Magnetic properties

Figure 7.12 shows the temperature dependence of the molar magnetic susceptibility multiplied by temperature,  $\chi_{\text{M}}T$ , of **1** in an external magnetic field of 5000 Oe. The  $\chi_{\text{M}}T$  value at room temperature is  $4.07 \text{ cm}^3 \text{ K mol}^{-1}$ . It is slightly larger than the spin-only value ( $3.75 \text{ cm}^3 \text{ K mol}^{-1}$ ) expected for three noninteracting magnetic centres: one HS  $\text{Fe}^{\text{II}}$  ( $S = 2$ ) and two  $\text{vdCOO}^-$  radicals ( $S = 1/2$ ,  $g = 2$ ). When the temperature is decreased the  $\chi_{\text{M}}T$  product of **1** decreases continuously with a slight inflexion around 15 K. The overall shape of the curve indicates the presence of at least two antiferromagnetic (AF) couplings of different magnitude with a possible contribution from the zero-field splitting (ZFS) of the iron(II) center.

In order to estimate quantitatively the corresponding parameters, it is necessary to adopt a

realistic spin model. The most natural one is given by the results of the X-ray diffraction analysis. Here, the  $J_{\text{Fe-vd}}$  and  $J_{\text{vd-vd}}$  exchange interactions according to Scheme 7.2 as well as the ZFS  $D_{\text{Fe}}$  on the iron(II) center are introduced in the Hamiltonian:

$$\begin{aligned} \mathbf{H} = & -J_{\text{Fe-vd}}(\mathbf{S}_{\text{vd1}}\mathbf{S}_{\text{Fe}} + \mathbf{S}_{\text{vd2}}\mathbf{S}_{\text{Fe}}) - J_{\text{vd-vd}}\mathbf{S}_{\text{vd1}}\mathbf{S}_{\text{vd2}} \\ & + D_{\text{Fe}}[S_{z,\text{Fe}}^2 - 1/3S_{\text{Fe}}(S_{\text{Fe}} + 1)] + g_{\text{Fe}}\mu_{\text{B}}\mathbf{S}_{\text{Fe}}\mathbf{B} \\ & + g_{\text{vd}}\mu_{\text{B}}(\mathbf{S}_{\text{vd1}} + \mathbf{S}_{\text{vd2}})\mathbf{B} \end{aligned} \quad (7.2)$$

where  $\mathbf{S}_i$  are the spins,  $g_i$  are the Landé factors,  $\mathbf{B}$  the magnetic induction and  $\mu_{\text{B}}$  the Bohr magneton.

Assuming the  $g_{\text{vd}}$  value of the verdazyl radicals to be 2, the parameters extracted from the fit of the experimental data are  $J_{\text{Fe-vd}} = -27.1 \text{ cm}^{-1}$ ,  $J_{\text{vd-vd}} = -42.8 \text{ cm}^{-1}$ ,  $g_{\text{Fe}} = 2.25$ , and  $D_{\text{Fe}} = +3.37 \text{ cm}^{-1}$ . The fitted curve matches the experimental data in the whole temperature range (Figure 7.12). The derived values of  $J_{\text{Fe-vd}}$  and  $J_{\text{vd-vd}}$  confirm the existence of AF interactions between the spin bearers. It should be noted that, in these systems, AF intermolecular interactions are likely to occur through H-bonds or  $\pi$ - $\pi$  interactions.<sup>[20]</sup> They have been neglected to avoid any overparametrization of the system and allow the comparison to the nickel and cobalt analogues.<sup>[7]</sup> In this series of complexes, this assumption is much reasonable since the closest contact between verdazyl ligands involves the oxygen atom of the carbonyl group which bears a vanishingly small spin density.<sup>[21]</sup>

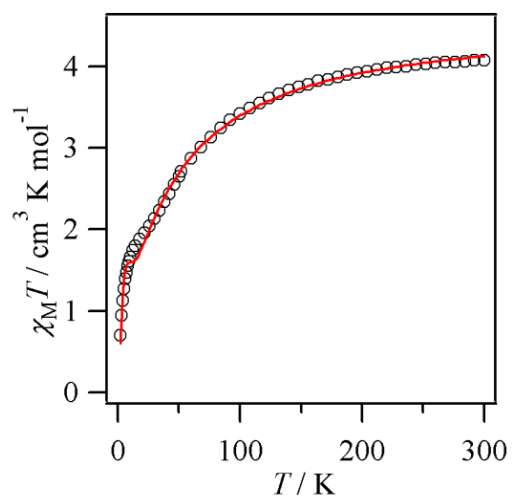
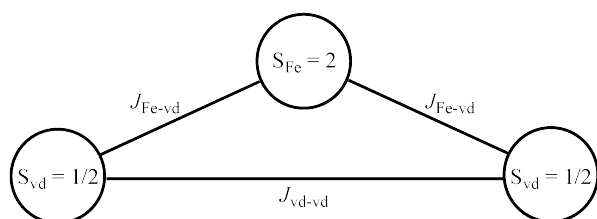


**Figure 7.12.** The  $\chi_M T$  versus  $T$  plots for **1**. The red solid line represents a fitting curve, and the black open circles are experimental values.



**Scheme 7.2.** Schematic representation of vd–Fe<sup>II</sup>–vd spin model.

## 7.4 Discussion

### Temperature-dependent H-bonding

In the  $^{57}\text{Fe}$ Mössbauer spectrum of **1**, the coexistence of two doublets was observed in a wide temperature range and the remarkable temperature dependence of their intensity ratio in spite of the single iron(II) site in a unit cell, which motivated more accurate structural and spectroscopic determination than those published on the cobalt(II) and nickel(II) analogues.<sup>[7]</sup> Thus, the single-crystal X-ray diffraction at room temperature and 90 K on **1** and **2**,  $^{57}\text{Fe}$  Mössbauer spectroscopy on **1** and **2** between 300 and 10 K and solid-state  $^2\text{H}$ -MAS-NMR spectroscopy on **2** between 310 and 193 K have been performed. The results of these different techniques are now discussed and compared below.

The X-ray diffraction analysis provides a snapshot of the system at room temperature and at 90 K. Whereas at 300 K, the situation is blurry, at 90 K, two forms of the compound can be identified, one where the coordinated water molecule II establishes short H-bonds with neighboring molecules (O3 and O7 in Figure 7.6(b)) and the other where it does not establish any H-bonds. The presence of H-bonds in one of the two forms indicates that this form should be the most stable. It should thus correspond to the LT form identified by Mössbauer spectroscopy. This technique shows that the LT and HT forms are coexisting in a wide range of temperatures. The HT-to-LT ratio found for **1** at 90 K is close to the occupation factor refined from X-ray for H2C and H2D at this temperature. As stated by solid-state NMR, this coexistence is possible because the motion of coordinated water molecule II, though reduced when the temperature decreases, remains high even at 193 K.

The values of the thermodynamic quantities associated with the two forms of the compound were extracted from Mössbauer spectroscopy. They are much smaller than those encountered in

valence tautomeric cobalt(II/III) complexes and iron(II) SCO systems. In these systems, the entropy variations associated with the change in spin multiplicity  $\Delta S_{\text{spin}}$  is worth  $R \ln(16/4) = 11.53 \text{ J K}^{-1} \text{ mol}^{-1}$  for the tautomeric cobalt systems and  $R \ln(5/1) = 13.38 \text{ J K}^{-1} \text{ mol}^{-1}$  for the iron(II) SCO systems. Accordingly, the vibrational contribution to the entropy variation  $\Delta S_{\text{vib}}$  ranges between 35 and  $65 \text{ J K}^{-1} \text{ mol}^{-1}$ . These values of  $\Delta S_{\text{vib}}$  arise from the variation (*ca.*  $0.2 \text{ \AA}$ ) of metal–ligand bond lengths.<sup>[18b,22]</sup> In the present case, there is no change in valence or spin states, and thereby  $\Delta S_{\text{spin}}$  is zero. Moreover, as shown by X-ray diffraction, the structural changes are much less dramatic. Around the metal ion, the change in  $\text{Fe}^{\text{II}}$ –ligand bond lengths ranges from  $0.001$  to  $0.027 \text{ \AA}$ . This is essentially related to thermal contraction. The main structural change between the two forms of the compound is attributed to the modification of the H-bonding of one of the two coordinated molecules, explaining the weak values of the thermodynamical quantities associated with the HT-to-LT equilibrium. As shown in the Mössbauer spectra, the interconversion remains possible even when the temperature is severely lowered. Accordingly, the two forms of the compounds are seen by X-ray diffraction at  $90 \text{ K}$  and down to  $10 \text{ K}$  by Mössbauer spectroscopy whereas the motion of the coordinated water molecule II is still very rapid at  $193 \text{ K}$  justifying that they cannot be distinguished by single-crystal X-ray diffraction at  $300 \text{ K}$ .

By exploiting the different timescales of Mössbauer and NMR spectroscopies, it is possible to specify a range for the exchange rate between the HT and LT forms of the complex. This rate is indeed well below  $\sim 10 \text{ MHz}$  (the time scale ( $\tau \sim 10^{-7} \text{ s}$ ) in Mössbauer spectroscopy), since the two forms were clearly distinguished by Mössbauer spectroscopy between  $10$  and  $300 \text{ K}$ . Moreover, only the rapid  $180^\circ$  flip-flop motion was detected by NMR for the coordinated water molecule II in the whole temperature range. Accordingly, the exchange rate must be much smaller than the quadrupole interaction of the deuterium atom, *e.g.* less than or in the kHz range.

In conclusion, it appears that each technique brings a complementary vision of the structure of

this intriguing system. Their combination leads to a complete description of the system, summed up in Figure 7.13.

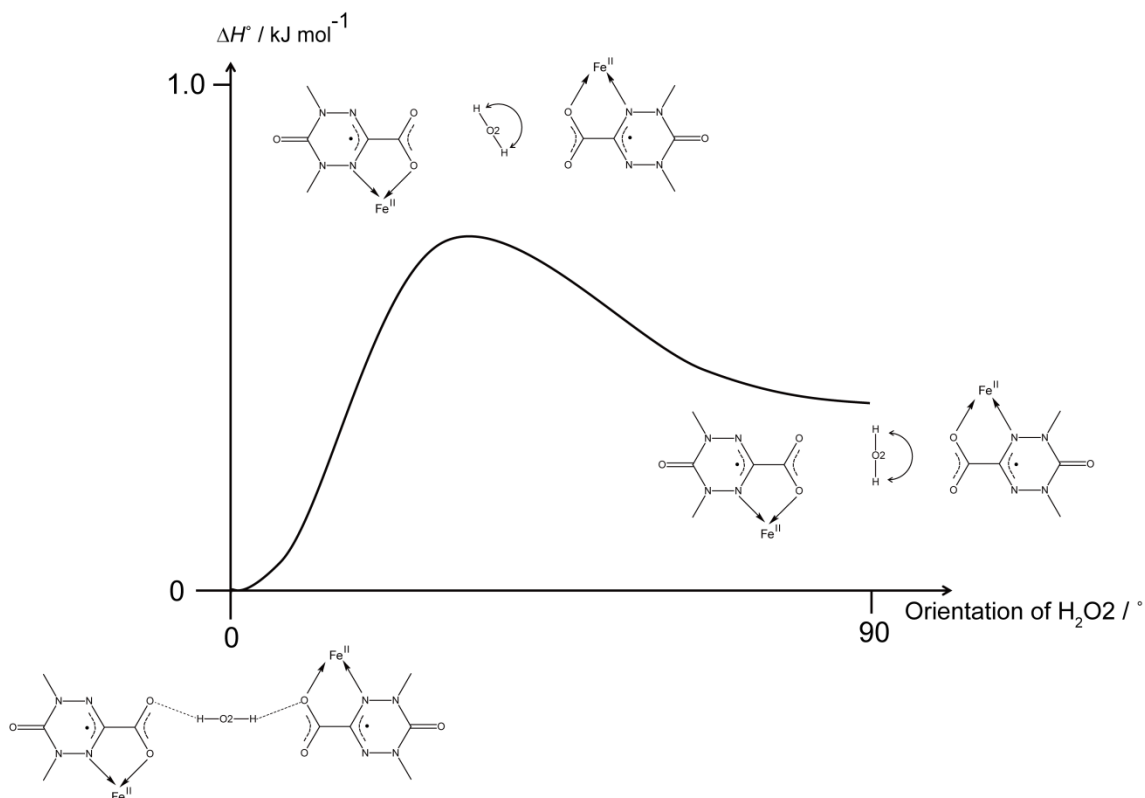


**Figure 7.13.** Schematic representation of the equilibrium between the two forms of the compound based on the combined conclusions of all the physico-chemical techniques.

### Exchange coupling

The fit of the magnetic susceptibility (Figure 7.12) is not sensitive to these subtle changes in the structure of the compounds because the intermolecular interactions are not considered. Compound **1** is interesting because its magnetic behavior can be compared with the ones of cobalt(II) and nickel(II) analogues.<sup>[7]</sup> Figure 7.14 shows the plot of the exchange interaction parameters,  $J_{M-vd}$  and  $J_{vd-vd}$ , extracted from the fits versus the number of 3d electrons of the  $M^{II}$  center. The coupling constant  $J_{M-vd}$  between the metal ion and the verdazyl radicals varies from strongly ferromagnetic

(F) for Ni<sup>II</sup> to weakly AF for Fe<sup>II</sup> when decreasing the number of 3d electrons, whereas  $J_{\text{vd-vd}}$  values remain practically unchanged and are AF. A simple qualitative orbital interpretation of such a phenomenon can be proposed using Kahn's model.<sup>[1a,d,24]</sup> In this frame, in a system with  $n_{\text{M}}$  unpaired electrons on the metal ion and  $n_{\text{vd}}$  on the ligand, the overall coupling constant  $J_{\text{M-vd}}$  is decomposed into two-electrons/two-orbitals pathways and becomes the weighted sum of the different exchange pathways  $j_{\text{M-vd}}$  between the singly occupied orbital of the radical and those of the d metal ion.

$$J_{\text{M-vd}} = \frac{1}{n_{\text{M}}n_{\text{vd}}} \sum_{\text{M,vd}} j_{\text{M-vd}} \quad (7.3)$$

The radical has one magnetic orbital ( $n_{\text{vd}} = 1$ ) which is essentially an antibonding  $\pi^*$  orbital delocalized over the verdazyl ring.<sup>[21]</sup> For the metal ion, going from nickel(II) to HS iron(II), the electronic structures are Ni<sup>II</sup>:  $t_{2g}^6 e_g^{*2}$ , Co<sup>II</sup>:  $t_{2g}^5 e_g^{*2}$ , and Fe<sup>II</sup>:  $t_{2g}^4 e_g^{*2}$ . The two electrons in the antibonding  $e_g^*$  orbitals remain unpaired, whereas the  $t_{2g}$  orbitals are gradually emptied. The number of  $t_{2g}$  magnetic orbitals increases from 0 in nickel(II) to 2 in iron(II) and the total number of magnetic orbitals  $n_{\text{M}}$  increases from 2 in Ni<sup>II</sup> to 4 in Fe<sup>II</sup>. The interaction pathways are F when orthogonality prevails as in  $j_{e_g^*-\pi^*}$  (Figure 7.15(a)) or AF when overlap is present as in  $j_{t_{2g}-\pi^*}$  (Figure 7.15(b)).

The interpretation is then straightforward for the nickel(II) derivative – the metal-centered magnetic orbitals ( $e_g^*$ ) are orthogonal to the magnetic orbital of the radicals (Figure 7.15(a)) hence the two exchange pathways  $j_{e_g^*-\pi^*}$  are F and the overall interaction is therefore F.<sup>[7]</sup> In the cobalt(II) derivative, the withdrawn electron creates a  $t_{2g}$  magnetic orbital which has a nonzero overlap with the magnetic orbital of the radicals (Figure 7.15(b)) and a third pathway leading to a  $j_{t_{2g}-\pi^*}$  AF contribution to the exchange interaction that reduces the overall F exchange interaction. In the high

spin iron(II) derivative, a new magnetic  $t_{2g}$  orbital creates a fourth pathway and a second  $j_{t_{2g}-\pi^*}$  AF interaction leading to an overall AF contribution. In summary, the antiferromagnetic contributions are more and more important from the nickel(II) ion to the iron(II) ion and the  $J_{M-vd}$  values vary accordingly from F to AF. This series can thus appear as a textbook example of Kahn's model.<sup>[1a,d]</sup> Finally, the verdazyl–verdazyl interaction is governed by the overlap of the two ligands'  $\pi^*$  magnetic orbitals (Figure 7.15), due to the *trans*-localization of the two verdazyl rings with respect to the metal ion (Figure 7.1). The intramolecular exchange interaction is then AF and also follows the aforementioned Kahn's model.

The variation of  $J_{M-vd}$  with the number of 3d electrons of the metal ion (Figure 7.14) nicely illustrates our qualitative discussion. To go further, it is possible to combine the experimental data for the three complexes (Table 7.6) and Eq. (7.3) to estimate  $j_{e_g^*-\pi^*}$  and  $j_{t_{2g}-\pi^*}$ , the exchange interaction parameters between the two types of 3d orbitals ( $t_{2g}$ ,  $e_g^*$ ) of  $M^{II}$  and the  $\pi^*$  orbital of the verdazyl radical. With no  $j_{t_{2g}-\pi^*}$  term, the nickel(II) case directly leads to  $j_{e_g^*-\pi^*} = +188 \text{ cm}^{-1}$ . Assuming this value as metal-independent does not allow us to converge to a single value for  $j_{t_{2g}-\pi^*}$ . This is an indication that both parameters are indeed metal-dependent. This dependency, which is not taken into account in the magnetic orbitals model, is related to the existence of other interaction mechanisms as those previously identified in other metal–verdazyl complexes.<sup>[23]</sup> They are more sophisticated, involve other orbitals, vacant or doubly filled, necessitate time-consuming computations. They have been implemented with success in the study of the copper(II)–verdazyl interaction, *e.g.* with two unpaired electrons.<sup>[23]</sup> Their extrapolation to the present series with more unpaired electrons represents a challenge. A refined interpretation, including other orbitals on the ligand and on the metal center can be expected.<sup>[1d]</sup>

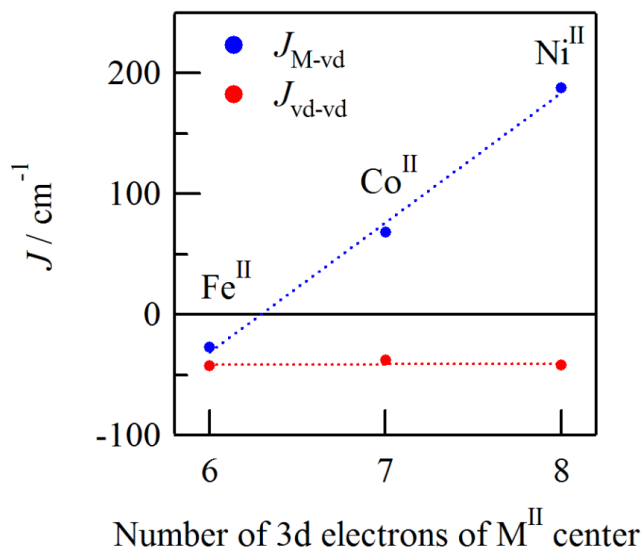


**Figure 7.14.** Plots for the exchange coupling constants  $J_{ij}$  ( $\mathbf{H} = -J_{ij}\mathbf{S}_i\mathbf{S}_j$ ) vs. 3d electron number of the M<sup>II</sup> center. The values for Co<sup>II</sup> and Ni<sup>II</sup> complexes are adapted from ref.[7]. The dotted lines are guides to the eye.

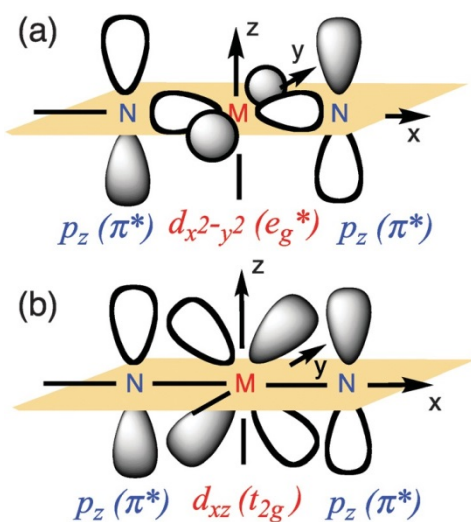


**Figure 7.15.** Interaction between the magnetic orbitals of the ligands (blue) and of the metal (red): orthogonality between ligands  $p_z(\pi^*)$  and metal  $e_g^*$  orbitals (a); overlap between ligands  $p_z(\pi^*)$  and metal  $t_{2g}$  orbitals (b).

**Table 7.6a.** Experimental  $J$  values ( $H = -J_{ij}S_iS_j$ )

$J / \text{cm}^{-1}$	$J_{M-rad}$	$J_{rad-rad}$	Ref.
$\text{Fe}^{\text{II}}$	-27.1	-42.8	this work
$\text{Co}^{\text{II}}$	+68	-42	[7]
$\text{Ni}^{\text{II}}$	+188	-38	[7]

**Table 7.6b.** Equations for the analysis of the magnetic data using Eq. (7.3)

Metal ion	$J_{M-rad}$	Eq. number
$\text{Fe}^{\text{II}}$	$(1/2) [j_{t2g-\pi^*} + j_{eg^*-\pi^*}]$	(7.3.1)
$\text{Co}^{\text{II}}$	$(1/3) [j_{t2g-\pi^*} + 2j_{eg^*-\pi^*}]$	(7.3.2)
$\text{Ni}^{\text{II}}$	$j_{eg^*-\pi^*}$	(7.3.3)

**Table 7.6c.** The calculated  $j_{t2g-\pi^*}$  values from Eqs. (7.3.1)-(7.3.3) with the obtained  $J_{M-rad}$  values.

Set of equations	$j_{t2g-\pi^*}$
(7.3.1) and (7.3.2)	$-312 \text{ cm}^{-1}$
(7.3.2) and (7.3.3)	$-172 \text{ cm}^{-1}$
(7.3.3) and (7.3.1)	$-242 \text{ cm}^{-1}$

## 7.5 Conclusion

The first complexes where an iron(II) ion is directly coordinated to a verdazyl radical have been successfully prepared. The crystal structure of these complexes determined by X-ray diffraction at room temperature is isomorphous to those previously reported for the nickel(II) and cobalt(II) analogues:<sup>[7]</sup> the system is built from  $[M(\text{vdCOO})_2(\text{H}_2\text{O})_2]$  discrete complexes and crystallization water molecules. At 300 K, one of the coordinated water molecules establishes two long H-bonds with the oxygen atoms of two neighboring carboxylate moieties. At 90 K, this molecule forms either two short H-bonds (LT form) or no H-bonds at all (HT form) (Figure 7.13). Temperature-dependent  $^{57}\text{Fe}$  Mössbauer spectroscopic measurements indicated that the system is composed of HS iron(II) species in the whole temperature range. They also revealed that the two forms of the compound identified at 90 K by X-ray diffraction on a single crystal coexist between 10 and 300 K and allowed determining the thermodynamic parameters associated with the LT-to-HT equilibrium. Finally,  $^2\text{H}$ -MAS-NMR measurements identified a  $180^\circ$  flip-flop motion in the kHz range within the compound and, combined with other structural and spectroscopic methods, allows us to propose a clear picture of this apparently tricky system. The magnetic behavior of the system has been analyzed. It allows us to complete the series previously published.<sup>[7]</sup> It then appears that the exchange interaction between the metal ion and the verdazyl radicals varies from strongly ferromagnetic for the nickel(II) derivative to weakly antiferromagnetic for the iron(II) complex. Such evolution can be considered as a textbook example of the usefulness of Kahn's two-electrons/two-orbitals model as a simple tool in the rational design of molecule-based magnetic compounds.

## References

- [1] (a) O. Kahn, *Molecular Magnetism*, Wiley-VCH, **2003**; (b) *Magnetism: Molecules to Materials I-V*, ed. J. S. Miller and M. Drillon, Wiley-VCH Verlag, **2001-2005**; (c) ed. J. S. Miller and D. Gatteschi, *Chem. Soc. Rev.*, **2011**, *40*, 3053; (d) M. Verdaguer and V. Robert, in *Comprehensive Inorganic Chemistry II*, ed. J. Reedijk and K. Poeppelmeier, Elsevier, Oxford, **2013**, vol. 8, p. 132.
- [2] A. Caneschi, D. Gatteschi and P. Rey, *Prog. Inorg. Chem.*, **1991**, *39*, 331.
- [3] (a) K. Fegy, D. Luneau, T. Ohm, C. Paulsen and P. Rey, *Angew. Chem., Int. Ed.*, **1998**, *37*, 1270; (b) K. Bernot, L. Bogani, A. Caneschi, D. Gatteschi and R. Sessoli, *J. Am. Chem. Soc.*, **2006**, *128*, 7947.
- [4] (a) K. E. Preuss, *Dalton Trans.*, **2007**, 2357; (b) N. Roques, D. Maspoch, I. Imaz, A. Datcu, J. P. Sutter, C. Rovira and J. Veciana, *Chem. Commun.*, **2008**, 3160.
- [5] (a) B. D. Koivisto and R. G. Hicks, *Coord. Chem. Rev.*, **2005**, *249*, 2612; (b) C. Train, L. Norel and M. Baumgarten, *Coord. Chem. Rev.*, **2009**, *253*, 2342.
- [6] (a) R. G. Hicks, M. T. Lemaire, L. K. Thompson and T. M. Barclay, *J. Am. Chem. Soc.*, **2000**, *122*, 8077; (b) L. Norel, F. Pointillart, C. Train, L.-M. Chamoreau, K. Boubekeur, Y. Journaux, A. Brieger and D. J. R. Brook, *Inorg. Chem.*, **2008**, *47*, 2396.
- [7] T. M. Barclay, R. G. Hicks, M. T. Lemaire, L. K. Thompson and Z. Q. Xu, *Chem. Commun.*, **2002**, 1688.
- [8] (a) F. A. Neugebauer, H. Fischer, R. Siegel and C. Krieger, *Chem. Ber.*, **1983**, *116*, 3461; (b) C. L. Barr, P. A. Chase, R. G. Hicks, M. T. Lemaire and C. L. Stevens, *J. Org. Chem.*, **1999**, *64*, 8893.
- [9] G. M. Sheldrick, *Acta Crystallogr., Sect. A: Found. Crystallogr.*, **2008**, *64*, 112.
- [10] MossWinn – Mössbauer spectrum analysis and database software, <http://www.mosswinn.com/>.
- [11] (a) G. Maruta, S. Takeda, R. Imachi, T. Ishida, T. Nogami and K. Yamaguchi, *J. Am. Chem. Soc.*,

**1999**, 121, 424;

(b) P. A. Beckmann and C. Dybowski, *J. Magn. Reson.*, **2000**, 146, 379.

[12] E. Bill, julX, version 1.4.1, Max Planck Institute for Bioinorganic Chemistry, Mulheim an der Ruhr, Germany, 2008, [http://www.mpibac.mpg.de/bac/logins/bill/julX\\_en.php](http://www.mpibac.mpg.de/bac/logins/bill/julX_en.php).

[13] D. J. R. Brook, S. Fornell, B. Noll, G. T. Yee and T. H. Koch, *J. Chem. Soc., Dalton Trans.*, **2000**, 2019.

[14] F. Pointillart, C. Train, P. Herson, J. Marrot and M. Verdaguer, *New J. Chem.*, **2007**, 31, 1001.

[15] P. A. Wood, E. Pidcock and F. H. Allen, *Acta Crystallogr., Sect. B: Struct. Sci.*, **2008**, 64, 491.

[16] (a) P. Gütllich, R. Link and A. X. Trautwein, *Mössbauer Spectroscopy and Transition Metal Chemistry*, Springer, Berlin, **1978**; (b) E. Münck, in *Physical Methods in Bioinorganic Chemistry*, ed. L. Que Jr., University Science Books, Sausalito, **2000**, p. 287; (c) S. Hayami, Z. Gu, M. Shiro, Y. Einaga, A. Fujishima and O. Sato, *J. Am. Chem. Soc.*, **2000**, 122, 7126.

[17] S. Decurtins, P. Gütllich, C. P. Köhler, H. Spiering and A. Hauser, *Chem. Phys. Lett.*, 1984, 105, 1.

[18] (a) K. Morii, G. Maruta and S. Takeda, *Polyhedron*, **2005**, 24, 2607; (b) D. N. Hendrickson and C. G. Pierpont, in *Spin-Crossover in Transition Metal Compounds II*, Topics in Current Chemistry, ed. P. Gütllich and H. A. Goodwin, **2004**, vol. 234, p. 63; (c) M. Sorai, *Spin Crossover in Transition Metal Compounds III*, *Top. Curr. Chem.*, **2004**, 235, 153.

[19] *Nuclear Magnetic Resonance Probes of Molecular Dynamics*, ed. R. Tycko, Kluwer Academic Publishers, The Netherlands, **1994**.

[20] L. Norel, L.-M. Chamoreau and C. Train, *Polyhedron*, **2010**, 29, 342.

[21] J. Rota, C. J. Calzado, C. Train and V. Robert, *J. Chem. Phys.*, **2010**, 132, 154702.

[22] P. Gütllich, A. Hauser and H. Spiering, *Angew. Chem., Int. Ed. Engl.*, **1994**, 33, 2024.

[23] O. Oms, J.-B. Rota, L. Norel, C. J. Calzado, H. Rousselière, C. Train and V. Robert, *Eur. J.*

*Inorg. Chem.*, **2010**, 5373.

[24] J. P. Launay and M. Verdaguer, *Electrons in Molecules, From Basic Principles to Molecular Electronics*, Oxford University Press, Oxford, **2014**, p. 157sq.

## 8. General Conclusions and Perspectives

In this thesis, the development of five sets of molecular systems in terms of the “multifunctionality” in the solid state and the investigation of their physical properties have been described.

Chapter 3 described the development of the functional transparent films with pH-sensitive spin-crossover Fe<sup>II</sup> complex, [Fe<sup>II</sup>(diAMsar)], immobilized in Nafion membrane. The spin state and the color of [Fe<sup>II</sup>(diAMsar)]@Nafion were successfully controlled by buffer solution. Besides, the spin state can be detected by the megascopic color change due to the change in d-d splitting. This system is breakthrough not simply because transparent films can be produced by a very simplified method but because the spin state can be controlled by proton flow induced by the applied voltage. This is hardly achieved in a solution state and in other nonconducting polymeric membranes. Particularly, proton conduction may not occur due to the electric double layer in a usual solution state. In the future, it is desired to make an effort to control the spin state of [Fe<sup>II</sup>(diAMsar)]@Nafion by proton flow at will by changing incorporated quantity of the complex into Nafion, pH condition, humidity, and so forth.

Expanding beyond the study described in Chapter 3, Chapter 4 described the development of pH-dependent emissive complex films, where the ruthenium(II) complex [(bpy)<sub>2</sub>Ru<sup>II</sup>(H<sub>2</sub>bpib)Ru<sup>II</sup>(bpy)<sub>2</sub>] and the iridium(III) complex [Ir<sup>III</sup>(Hbip)(Mebib)] were immobilized in Nafion and investigated their emission properties. The pH-sensitive emission property of [(bpy)<sub>2</sub>Ru<sup>II</sup>(H<sub>2</sub>bpib)Ru<sup>II</sup>(bpy)<sub>2</sub>]@Nafion was successfully observed, but the proton conduction hardly occurred due to the bulkiness of [(bpy)<sub>2</sub>Ru<sup>II</sup>(H<sub>2</sub>bpib)Ru<sup>II</sup>(bpy)<sub>2</sub>]. In the film of [Ir<sup>III</sup>(Hbip)(Mebib)]@Nafion, not only the pH-dependent emission intensity but also pH-dependent quantum yield ( $\Phi$ ) and lifetime ( $\tau$ ) was observed. Furthermore,  $\Phi$  and  $\tau$  in the film state were superior to those in the solution state; this result clearly shows a great advantage for immobilizing

the emissive complex in Nafion. In the future, development of transparent emissive materials whose emission property including emission colors can be controlled by applied voltage (via proton flow) is desired.

Chapter 5 described the ligand field analysis in the pre-edge region of XANES (X-ray absorption near edge structure) spectra for one-dimensional Fe<sup>II</sup> spin-crossover polymers [Fe<sup>II</sup>(NH<sub>2</sub>-trz)<sub>3</sub>](C<sub>n</sub>H<sub>2n+1</sub>SO<sub>3</sub>)<sub>2</sub>·xH<sub>2</sub>O (*n* = 1–9). The changes in spin-transition temperatures (*T*<sub>1/2</sub>) and ligand field parameters (10*Dq* and the Racah parameter *B*) were investigated for one-dimensional Fe<sup>II</sup> spin-crossover polymers with alkanesulfonate as counteranions. *T*<sub>1/2</sub> and 10*Dq*/*B* are closely linked and dominated by a uniaxial chemical pressure along the Fe<sup>II</sup> chain axis due to “fastener effect” between alkyl chain of counteranions, which are clarified from the minute analysis of XANES and <sup>57</sup>Fe Mössbauer spectroscopy. At the present time, this is the first report on the systematic relationship between the spin-crossover behaviors and ligand field parameters. Future works should perform a calculation of the Fe-N coordination bond angles by DFT method and make clear much further the relationship between *T*<sub>1/2</sub> and p-d mixing.

Chapter 6 described the attempt to control the spin state of Fe<sup>III</sup> spin-crossover complex by the photoisomerization of counter-anion SPSO<sub>3</sub><sup>-</sup>. The light irradiation at room temperature induced the remarkable change in the temperature dependence of  $\chi_{\text{mol}}T$  below 150 K, but the precise crystal structures of [Fe<sup>III</sup>(qsal)<sub>2</sub>]SPSO<sub>3</sub> after the irradiation remain unclear. At least, the spin state after the irradiation is desired to be confirmed by <sup>57</sup>Fe Mössbauer spectroscopy or other valuable methods in the future.

Chapter 7 described the two essential points, namely, molecular magnetism and the anomalous behavior of <sup>57</sup>Fe Mössbauer spectra of verdazyl radical-coordinated Fe<sup>II</sup> complex [Fe<sup>II</sup>(vdCOO)<sub>2</sub>(H<sub>2</sub>O)<sub>2</sub>]·2H<sub>2</sub>O responsible for the “tricky” water molecule occupied in the axial position. The first concerns the magnetic properties of the complex, specifically detailing the

intramolecular exchange (Fe-radical, radical-radical) interactions. The second issue concerns the structure itself, which contains both coordinated and free (but hydrogen bonded) water molecules in the crystal lattice. The structure and dynamics were probed using a combination of  $^{57}\text{Fe}$  Mössbauer, solid-state  $^2\text{H}$ -MAS-NMR, and X-ray crystallography. They identified the two forms of the complex and provided the clear picture of this apparently tricky system. Although the dynamics of the coordinated water molecule is not directly related with the magnetic properties of the system, that finding are unprecedented in such metal-radical complexes. The structural analysis will be of interest to supramolecular chemists and crystal engineers interested in non-covalent interactions.

In this way, the researches on developing multifunctional material have been conducted. It is very important to control energies of electronic state, crystal structures, intermolecular interactions, and so forth. In addition, metal complexes are highly useful to establish multifunctional systems by choosing appropriate combination of metal ions and chemically-modified ligands. In the future, crystal engineering and chemistry of soft matter will be critical to achieve the practical use of multifunctional materials. Specifically, taking into account the importance of non-covalent interactions in various materials, some of the efforts should go to developments of soft materials with multifunctionality. It is desired that the molecular science and the materials science of multifunctional materials will blossom more than ever.